

**Simulating the Selective Adsorption of
Pertechnetate to Oxyanion-SAMMS**

Doctor of Philosophy

Department of Materials Science and Engineering

University of Sheffield

Christopher D. Williams

November 2014

Abstract

The environmental remediation of ^{99}Tc contaminated land and water is one of the most difficult challenges facing the nuclear industry. The problem stems from the fact that ^{99}Tc has a long half-life, high fission yield and readily forms the extremely mobile pertechnetate oxyanion, TcO_4^- , in aqueous solution. Many of the current methods for remediating TcO_4^- suffer from poor selectivity in the presence of competing anions and are dependent on specific reducing conditions. However, self-assembled monolayers on mesoporous supports (SAMMS) have been proposed as an effective alternative for TcO_4^- remediation. SAMMS combine a robust inorganic mesoporous support with a highly selective functionalised monolayer that can be tuned to target the contaminant species of interest. When functionalised with a monolayer of Fe^{3+} complexes it has been shown experimentally to selectively adsorb the monovalent TcO_4^- preferentially over competing divalent species, such as sulphate (SO_4^{2-}). In order to tailor the design of oxyanion-SAMMS to optimise its performance, an improved understanding of the cause of this selectivity is required.

In this thesis, a novel approach to the construction of realistic models of oxyanion-SAMMS is reported, with the aim of performing simulations to advance our understanding of the use of SAMMS as a TcO_4^- remediation tool. In order to investigate the properties of SAMMS on many length scales, a multiscale modelling approach was adopted, involving quantum mechanics, atomistic simulations (molecular dynamics and Monte Carlo) and equilibrium calculations based on Poisson-Boltzmann theory. This is the first reported model of SAMMS for use in the aqueous environment and the overall approach could be extended to many other remediation problems. The simulations show that a single Fe^{3+} complex is selective for SO_4^{2-} over TcO_4^- in aqueous solution. This result is contrary to the experimental evidence and implies that the mesoscopic structure of the material must in part be responsible for the observed selectivity. Further simulations suggest Cl^- counterions generate a negative electrostatic potential in the SAMMS pore, resulting in significantly larger free energy barriers to pore entry for divalent anions compared to monovalent ones. This observation may have much more general implications for the selective remediation of contaminant ions using porous materials.

Table of Contents

| | |
|--|-----------|
| Acknowledgements | vi |
| List of Figures | vii |
| List of Tables | xiv |
| List of Abbreviations | xvii |
| List of Symbols | xviii |
| | |
| 1. Introduction | 1 |
| 1.1. Nuclear Waste Management | 1 |
| 1.2. Project Scope | 2 |
| 1.2.1. Aims and Hypothesis | 2 |
| 1.2.2. Structure of this Thesis | 3 |
| | |
| 2. Technetium | 4 |
| 2.1. Sources | 4 |
| 2.2. Technetium in the Environment | 6 |
| 2.2.1. Geochemical Mobility | 7 |
| 2.2.2. Accumulation in Food | 8 |
| 2.3. Options for Technetium Remediation | 9 |
| 2.3.1. Performance Criteria | 10 |
| 2.3.2. Natural Materials | 11 |
| 2.3.3. Other Materials | 12 |
| 2.3.4. Summary | 14 |
| | |
| 3. SAMMS | 16 |
| 3.1. Structure | 16 |
| 3.2. Synthesis | 17 |
| 3.2.1. MCM-41 | 17 |
| 3.2.2. Functionalised MCM-41 | 18 |
| 3.3. Oxyanion-SAMMS | 20 |

| | |
|--|-----------|
| 3.3.1. Amine Monolayers | 20 |
| 3.3.2. Transition Metal Complex Monolayers | 21 |
| 3.4. Summary | 23 |
| | |
| 4. Computational Methods | 24 |
| 4.1. Electronic Structure Methods | 24 |
| 4.1.1. Density Functional Theory | 26 |
| 4.1.2. Exchange-Correlation Functionals | 29 |
| 4.1.3. Basis Sets | 30 |
| 4.1.4. Practical Considerations for DFT Calculations | 32 |
| 4.2. Classical Potential Energy Functions | 33 |
| 4.2.1. Intermolecular Potentials | 34 |
| 4.2.2. Intramolecular Potentials | 35 |
| 4.3. Statistical Mechanics | 36 |
| 4.3.1. Statistical Ensembles | 37 |
| 4.4. Molecular Simulation | 40 |
| 4.4.1. Monte Carlo Simulations | 41 |
| 4.4.2. Molecular Dynamics Simulations | 42 |
| 4.4.3. Practical Considerations for Molecular Simulations | 44 |
| 4.4.4. Free Energy Calculations | 50 |
| 4.5. Implementation of Computational Methods in this Thesis | 52 |
| | |
| 5. Hydrated Oxyanions | 53 |
| 5.1. Introduction | 53 |
| 5.2. Quantum Mechanical Models | 53 |
| 5.2.1. Geometry Optimisation | 53 |
| 5.2.2. Free Energy of Hydration | 55 |
| 5.3. Development of a Classical Force Field | 60 |
| 5.3.1. Initial Parameter Set | 60 |
| 5.3.2. Parameter Optimisation | 61 |
| 5.4. Molecular Dynamics Simulations | 66 |
| 5.4.1. Hydrated Structure | 66 |
| 5.4.2. Transport Properties | 71 |
| 5.4.3. Enthalpy of Hydration | 74 |

| | |
|---|-----------|
| 5.5. Conclusions | 75 |
| 6. Adsorption of Oxyanions to the Fe³⁺-EDA Complex | 77 |
| 6.1. Introduction | 77 |
| 6.2. Quantum Mechanical Models | 78 |
| 6.2.1. Structure of the Fe ³⁺ -EDA Complex | 78 |
| 6.2.2. Free Energy of Ligand Exchange | 79 |
| 6.3. Development of a Classical Force Field for Fe ³⁺ -EDA | 82 |
| 6.4. PMF Simulations | 85 |
| 6.4.1. PMFs for Water Exchange on Fe ³⁺ -EDA | 86 |
| 6.4.2. PMFs for Anion Exchange with Water on Fe ³⁺ -EDA | 89 |
| 6.4.3. PMFs for Oxyanion Exchange with Chloride on Fe ³⁺ -EDA | 93 |
| 6.4.4. PMF for Direct Exchange of TcO ₄ ⁻ with SO ₄ ²⁻ on Fe ³⁺ -EDA | 94 |
| 6.5. Conclusions | 96 |
| 7. MCM-41 | 98 |
| 7.1. Introduction | 98 |
| 7.2. Previous Models of MCM-41 | 98 |
| 7.3. MCM-41 Model Construction and Validation | 100 |
| 7.3.1. Force Field Parameters | 100 |
| 7.3.2. Model Preparation | 101 |
| 7.3.3. Validity of the Model Structure | 103 |
| 7.4. Adsorption Isotherms | 108 |
| 7.4.1. Force Field Parameters | 108 |
| 7.4.2. Grand Canonical Monte Carlo Simulations | 109 |
| 7.4.3. Carbon Dioxide | 110 |
| 7.4.4. Dinitrogen | 115 |
| 7.5. Isosteric Heats of Adsorption | 117 |
| 7.5.1. Adsorption at Zero Coverage | 118 |
| 7.5.2. Development of a Monte Carlo Algorithm | 118 |
| 7.5.3. Isosteric Heats of Adsorption in Amorphous Silica | 124 |
| 7.6. Conclusions | 131 |

| | |
|---|------------|
| 8. Functionalised MCM-41 | 133 |
| 8.1. Introduction | 133 |
| 8.2. Previous Models of Functionalised MCM-41 | 133 |
| 8.3. A New Model for Functionalised MCM-41 | 134 |
| 8.3.1. Model Preparation | 137 |
| 8.3.2. Force Field Parameters | 138 |
| 8.3.3. Simulation Protocol | 139 |
| 8.3.4. Monolayer Structure | 140 |
| 8.4. Determining the Affinity of Oxyanions for Functionalised MCM-41 | 147 |
| 8.4.1. Model Preparation | 147 |
| 8.4.2. Simulation Protocol | 147 |
| 8.4.3. PMFs for Oxyanions Entering the Functionalised Pores | 150 |
| 8.4.4. Electrostatic Potential in Functionalised Pores | 152 |
| 8.4.5. Oxyanion Dehydration in Functionalised Pores | 158 |
| 8.5. Conclusions | 160 |
| | |
| 9. Speciation of Oxyanions at the Silica - Water Interface | 161 |
| 9.1. Introduction | 161 |
| 9.2. Calculation Setup | 162 |
| 9.2.1. Modelling the Solution | 162 |
| 9.2.2. Modelling the Surface | 163 |
| 9.2.3. Determination of Activity Coefficients | 165 |
| 9.3. Results | 168 |
| 9.3.1. Concentration Effects | 168 |
| 9.3.2. pH Effects | 170 |
| 9.4. Conclusions | 173 |
| | |
| 10. Conclusions | 175 |
| 10.1. Summary of Key Findings | 176 |
| 10.2. General Remarks for TcO_4^- Remediation | 178 |
| 10.3. Suitability of Computational Modelling Techniques | 179 |
| 10.4. Scope for Further Work | 180 |
| 10.4.1. Model Development | 180 |
| 10.4.2. Additional Simulations | 181 |

| | | |
|--|-------|------------|
| References | | 183 |
| Appendix One: Classical Force Field Parameters | | 201 |
| Appendix Two: MCM-41 Model Structural Data | | 208 |

Acknowledgements

Throughout this project I have been extremely fortunate to have several supervisors so closely linked with the day-to-day research. Karl Travis, my main supervisor, provided the original idea for the project. Without his close supervision and eye for detail the research almost certainly would not have advanced as far as it has. The numerous discussions I held with my co-supervisor, Neil Burton, were occasionally mind-boggling but always thought provoking. I have hugely benefitted from Karl and Neil's combined academic wisdom and passion for research. As a third supervisor, John Harding's contribution to the project should not be overlooked, especially in our quarterly progress meetings. There are numerous others on both sides of the Pennines that have helped me along the way and I'd like to thank everyone from the ISL and MESAS modelling group in Sheffield and the theoretical chemistry group in Manchester, as well as those from my Nuclear FiRST cohort. Many others have provided insightful discussions about the research, including Peter Monson, Keith Gubbins, Matthias Thommes, John Purton and Nigel Seaton. In addition, Tina Düren and Yufeng He generously provided useful experimental data for the purpose of model validation.

Finally, I should acknowledge the continuing support of my parents over the last four years and all my close friends for doing their best to hinder my progress by continuously teasing me with rivers, mountains and triathlons when I should have been locked in an office working on this project.

As part of the Nuclear FiRST Centre for Doctoral Training, the project was funded by the Engineering and Physical Sciences Research Council (EPSRC).

List of Figures

| | | |
|-----|---|----|
| 2.1 | Pourbaix diagram showing Tc speciation in various E_h /pH conditions. | 7 |
| 2.2 | Discharge of Tc from the pipeline at Sellafield and the concentration of Tc in lobster in the Irish Sea from 1994 to 2012. | 9 |
| 2.3 | The mechanism for adsorption of TcO_4^- to the Cu-EDA functionalised TiO_2 particles. On the right-hand side the displaced H_2O is not pictured. | 14 |
| 3.1 | The surfactant templating mechanism used to synthesize MCM-41. | 18 |
| 3.2 | A pair of propyl-EDA chains grafted onto an amorphous silica surface. | 19 |
| 3.3 | The amino-azacryptand used to encapsulate ReO_4^- and TcO_4^- . | 20 |
| 3.4 | Proposed mechanism of oxyanion binding to Cu^{2+} -EDA-SAMMS. | 22 |
| 3.5 | Proposed mechanism of oxyanion binding to Fe^{3+} -EDA-SAMMS. | 23 |
| 4.1 | A 2D illustration of cubic PBCs. When a particle from the central cell (bold line), b, moves past the right hand boundary, an identical image particle, b', replaces it by entering through the left hand boundary | 46 |
| 4.2 | The Ewald summation (d), in which each point charge (a) is screened by a Gaussian distribution, evaluated in real space (b) that is cancelled out by an equal and opposite Gaussian distribution evaluated in reciprocal space (c). | 49 |
| 5.1 | Potential energy surface for the Tc – O bond stretch generated at the M06 level of theory. | 61 |
| 5.2 | Model used to parameterise the TcO_4^- force field. The same procedure was used for SO_4^{2-} . | 62 |
| 5.3 | Radial distribution functions showing the structure of SPC/E water molecules around XO_4^{n-} ions. $g_{X-Ow}(r)$ is represented by solid lines and $g_{O-Ow}(r)$ by dashed lines. X = Tc (black) and X = S (red). | 68 |

| | | |
|------------|--|----|
| 5.4 | $g_{\text{O-HW}}(r)$ for XO_4^{n-} in SPC/E H_2O . $X = \text{Tc}$ (black) and $X = \text{S}$ (red). | 69 |
| 5.5 | $g_{\text{X-OW}}(r)$ (solid line), and its integral (dotted line), for $X = \text{Tc}$ (black) and $X = \text{S}$ (red) in H_2O . | 70 |
| 5.6 | Snapshots from the MD simulations showing H_2O structure around TcO_4^- (left) and SO_4^{2-} (right). The colours correspond to element type; Tc (pink), S (yellow), O (red), H (white). | 70 |
| 5.7 | $g_{\text{Cl-OW}}(r)$ (solid) and its integral (dots) for Cl^- in SPC/E H_2O . | 71 |
| 5.8 | MSDs of XO_4^{n-} where $X = \text{Tc}$ (black) and S (red) obtained from the $L = 32 \text{ \AA}$ simulation cell. | 73 |
| 5.9 | Diffusion coefficients for XO_4^{n-} in water, where $X = \text{Tc}$ (black) and S (red) obtained from simulations with various cell lengths. | 74 |
| 6.1 | Exchange of ligands, L ($L = \text{Cl}^-/\text{H}_2\text{O}$), with a general oxyanion, XO_4^{n-} ($X = \text{Tc}/\text{S}$), on the Fe^{3+} -EDA complex. EDA hydrogen atoms are omitted for clarity and each species is in aqueous solution. | 77 |
| 6.2 | The geometry of the <i>trans</i> (left) and <i>cis</i> (right) isomers of the initial $[\text{Fe}(\text{EDA})_2(\text{Cl})_2]^+$ complex. | 78 |
| 6.3 | Contributions to the aqueous ligand exchange process. $L = \text{H}_2\text{O}/\text{Cl}^-$, $X = \text{Tc}/\text{S}$. | 79 |
| 6.4 | Model used to parameterise the force field by fitting ΔE and r_{eq} to the DFT interaction of two TcO_4^- ligands with <i>trans</i> Fe^{3+} -EDA from DFT. An analogous fitting procedure was used for the other ligands. | 84 |
| 6.5 | $g_{\text{Fe-OW}}(r)$ (black, solid line) and its integral (red, dashed line) obtained from a simulation of the Fe^{3+} -EDA complex in water. | 87 |
| 6.6 | PMFs for H_2O exchange at the axial positions of the Fe^{3+} -EDA complex, estimated from $g_{\text{Fe-OW}}(r)$ (solid line), Equation 6.3, and obtained from umbrella sampling simulations and Equation 4.84 (dashed line). | 88 |
| 6.7 | Histograms (generated using WHAM) showing the overlap of sampling | 89 |

| | | |
|-------------|---|-----|
| | between adjacent simulation windows. | |
| 6.8 | PMF for Cl^- exchange with H_2O . | 90 |
| 6.9 | PMFs for XO_4^{n-} exchange with H_2O . $\text{X} = \text{Tc}$ (solid line) and $\text{X} = \text{S}$ (dashed line). | 92 |
| 6.10 | Snapshots of typical configurations at the point of XO_4^{n-} exchange with H_2O showing average Fe^{3+} - ligand distances; a) $\text{X} = \text{Tc}$, from the 4.75 Å window, b) $\text{X} = \text{S}$, from the 4.5 Å window. | 93 |
| 6.11 | PMFs for XO_4^{n-} exchange with Cl^- . $\text{X} = \text{Tc}$ (solid line) and $\text{X} = \text{S}$ (dashed line). | 94 |
| 6.12 | PMF for the exchange of TcO_4^- with SO_4^{2-} on Fe^{3+} -EDA. | 95 |
| 6.13 | Snapshots obtained from the MD simulations for the exchange of TcO_4^- with SO_4^{2-} from the a) 6.5, b) 4.3 and c) 3.6 Å windows. | 96 |
| 7.1 | A view down the central pore of the Maddox <i>et al.</i> model of MCM-41. | 99 |
| 7.2 | The sequence of steps in the preparation of the MCM-41 models; a) quenched amorphous silica, b) carving of cylindrical pores, c) relaxation after removal of silicon and oxygen atoms on the pore surface and d) addition of hydrogen atoms to non-bridging oxygen atoms. Yellow, red and white atoms are silicon, oxygen and hydrogen, respectively. | 102 |
| 7.3 | The periodic hexagonal mesoporous network of MCM-41, generated by replication of the central simulation cell four times in the x and y directions. | 102 |
| 7.4 | $g_{\text{O-O}}(r)$ in amorphous silica obtained after quenching from 7300 to 300 K at rates of 1 (solid line), 10 (dashes), and 7000 (dots/dashes) K ps^{-1} and for the silica melt at 7300 K (dots). Inset: expanded $g_{\text{O-O}}(r)$ for the region between 2.5 and 5.5 Å. | 104 |
| 7.5 | The difference between surface areas defined by the solvent accessible and Connolly approaches. | 105 |

- 7.6** MCM-41 models with a wall thickness of 0.95 nm and pore diameters increasing from 2.41 nm (top left) to 5.90 nm (bottom right) 106
- 7.7** The dependence of surface area (left) and pore volume (right) on preparation quench rate for MCM-41 models with 3.5 nm pore diameter and 0.95 nm wall thickness. 107
- 7.8** Optimisation of ϵ_0 to fit the simulated (red) CO₂ adsorption isotherm to experiment (black). $\epsilon_0/k_B = 228.4$ K (dashes), 250 K (solid), 275 K (dots) and 300 K (dashes/dots). 112
- 7.9** Isotherm for CO₂ adsorption to MCM-41 with a pore diameter of 3.16 nm at 265 K for the pressure regions: a) up to the pore filling, b) less than 1 atm and c) the linear region. The solid black line is the experimental data and the red circles indicate the simulated data. The red dashed line through the simulated data is a guide to the eye in a) and b) and a line of best fit in the linear region for c). 113
- 7.10** Final configurations of GCMC simulations for CO₂ adsorption in MCM-41 at pressures: a) prior to monolayer formation (1 atm), b) on formation of a monolayer (5 atm), c) multilayer formation prior to capillary condensation (10 atm) and d) for the pore approaching its maximum capacity (15 atm). 114
- 7.11** Simulated isotherms for adsorption of CO₂ in MCM-41 with pore diameters of 2.41 (squares), 2.81 (crosses), 3.16 (diamonds), 3.50 (circles) and 3.85 (triangles) nm. 115
- 7.12** Simulated isotherm for adsorption of N₂ in MCM-41 with a pore diameter of 3.16 nm at 77 K. 116
- 7.13** Density profile for oxygen atoms, N_O , within a 5.0 Å radius of atom i in an MCM-41 model. 119
- 7.14** V_N^{real} (red) and $V_N^{\text{recip}} + V_N^{\text{self}}$ (blue) contributions to the overall energy V_N^{elec} (black) as a function of α in the Ewald summation for the electrostatic energy of the neutral 3.16 nm pore diameter and 0.95 nm wall thickness 122

- MCM-41 model.
- 7.15** V_N^{real} (red), $V_N^{\text{recip}} + V_N^{\text{self}}$ (blue) and V_N^{neut} (green) contributions to the overall energy V_N^{elec} (black) as a function of α in the Ewald summation for the electrostatic energy of the deprotonated 3.16 nm pore diameter MCM-41 model. 122
- 7.16** q_{st}^0 obtained from a calculation of CO₂ in MCM-41 (pore diameter = 3.5 nm) using the Ewald potential tabulated at different grid resolutions (black) compared to the value obtained for the computation of the Ewald sum at every new configuration (red). 123
- 7.17** The convergence of q_{st}^0 with decreasing quench rate for CO₂ (squares), Kr (circles), Ar (crosses) and N₂ (triangles) in MCM-41. The dashed lines are added as a guide to the eye. 125
- 7.18** The relationship between q_{st}^0 and pore diameter for the four adsorbates studied; CO₂ (squares), Kr (circles), Ar (crosses) and N₂ (triangles), at 298 K in a MCM-41 model with pore walls of 0.95 nm thickness. 127
- 7.19** The effect of MCM-41 model wall thickness on q_{st}^0 for the four adsorbates studied; CO₂ (squares), Kr (circles), Ar (crosses) and N₂ (triangles), at 298 K for models with a constant pore diameter of 3.5 nm. 128
- 7.20** Favourable end-on adsorption of CO₂ on the amorphous silica surface. 129
- 7.21** The slit-pore model with a diameter of 3.5 nm. 130
- 8.1** Q¹, Q² and Q³ chains comprising the propyl-EDA functionalised amorphous silica surface. 136
- 8.2** The [Fe(EDA)₂(Cl)₂]⁺ complex, formed by addition of FeCl₃ to a propyl-EDA functionalised amorphous silica surface. 136
- 8.3** A single propyl-EDA chain on the slit pore surface at the end of equilibration in the gas phase (top) and in aqueous solution (bottom). 142
- 8.4** A single [Fe(EDA)₂(Cl)₂]⁺ complex on the slit pore surface at the end of 143

- 100 ps of equilibration in solution. The pink and turquoise spheres are the Fe^{3+} and Cl^- ions, respectively.
- 8.5** The radial distribution function (black, solid line) and its integral (red, dashed) for the Fe – Cl pair. 144
- 8.6** Radial density profiles, ρ_{xy} , of Fe^{3+} (black) and Cl^- (red) in the $[\text{Fe}(\text{EDA})_2(\text{Cl})_2]^+$ functionalised MCM-41 pore. 145
- 8.7** The model of MCM-41 (bare pore diameter = 2.81 nm) functionalised with a monolayer of $[\text{Fe}(\text{EDA})_2(\text{Cl})_2]^+$ complexes where the pores have been filled with one Cl^- ion per complex and SPC/E water. 146
- 8.8** A snapshot of the external face (x - y plane) of the ‘open’ propyl-EDA functionalised MCM-41 models (pore diameters of a) 2.41 nm, b) 2.81 nm and c) 3.16 nm) used in the PMF simulations. 149
- 8.9** A snapshot of the side (x - z plane) of the propyl-EDA functionalised MCM-41 model, taken from the $z = 20 \text{ \AA}$ window of the PMF for TcO_4^- entering the 2.81 nm pore diameter model. 150
- 8.10** PMFs for TcO_4^- (red) and SO_4^{2-} (blue) entering propyl-EDA functionalised MCM-41 models, with pore diameters of 2.41 (solid), 2.81 (dashed) and 3.16 (dots) nm. 151
- 8.11** Profiles of the mean electrostatic potential through the open propyl-EDA functionalised MCM-41 with pore diameters of 2.41 (solid), 2.81 (dashed) and 3.16 (dots) nm. 153
- 8.12** PMFs estimated from the electrostatic potential profiles for XO_4^{n-} , ($\text{X} = \text{Tc}$ (red) and $\text{X} = \text{S}$ (blue)) entering open propyl-EDA functionalised MCM-41 models with pore diameters of 2.41 (solid), 2.81 (dashed) and 3.16 (dots) nm. 155
- 8.13** Electrostatic potential profile in the periodic $[\text{Fe}(\text{EDA})_2(\text{Cl})_2]^+$ functionalised pore. 157
- 8.14** The number of H_2O molecules in the primary (squares) and secondary 159

- (circles) hydration shells of SO_4^{2-} (ie. those less than 4.4 Å and 6.8 Å from S, respectively) in each window for the 2.41 nm pore diameter model.
- 9.1** A flow chart summarising the procedure for determining the electrostatic potential profile and ion concentration profiles using Poisson-Boltzmann theory. 167
- 9.2** Profile of the electrostatic potential in solution near an amorphous silica surface at bulk solution pH 7. 168
- 9.3** Ion concentration profiles for a solution containing $10^{-3} \text{ mol dm}^{-3}$ concentrations of KTcO_4 and K_2SO_4 at pH 7 in contact with an amorphous silica surface. Concentrations of H^+ (solid) and OH^- (dashed) ions are shown with a black line and K^+ , TcO_4^- and SO_4^{2-} are shown with green, red and blue lines, respectively. 169
- 9.4** Ion concentration profiles for a solution containing $10^{-3} \text{ mol dm}^{-3}$ of K_2SO_4 and $10^{-10} \text{ mol dm}^{-3}$ of KTcO_4 at bulk pH 7 in contact with an amorphous silica surface. Concentrations of H^+ (solid) and OH^- (dashed) ions are shown with a black line and K^+ , TcO_4^- and SO_4^{2-} are shown with green, red and blue lines, respectively. 170
- 9.5** Effect of bulk pH on electrostatic potential near the charged amorphous silica surface. 171
- 9.6** Dependence of $[\text{TcO}_4^-]$ (red, circles) and $[\text{SO}_4^{2-}]$ (blue, squares) on bulk solution pH, 1.0 nm from the surface. 172

List of Tables

| | | |
|------|---|----|
| 2.1 | Isotopes of Tc produced in the fission of ^{235}U . | 5 |
| 5.1 | The dependence of r_{TcO} on basis set and the percentage error from the experimentally determined bond length. | 55 |
| 5.2 | The standard thermodynamic quantities of anion hydration for TcO_4^- , SO_4^{2-} and Cl^- at 1 atm and 298 K. | 56 |
| 5.3 | Comparison of ΔG_{hyd} for anions using implicit solvation models and the B3LYP functional. Units: kJ mol^{-1} . | 58 |
| 5.4 | Comparison of ΔG_{hyd} for anions using implicit solvation models and the M06 functional. Units: kJ mol^{-1} . | 58 |
| 5.5 | Force field parameters for the SPC/E model of water. | 63 |
| 5.6 | Comparison of ΔE and r_{eq} calculated using the optimised force field and DFT for the two oxyanions. | 64 |
| 5.7 | Final optimised force field parameters used for TcO_4^- and SO_4^{2-} . | 65 |
| 5.8 | The performance of several Cl^- force fields and the percentage errors in ΔE and r_{eq} compared to the DFT calculations. | 66 |
| 5.9 | Anion ΔH_{hyd} obtained from the MD simulations and the percentage error compared to experiment. Units: kJ mol^{-1} . | 75 |
| 5.10 | Summary of selected data obtained from the MD simulations of the two hydrated oxyanions. | 76 |
| 6.1 | The free energy terms contributing to the thermochemical cycle for ligand exchange using the CPCM-UAKS solvation model. Units: kJ mol^{-1} . | 81 |
| 6.2 | The free energy terms contributing to the thermochemical cycle for ligand exchange using the SMD solvation model. Units: kJ mol^{-1} . | 81 |

| | | |
|------------|--|-----|
| 6.3 | Force field parameters for the Fe^{3+} -EDA complex. | 83 |
| 6.4 | Comparison of ΔE and r_{eq} for the interaction between Fe^{3+} and each ligand, calculated from the optimised force field and DFT. | 84 |
| 6.5 | Final optimised values of σ_{Fe} for each ligand interaction. | 85 |
| 6.6 | Contributions to $\Delta G_{\text{ex, aq}}$ for each ligand exchange event on the <i>trans</i> Fe^{3+} -EDA complex at 298 K. Units: kJ mol^{-1} . | 90 |
| 7.1 | Parameters used in the preparation of MCM-41 models. | 100 |
| 7.2 | TraPPE parameters for CO_2 and N_2 . | 109 |
| 7.3 | Optimised parameters for MCM-41 used in the MC simulations. | 112 |
| 7.4 | The relative contributions to the Ewald sum and a comparison of the total sum with DL_POLY Classic using the 3.16 nm pore diameter MCM-41 model. | 121 |
| 7.5 | Parameters for single-site models of the gas adsorbate species. | 124 |
| 7.6 | q_{st}^0 and K_{H} in MCM-41, averaged over 12 models with pore diameters ranging from 2.41 to 5.90 nm and a pore wall thickness of 0.95 nm. | 126 |
| 7.7 | Adsorption data for CO_2 and N_2 in MCM-41 with a pore diameter of 3.5 nm and wall thickness of 0.95 nm at 298 K. | 129 |
| 7.8 | q_{st}^0 and K_{H} for each adsorbate in the amorphous silica slit-pore at 298 K. | 131 |
| 8.1 | Parameters for the organic chain linking the amorphous silica to the first N in the propyl-EDA chain. | 139 |
| 8.2 | $\Delta F_{\text{barrier}}$ associated with each oxyanion entering the propyl-EDA functionalised MCM-41 pores. | 151 |
| 8.3 | The magnitude of the electrostatic potential in the centre of the pore and the estimated Helmholtz free energy barriers for oxyanion pore entry. | 155 |
| 9.1 | Acid dissociation constants for species in solution. | 163 |

| | | |
|------------|---|-----|
| 9.2 | Pitzer parameters for the binary interaction between atoms i and j . | 166 |
| 9.3 | Pitzer parameters for the ternary interaction between atoms i, j and k . | 166 |
| 9.4 | The effect of bulk pH on the extent of surface ionisation, electrostatic potential and oxyanion concentration, 1.0 nm from the surface. | 173 |

List of Abbreviations

| | |
|--------|---|
| BKS | van Beest, Kramer, van Santen |
| (C)PCM | (conductor-like) polarizable continuum model |
| DFT | density functional theory |
| EARP | Enhanced Actinide Removal Plant |
| EDA | ethylenediamine |
| EXAFS | extended X-ray absorption fine structure |
| GCMC | grand canonical MC |
| GDF | geological disposal facility |
| GGA | generalized gradient approximation |
| GTO | Gaussian type orbital |
| HF | Hartree-Fock |
| IUPAC | International Union of Pure and Applied Chemistry |
| LJ | Lennard-Jones |
| LSDA | local spin density approximation |
| MC | Monte Carlo |
| MCM | Mobil Composition of Matter |
| MD | molecular dynamics |
| MSD | mean squared displacement |
| MUE | mean unsigned error |
| OPLS | optimised potentials for liquid simulations |
| PB | Poisson-Boltzmann |
| PBC | periodic boundary conditions |
| PES | potential energy surface |
| PMF | potential of mean force |
| PNNL | Pacific Northwest National Laboratory |
| QM | quantum mechanics |
| SAMMS | self-assembled monolayers on mesoporous supports |
| SCRf | self consistent reaction field |
| SMD | solvation model based on density |
| SPC/E | extended simple point charge |
| TPPB | tetraphenylphosphonium bromide |
| TraPPE | transferrable potentials for phase equilibria |
| VDW | van der Waal |
| WHAM | weighted histogram analysis method |

List of Symbols

| | |
|-----------------------|---|
| A | instantaneous value of a thermodynamic observable |
| A_{obs} | average value of a thermodynamic observable |
| D | diffusion coefficient |
| D_{T} | tracer diffusion coefficient |
| E | total energy |
| E_{el} | total electronic energy |
| E_{DFT} | total DFT energy |
| E_{c} | electron correlation energy |
| E_{x} | electron exchange energy |
| E_{xc} | exchange-correlation energy |
| F | Helmholtz free energy |
| G | Gibbs free energy |
| H | enthalpy |
| \hat{H} | Hamiltonian operator |
| \hat{H}_{el} | electronic Hamiltonian operator |
| I | ionic strength |
| J | flux |
| K | kinetic energy |
| K_{N} | total kinetic energy of N particles |
| K_{a} | acid dissociation constant |
| K_{d} | distribution coefficient |
| K_{H} | Henry law constant |
| K_{M} | formation constant for cation M |
| K_{ni} | kinetic energy of a non-interacting system of electrons |
| L | length of the side of a simulation cell |
| N | number of particles |
| N_{c} | number of constraints |
| N_{e} | number of electrons |
| N_{f} | number of degrees of freedom |
| N_{orb} | number of orbitals |
| N_{n} | number of nuclei |

| | |
|--------------------|--|
| N_{trial} | number of MC moves |
| N_0 | normalisation constant |
| M | Madelung constant |
| P | pressure |
| P_c | critical pressure |
| Q | partition function |
| R | ideal gas constant ($8.314 \text{ J K}^{-1} \text{ mol}^{-1}$) |
| \mathbf{R} | position vector of an atomic nucleus |
| S | entropy |
| T | temperature |
| T_c | critical temperature |
| T_{req} | target simulation temperature |
| U | internal energy |
| V | volume |
| V_N | total potential energy of N particles |
| V_N^{b} | biased potential energy |
| V_{ee} | potential energy due to interelectronic repulsion |
| V_{elec} | potential energy due to Coulomb interactions |
| V_{ne} | potential energy due to nuclear-electron attraction |
| W | potential of mean force |
| Z | configurational integral |
| a | activity |
| c | molecular orbital coefficient |
| d | Gaussian orbital coefficient |
| e | elementary charge ($1.602 \times 10^{-19} \text{ C}$) |
| erfc | complementary error function |
| f | fugacity |
| \mathbf{f} | force vector |
| g | radial distribution function |
| \hat{h}_i | single-electron Hamiltonian operator |
| h | Planck constant ($6.626 \times 10^{-34} \text{ J s}$) |
| \hbar | reduced Planck constant |
| \mathbf{k} | lattice vector in reciprocal space |

| | |
|--------------------------|---|
| k_B | Boltzmann constant ($1.381 \times 10^{-23} \text{ J K}^{-1}$) |
| k_{ex} | exchange rate |
| k_{cut} | reciprocal space cut off distance |
| k_{max} | maximum number of lattice vectors in the Ewald summation |
| k_{θ} | angle bending force constant |
| k_r | bond stretching force constant |
| k_w | weight function force constant |
| l | lattice vector in one-dimension of reciprocal space |
| m | mass |
| p | probability |
| p^b | biased probability |
| pH_{pzc} | pH at the point of zero charge |
| \mathbf{p} | momentum vector |
| q | partial charge |
| q_{st} | isosteric heat of adsorption |
| q_{st}^0 | isosteric heat of adsorption at zero coverage |
| \mathbf{r} | position vector |
| r_{cut} | cut off distance for VDWs interactions |
| r_{eq} | equilibrium distance |
| r_{H} | hydrated radius |
| r | distance |
| t | time |
| t_{obs} | observation time |
| v | pair potential |
| w | weight function |
| z | charge |
| Γ | point in phase space |
| Δt | MD time step |
| Λ | thermal de Broglie wavelength |
| Ψ | wavefunction |
| α | Gaussian width |
| β | inverse temperature |
| γ | fugacity or activity coefficient |
| ε | VDWs well-depth |

| | |
|----------------------|---|
| ϵ_0 | vacuum permittivity ($8.854 \times 10^{-12} \text{ J}^{-1} \text{ C}^2 \text{ m}^{-1}$) |
| ϵ_r | relative permittivity |
| θ | bond angle |
| θ_{eq} | equilibrium bond angle |
| ζ | orbital exponent |
| η | viscosity |
| μ | chemical potential |
| ξ | random number <i>or</i> general reaction coordinate |
| ξ_{eq} | equilibrium value of general reaction coordinate |
| ρ | density |
| φ | Gaussian function |
| σ_i | VDWs diameter |
| σ | charge density |
| ψ | single-electron wavefunction |
| ϕ | basis function |
| ϕ_{elec} | electrostatic potential |

Chapter One

Introduction

1.1 Nuclear Waste Management

There is renewed impetus in the expansion of nuclear power production in many countries around the world, driven by a desire to reduce an over-reliance on fossil fuels as a source of energy. Indeed, the Intergovernmental Panel on Climate Change recently suggested that the use of fossil fuels should be completely eliminated by 2100 [1]. Energy generated by nuclear fission is accompanied by the production of a multitude of radioactive waste products, each of which have different chemistries and radiological half-lives. In the UK there is also a backlog of legacy waste that is currently held in interim storage facilities. The future expansion of nuclear power programmes is reliant on the ability to safeguard and assure the public and protect the environment by careful disposal of these waste products.

The current plan for dealing with radioactive waste in many countries, including the UK, is to encapsulate or immobilise it in a cementitious or vitreous wastefrom and put into long-term storage in an underground repository. In the UK's geological disposal facility (GDF) proposal [2], based on SKB's (the Swedish waste management organisation) KBS-3 concept [3], the wastefrom is placed in a suitable waste package to provide a physical barrier to radionuclide release that is in turn surrounded by a backfill material. Both the backfill and the local geology play an important role in forming a chemical barrier to radionuclide release. This multi-barrier approach is designed to simultaneously ensure that the majority of short-lived radioisotopes will decay in the waste packages and the subsequent release (when waste packages eventually degrade after 10^3 to 10^4 years) and migration in the environment of longer-lived radioisotopes is retarded. The major sources of radioactivity in the period up to about 100 years are from ^{90}Sr and ^{137}Cs . After this time the actinides and long-lived fission products remain important and the solubility of these radioisotopes in natural waters and their adsorption affinity to the backfill or surrounding rock minerals becomes crucial in underpinning the safety case of the GDF. Other strategies for dealing with radioactive waste have been proposed, such as the deep borehole

disposal concept [4].

Due to its high mobility in the environment, long half-life and high fission yield, ^{99}Tc is predicted to be one of the most abundant and problematic radioisotopes from 10^4 years after GDF closure [5]. In addition, there are already some locations highly contaminated with ^{99}Tc resulting from the nuclear legacy in need of remediation [6, 7]. An effective method for adsorbing ^{99}Tc both in the near-field region of the proposed GDF and in already contaminated environmental water is therefore crucial in underpinning the case for waste disposal strategies. A novel adsorbent material that has previously been used for difficult environmental contamination problems and has the potential to deal with the ^{99}Tc problem is known as self-assembled monolayers on mesoporous supports (SAMMS) [8].

1.2 Project Scope

1.2.1 Aims and Hypothesis

Molecular modelling can be used to provide additional insight and complement experimental observations of physical and chemical processes by probing mechanistic information on the atomic scale [9]. Models are particularly useful in avoiding the radiation protection challenges faced when dealing with radioactive materials experimentally.

The overarching aim of this work is to construct and validate realistic atomistic models of the SAMMS material and simulate the selective adsorption of ^{99}Tc to it using a variety of techniques. The hypothesis is that the experimentally observed selectivity of the SAMMS material can be explained using these models and is dependent not only on the specific nature of the surface chemistry but also the overall mesoscopic structure of the porous material. By elucidating the mechanistic detail of the adsorption mechanism suggestions can be made about how best to optimise the structural parameters of the real material to further enhance selectivity. Additionally, there is a wider fundamental academic and industrial interest in the thermodynamics of solvated ions, particularly under confinement in porous materials.

1.2.2 Structure of this Thesis

The next two chapters seek to review all the information in the scientific literature that has relevance to the ^{99}Tc problem outlined in Section 1.1. The first (Chapter Two) presents an overview of the current situation regarding ^{99}Tc contamination and the challenges associated with its remediation, followed by discussion of the structure, synthesis and suitability of the SAMMS material for dealing with this problem (Chapter Three). Chapter Four provides a brief overview of the theoretical background and practical implementations of the molecular modelling and simulation techniques used in this work, including density functional theory, molecular dynamics and Monte Carlo simulations. The remaining chapters of this thesis are organised so as to present the construction of the SAMMS models in a sequential manner. They review any relevant existing models in the literature and provide a detailed description of how the models in this work were constructed and validated. Detailed results regarding the properties of ^{99}Tc in solution and its selective adsorption to SAMMS are presented in these chapters. The final chapter summarises all the important conclusions, with particular emphasis on the ^{99}Tc adsorption process and how SAMMS materials could be optimised to further enhance ^{99}Tc selectivity.

Chapter Two

Technetium

Technetium, Tc, is the lightest element (atomic number 43) without any stable isotopes. It was first produced synthetically by the deuteron activation of molybdenum metal in 1937 by Perrier and Segré [10, 11]. The fact that almost all the global inventory of Tc is anthropogenic justifies its name, which derives from the Greek word ‘technetos’, or artificial. A large number of radioactive isotopes of Tc are known, with mass numbers ranging from 85 to 118, but only three (^{95}Tc , ^{97}Tc and ^{99}Tc) are long lived [12].

2.1 Sources

Nuclear fission is known to occur in natural ‘reactors’ under very specific geochemical conditions; for instance from the ore deposits at Oklo in Africa [13]. There is also evidence of a small number of other natural reactors around the world and over 700 kg of Tc are thought to have been generated via these processes [14]. Despite this, the vast majority of Tc on Earth has been artificially produced.

In civilian nuclear power production the neutron induced fission of ^{235}U results in a bimodal mass distribution of products. Since their mass numbers are near the centre of this distribution, several isotopes of Tc are produced in appreciable quantities in this process (^{99}Tc to ^{107}Tc) [15]. The radiological half-lives, $t_{1/2}$, of the high yield Tc isotopes produced in fission are given in Table 2.1. Uniquely amongst the other high yield isotopes ^{99}Tc has a long half-life (2.12×10^5 years), decaying to ^{99}Ru by beta-emission with a maximum energy of 0.294 MeV. Garten [16] estimated that a typical Gen III light water reactor yields approximately 27.5 kg of ^{99}Tc per 1000 MW-year of electricity produced. The total radioactivity resulting from global civilian nuclear power programmes up to 2005 has been estimated to be around 6.0×10^5 TBq [17].

Much of the environmental inventory of ^{99}Tc is due to past liquid effluent discharges from reprocessing plants, which serve to separate fissile elements from the waste products of spent nuclear fuel. For example, the total discharge of ^{99}Tc into the Irish Sea from Sellafield increased in the 1990s due to the processing of a backlog of

effluent when the Enhanced Actinide Removal Plant (EARP) began to operate, which was ineffective at the removal of ^{99}Tc . Discharges peaked in 1995 when nearly 200 TBq of ^{99}Tc was released [18] but in 2000 the total discharge from Sellafield was restricted to 90 TBq per year [19]. Under mounting domestic and international pressure the authorised limit was further reduced to 10 TBq per year from 2006. Sellafield Ltd's monitoring and discharge annual report states that the mean annual ^{99}Tc discharge into the Irish Sea was as little as 1.9 TBq between 2008 and 2012 [6]. There are other nuclear facilities where the surrounding environment has become contaminated with Tc, such as the Hanford site in the US [7].

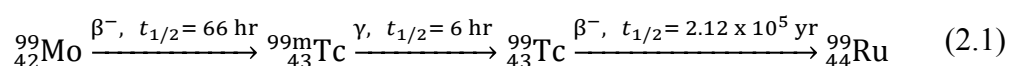
| Mass Number | Fission Product Yield (%) | Half-life (mins) |
|-------------|---------------------------|----------------------|
| 99 | 6.0 | 1.1×10^{11} |
| 101 | 5.6 | 14.3 |
| 102 | 4.3 | 4.5 |
| 103 | 3.0 | < 1 |
| 104 | 1.8 | 18.0 |
| 105 | 0.9 | 7.7 |
| 107 | 0.2 | < 1 |

Table 2.1 Isotopes of Tc produced in the fission of ^{235}U [15].

Historical nuclear weapons tests produced ^{99}Tc , resulting in the formation of Tc_2O_7 and HTcO_4 (pertechnetetic acid) in the atmosphere. The total fallout of ^{99}Tc from these sources is estimated to be between 140 and 160 TBq [20], although the amount released now is very low due to international treaties banning weapons testing. A small amount of ^{99}Tc has also been released to the atmosphere as a direct result of nuclear accidents, most notably Chernobyl in 1986, which is predicted to have liberated 0.75 TBq of ^{99}Tc [21].

The metastable $^{99\text{m}}\text{Tc}$ isotope, discovered by Seaborg and Segré [22], decays by

gamma-emission to ^{99}Tc , with a half-life of just six hours, making it suitable for use as an organ-imaging radioisotope. This suitability, combined with the complex chemistry and wide range of possible coordination numbers displayed by Tc, has driven the development of a multitude of different $^{99\text{m}}\text{Tc}$ containing radiopharmaceuticals and the rapid progress of nuclear medicine in recent decades [23-25]. There are now several nuclear reactors around the world specifically devoted to the production of radioisotopes for medicine to fulfil this demand. They provide hospitals with the ^{99}Mo parent isotope that decays by beta-emission to $^{99\text{m}}\text{Tc}$,



The radioactivity of an individual medical investigation, typically performed using the single photon emission computed tomography technique [26], varies between 20 and 1000 MBq. However, the contribution from nuclear medicine to the global ^{99}Tc inventory is negligible by comparison to nuclear power.

2.2 Technetium in the Environment

The electronic configuration of a neutral Tc atom is $[\text{Kr}] 4\text{d}^5 5\text{s}^2$. Although it can exist in a wide variety of oxidation states ranging from -1 to $+7$, the $+7$ state is particularly stable as this corresponds to a Tc atom having lost its entire valence shell of electrons.

Pourbaix diagrams are commonly used to study speciation in the wide range of conditions encountered in the environment. They are equilibrium phase diagrams corresponding to the predominant species of a given element, plotted as function of pH and reducing potential (E_h). The Pourbaix diagram for Tc (Figure 2.1) [27], shows that the tetrahedral pertechnetate oxyanion (TcO_4^-) readily forms, which is soluble across a broad range of pH and E_h conditions in environmental waters and is therefore the main species of concern for the remediation of Tc contaminated land. It is also the dominant species in the presence of the oxidising and alkaline glass and cement leachates that would result from the eventual degradation of primary waste packages in the UK's GDF proposal. Tc is only insoluble at low pH and in highly reducing conditions.

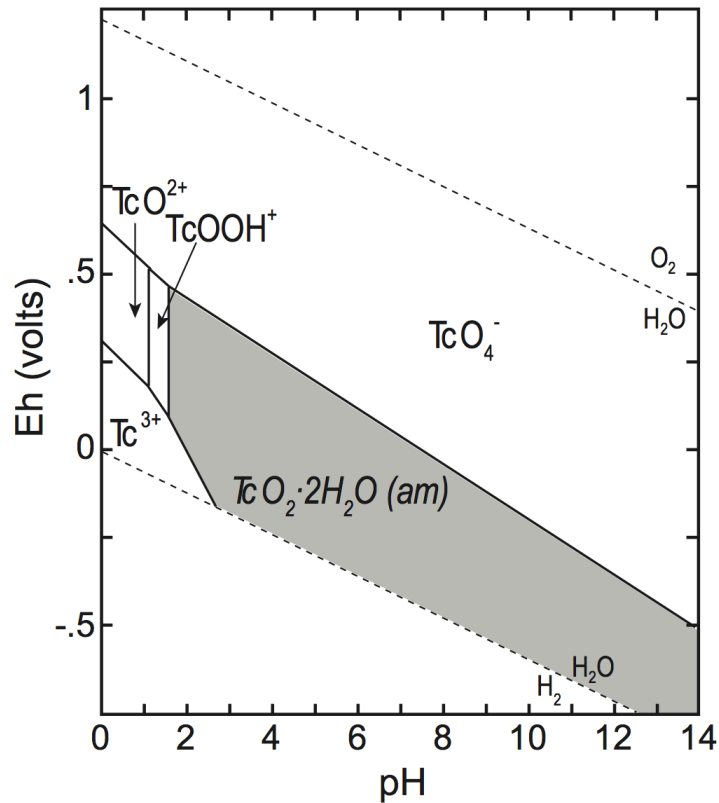


Figure 2.1 Pourbaix diagram showing Tc speciation in various E_h/pH conditions [27].

2.2.1 Geochemical Mobility

The Oklo natural reactor has the potential to provide a useful insight into the migration of radionuclides over geological timescales and the evidence from this site suggests that Tc does not migrate far [28]. However, this evidence should be treated with caution as the local geology is unusually rich in organic sediments such as bitumen and the reducing conditions provided by this organic matter have the potential to slow the migration of many radionuclides [29]. There is a much larger body of evidence suggesting that TcO_4^- is extremely mobile in the environment [15, 30], leading to large dispersion areas in environmental waters, even over quite short timescales. The high geochemical mobility of Tc in seawater was highlighted by Aarkrog *et al.* [31] who suggested that in the space of just eight years, Tc discharged from Sellafield was able to reach the Arctic Circle. The migration rate of aqueous ions in the environment is typically determined by the extent of adsorption to the mineral components of soils and sediments, which generally have negatively charged surfaces [32]. Anions have a tendency to migrate much further in the environment than cations

due to electrostatic repulsion from these surfaces. Many oxyanions (eg. sulphate (SO_4^{2-}), phosphate (PO_4^{3-}), carbonate (CO_3^{2-}) and nitrate (NO_3^-)) are particularly prevalent in the environment and present in much higher concentrations than the typical trace quantities of TcO_4^- found in contaminated waters. For instance, groundwater near the Hanford site has typical concentrations of 27.1, 119 and 5.7 mg L^{-1} of SO_4^{2-} , CO_3^{2-} and NO_3^- , respectively [33]. TcO_4^- often remains in solution because many of these competing oxyanions also have a higher charge density and are likely to inhibit the adsorption of TcO_4^- to any favourable adsorption sites that are present [34].

The mobility of TcO_4^- through soils and sediments has been investigated in detail [35, 36]. Adsorption of TcO_4^- to their mineral components in the typical oxidising and pH conditions in the environment is limited and in many experiments at least 90% of TcO_4^- remains in solution [27]. It was noted that decreasing the oxygen content of test solutions reduces Tc^{7+} to Tc^{4+} and leads to its immobilisation by the formation of the insoluble $\text{TcO}_2(\text{H}_2\text{O})_2$ [37]. Under these reducing conditions Tc can also form insoluble complexes with amine, carboxyl or hydroxyl donors in organic matter. However, when this matter is exposed to oxidising conditions (e.g. an influx of seawater) Tc is able to return to its soluble TcO_4^- form [38].

2.2.2 Accumulation in Food

Preventing the entry of radionuclides into the food chain via plants or seafood is important as this is the key parameter governing the total radiation dose to humans (the maximum permitted effective annual dose to members of the public in the UK is 1 mSv yr^{-1}) [39]. Tc has several possible routes into the food chain. Uptake of TcO_4^- in plants occurs via their SO_4^{2-} transport mechanisms, whereby it can readily be transported up the negatively charged cell walls of the xylem [40]. Transfer factors from soil or sediment to plants vary considerably depending on the species of plant, soil composition and concentration of Tc [37]. A study into Tc pollution in the Irish Sea, as a result of the significant discharges from Sellafield in the 1990s [18], demonstrated its tendency to accumulate in fish, crustaceans and seaweed. The authors concluded that in 1998 the maximum effective dose due to Tc was $0.24 \text{ } \mu\text{Sv yr}^{-1}$ for consumers of large quantities of seafood. Figure 2.2 shows the correlation, with approximately two years lag time, between the discharge of Tc from

Sellafield and the concentration detected in Irish Sea lobster [6]. It is reasonable to assume the maximum dose to humans has now significantly decreased due to the restriction placed on discharges in recent years. When ingested, the biological half-life of Tc in humans is approximately 60 hours. This short biological half-life coupled with its relatively low energy beta emission means that consumption of small amounts of Tc is unlikely to pose a significant radiological threat. However, the bioaccumulation of Tc in the food chain is an obvious concern as this could lead to the consumption of much larger quantities.

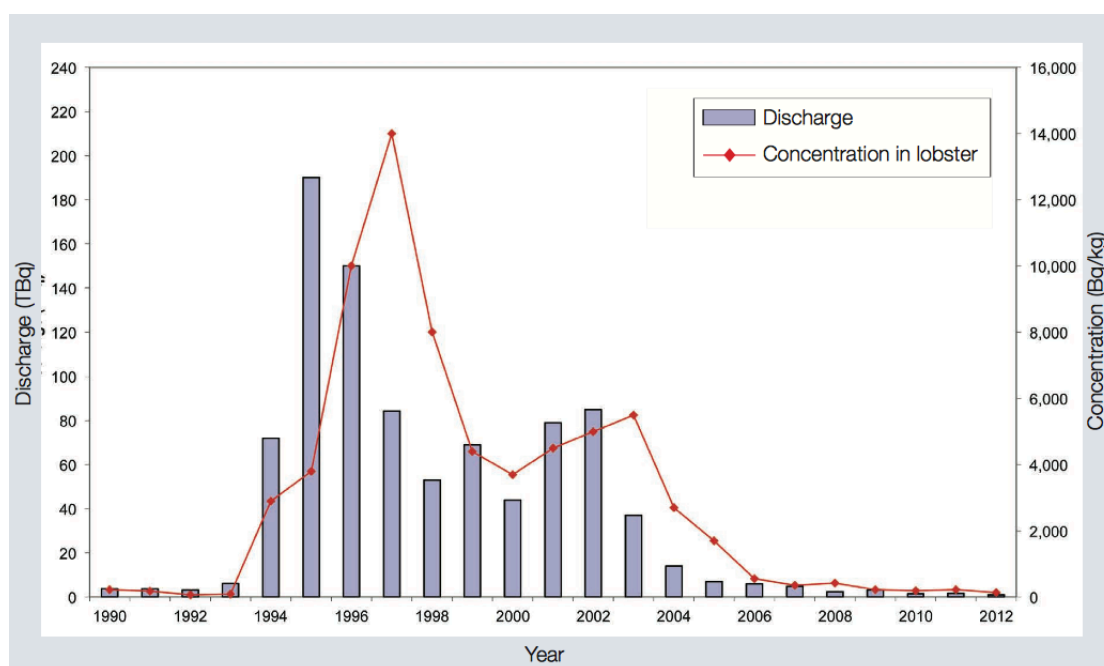


Figure 2.2 Discharge of Tc from the pipeline at Sellafield and the concentration of Tc in lobster in the Irish Sea from 1994 to 2012 [6].

2.3 Options for Technetium Remediation

The decline in Tc discharges from Sellafield shown in Figure 2.2 is associated with the introduction of tetraphenylphosphonium bromide (TPPB) as a precipitating agent in EARP to remove Tc in the form of $\text{TPP}^+\text{TcO}_4^-$. Although the TPP ion is stable at neutral pH it is susceptible to hydrolytic degradation in the high pH environment that is expected in a GDF [41]. Radiolytic degradation is also likely. Despite the GDF providing a reducing environment [5] both of these mechanisms have the potential to solubilise TcO_4^- so TBBP is unsuitable as a long-term storage solution for Tc-containing waste [42].

New materials are required for the retrieval of TcO_4^- to fulfil several distinct needs. Firstly, there is a requirement to selectively remove Tc from liquid waste streams and directly incorporate it into a wasteform. Remediation materials are also needed for deployment as an adsorbent barrier to prevent the spread of Tc in the near-field region of the GDF when the waste containers finally degrade. Finally, materials are required for the remediation of land and water already contaminated with Tc resulting from the nuclear legacy.

2.3.1 Performance Criteria

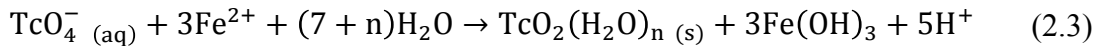
There are a number of performance criteria a TcO_4^- adsorbent material must fulfil. Primarily it must be highly selective for TcO_4^- over all common competing anions by several orders of magnitude. The extent of a material's selectivity for TcO_4^- can be measured using distribution coefficients, K_d ,

$$K_d = \frac{[\text{Tc}]_0 - [\text{Tc}]}{[\text{Tc}]} \times \frac{V}{m} \quad (2.2)$$

where $[\text{Tc}]_0$ is the initial concentration of Tc in solution, $[\text{Tc}]$ is the final concentration in equilibrated solution in contact with the adsorbent, V is the volume of the effluent and m is the sorbent mass. K_d values should be obtained using test solutions that have a realistic chemical composition. The solutions concerned, principally contaminated groundwater plumes or waste leachates, contain very low concentrations of TcO_4^- compared to other competing anions common in the environment and many of these anions are not only similar in shape and size but also carry a higher negative charge, often causing problems with TcO_4^- specificity. In addition to its selectivity the material should have a large capacity for TcO_4^- for a given quantity of material and the adsorption process should also be irreversible, so that TcO_4^- cannot return to solution. The material should ideally have the capability to be directly incorporated into a cementitious or vitreous wasteform that must be chemically and physically robust and not rapidly degrade in the context of the hostile conditions expected in the GDF. The behaviour of the material while Tc remains radioactive must be predictable and it should not have an adverse effect on the performance of other wasteforms. Finally, it must be cost-effective, especially if it is intended for large-scale deployment.

2.3.2 Natural Materials

The ability of natural minerals to adsorb and immobilise TcO_4^- have been studied in detail, and there are a number of investigations into the selectivity of oxide and hydroxide minerals, giving some modest K_d values. Early studies found iron oxide minerals had a very low affinity for TcO_4^- ($K_d = 0.2 - 5.0 \text{ mL g}^{-1}$) [43], which decreased with increasing pH. However, van der Graaf *et al.* [44] observed adsorption of TcO_4^- to iron oxide minerals, in particular magnetite ($K_d = 4 - 490 \text{ mL g}^{-1}$), under reducing conditions, followed by the formation of Tc^{4+} ,



This three-electron reduction process results in a complex mix of co-precipitates on the solid surface [45]. There is also evidence that Tc could become incorporated into the bulk structure of iron oxide. Cui and Eriksen [46, 47] noticed that the reduction of Tc by various iron containing mineral surfaces is a kinetically hindered process for which the rate varies considerably depending on the surface area and Fe^{2+} content, with magnetite again proving to be the mineral with most promise. Competition for adsorption sites from other environmentally relevant anions, especially SO_4^{2-} [48], has been regularly observed leading to conclusions that iron oxide minerals have poor TcO_4^- selectivities from solutions with realistic groundwater compositions [49]. The aluminium containing boehmite mineral was found to effectively adsorb perchlorate, ReO_4^- , which is often used as a non-radioactive analogue for TcO_4^- [50]. As a result the authors suggested that boehmite should be incorporated into a backfill to retard migration TcO_4^- . However, they found that increasing NO_3^- concentration dramatically reduced the amount adsorbed and they did not perform experiments with solutions that mimic the high pH expected in the backfill. Some sulphide minerals exhibit good TcO_4^- immobilisation properties, such as finely ground galena, pyrite and pyrrhotite, with K_d values of 50-1000, 70-100 and 50000 mL g^{-1} , respectively [51, 52]. The mechanism for immobilisation by these minerals is thought to be due to the reduction to Tc^{4+} and formation of Tc_2S_7 as well as $\text{TcO}_2(\text{H}_2\text{O})_2$ [53, 54]. However, in another investigation TcO_4^- was found to have a much lower affinity for sulphides [49]. Other minerals tested such as Cu and Pb oxides and silicates were not found to adsorb TcO_4^- in any appreciable quantity [55].

There is one other ‘natural’ possibility for Tc remediation that is worthy of brief discussion. Microbial reduction and immobilisation of Tc was first observed by Lloyd and Macaskie [56]. Studies have shown that the rate of reduction by microbes could be increased by the addition of sulphate-reducing bacteria to the soil [57]. Unfortunately, since the bacteria accept TcO_4^- as an analogue to SO_4^{2-} this does not offer a solution for the selective removal of TcO_4^- in the presence of competing SO_4^{2-} . In addition, the use of carbon containing precipitates, such as bacteria, would lead to the formation of gases, which are likely to have detrimental effect on the proposed GDF.

Overall, reasonable K_d values can be obtained for adsorption of TcO_4^- to oxide and hydroxide minerals under certain limited conditions, but show poor capacity and selectivity when realistic solutions containing competing ions were tested. The results obtained for sulphide minerals show some promise but are highly variable and sensitive to particle size and solution composition. In addition, the release rate of TcO_4^- from these precipitates is yet to be fully established. It has also been reported that Tc^{4+} is known to form the soluble TcCl_4 species in the presence of the Cl^- ions [58]. Van der Graaf *et al.* [44] suggested this process has the potential to return Tc to solution from its insoluble form on mineral surfaces. It has also been observed that exposing mineral surfaces to small radiation doses adversely effects their ability to adsorb TcO_4^- [54].

2.3.3 Other Materials

Although typical commercial anion-exchange resins have been shown to strongly bind TcO_4^- from concentrated solutions ($K_d = 250 \text{ mL g}^{-1}$) [59], they are not as effective at removing TcO_4^- at the low concentrations found in contaminated groundwater. Del Cul *et al.* tested standard polyvinylpyridine and quaternary ammonium resins with only modest selectivity and slow reaction kinetics [60]. Bifunctional resins with large cationic quaternary amine groups have demonstrated improved performance compared to conventional anion exchange resins [61]. They selectively target large and poorly hydrated oxyanions, such as TcO_4^- and ClO_4^- , over others, resulting in K_d values approximately five times greater than conventional anion-exchange resins ($K_d = 4.8 \times 10^4 \text{ mL g}^{-1}$). There is a wealth of literature surrounding the use of synthetic layered double hydroxides to capture oxyanions by anion exchange based on

their ionic radii [62]. These materials have been shown to adsorb TcO_4^- [63], but not in solutions containing competing CO_3^{2-} . A novel 3D porous thorium borate material was also successful, removing up to 72% of TcO_4^- from a dilute solution, by exchanging its borate ions [64]. Cationic metal organic frameworks have also recently been found to strongly adsorb monovalent oxyanions such as ReO_4^- over others [65].

Gu *et al.* first observed that activated carbons were able to selectively remove TcO_4^- from solutions across a wide range of pH and electrolytic compositions ($K_d = 2.7 \times 10^4 \text{ mL g}^{-1}$) [66]. In addition, Li *et al.* studied the ability of a number of different sorbent materials for removing oxyanions from groundwater and sediments and found activated carbons, which have high surface areas and variable functional groups, to be one of the most effective [67]. They observed high selectivity for TcO_4^- at neutral pH ($K_d = 1.0 \times 10^5 \text{ mL g}^{-1}$), but the distribution coefficient reduced to just 120 mL g^{-1} at pH 9.2. Wang *et al.* [68] compared the performance of some commercially available activated carbon materials containing a range of different adsorption sites and reported that some of the carbons adsorb TcO_4^- via mechanisms that were independent of the solution pH ($K_d = 3.2 \times 10^3 \text{ mL g}^{-1}$). Activated carbons have also been previously tested as an additive to bentonite (a proposed GDF backfill material) in order to achieve selective TcO_4^- removal in reducing conditions [69]. The problem with activated carbons is that they often have a wide distribution of pore sizes ranging from the micro- to mesoscale and thus not ideally suited for use as an adsorbent material [70].

The success of iron oxide minerals prompted an investigation into the use of fine metallic iron for TcO_4^- sorption by reduction yielding some impressive results ($K_d = 5.0 \times 10^3 \text{ mL g}^{-1}$) in spiked granitic groundwater [44], suggesting that iron nanoparticles may also have potential as a remediator. Supported nanoiron (Fe^0) consists of 10 – 30 nm diameter nanoparticles of iron immobilised on a high surface area inorganic support material and have been shown to remove a range of aqueous metal ions from solution [71]. Darab *et al.* [72] studied the ability of nanoiron supported by zirconia to immobilise Tc by adsorption of TcO_4^- and subsequent reduction to $\text{TcO}_2(\text{H}_2\text{O})_2$, a process accompanied by the oxidation of Fe to FeOOH . They were able to remove a significant amount of Tc ($K_d = 370 \text{ mL g}^{-1}$) from both a highly alkaline waste stream in the presence of high concentrations of competing

anions (similar to the waste tank conditions at the Hanford site). Zirconia was used as a support due to its very low solubility even at pH 14. They also studied the removal of TcO_4^- from a near neutral pH solution, representative of contaminated ground water using nanoiron supported by silica gel ($K_d = 290 \text{ mL g}^{-1}$).

Mattigod and co-workers [73] functionalised anatase (TiO_2) nanoparticles with organosilane tethered Cu^{2+} -EDA complexes. They injected groundwater from the Hanford site into a suspension of the nanoparticles and observed highly selective removal of TcO_4^- ($K_d = 4.0 \times 10^3 \text{ mL g}^{-1}$). In this process, TcO_4^- preferentially displaces a H_2O ligand, despite the expected greater electrostatic attraction between the divalent SO_4^{2-} and the Cu^{2+} ion. In this process TcO_4^- acts as a ligand to the Cu^{2+} ion and adsorbs by bonding through one of its oxygen atoms, unlike so many of the other Tc remediation approaches discussed, which rely on specific E_h /pH conditions to facilitate the reduction of Tc^{7+} to Tc^{4+} .

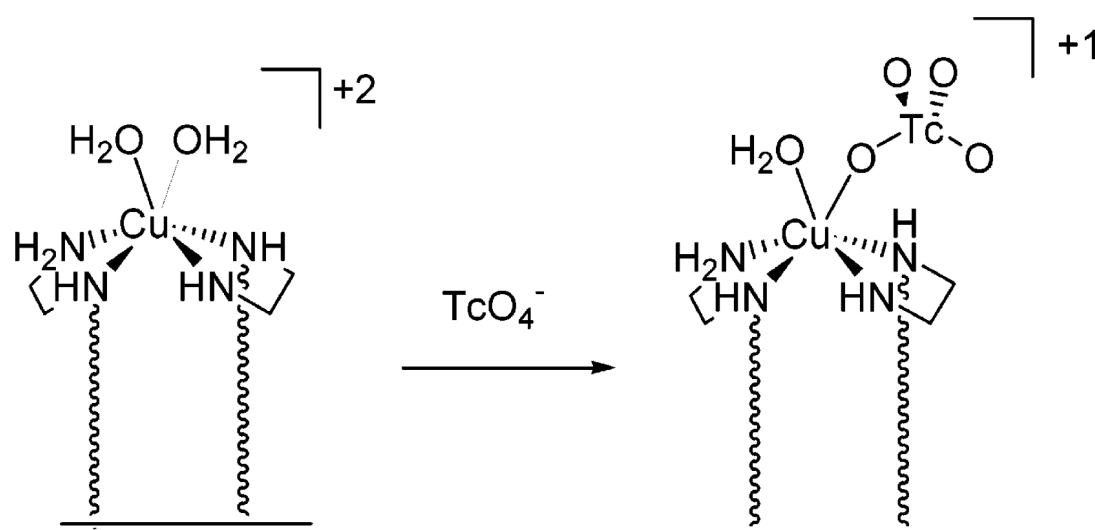


Figure 2.3 The mechanism for adsorption of TcO_4^- to Cu-EDA functionalised TiO_2 particles [73]. On the right-hand side the displaced H_2O is not pictured.

2.3.4 Summary

Although the literature covering the subject of which natural or synthetic materials can be used to immobilise TcO_4^- or retard its migration is vast the fact that TPPB is still being used highlights the fact that many of these have drawbacks. There are numerous studies of materials that are ineffective, and this literature review has largely focused on materials that have shown some promise. The selectivity of the

different methods can be compared using the K_d values but these comparisons must be made in the light of the chemical conditions under which the value was obtained, ie. whether the solution used has a representative ionic composition and if the E_h/pH conditions are realistic under a variety of remediation scenarios.

Chapter Three

SAMMS

The challenge of remediating contaminated environmental waters cannot easily be tackled using traditional adsorbent materials. The main problem is due to the complex mix of ions in solution that act to inhibit the removal of contaminant species by saturating adsorption sites. An alternative sorbent material, which satisfies the criteria discussed in Section 2.3.1, is needed to tackle the TcO_4^- problem discussed at length in the previous chapter. One group of highly chemically selective materials that offer considerable promise are self-assembled monolayers on mesoporous supports (SAMMS).

3.1 Structure

SAMMS were first developed at Pacific Northwest National Lab (PNNL) in 1997 [8, 74]. They combine a robust inorganic support, typically MCM-41 (MCM = Mobil Composition of Matter), with a chemically specific monolayer. Since it was first invented in 1992 [75, 76], there has been significant academic and industrial interest in the unique properties of the mesoporous molecular sieve MCM-41. The MCM-41 structure consists of a uniform hexagonal arrangement of cylindrical mesopores of controllable size and narrow distribution. Despite the ordered structure on the mesoscale, the pore walls are composed of disordered amorphous silica, unlike related zeolite materials. Pore diameters can be tuned between 1.5 and 10 nm [75, 77-81], the thickness of the walls separating these pores may vary between 0.6 and 2 nm [80, 82] and a wide range of silanol densities on the internal pore surface have been reported [83-86], depending on the exact conditions of synthesis. Due to its unique structural features and exceptional hydrothermal stability [82, 87] MCM-41 itself has attracted considerable attention as an adsorbent across a wide range of disciplines including gas separation [88], catalysis [89], electrochemistry [90] and medicine [91]. In SAMMS the internal pore surface of MCM-41 is functionalised with organosilane molecules that self-assemble to form a monolayer, which is especially attractive as the resulting material combines a rigid porous support with the chemical specificity offered by an organic molecule.

As well as the ability to tune the terminating groups of the monolayer to target specific ionic contaminants, the size of the pores in MCM-41 can be adjusted to exclude other ions that may act to inhibit the adsorption process. Ions are able to diffuse through the porous network and the effect of confinement keeps them in close contact with the monolayer, resulting in fast adsorption kinetics. The material has an extremely high contaminant loading capacity due to its high surface area and dense monolayer coverage. The rigidity of MCM-41 prevents pore swelling from occurring, as is commonly observed in some porous polymeric adsorbents [70]. Whilst SAMMS are more expensive than most traditional adsorbents per gram of material they have the advantage that less material is needed for a given contamination problem because of their high selectivity and loading capacity. The combination of these features makes SAMMS an attractive prospect as an adsorbent material for the environmental remediation of contaminated land [92-94]. For example, SAMMS have been used extensively for the large-scale removal of mercury ions, Hg^{2+} , from contaminated groundwater [95]. In this case a monolayer consisting of thiol functionalities (R-SH) was designed to take advantage of hard-soft acid base theory, exploiting the affinity between the 'soft' Lewis base (S) and acid (Hg^{2+}). Based on this principle thiol-functionalised SAMMS have also been used to remove soft precious metal ions such as Ag^+ [94].

SAMMS are particularly appealing for radioactive contaminants given the need to remove radionuclides to extremely low detection limits. In addition, since the inorganic support is composed of amorphous silica there is a possibility of it being directly incorporated into a waste vitrification program. As a result, it has been tested for the clean up of a number radioactive contaminants including actinides [96], caesium [97] and iodine [98].

3.2 Synthesis

3.2.1 MCM-41

The mesoporous framework of MCM-41 is synthesized by mixing a surfactant with a silica precursor, such as tetraethyl orthosilicate. Over several days the mixture separates as the surfactant molecules arrange into micelles, around which the silica forms a network of siloxane (Si – O – Si) bonds. Calcination between 600 and 900 K rigidifies the ceramic backbone and burns off the surfactant molecules that act as a

template for the resulting array of mesopores. Originally, quaternary ammonium salts were used as a surfactant [76], but now neutral polymeric surfactants [99] are more commonly used instead. The structure of MCM-41 can be tailored by careful choice of surfactant size, additives and reaction conditions resulting in materials with wide ranging pore diameters and wall thicknesses.

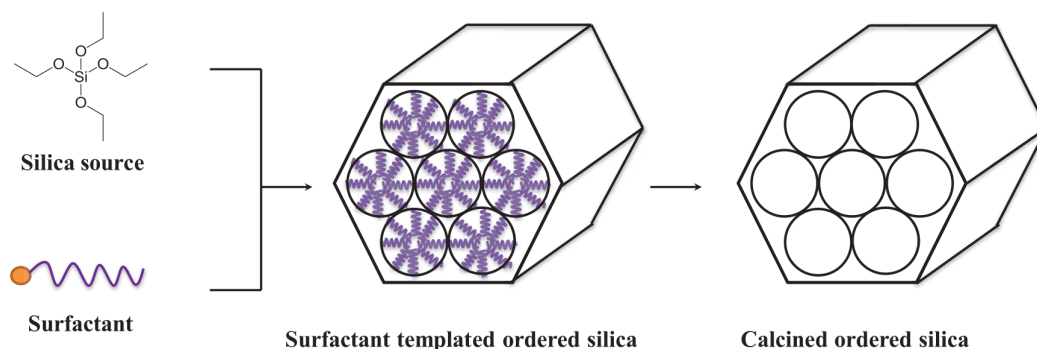


Figure 3.1 The surfactant templating mechanism used to synthesize MCM-41 [100].

3.2.2 Functionalised MCM-41

There are two approaches to functionalising the internal pore surface of MCM-41 with organosilane molecules [101]. Firstly, in the co-condensation (or one-pot) method [102] a fraction of the surfactant molecules in the micelle are replaced by organosilanes where the silane end of the molecule becomes incorporated into the silica surface when calcined. This approach, which results in a well-defined homogeneous monolayer, is not suitable if the desired functionality requires a precursor organosilane that is unstable under the conditions of calcination required to generate MCM-41.

Instead, functionalities can be introduced by grafting an organic molecule post-synthesis (Figure 3.2) [70]. This is achieved by a condensation reaction between silanols (SiOH) on the pore surface and the alkoxy- groups of an organosilane (SiOR). The grafting method allows the surface to be functionalised with monolayers consisting of fragile molecules that cannot be incorporated using the co-condensation method. This is generally carried out in a dry environment to prevent water mediated self-condensation reactions between organosilanes away from the pore walls. The process results in a defective monolayer structure with a number of vacancies (ie.

unreacted silanols) due to the organosilanes lying flat on the surface blocking access of more organosilanes to the silanols on the surface. In SAMMS rather than assembling the monolayer under completely dehydrated conditions, enough water is added to form two layers on the surface [8]. The interfacially bound water plays an important role in the self-assembly process, hydrolysing the organosilane to form tris(hydroxy)silane intermediates which are then able to migrate across the surface by the repeated forming and breaking of hydrogen bonds with surface silanols until it is attracted to another silane intermediate by van der Waals (VDW) forces and hydrogen bonds. The intermediates begin to aggregate and become less mobile, at which point condensation can occur between the molecule and the surface silanol. Condensation reactions between adjacent organosilanes also occur, resulting in cross-linking. The self-assembly process is driven by the mobility of the tris(hydroxy)silane so the interfacial layer of water is critically important in forming a denser monolayer (~ 5 silanes nm^{-2}) than can be achieved in dry conditions.

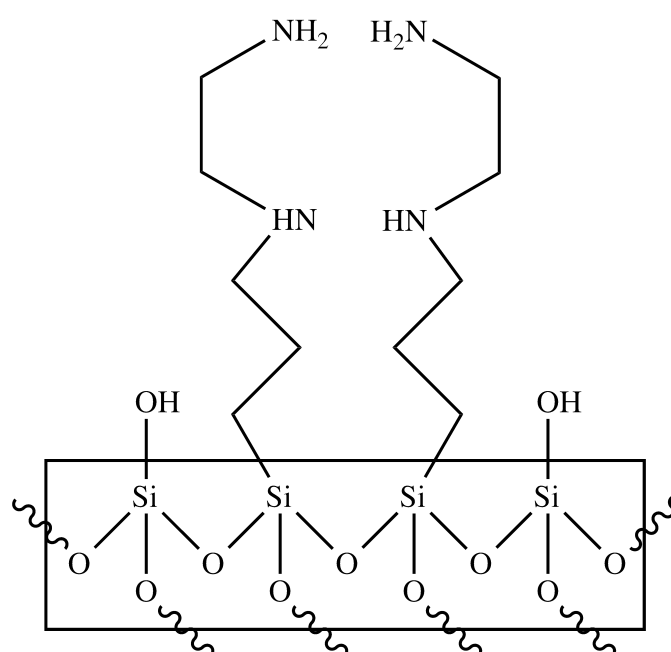


Figure 3.2 A pair of propyl-EDA chains grafted onto an amorphous silica surface.

The grafting method, used to functionalise amorphous silica surfaces, predates the invention of MCM-41 [103]. MCM-41 functionalised with a monolayer of propyl-EDAs (EDA = ethylenediamine) is particularly interesting in its own right (for instance, in the case of flue gas separation by CO_2 adsorption [104]). It also behaves

as versatile precursor material for the formation of more complicated monolayers since EDA is a common bidentate ligand for transition metal cations [105, 106].

3.3 Oxyanion-SAMMS

3.3.1 Amine Monolayers

The adsorption of HAsO_4^{2-} and CrO_4^{2-} oxyanions to MCM-41 functionalised with mono-, di- and triamines has been investigated experimentally [107]. Under acidic conditions the amines become protonated and can act as adsorption sites for the oxyanions resulting in distribution coefficients exceeding 10^5 mL g^{-1} with the triamine functionalities found to be the most effective. The work of Stephan *et al.* [108] demonstrated that in aqueous solution amino-azacages could also be used to extract oxyanions such as TcO_4^- by encapsulation. The success of this study suggested that this type of functionality could be used as a monolayer in MCM-41 leading to research that showed azacryptand (Figure 3.3) functionalised MCM-41 selectively encapsulates ReO_4^- , a structural surrogate for TcO_4^- , despite a high concentration of competing Cl^- ions [109].

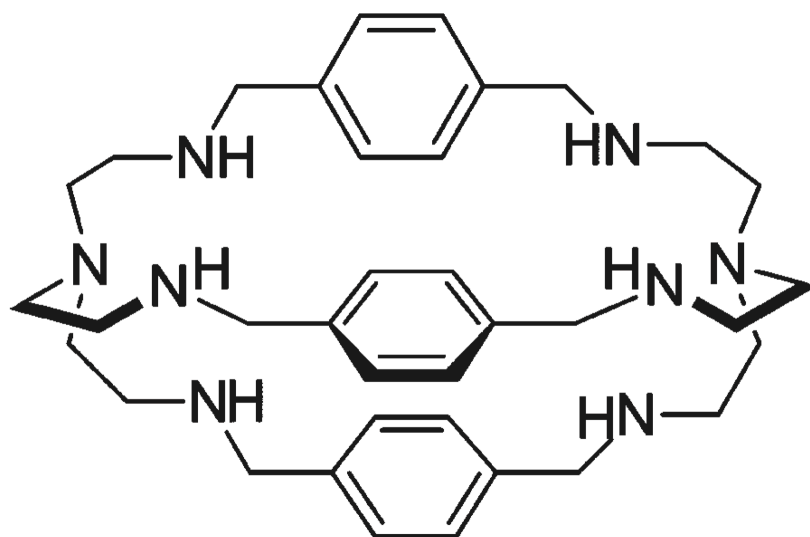


Figure 3.3 The amino-azacryptand used to encapsulate ReO_4^- and TcO_4^- [109].

Although oxyanions have a strong affinity for these molecules, the amine groups must be protonated so the effectiveness of this type of functionality is strongly dependent on pH; in the case of the azacryptand functionality the oxyanion was released back into solution at $\text{pH} > 5$. The suitability of an adsorbent material that can only remove

TcO_4^- under very specific pH conditions has already been questioned in Section 2.3. These studies did not report the effects of competition from environmentally ubiquitous oxyanions on adsorption, but in the case of the azacryptand functionality ClO_4^- was found to be an effective inhibitor for the adsorption of the ReO_4^- analogue. These simple amine functionalised materials do not therefore offer any significant advantage over the plethora of traditional adsorbents that have previously been investigated.

3.3.2 Transition Metal Complex Monolayers

SAMMS type materials containing a monolayer of amino-functionalities are useful as precursors to the development of more elaborate monolayers. The propyl-EDA functionality (Figure 3.2) is of particular interest because EDA is an effective chelating ligand for transition metal complexes, allowing highly specific transition metal chemistry to be introduced into the adsorbent material. The ability of transition metal EDA complexes to adsorb TcO_4^- by ligand exchange has previously been discussed (Section 2.3.3) in the case of functionalised anatase particles [73].

Fryxell *et al.* [105] developed a SAMMS material in which three ethylenediamine (EDA) functionalities, tethered to the surface of MCM-41 by propyl chains, coordinate a Cu^{2+} ion forming an octahedral complex (Figure 3.4). These workers then performed adsorption experiments to study the selectivity of this Cu^{2+} -EDA monolayer towards oxyanions. The material was found to be highly selective for Cr (CrO_4^{2-}) and As (H_2AsO_4^-) even in the presence of high concentrations of the competing SO_4^{2-} and demonstrated almost complete removal of these contaminant species. They proposed a mechanism, confirmed by extended X-ray absorption fine structure (EXAFS) experiments [110], in which the oxyanion binds directly and monodentately to Cu^{2+} by ligand exchange, displacing the amine termini on two of the tethered EDA ligands. Cu^{2+} is a d^9 transition metal so undergoes Jahn-Teller distortion to relieve orbital degeneracy. They suggested that two amines are so readily displaced because the complex is not well suited to the distorted geometry when bidentately coordinated by three tethered EDA ligands. The adsorption of other oxyanions, such as MoO_4^{2-} , SeO_4^{2-} and PO_4^{3-} , to this material has also been investigated [111, 112].

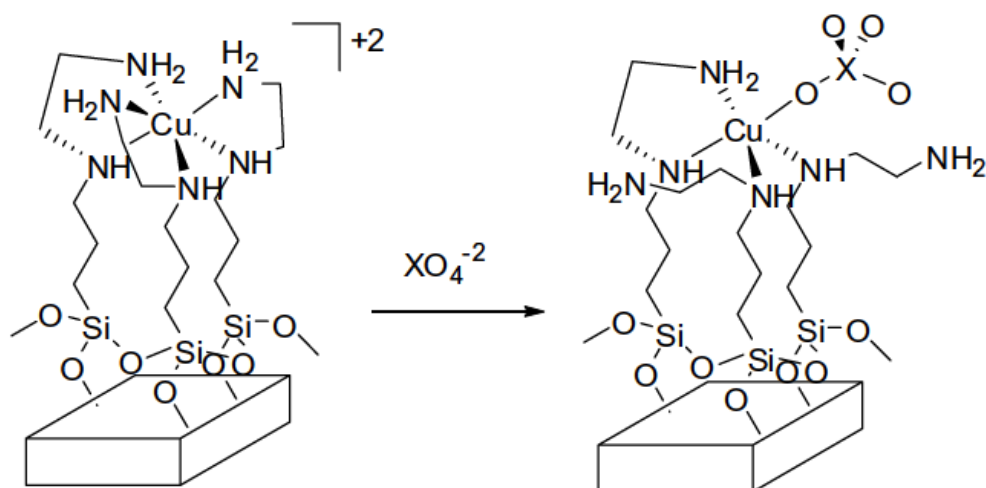


Figure 3.4 Proposed mechanism of oxyanion binding to Cu^{2+} -EDA-SAMMS [111].

Yoshitake *et al.* [106, 113] studied the adsorption of H_2AsO_4^- to MCM-41 functionalised with various transition metal (Fe^{3+} , Co^{2+} , Ni^{2+} , Cu^{2+}) EDA complexes. They proposed the formation of an octahedral complex with two bidentate EDA ligands and two Cl^- ligands, present due to the addition of the transition metals as chloride salts in the synthetic procedure, although it was not suggested whether the Cl^- ligands were *cis* or *trans* to each other. It is also possible that H_2O ligands occupy a small number of these coordination sites. The observed Cu/As ratio (0.69) was in very good agreement with the work of Fryxell *et al.* [93] (0.71) but they found the Fe^{3+} complex (Figure 3.5) to have a far greater H_2AsO_4^- capacity than Cu^{2+} (Fe/As = 1.6) and suggested this complex is capable of binding multiple oxyanions by the successive exchange of both Cl^- ligands [114]. The selectivity of the Fe^{3+} complex for H_2AsO_4^- was also largely unaffected by competing SO_4^{2-} and Cl^- ions, which was not found to be the case for the corresponding Cu^{2+} complex. The number of chelating EDA ligands in each complex in Fryxell *et al.* [105] and Yoshitake *et al.* [106] is dependent on the density of the propyl-EDA monolayer. In Fryxell's work the material was prepared in the presence of interfacial water, which facilitated the migration and subsequent aggregation of the tris(hydroxy)silane intermediates, resulting in a density of 4.9 propyl-EDA nm^{-2} and leading to the possibility of coordinating transition metals with three EDA ligands. In Yoshitake's studies the material was functionalised in a dry environment so a self-assembly mechanism was

not possible and the resulting monolayer density reported was much lower ($1.4 \text{ propyl-EDA nm}^{-2}$). They commented that a minimum density of $3.0 \text{ propyl-EDA nm}^{-2}$ was required to obtain a transition metal complex with an EDA coordination number greater than two.

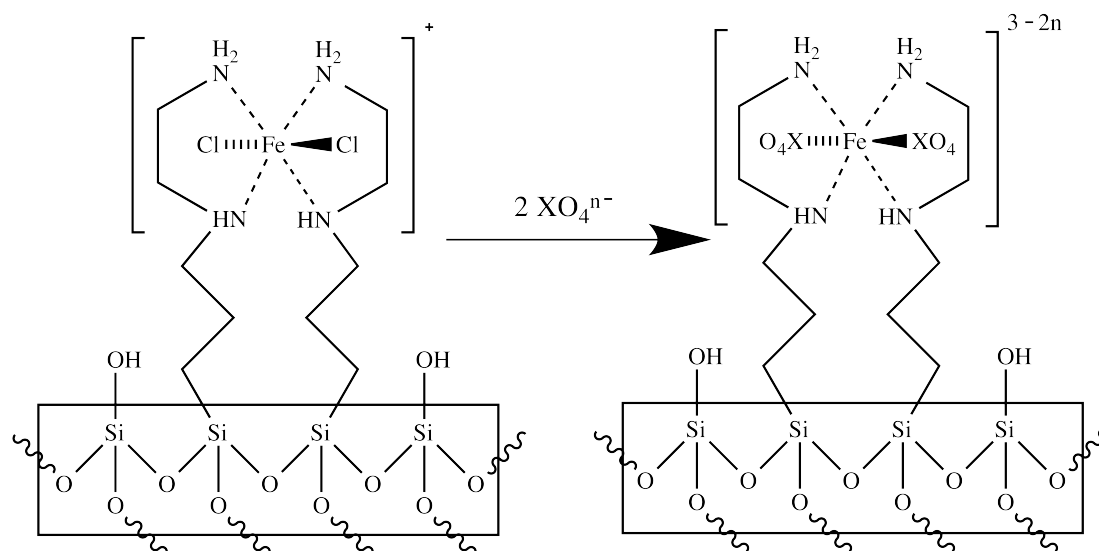


Figure 3.5 Proposed mechanism of oxyanion binding to Fe³⁺-EDA-SAMMS [106].

3.4 Summary

In the case of anatase particles functionalised with transition metal – EDA complexes the affinity for TcO₄⁻ in preference to a divalent oxyanion, such as SO₄²⁻, has been proven [73]. It has also been established that MCM-41 functionalised with a monolayer of closely related complexes has the ability to irreversibly bind monovalent oxyanions [93, 106]. Unlike many of the current options for TcO₄⁻ removal discussed in Section 2.3 the performance of the material is not dependent on specific low pH conditions and is unaffected by the presence of competing anions. These novel materials therefore offer great promise for dealing with the ⁹⁹Tc contamination problem.

Chapter Four

Computational Methods

Molecular modelling can be used to complement experimental observations by providing additional insight into physical and chemical processes [9]. Models are also particularly useful for avoiding the radiation protection challenges faced when dealing with radioactive materials experimentally (eg. with ^{99}Tc). A multiscale modelling approach is often necessary to fully understand a given problem that involves processes occurring over a wide range of length and time scales. The computational modelling methods discussed in this chapter are broadly divisible based on the size of the particles under investigation and whether they obey the laws of classical (atoms and molecules) or quantum (electrons) mechanics. In both cases the Hamiltonian operator, \hat{H} , which corresponds to the total energy of a system, \hat{E} , can be written as

$$\hat{H} \equiv \hat{E} = \hat{K} + \hat{V} \quad (4.1)$$

where \hat{K} and \hat{V} are the kinetic and potential energy operators.

4.1 Electronic Structure Methods

Electrons possess wave-like properties and are limited to discrete energy levels so require a quantum mechanical treatment. It is a fundamental postulate of quantum mechanics that a wavefunction, Ψ , exists for any given chemical system and observable properties are retrieved from it using suitable operators. The primary focus of electronic structure methods is to solve the electronic Schrödinger equation in order to obtain an accurate wavefunction for a system of electrons. For a given molecule there are many acceptable wavefunctions. Electrons are able to rapidly adjust to any change in nuclear coordinates, due to their much smaller size, and can therefore be assumed to be moving within a field of nuclei at fixed positions. This assumption, known as the Born-Oppenheimer approximation [115], is fundamental in molecular modelling studies as it allows nuclear and electronic motions to be decoupled. The electronic Schrödinger equation can therefore be defined as

$$\hat{H}_{\text{el}}(\mathbf{r})\Psi(\mathbf{r}) = E_{\text{el}}\Psi(\mathbf{r}) \quad (4.2)$$

where E_{el} is the total electronic energy, \hat{H}_{el} is the electronic Hamiltonian operator and \mathbf{r} refers to the set of electron coordinates,

$$\mathbf{r} = (\mathbf{r}_1, \mathbf{r}_2, \mathbf{r}_3 \dots \mathbf{r}_{N_e}) \quad (4.3)$$

where N_e is the total number of electrons and \mathbf{r}_i is the position vector of electron i ,

$$\mathbf{r}_i = (x_i, y_i, z_i) \quad (4.4)$$

Coulomb repulsions ensure that exact solutions to the electronic Schrödinger equation are not possible, even for very simple systems. However, the problem can be simplified by assuming that the overall multi-electron wavefunction can be written as the product of the single-electron wavefunctions (or orbitals), ψ_i ,

$$\Psi(\mathbf{r}) = \psi_1(\mathbf{r}_1)\psi_2(\mathbf{r}_2) \dots \psi_{N_e}(\mathbf{r}_{N_e}) \quad (4.5)$$

allowing the overall Hamiltonian to be separated into a sum of one-electron operators, \hat{h}_i ,

$$\hat{H}_{el}(\mathbf{r}) = \sum_{i=1}^{N_e} \hat{h}_i(\mathbf{r}) \quad (4.6)$$

$$\hat{h}_i(\mathbf{r}_i)\psi_i(\mathbf{r}_i) = \varepsilon_i\psi_i(\mathbf{r}_i)$$

where ε_i is the one-electron energy.

In practice, the electronic Schrödinger equation is solved according to the variational principle, which states that E_{el} computed from a given wavefunction must always be greater than or equal to the true electronic energy of the system. This means that the best wavefunction must be the one that gives the lowest energy solution and the Schrödinger equation is therefore typically solved using an iterative self-consistent process that minimises this quantity. The Hartree-Fock (HF) approach is frequently used to find approximate solutions to Equation 4.2 by this method [116]. Although the Hartree-Fock approach accounts for quantum mechanical exchange (due to the fermionic nature of electrons) exactly, it only calculates the average interaction between electrons so does not properly account for their correlated motion.

4.1.1 Density Functional Theory

Density functional theory (DFT) includes the effect of electron correlation in an approximate manner so can be used for more accurate calculations than HF in many instances. The DFT approach is also typically faster than HF. The central premise of DFT is the proof by Hohenberg and Kohn [117], known as the existence theorem, that the electronic energy of a system of electrons is determined completely by its electron probability density. This density can also be related to the individual one-electron orbitals that appear in Equation 4.5 by

$$\rho(\mathbf{r}) = \sum_{i=1}^{N_{\text{orb}}} |\psi_i(\mathbf{r})|^2 \quad (4.7)$$

where N_{orb} is the number of orbitals. The term “functional” (denoted by square brackets) derives from the fact that the energy can be written as a function of the electron density, which in turn is a function of the electron positions. The total DFT energy, corresponding to Equation 4.1, can be written as

$$E_{\text{DFT}}[\rho(\mathbf{r})] = K[\rho(\mathbf{r})] + V_{\text{ne}}[\rho(\mathbf{r})] + V_{\text{ee}}[\rho(\mathbf{r})] \quad (4.8)$$

which includes contributions due to the kinetic energy of the electrons, K , attraction between the nuclei and electrons, V_{ne} , and interelectronic repulsion, V_{ee} . The energy due to internuclear repulsions is a constant for a given molecular geometry.

In order to exploit this equation and use the electron density to obtain the energy of a system, appropriate density functionals must first be constructed. Kohn and Sham [118] realised the problem of developing functionals for a system could be simplified if the Hamiltonian could be written for a fictitious system of electrons that do not interact with each other. By treating the electrons in this way, the Kohn-Sham (KS) methodology allows Equation 4.8 to be separated into terms for the non-interacting system of electrons and terms that correct for this approximation.

The kinetic energy can be separated by

$$K[\rho(\mathbf{r})] = K_{\text{ni}}[\rho(\mathbf{r})] + \Delta K[\rho(\mathbf{r})] \quad (4.9)$$

where K_{ni} is the kinetic energy of the non-interacting system of electrons and ΔK is the correction to account for the interacting nature of electrons in a real system. The potential energy of interaction between electrons can also be separated into two terms

$$V_{\text{ee}} = V_{\text{elec}}[\rho(\mathbf{r})] + \Delta V[\rho(\mathbf{r})] \quad (4.10)$$

where V_{elec} is the coulombic repulsion and ΔV includes corrections for exchange and correlation due to the quantum mechanical nature of electrons. Equation 4.8 can now be rewritten as

$$E_{\text{DFT}}[\rho(\mathbf{r})] = K_{\text{ni}}[\rho(\mathbf{r})] + V_{\text{ne}}[\rho(\mathbf{r})] + V_{\text{elec}}[\rho(\mathbf{r})] + E_{\text{xc}}[\rho(\mathbf{r})] \quad (4.11)$$

where K_{ni} , V_{ne} and V_{elec} can be evaluated exactly and all the corrections are incorporated into a single term known as the exchange-correlation energy, E_{xc} . Since the momentum operator, \hat{p} , for a single QM particle can be written as

$$\hat{p} = -i\hbar\nabla \quad (4.12)$$

where \hbar is the reduced Planck constant ($h/2\pi$) and ∇ is the gradient operator, the kinetic energy of the non-interacting electrons is given by the equation

$$K_{\text{ni}}[\rho(\mathbf{r})] = \sum_{i=1}^{N_e} \int \psi_i^*(\mathbf{r}) \left(-\frac{\hbar^2}{2m_e} \nabla_i^2 \right) \psi_i(\mathbf{r}) d\mathbf{r} \quad (4.13)$$

where m_e is the mass of an electron and ∇_i^2 is the Laplace operator,

$$\nabla_i^2 = \frac{\partial^2}{\partial x_i^2} + \frac{\partial^2}{\partial y_i^2} + \frac{\partial^2}{\partial z_i^2} \quad (4.14)$$

The second term in Equation 4.11 accounts for the attractions between each nucleus, k , and an electron's charge density

$$V_{\text{ne}}[\rho(\mathbf{r})] = -\frac{e^2}{4\pi\epsilon_0} \sum_{k=1}^{N_n} \int \frac{q_k \rho(\mathbf{r})}{|\mathbf{r} - \mathbf{R}_k|} d\mathbf{r} \quad (4.15)$$

where N_n is the number of atomic nuclei, e is the elementary charge and ϵ_0 is the vacuum permittivity. \mathbf{R}_k and q_k are the positions and point charges of the nuclei. The electrostatic repulsion between two charge densities $\rho(\mathbf{r}_1)$ and $\rho(\mathbf{r}_2)$ is given by

$$V_{\text{elec}}[\rho(\mathbf{r})] = \frac{e^2}{4\pi\epsilon_0} \cdot \frac{1}{2} \iint \frac{\rho(\mathbf{r}_i)\rho(\mathbf{r}')}{|\mathbf{r}_i - \mathbf{r}'|} d\mathbf{r}_i d\mathbf{r}' \quad (4.16)$$

Equation 4.6 can be used to define a set of Kohn-Sham equations

$$\hat{h}_i^{\text{KS}}\psi_i(\mathbf{r}) = \epsilon_i\psi_i(\mathbf{r}) \quad (4.17)$$

where ψ_i are the Kohn-Sham orbitals and \hat{h}_i^{KS} are the corresponding one-electron operators. In atomic units the constants in Equations 4.13, 4.15 and 4.16 are all equal to unity so the one-electron operator can be given as

$$\hat{h}_i^{\text{KS}} = -\frac{1}{2}\nabla_i^2 - \sum_{k=1}^{N_n} \frac{q_k}{|\mathbf{r}_i - \mathbf{R}_k|} + \int \frac{\rho(\mathbf{r}')}{|\mathbf{r}_i - \mathbf{r}'|} d\mathbf{r}' + \frac{\delta E_{\text{xc}}[\rho(\mathbf{r}_i)]}{\delta\rho(\mathbf{r}_i)} \quad (4.18)$$

The final term is the functional derivative of E_{xc} , which can be written as

$$E_{\text{xc}}[\rho(\mathbf{r})] = E_{\text{x}}[\rho(\mathbf{r})] + E_{\text{c}}[\rho(\mathbf{r})] \quad (4.19)$$

incorporating all corrections for the exchange potential energy, E_{x} , and the kinetic and potential correlation energy, E_{c} , and is therefore the difference between the real and fictitious (Kohn-Sham) system. In DFT most of the effort expended is the construction of suitable functionals to approximate this exchange-correlation term.

To solve the Kohn-Sham equations the molecular orbitals can be expressed as a linear combination of atom-centred functions, ϕ_i ,

$$\psi_i(\mathbf{r}) = \sum_{i=1}^{N_{\text{orb}}} c_i\phi_i(\mathbf{r}) \quad (4.20)$$

where c_i is a molecular orbital coefficient and N_{orb} is the total number of functions used. This is known as a basis set expansion. In practice the basis functions for each orbital, which are usually chosen to be orthogonal, are substituted into the Kohn-Sham equations (4.17) and stored in matrix form. Hohenberg and Kohn's second theorem [117] states that the correct ground state electron density minimises the energy functional, and is analogous to the variational principle. The initial density matrix is estimated from the basis set and molecular geometry provided, from which the exchange-correlation functional can be constructed, the Kohn-Sham equations are solved and then a new density matrix is constructed from the occupied orbitals. This

iterative process is repeated until the new density is sufficiently similar to the old one, at which point the density is said to have converged in a self-consistent manner.

4.1.2 Exchange-Correlation Functionals

The most basic method of determining the exchange-correlation energy uses the local spin density approximation (LSDA). In this method the electron density is treated as a uniform electron gas, in which the electron density is a constant at every position in space. The exact exchange-correlation energy for the uniform electron gas is known. Using this approximation the exchange-correlation energy can be determined by

$$E_{xc}^{\text{LSDA}}[\rho(\mathbf{r})] = \int \rho(\mathbf{r})\varepsilon_{xc}[\rho(\mathbf{r})]d\mathbf{r} \quad (4.21)$$

where the exchange-correlation energy is obtained by integrating a per electron value, ε_{xc} , over all space. Most efforts aimed at developing suitable functionals rely on the fact that the individual exchange and correlation terms are separable

$$\int \rho(\mathbf{r})\varepsilon_{xc}[\rho(\mathbf{r})]d\mathbf{r} = \int \rho(\mathbf{r})\varepsilon_x[\rho(\mathbf{r})]d\mathbf{r} + \int \rho(\mathbf{r})\varepsilon_c[\rho(\mathbf{r})]d\mathbf{r} \quad (4.22)$$

Electron densities are typically far from being spatially uniform so LSDA is an inadequate approximation in most situations. The logical improvement to this solely local dependence on the electron density is to use its first derivative, $\nabla\rho(\mathbf{r})$, at the local position and add this as a correction term to the result from the LSDA approach,

$$\varepsilon_{x/c}^{\text{GGA}}[\rho(\mathbf{r})] = \varepsilon_{x/c}[\rho(\mathbf{r})] + \Delta\varepsilon_{x/c} \frac{|\nabla\rho(\mathbf{r})|}{\rho^{4/3}(\mathbf{r})} \quad (4.23)$$

where the x/c subscript shows that this method, known as the generalised gradient approximation (GGA), can be used to approximate either exchange or correlation. One of the most popular GGA exchange functionals is the one proposed by Becke [119], ΔE_c^{B} , in which the GGA correction term incorporates a single empirical parameter fitted to the exchange energies of the noble gases. An example of a GGA functional for correlation energy is that of Lee, Yang and Parr [120], ΔE_c^{LYP} . A further improvement can be made by also including a dependence on the kinetic energy density and these are known as meta-GGA functionals.

The basic LSDA functional can be improved upon by making a smooth connection between the non-interacting Kohn-Sham reference system and the real system by incorporating exchange energy, calculated exactly in the HF method, E_x^{HF} , in a ‘hybrid’ manner. One example of a hybrid functional is the popular B3LYP [121] which combines Becke exchange and LYP correlation

$$E_{xc}^{\text{B3LYP}} = (1 - a)E_x^{\text{LSDA}} + aE_x^{\text{HF}} + b\Delta E_x^{\text{B}} + (1 - c)E_c^{\text{LSDA}} + c\Delta E_c^{\text{LYP}} \quad (4.24)$$

where a , b and c are empirically determined coefficients.

4.1.3 Basis Sets

In order to solve the Kohn-Sham equations a description of the one-electron orbitals is required. The approximate shape of an atomic orbital is best described by a Slater function of the form

$$\phi_i(\mathbf{r}) = N_0 x^a y^b z^c \exp[-\zeta_i \mathbf{r}] \quad (4.25)$$

where N_0 is a normalization constant, ζ_i is an orbital exponent, chosen to control its width, and the three integers a , b and c determine the type of atomic orbital (ie. s, p and d). In practice, coulomb integrals constructed with these functions are very difficult to evaluate. Gaussian functions (or Gaussian type orbitals, GTOs) offer the advantage that two functions centred on different atoms can be expressed as a single function on a point along the axis connecting them, which is not possible with Slater functions. However, a single Gaussian function provides a poor description of the shape of an atomic orbital due to the fact that they do not have a cusp at the origin and decay too rapidly as \mathbf{r} increases. Instead, the shape of a Slater function can be approximated using a linear combination of GTOs [122],

$$\phi_i(\mathbf{r}) = \sum_{i=1}^{N_{\text{GTO}}} d_i \varphi_i(\mathbf{r}) \quad (4.26)$$

where N_{GTO} is the number of Gaussian functions used in the linear combination, d_i is a coefficient chosen to optimize the shape of the orbital, and the Gaussian function is given by

$$\varphi_i(\mathbf{r}) = N_0 x^a y^b z^c \exp[-(\alpha_i \mathbf{r})^2] \quad (4.27)$$

where α_i controls the width of the Gaussian function.

The accuracy of an electronic structure calculation is dependent on both the number and type of functions used in Equation 4.26. A minimal basis set contains the same number of functions as atomic orbitals in the molecule. Doubling or tripling the number of basis functions will improve the quality of the basis set but this is associated with an increase in computational cost. It is quite common to only double the number of valence basis functions since chemical properties are generally independent of core electrons. Basis sets are typically energy-optimised and the energy mainly depends on the inner-shell electrons, which are chemically unimportant. It is possible to increase the relative importance of the valence orbitals by reducing the number of basis functions used to model core electrons into a smaller set of functions. This process is known as basis set contraction and results in significant rewards in computational cost. In Pople's '*k-nlmG*' series of basis sets [123] the integer *k* refers to the number of GTOs used in the contraction for core orbitals. The integers *n*, *l* and *m* refer to the number of functions used for valence orbitals and the number of contracted GTOs used for each of these functions. For example, 6-311G is a triple split valence basis set, where the core orbitals are a contraction of six GTOs and valence orbitals are split into three functions, each of which is a contraction of three, one and one GTOs, respectively [124].

Polarisation Functions

The electron density of an atom is distorted in a molecule compared to the electron density of that same atom in isolation. In many cases a standard basis set does not provide sufficient mathematical flexibility to correctly describe the asymmetrical nature of molecular orbitals. Additional basis functions known as polarisation functions, that are one orbital quantum number higher in angular momentum than the atom's valence orbitals, can provide this extra flexibility [125]. For example, d-type functions can be used to introduce asymmetry into the p-orbital electron distribution of the first and second row elements. A set of polarisation functions on the Pople split-valence basis sets is typically denoted with an asterisk. Therefore, the 6-311G** basis set has two sets of polarisation functions; one set of p-type functions that polarizes the s-orbitals on hydrogen and helium and another that polarizes valence p-orbitals using d-type functions on other atoms.

Diffuse Functions

Additional functions may be required to describe molecular orbitals, which are more delocalised with respect to the nucleus, particularly when dealing with anions. Diffuse functions, which have very wide Gaussian distributions (large α), can be used to account for the electron density far from atom centres. In the Pople style split valence basis set these are denoted '+’.

Pseudopotentials

Heavy elements pose two distinct problems to electronic structure calculations. They have many core electrons, which are chemically unimportant compared to the valence electrons. Secondly, the core electrons manifest relativistic effects that cannot be accounted for using a standard basis set. These two problems can be simultaneously addressed by replacing a number of core electrons with functions that model the interactions between an ‘effective’ core of an atom (ie. the nucleus and inner shell electrons) and its valence electrons. This type of function is known as a pseudopotential and is normally derived by fitting the properties of the valence electrons in an atom containing a pseudopotential to those of an all electron calculation.

4.1.4 Practical Considerations for DFT Calculations

Numerical Quadrature

Equation 4.21 suggests we need to integrate over the entire space occupied by a molecule to obtain the exchange and correlation energy densities on each KS cycle. Since ϵ_{xc} implicitly depends on the integration variable, \mathbf{r} , this integration cannot be performed analytically. Instead Equation 4.21 can be approximated by numerical integration on a grid. The grid is normally specified as a number of points distributed around spherical radial shells around an atomic nucleus.

Geometry Optimisation

Once the electron density of a molecule for a given input geometry has converged its final energy can be computed using Equation 4.11. If the goal was simply to determine the energy of this structure (a single-point energy calculation) then the calculation ends at this stage. One of the purposes of electronic structure methods is to

explore the potential energy surface (PES) of a molecule (the change in energy as a function of the $3N - 6$ nuclear coordinates). It is not feasible to explore the entire PES over all possible $3N - 6$ nuclear coordinates but by constraining efforts to the chemically relevant areas of the PES stationary points that correspond to the minima (local or global) and transition states of interest can be found. In this case, once the initial energy has been calculated the geometry can be adjusted to find another point on the PES using schemes such as the Berny algorithm [126]. At the new geometry the DFT calculation is performed again and this process is repeated until a stationary point is found, which either corresponds to a transition state or a minimum (local or global) on the PES.

Implicit Solvation

Most chemical processes occur in the presence of a solvent. The relevant solvent molecules can be explicitly included in a calculation but this is normally prohibitively expensive especially when dealing with large molecules or ions where many solvent molecules must be considered. There are many solvation models that take into account the effect of bulk solvent properties such as the dielectric constant in an implicit manner. One of the most common types of solvation model used in electronic structure methods is based on the reaction field methodology in which the solute is considered to be in a cavity surrounded by a uniform and polarizable solvent. The effect of the solvent medium must be considered in a self-consistent manner because the charge distribution of the solute polarises the dielectric medium that must be included by modifying the Kohn-Sham operator, resulting in a new solute electron distribution. The incorporation of solvation effects by this iterative process is known as the self-consistent reaction field (SCRF) method.

4.2 Classical Potential Energy Functions

The positions and momenta of atoms and molecules in a system vary continuously and cannot therefore be treated using a quantum mechanical description. Instead, classical mechanics is used to describe the motions of the individual atoms in such a system. Classical potential energy functions (or force fields) are used to determine interactions between the atoms of separate molecules (intermolecular forces) and between atoms in the same molecule (intramolecular forces). In an atomistic

simulation, where each atom is modelled using a single particle, potential energy functions must be defined in order to calculate the forces acting on each particle.

4.2.1 Intermolecular Potentials

In the absence of any chemical bonds the overall potential energy of a system of N atoms can be written purely in intermolecular terms

$$V_N(\mathbf{r}^N) = \sum_i^N v_i(\mathbf{r}_i) + \sum_i^N \sum_{j>i}^N v_{ij}(\mathbf{r}_i, \mathbf{r}_j) + \sum_i^N \sum_{j>i}^N \sum_{k>j>i}^N v_{ijk}(\mathbf{r}_i, \mathbf{r}_j, \mathbf{r}_k) + \dots \quad (4.28)$$

where the terms are separated according to their dependence on the coordinates of individual atoms (v_i), pairs of atoms (v_{ij}), triplets of atoms (v_{ijk}), etc. Other than the first term in the series the potential energies correspond to interactions between particles in the system. Three-body terms and above are normally ignored because they are time-consuming to compute and only make a minor contribution to V_N compared to the pairwise interactions. Often, they are effectively incorporated into the pairwise term anyway. The pair potential, v_{ij} , only depends on the separation between two atoms, defined as

$$r_{ij} = |\mathbf{r}_i - \mathbf{r}_j| \quad (4.29)$$

At infinite separation two neutral atoms do not interact with each other and $v(r_{ij})$ tends to 0. As these two atoms approach each other they develop electrical moments that orient to become mutually attractive ($v(r_{ij}) < 0$) until they become so close that their surrounding electron densities begin to overlap resulting in a rapid increase in energy ($v(r_{ij}) > 0$) caused by Pauli repulsion. One simple function that can properly account for all of these effects is the Lennard-Jones 12-6 potential

$$v_{LJ}(r_{ij}) = 4\varepsilon_{ij} \left[\left(\frac{\sigma_{ij}}{r_{ij}} \right)^{12} - \left(\frac{\sigma_{ij}}{r_{ij}} \right)^6 \right] \quad (4.30)$$

where the first term in the square brackets accounts for short-range repulsion and the second term the attractive dispersion interaction; σ_{ij} and ε_{ij} are the two van der Waals (VDW) parameters. The VDW diameter, σ_{ij} , is defined as the distance at which the potential energy is zero and ε_{ij} is the depth of the potential energy well. When $i \neq j$

these parameters must be approximated using suitable combining rules. The Lorentz-Berthelot combining rules are

$$\begin{aligned}\sigma_{ij} &= \frac{1}{2}(\sigma_i + \sigma_j) \\ \varepsilon_{ij} &= \sqrt{\varepsilon_i \varepsilon_j}\end{aligned}\tag{4.31}$$

where cross interaction terms are obtained as the arithmetic and geometric means of the individual atomic parameters. Electrostatic interactions are calculated according to Coulomb's law

$$v_{\text{elec}}(r_{ij}) = \frac{z_i z_j}{r_{ij}^2}\tag{4.32}$$

where z_i is given by

$$z_i = \frac{q_i e}{\sqrt{4\pi\varepsilon_0}}\tag{4.33}$$

4.2.2 Intramolecular Potentials

In a molecular system potentials are also required to describe the interactions between atoms that belong to the same molecule. Under the assumption that intramolecular motions can be decoupled, separate potentials are used to describe the motion of bond stretching, angle bending and torsions in molecule. The simplest function that can be used to describe the motion of a stretching bond is Hooke's law for a spring

$$v_{\text{bond}}(r_{ij}) = \frac{1}{2}k_r(r_{ij} - r_{\text{eq}})^2\tag{4.34}$$

where r_{eq} is the equilibrium bond distance and k_r is the force constant, which governs how the potential energy varies as r_{ij} deviates from r_{eq} . Angle bending motions can also be treated with a harmonic potential of the form

$$v_{\text{angle}}(\theta_{ijk}) = \frac{1}{2}k_\theta(\theta_{ijk} - \theta_{\text{eq}})^2\tag{4.35}$$

where θ_{ijk} and θ_{eq} are the angle between atoms, i , j and k , and the equilibrium bond angle, respectively. Potential energy functions for dihedral angles typically have a

slightly more complex form to account for the periodic nature of torsional motion. One function commonly used to account for this motion is a triple cosine

$$v_{\text{tors}}(\phi_{ijkl}) = v_1(1 + \cos(\phi_{ijkl})) + v_2(1 - \cos(2\phi_{ijkl})) + v_3(1 + \cos(3\phi_{ijkl})) \quad (4.36)$$

where ϕ_{ijkl} is the dihedral angle between atom i and l connected via bonds with j and k , which can vary from $-\pi$ to π . v_1 , v_2 and v_3 are the heights of the rotation barriers.

Assuming pairwise additivity and that intramolecular motions can be decoupled, the overall potential energy function, V_N , for a set of N particles in a given configuration can be written as the sum over all terms for all of the particles.

$$V_N(\mathbf{r}^N) = \sum_{\text{bonds}} v_{\text{bond}}(r_{ij}) + \sum_{\text{angles}} v_{\text{angle}}(\theta_{ijk}) + \sum_{\text{torsions}} v_{\text{tors}}(\phi_{ijkl}) + \sum_{\text{non-bonded}} v_{LJ}(r_{ij}) + v_{\text{elec}}(r_{ij}) \quad (4.37)$$

In general, the parameters used in the potential energy function can be optimised by either fitting to quantum mechanical calculations or experimental data. One desirable property for parameters is that they are transferable, ie. the same parameters can be used for a given atom or group of atoms in a variety of different chemical environments and situations.

4.3 Statistical Mechanics

Statistical mechanics provides the important link between macroscopic thermodynamic observables and the properties of microscopic systems. Experiments are conducted on macroscopic samples with the number of particles (atoms or molecules) involved far greater ($N \approx 10^{23}$) than can easily be accommodated by computer calculations ($N \approx 10^6$). In an experiment it is reasonable to assume a typical thermodynamic observable for a system, A_{obs} , will be measured over a period of time, t_{obs} , so A_{obs} will in fact be obtained as a time average, $\langle A \rangle_{\text{time}}$,

$$A_{\text{obs}} = \langle A \rangle_{\text{time}} = \lim_{t_{\text{obs}} \rightarrow \infty} \frac{1}{t_{\text{obs}}} \int_0^{t_{\text{obs}}} A(t) dt \quad (4.38)$$

where $A(t)$ is the instantaneous value of A measured at time t in the time interval from $t = 0$ until $t = t_{\text{obs}}$, which becomes more accurate as the observation time increases. This system can be considered as a set of N indistinguishable particles each of which has a position, \mathbf{r}_i , and momentum, \mathbf{p}_i . One set of particle positions, \mathbf{r}^N , and momenta, \mathbf{p}^N , can be thought of as a single point in $6N$ ($3N$ positions and $3N$ momenta) multi-dimensional phase space, Γ ,

$$\begin{aligned}\Gamma &= (\mathbf{r}^N, \mathbf{p}^N) \\ \mathbf{r}^N &= (\mathbf{r}_1, \mathbf{r}_2, \mathbf{r}_3 \dots \mathbf{r}_N) \\ \mathbf{p}^N &= (\mathbf{p}_1, \mathbf{p}_2, \mathbf{p}_3 \dots \mathbf{p}_N)\end{aligned}\tag{4.39}$$

As time progresses, particles interact with each other and trace out a path in phase space known as the trajectory, so $A(t)$ is really $A(\Gamma(t))$.

Gibbs first suggested, in his Ergodic hypothesis, that instead of using the time average in Equation 4.38 an ensemble average value of the property, $\langle A \rangle_{\text{ens}}$, could be calculated. This average can be obtained from a number of instantaneous points in phase space, $A(\Gamma)$, distributed according to a probability density, $p(\Gamma)$,

$$A_{\text{obs}} = \langle A \rangle_{\text{ens}} = \int A(\Gamma)p(\Gamma)d\Gamma\tag{4.40}$$

The weighted average reflects the fact that more favourable points in phase space will be visited more often. The sum over all the weighted points is the partition function, Q , and if Q is known all of the system's thermodynamic quantities of interest can be derived [127].

4.3.1 Statistical Ensembles

In each type of statistical ensemble some thermodynamic variables are fixed and the remainder are allowed to fluctuate. The exact formula used to calculate the partition function is ensemble dependent. The most fundamental ensemble represents an isolated system (constant N , V and E) and is known as the microcanonical ensemble. The partition function for this ensemble can be written as

$$Q_{\text{NVE}} = \frac{1}{N!} \frac{1}{h^{3N}} \int \delta(H(\mathbf{\Gamma}) - E) d\mathbf{\Gamma} \quad (4.41)$$

where H , the classical Hamiltonian, expresses the total energy of a point in phase space and the $N!$ term accounts for the indistinguishability of the particles. The Dirac delta function in Equation 4.41 ensures that only phase space points that conserve total energy are considered. The natural logarithm of Q_{NVE} is related to the entropy, S , via the Boltzmann constant, k_B , by

$$S = k_B \ln Q_{\text{NVE}} \quad (4.42)$$

This equation is an example of the important link between configurations of particles on the microscale and a macroscopic thermodynamic variable using the partition function.

There are many situations where precise temperature control of a system is desirable. In the canonical ensemble temperature is conserved instead of energy. The canonical partition function is given by

$$Q_{\text{NVT}} = \frac{1}{N!} \frac{1}{h^{3N}} \int \exp[-\beta H(\mathbf{\Gamma})] d\mathbf{\Gamma} \quad (4.43)$$

where

$$\beta = \frac{1}{k_B T} \quad (4.44)$$

and T is the temperature. The negative exponential of the ratio of energy to temperature inside the integral in Equation 4.43 is known as the Boltzmann factor.

Using Q_{NVT} , the Helmholtz free energy, F , can be determined from the equation

$$F = -k_B T \ln Q_{\text{NVT}} \quad (4.45)$$

Crucially, the definition of the Hamiltonian in Equation 4.1 permits the separation of the momentum dependent kinetic ideal gas term and the position dependent (configurational) residual term. As a result the partition function can now be factorised resulting in

$$Q_{\text{NVT}} = \frac{1}{N!} \frac{1}{h^{3N}} \int \exp[-\beta K_N(\mathbf{p}^N)] d\mathbf{p}^N \int \exp[-\beta V_N(\mathbf{r}^N)] d\mathbf{r}^N \quad (4.46)$$

enabling the ideal gas, $Q_{\text{NVT}}^{\text{id}}$, and configurational, Z_{NVT} , contributions to any thermodynamic variable to be calculated independently,

$$Q_{\text{NVT}} = Q_{\text{NVT}}^{\text{id}} \frac{Z_{\text{NVT}}}{V^N} \quad (4.47)$$

Evaluation of the ideal gas term is trivial,

$$Q_{\text{NVT}}^{\text{id}} = \frac{\Lambda^{-3N}}{N!} V^N \quad (4.48)$$

where Λ is the de Broglie thermal wavelength,

$$\Lambda = \left(\frac{2\pi\beta\hbar^2}{m} \right)^{1/2} \quad (4.49)$$

and m is the mass of a particle. Most effort is therefore expended calculating the residual part, where

$$Z_{\text{NVT}} \equiv \int \exp[-\beta V_N(\mathbf{r}^N)] d\mathbf{r}^N \quad (4.50)$$

The calculation of a thermodynamic property of interest can now be achieved by dividing its weighted average by the configurational integral,

$$\langle A \rangle_{\text{ens}} = \frac{\int A(\mathbf{r}) \exp[-\beta V_N(\mathbf{r}^N)] d\mathbf{r}^N}{Z_{\text{NVT}}} \quad (4.51)$$

in a process known as Boltzmann averaging.

Most experiments are performed under conditions of constant pressure, P . If the aim is to reproduce these conditions as closely as possible then the isothermal-isobaric (constant N , P and T) ensemble will be the most suitable. The partition function for this ensemble can be adapted from Equation 4.43 to permit the system volume, V , to fluctuate

$$Q_{\text{NPT}} = \frac{1}{N!} \frac{1}{h^{3N}} \frac{1}{V_0} \iint \exp[-\beta(H(\mathbf{\Gamma}) + PV)] d\mathbf{\Gamma} dV \quad (4.52)$$

where V_0 , a normalization factor, is required to render Q_{NPT} dimensionless. In the same way as Equation 4.45 the partition function can be used to give

$$G = -k_{\text{B}}T \ln Q_{\text{NPT}} \quad (4.53)$$

where G is the Gibbs free energy. Once again the position dependent terms in the partition function can be factorised out so that the configurational integral can be written as

$$Z_{\text{NPT}} \equiv \int \exp[-\beta V_N(\mathbf{r}^N)] d\mathbf{r}^N \int \exp[-\beta PV] dV \quad (4.54)$$

and in the event of changes in system volume particle coordinates must be scaled appropriately. The final commonly used statistical ensemble is the grand canonical, for which the partition function is given by

$$Q_{\mu\text{VT}} = \sum_N \frac{1}{N!} \frac{1}{h^{3N}} \exp[\beta\mu N] \int \exp[-\beta H(\mathbf{\Gamma})] d\mathbf{\Gamma} \quad (4.55)$$

and the exchange of particles with a fictitious external reservoir imposing conditions of constant chemical potential, μ , allows N to fluctuate. N cannot really be considered a continuous variable so a summation is used instead of an integral in this equation.

4.4 Molecular Simulation

Although the momentum dependent term in the partition function can easily be evaluated analytically this is not possible for the configurational term. This is because of the unfeasibly large number of configurations that must be considered, the vast majority of which have a very low probability. Molecular simulation provides a means of evaluating the configurational term. The two general types of simulation used to achieve this are Monte Carlo (MC) and molecular dynamics (MD) [128]. It is important to note the key difference between the two approaches. MC simulations are stochastic; a random succession of phase space points is generated so that it is not possible to predict the future state of the system. Alternatively, MD is a deterministic method, which means that the state of the system at any time in the future can in principle be determined from the initial particle positions and momenta. A description of the basic algorithm for these two methods is given in the following sections, as

well as some general information on practical considerations for performing a molecular simulation.

4.4.1 Monte Carlo Simulations

MC simulations seek to provide a means of calculating the thermodynamic quantities of interest by sampling only from the high probability regions of phase space. Points in configuration space are sampled at random and thermodynamic properties are computed as ensemble averages. The most basic MC algorithm generates a random configuration of particles completely independent of the previous one, determines the potential energy of this configuration and uses it to calculate the Boltzmann factor. In a MC simulation the configurational integral is discretised. In the canonical ensemble,

$$Z_{\text{NVT}} = \sum_{i=1}^{N_{\text{trial}}} \exp[-\beta V_N(\mathbf{r}_i^N)] \quad (4.56)$$

where N_{trial} is the total number of random configurations generated. Using this definition of the configuration integral and Equation 4.51 thermodynamic properties can be obtained using

$$\langle A(\mathbf{r}^N) \rangle = \frac{\sum_{i=1}^{N_{\text{trial}}} A(\mathbf{r}_i^N) \exp[-\beta V_N(\mathbf{r}_i^N)]}{Z_{\text{NVT}}} \quad (4.57)$$

For most purposes this purely random sampling approach is insufficient due to the very large number of configurations that have unfavourable potential energies (and effectively zero Boltzmann factor) that must be considered. A more useful approach is to bias the random generation of new configurations towards those that have the largest contributions to the configuration integral.

Metropolis Sampling

In the Metropolis method [129] a new configuration, $\mathbf{r}_{\text{new}}^N$, is generated from a perturbation (MC trial move) of the previous configuration, $\mathbf{r}_{\text{old}}^N$, and this sequence of points generated in phase space is called a Markov chain. Rather than Boltzmann weighting the potential energy of each new configuration, the acceptance decision itself is Boltzmann weighted so that not all newly generated configurations are

accepted. The probability of accepting each new configuration is based on a potential energy difference, ΔV_N ,

$$\Delta V_N = V_N(\mathbf{r}_{\text{new}}^N) - V_N(\mathbf{r}_{\text{old}}^N) \quad (4.58)$$

where $V_N(\mathbf{r}_{\text{new}}^N)$ and $V_N(\mathbf{r}_{\text{old}}^N)$ are the potential energies of the new and old configurations. The probability of accepting the move is

$$p(\mathbf{r}_{\text{old}}^N \rightarrow \mathbf{r}_{\text{new}}^N) = \min[1, \exp(-\beta\Delta V_N)] \quad (4.59)$$

This equation states that if $V_N(\mathbf{r}_{\text{new}}^N) < V_N(\mathbf{r}_{\text{old}}^N)$ then the new configuration is always accepted. If $V_N(\mathbf{r}_{\text{new}}^N) > V_N(\mathbf{r}_{\text{old}}^N)$ then a random number, ξ , is sampled from the interval $[0, 1]$ and the MC move only then accepted if $\xi < \exp(-\beta\Delta V_N)$. If rejected, then the old configuration is counted again and a new attempt is made to generate a random configuration. One consideration for a MC simulation is that the acceptance rules should obey the detailed balance principle, that is to say that the probability of attempting a trial move is equal to the probability of attempting the reverse move. The size of the MC move in the simulation is crucial. If the move is too large then the rejection rate of new configurations will be very high. If it is too small then the new and old configurations will be very similar. Both lead to inefficient sampling of phase space. MC simulations in the grand canonical ensemble (GCMC) are particularly well suited to studying adsorption processes since N is a variable. This offers a significant advantage over MD simulations which cannot deal with discrete processes such as particle insertions and deletions [127].

4.4.2 Molecular Dynamics Simulations

The aim of MD is to explore phase space by evolving particle trajectories using classical equations of motion. Providing that the initial particle positions and momenta have been specified, the instantaneous force, \mathbf{f}_i , acting on each particle i due the other $N - 1$ particles can be determined from the potential energy function by

$$\mathbf{f}_i = -\frac{\partial V_N}{\partial \mathbf{r}_i} \quad (4.60)$$

and trajectories can be obtained by solving the set of second order differential equations

$$\mathbf{f}_i = m_i \ddot{\mathbf{r}}_i \quad (4.61)$$

where $\ddot{\mathbf{r}}_i$ is the acceleration of particle i . Thermodynamic properties are then obtained from the set of particle positions and momenta. For instance, the instantaneous kinetic energy is calculated using

$$K_N(\mathbf{p}^N) = \sum_{i=1}^N \frac{\mathbf{p}_i^2}{2m_i} \quad (4.62)$$

Numerical Integration

In most cases the ordinary differential equations in Equation 4.61 cannot be solved analytically, so they are typically solved step-by-step, by numerical integration. One of the most popular schemes for numerically integrating the equations of motion is the Verlet algorithm [130], due to its accuracy and stability. The Verlet scheme advances positions and momenta using a discrete time step, Δt , and relies on a Taylor expansion in \mathbf{r}_i ,

$$\mathbf{r}_i(t + \Delta t) = \mathbf{r}_i(t) + \dot{\mathbf{r}}_i(t)\Delta t + \frac{1}{2!} \ddot{\mathbf{r}}_i(t)\Delta t^2 + \dots \quad (4.63)$$

where the expansion is truncated at second-order. Summing the Taylor expansions for forward ($+\Delta t$) and reverse ($-\Delta t$) time steps and rearranging gives

$$\mathbf{r}_i(t + \Delta t) = 2\mathbf{r}_i(t) - \mathbf{r}_i(t - \Delta t) + \ddot{\mathbf{r}}_i(t)\Delta t^2 \quad (4.64)$$

where the new position of the particle $\mathbf{r}_i(t + \Delta t)$ is computed without using the velocity. Although more accurate schemes exist, the velocity can be simply obtained from the position by

$$\dot{\mathbf{r}}_i(t) = \frac{\mathbf{r}_i(t + \Delta t) - \mathbf{r}_i(t - \Delta t)}{2\Delta t} \quad (4.65)$$

One of the most common modifications to the basic Verlet scheme is the Verlet Leap Frog algorithm [131] which uses the equations

$$\dot{\mathbf{r}}_i\left(t + \frac{\Delta t}{2}\right) = \dot{\mathbf{r}}_i\left(t - \frac{\Delta t}{2}\right) + \Delta t \ddot{\mathbf{r}}_i(t)$$

(4.66)

$$\mathbf{r}_i(t + \Delta t) = \mathbf{r}_i(t) + \Delta t \dot{\mathbf{r}}_i\left(t + \frac{\Delta t}{2}\right)$$

where the velocity is calculated half a time step after the position so that the velocity calculation ‘leap-frogs’ over the position calculation. The explicit computation of velocity in the Leap Frog algorithm results in improved accuracy compared to the standard Verlet scheme. Once the new positions are determined the forces are recalculated, the equations of motion are integrated again to obtain the new positions and velocities, and the simulation is conducted for the requested number of time steps allowing particle trajectories to be evolved. Thermodynamic properties can then be calculated as time averages over the total number of discrete time steps. There are many other approaches for numerically integrating the equations of motion, such as the Runge-Kutta and Gear predictor-corrector algorithms, and the advantages of each have been discussed in detail elsewhere [128].

Constraints

The length of a time step that can be used is limited by shortest timescale motion in the MD simulation. In many cases this would make the simulation very expensive due to high frequency intramolecular motions (such as a C – H bond vibration). Instead of representing these motions by terms in the potential energy function, they can be treated as rigid by constraining them to their equilibrium values. Constraint dynamics removes these specific degrees of freedom, allowing a longer time step to be used in the simulation. The most fundamental way of achieving this uses Gauss’ principle of least constraint [132] but the SHAKE algorithm provides a pragmatic approach in which the bond lengths are fixed in an iterative scheme and the normal equations of motion are integrated at each time step whilst satisfying this constraint [133].

4.4.3 Practical Considerations for Molecular Simulations

Equilibration

In any molecular simulation it is necessary to define an appropriate initial state. In MC this only requires particle positions, whereas in MD momenta (typically sampled at random from a Maxwell-Boltzmann distribution) are also required. Unless the

initial state of the system matches the end point of another simulation with the same potential energy function it is highly unlikely that it will correspond to a high probability region of phase space and a period of equilibration will be necessary to allow the system to relax to such a region. A simple way to check that a system has equilibrated is to monitor the instantaneous values of a fluctuating thermodynamic variable until it oscillates about the mean, so that there is no longer any systematic drift. A properly equilibrated simulation must be independent of its initial state.

Constant Temperature Simulations

The instantaneous temperature in a simulation, $T(t)$, is related to the individual particle momenta via

$$T(t) = \frac{1}{N_f k_B} \sum_{i=1}^N \frac{\mathbf{p}_i^2(t)}{m_i} \quad (4.67)$$

where N_f is the number of degrees of freedom ($N_f = 3N - N_c$, where N_c is the number of constraints). The simplest way of maintaining a constant temperature involves *ad hoc* rescaling of momenta

$$\mathbf{p}'_i = \mathbf{p}_i \sqrt{\frac{T_{\text{req}}}{T(t)}} \quad (4.68)$$

where \mathbf{p}'_i is the scaled momentum of particle i and T_{req} is the desired simulation temperature. A more elegant way of maintaining constant temperature is to abandon Newtonian mechanics and use the more general mechanics of Gauss or Nosé; the thermostat then appears explicitly in the equations of motion.

Periodic Boundary Conditions

Particles at the edge of a simulation cell inherently have fewer neighbours than those in the centre. In order that the simulations represent a bulk system, the effects of this edge must be eliminated. Periodic boundary conditions (PBCs) are often employed to allow images of the simulation cell to be replicated in each direction so that when a particle moves across the cell boundary an identical one will enter the cell through the opposite boundary (Figure 4.1). The periodic nature of the simulation cell means particle i will interact with particle j as well as any periodic images of j . The

minimum image convention is applied so that only the nearest interaction with j is considered, regardless of whether j is in the central simulation cell or a periodic image.

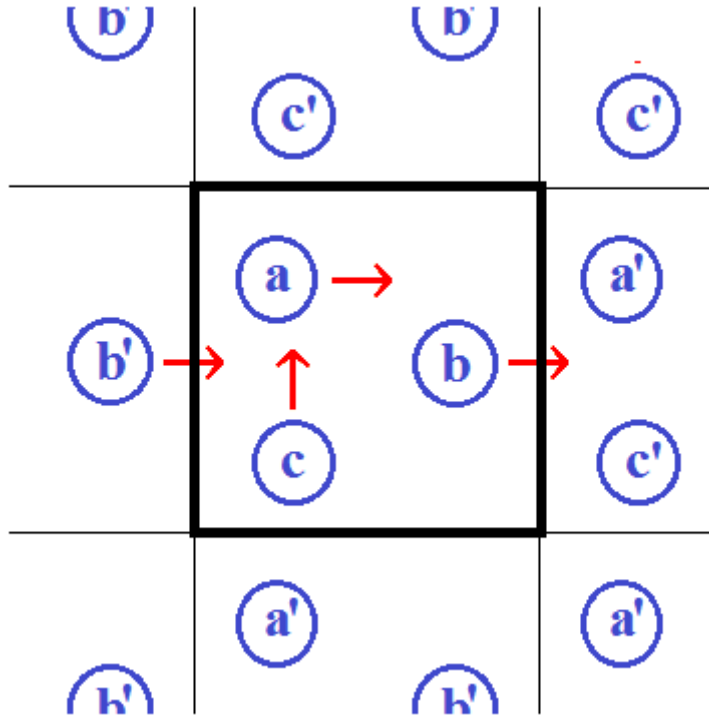


Figure 4.1 A 2D illustration of cubic PBCs. When a particle from the central cell (bold line), b , moves past the right hand boundary, an identical image particle, b' , replaces it by entering through the left hand boundary.

Potential Truncation

Evaluation of Equation 4.37 is the bottleneck in the speed of a molecular simulation so approximations need to be employed to attain reasonable computational cost. One example is to truncate the VDW interaction

$$v_{\text{LJ}}^{\text{trunc}}(r_{ij}) = \begin{cases} v_{\text{LJ}} & r_{ij} \leq r_{\text{cut}} \\ 0 & r_{ij} > r_{\text{cut}} \end{cases} \quad (4.69)$$

where r_{cut} is a spherical cut off radius. Increasing the size of r_{cut} reduces the error associated with such an approximation but increases the time taken to calculate the forces acting on a given particle. For Equation 4.30 this approximation is valid due to the r^{-6} dependence of the potential. For consistency with the minimum image

convention the short-range cut off cannot be greater than half the length of the simulation cell.

Long Range Forces

In a periodic and cubic simulation cell the total electrostatic potential energy is given by

$$V_N^{\text{elec}}(\mathbf{r}^N) = \frac{1}{2} \sum_{\mathbf{n}}' \left(\sum_{i=1}^N \sum_{j=1}^N \frac{z_i z_j}{|\mathbf{r}_{ij} + \mathbf{n}|} \right) \quad (4.70)$$

where the sum runs over all ions, N , and all periodic images of the simulation cell, \mathbf{n} ,

$$\mathbf{n} = (n_x L, n_y L, n_z L) \quad (4.71)$$

where L is the length of the cell and n_x , n_y and n_z are integers defining the periodic image. The prime on the first summation in Equation 4.70 indicates that for the central simulation cell ($\mathbf{n} = 0$) the interaction for $i = j$ is omitted since the indices refer to the same atom. The r^{-1} dependence of the Coulomb sum means that the electrostatic potential has an appreciable value even at large r_{ij} and straightforward truncation of Equation 4.70 results in serious inaccuracies [134]. The sum is conditionally convergent, meaning that the result depends on the order in which the terms are added, so cannot be used to reliably calculate the electrostatic potential energy.

The Ewald sum deals with this problem by dividing the overall potential into separate contributions (Figure 4.2). The first term accounts for the interactions between atoms in the central simulation box ('real' space) and the second term, which accounts for interactions between the atoms in the central box and those in image boxes ('reciprocal' space). In the Ewald summation each point charge is surrounded by a screening Gaussian charge distribution of equal magnitude but opposite charge that acts to neutralise the point charge

$$\varphi(\mathbf{r}_i) = \left(\frac{\alpha}{\sqrt{\pi}} \right)^3 z_i \exp[-(\alpha \mathbf{r}_i)^2] \quad (4.72)$$

where the parameter α controls the width of the Gaussian distribution. The sum in real space is then calculated over all point charges and their neutralising distributions. This

sum does converge rapidly so can be considered negligible past some real space cut off distance. The energy of the sum in real space is

$$V_N^{\text{real}}(\mathbf{r}^N) = \frac{1}{2} \sum_{i=1}^N \sum_{j=1}^N z_i z_j \frac{\text{erfc}(\alpha r_{ij})}{r_{ij}} \quad (4.73)$$

where erfc is the complementary error function [135],

$$\text{erfc}(a) = 1 - \text{erf}(a) = \frac{2}{\sqrt{\pi}} \int_a^{\infty} \exp(-b^2) db \quad (4.74)$$

A second set of Gaussian functions with opposite charges to the first is added (Figure 4.2c). This screening distribution is evaluated in reciprocal space and a Fourier transformation of the charge distribution in Equation 4.72 yields

$$\varphi(\mathbf{k}) = \frac{1}{V} \exp\left(\frac{-\mathbf{k}^2}{4\alpha^2}\right) z_i \exp(-i\mathbf{k} \cdot \mathbf{r}_i) \quad (4.75)$$

where \mathbf{k} is a lattice vector in reciprocal space. For a cubic simulation cell

$$\mathbf{k} = \frac{2\pi}{L} (l_x, l_y, l_z) \quad (4.76)$$

where l_x , l_y and l_z are the reciprocal lattice vectors in each dimension. By adopting this approach the charge distribution is a smoothly varying periodic function that can be considered negligible beyond a cut off distance, k_{cut} . A suitable value for the cut off can be determined using [136]

$$k_{\text{cut}} = \frac{1.05 \times 2\pi k_{\text{max}}}{L} \quad (4.77)$$

where the parameter k_{max} sets an integer limit on the values of l_x , l_y and l_z . Using Equation 4.75 the total reciprocal space contribution to the electrostatic energy can be calculated from

$$V_N^{\text{recip}}(\mathbf{r}^N) = \frac{1}{2V} \sum_{\mathbf{k} \neq 0}^{\infty} \left(\frac{4\pi}{k^2}\right) \exp\left(\frac{-k^2}{4\alpha^2}\right) \left| \sum_{i=1}^N z_i \exp(-i\mathbf{k} \cdot \mathbf{r}_i) \right|^2 \quad (4.78)$$

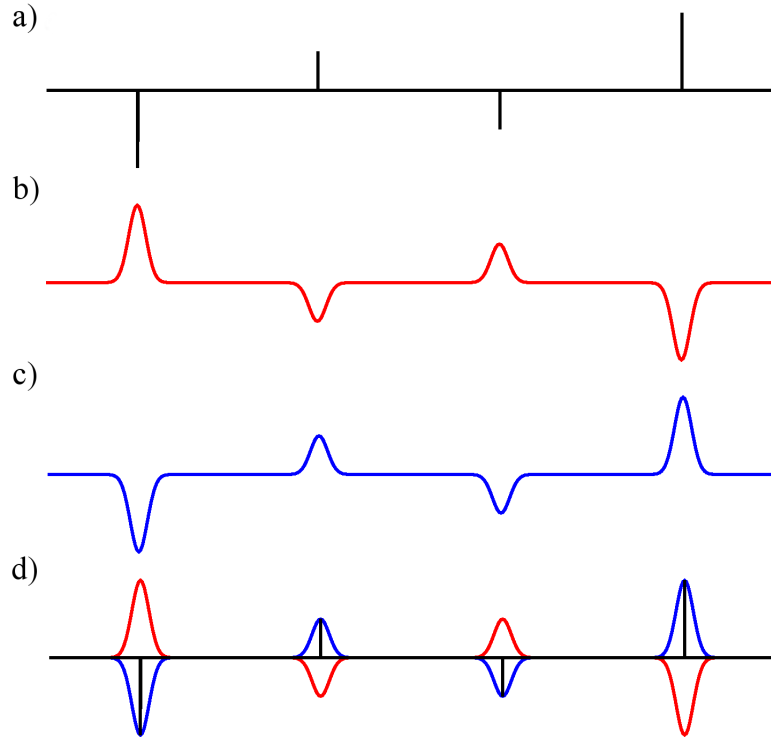


Figure 4.2 The Ewald summation (d), in which each point charge (a) is screened by a Gaussian distribution, evaluated in real space (b) that is cancelled out by an equal and opposite Gaussian distribution evaluated in reciprocal space (c).

The summation in reciprocal space includes the spurious interaction of each point charge with its own Gaussian distribution

$$V_N^{\text{self}} = -\left(\frac{\alpha}{\sqrt{\pi}}\right) \sum_{i=1}^N z_i^2 \quad (4.79)$$

which must be removed from the overall sum.

If the simulation cell is not neutral overall there will be an unphysical build up of background charge. To eliminate this effect, the Fuchs correction is applied [137]

$$V_N^{\text{neut}} = -\frac{\pi z_{\text{tot}}^2}{2V\alpha^2} \quad (4.80)$$

where z_{tot} is the total charge of the system.

The full electrostatic potential energy is therefore the sum of the individual real (Equation 4.73) and reciprocal space (Equation 4.78) terms and corrections due to self-interaction (Equation 4.79) and the non-neutral background (Equation 4.80). The

Ewald sum is sensitive to the real space cut off, the maximum number of reciprocal wave vectors and the width of the Gaussian charge distributions. A larger value of α (typically chosen as $5/L$) increases the contribution due to reciprocal space and decreases the contribution due to real space. Although the overall energy should be independent of the choice of α it will affect the rate of convergence of the sum.

4.4.4 Free Energy Calculations

Potentials of Mean Force

Rather than a potential energy surface in many cases we are instead concerned with defining a free energy surface for a process, as this is related to the activation energies obtained from experimental rate constants. The difference in free energy (Gibbs or Helmholtz) between state 0 and state 1, ΔW , is given by

$$\Delta W = W_1 - W_0 \quad (4.81)$$

which can be calculated using the partition functions, Q^1 and Q^0 , and either Equation 4.45 or 4.53,

$$\Delta W = -k_B T \ln \left(\frac{Q^1}{Q^0} \right) \quad (4.82)$$

We are interested in the change in W as a function of some suitable parameter or reaction coordinate, ξ , which provides a continuous path from 0 to 1. The change in free energy as a function of this reaction coordinate is called a potential of mean force (PMF), $W(\xi)$, given by

$$W(\xi) = -k_B T \ln p(\xi) + \text{constant} \quad (4.83)$$

The probability of configuration space being at a given value of the reaction coordinate, $p(\xi)$, is given by

$$p(\xi) = \frac{\int \delta[\xi'(\mathbf{r}^N) - \xi] \exp[-\beta V_N(\mathbf{r}^N)] d\mathbf{r}^N}{Z_{\text{NVT}}} \quad (4.84)$$

where ξ' is an arbitrary point in configuration space. The constant is added in Equation 4.83 so that the lowest energy value of $W(\xi)$ is set to zero. In a conventional simulation low energy regions of configuration space will be visited frequently,

whereas regions with higher energy will only rarely be visited. This poses a sampling problem when generating a PMF for a rare event (ie. a process with a significant free energy barrier).

Umbrella Sampling

The range of sampling in configuration space can be extended by instead defining a number of simulation ‘windows’, each of which samples a small region of the reaction coordinate, using a technique known as umbrella sampling. In order to sample the correct region of ξ in each window the potential energy function is modified using an additional term,

$$V_N^b(\mathbf{r}^N) = V_N(\mathbf{r}^N) + w_i(\xi) \quad (4.85)$$

where $V_N^b(\mathbf{r}^N)$ is the biased potential energy function. The function w_i is the umbrella potential for window i which typically takes quadratic form

$$w_i(\xi) = k_w(\xi - \xi_{\text{eq}})^2 \quad (4.86)$$

where ξ_{eq} is the target value of the reaction coordinate for the window and k_w is the window force constant. Sampling according to the biased potential energy function does not result in a Boltzmann distribution. However, Torrie and Valleau devised an approach that can be used to obtain the standard Boltzmann-weighted ensemble average thermodynamic properties from biased non-Boltzmann sampling [138, 139]. Using their prescription and Equations 4.84 and 4.85 the biased probability distribution of window i can be written as

$$p_i^b(\xi) = \frac{\int \delta[\xi'(\mathbf{r}^N) - \xi] \exp[-\beta V_N^b(\mathbf{r}^N)] d\mathbf{r}^N}{\int \exp[-\beta V_N^b(\mathbf{r}^N)] d\mathbf{r}^N} \quad (4.87)$$

and related to the unbiased probability distribution by the equation

$$p_i(\xi) = p_i^b \exp[\beta w_i(\xi)] \langle \exp[-\beta w_i(\xi)] \rangle \quad (4.88)$$

The ensemble average term in this equation cannot be obtained directly from a simulation so special methods are required. The weighted histogram analysis method (WHAM) can be used to evaluate the ensemble average in Equation 4.88, known as the window free energy constant, in order to obtain the unbiased probability

distribution for the window, $p_i(\zeta)$. WHAM then recombines the probability distributions from different windows to find a global probability distribution, $p(\zeta)$, which can then be used to generate the PMF from Equation 4.83. To achieve this WHAM requires sufficient overlap between sampling in adjacent simulation windows, which can be controlled by careful selection of k_w . The choice of k_w is a compromise; it must be large enough to overcome barriers on the free energy surface and sample near ζ_{eq} but not so large that many simulation windows are required because the biased distributions are so narrow.

4.5 Implementation of Computational Methods in this Thesis

In this thesis DFT calculations were performed using Gaussian 09 [140], MD simulations using DL_POLY Classic [141] and GCMC simulations using DL_MONTE [142].

Unless otherwise stated, the molecular simulations employed:

- 3D cubic PBCs
- the Ewald summation method [127] to evaluate electrostatic interactions with a precision of 1.0×10^{-6} kJ mol⁻¹
- spherical truncation of VDW forces at 10 Å
- the Nosé-Hoover thermostat [143] to maintain a constant temperature of 298 K, with a relaxation time of 0.1 ps
- the Nosé-Hoover barostat [144] to maintain a constant pressure of 1 atm, with a relaxation time of 0.1 ps
- the Verlet Leap Frog algorithm [127] with a 2 fs time step (MD only)

Chapter Five

Hydrated Oxyanions

5.1 Introduction

The primary aim of this chapter is to compare the structural and dynamic properties of oxyanions, XO_4^{n-} ($\text{X} = \text{Tc}, \text{S}$), in aqueous solution. SO_4^{2-} is chosen because it is commonly found in the environment and may act to inhibit TcO_4^- adsorption processes. Cl^- is also investigated because it is proposed to be the exchanged ion in oxyanion-SAMMS [106]. Since the acid dissociation constants, $\text{p}K_a$, of the oxyanions are very low ($\text{HTcO}_4 = 0.03$ [108], $\text{H}_2\text{SO}_4 = -2$, $\text{HSO}_4^- = 1.99$, and $\text{HCl} = -7$ [145]) each can be assumed to be deprotonated in any realistic pH range expected in environmental water. Firstly, the suitability of DFT calculations for describing anion hydration was assessed. By fitting to the DFT calculations, a classical force field that accounts for the interaction between each anion and the surrounding H_2O molecules was developed. Finally, using this force field, MD simulations were performed to analyse the structure, dynamics and thermodynamics of the anions in aqueous solution.

5.2 Quantum Mechanical Models

5.2.1 Geometry Optimisation

By conducting gas phase geometry optimisations a number of functionals and basis sets were investigated for their ability to reproduce the experimental structure of the tetrahedral TcO_4^- . The only geometrical parameter required to describe TcO_4^- is the Tc–O bond length (r_{TcO}), determined to be 1.724 (3) Å from the structure of KTcO_4 determined by X-ray crystallography [146]. Firstly, the HF method was compared with DFT at the B3LYP [121] level of theory. In this calculation all atoms were represented using 6-31G* basis set, apart from Tc, which was described using the def2-TZVP basis set [147] and 28 electron pseudopotential [148]. The bond length from HF theory ($r_{\text{TcO}} = 1.6673$ Å) is shorter than experiment by 0.057 Å and corroborates the conclusion of a previous study into OsO_4^- [149] that showed HF

theory systematically under predicts oxyanion bond lengths. However, the prediction from DFT ($r_{\text{TcO}} = 1.7153 \text{ \AA}$) lies closer to the experimental value (within 0.009 \AA).

Using the B3LYP functional the effect of basis set on r_{TcO} was investigated. Firstly, a geometry optimisation was performed using the same basis set for O (6-31G*) but instead describing Tc with the Los Alamos pseudopotential and either the double- (LANL2DZ) or triple-zeta (LANL2TZ) associated basis sets. These basis sets both predicted bond lengths ($r_{\text{TcO}} = 1.736 \text{ \AA}$) slightly further away from the experimental distance than def2-TZVP. We therefore proceeded with the def2-TZVP basis set to model Tc. Next, the effect of systematically improving the O basis set was analysed, with the investigation restricted to Pople's '*k-nlmG*' series [123]. The dependence of r_{TcO} on the quality of the basis set is summarised in Table 5.1. The most accurate was 6-31G, however, this is likely to be due to a fortuitous cancellation of errors associated with using a small overall basis set and not including polarisation functions. For oxyanions, polarisation functions are required to properly account for π -bonding between O atoms and the central atom, X. All of the basis sets that do not contain polarisation functions in Table 5.1 over predict r_{TcO} . The inclusion of an additional set of polarisation functions (3df, 2p) did not result in any further change in r_{TcO} . Supplementing the 6-311G basis set with a single set of diffuse functions results in longer bonds (r_{TcO} increases from 1.7281 \AA to 1.7283 \AA). Although this only represents a minor change in r_{TcO} , diffuse functions are critical for correctly describing electron density far from an atom's nucleus, especially in the case of low charge density anions such as TcO_4^- , and this feature will be important for fitting the force field parameters. The combination of 6-311+G* (O) and def2-TZVP (Tc) basis sets is therefore used in the remainder of DFT calculations in this thesis.

| Oxygen Basis Set | r_{TcO} (Å) | Error (%) |
|------------------|----------------------|-----------|
| 6-31G | 1.7264 | 0.14 |
| 6-31G* | 1.7153 | 0.50 |
| 6-31+G | 1.7277 | 0.21 |
| 6-31+G* | 1.7168 | 0.42 |
| 6-311G | 1.7281 | 0.24 |
| 6-311G* | 1.7163 | 0.45 |
| 6-311+G | 1.7283 | 0.25 |
| 6-311+G* | 1.7168 | 0.42 |

Table 5.1 The dependence of r_{TcO} on basis set and the percentage error from the experimentally determined bond length.

Finally, using the chosen basis set a different functional was investigated; the hybrid meta M06 exchange correlation functional [150]. M06 results in an optimised geometry with bonds ($r_{\text{TcO}} = 1.7045$ Å) that are 0.0123 Å shorter than in the equivalent calculation using the B3LYP functional and 0.0195 Å shorter than experiment. Both were in improved agreement with the experimental value than the only previously published DFT study ($r_{\text{TcO}} = 1.756$ Å) at the B3LYP/LANL2DZ level of theory [151]. The geometry of SO_4^{2-} was also optimised using both functionals and the 6-311+G* basis set, with predicted S – O bond lengths of 1.5005 Å (B3LYP) and 1.4870 Å (M06). In this case the shorter distance predicted by the M06 functional is in better agreement with experiment (1.490 Å) [152].

5.2.2 Free Energy of Hydration

A greater understanding of the contrasting energetic properties of hydrated ions is required to improve the selective materials needed for their remediation. In particular, the adsorption of a contaminant ion to an adsorbent must release sufficient energy to overcome its free energy of hydration, ΔG_{hyd} , otherwise it would simply remain in solution. ΔG_{hyd} is defined as the free energy change on transferring a mole of ions

from their isolated state in an ideal gas to aqueous solution. The thermodynamics of hydration can be described using the equation

$$\Delta G_{\text{hyd}} = \Delta H_{\text{hyd}} - T\Delta S_{\text{hyd}} \quad (5.1)$$

where ΔH_{hyd} and ΔS_{hyd} are the changes in enthalpy and entropy. ΔH_{hyd} is defined as the heat released on hydrating the ion and the $T\Delta S_{\text{hyd}}$ term is entropic penalty attributed to reorganizing the water molecules in hydration shells around the ion. The uncertainty in experimental measurements of ΔG_{hyd} for neutral molecules is quite low (typically within 1 kJ mol⁻¹). However, the free energy of formation of an individual ion is said to have ‘no operational physical meaning’ [153] since there is no way to measure this property directly. As a result the convention is to arbitrarily assign ΔG_{hyd} for a proton in the medium and then use this reference value and neutral combinations of cations and anions to calculate ΔG_{hyd} for single ions. Available experimental thermodynamic data for the three anions, corresponding to Equation 5.1, is given in Table 5.2.

| Anion | ΔG_{hyd} (kJ mol ⁻¹) | ΔH_{hyd} (kJ mol ⁻¹) | ΔS_{hyd} (J K ⁻¹ mol ⁻¹) |
|-------------------------------|--|--|---|
| TcO ₄ ⁻ | -251 | -271* | -69 |
| SO ₄ ²⁻ | -1064 | -1138 | -249 |
| Cl ⁻ | -345 | -367 | -75 |

Table 5.2 The standard thermodynamic quantities of anion hydration for TcO₄⁻, SO₄²⁻ and Cl⁻ at 1 atm and 298 K [154, 155]. *Not calculated from direct measurement, instead estimated from ΔS_{hyd} and ΔG_{hyd} and Equation 5.1.

Implicit Solvation Modelling

One common computational approach for dealing with the effect of hydration (discussed briefly in Section 4.1.4) is to perform quantum mechanical calculations combined with a suitable implicit continuum model for the surrounding bulk water [156]. This type of approach can be used to determine ΔG_{hyd} , which can be written in its constituent terms as

$$\Delta G_{\text{hyd}} = \Delta G_{\text{elec}} + \Delta G_{\text{vdw}} + \Delta G_{\text{cav}} \quad (5.2)$$

where ΔG_{elec} is due to the electrostatic interaction between the solute and solvent and ΔG_{vdw} is the sum of repulsive and dispersive interactions. ΔG_{cav} , the cavitation term, is the sum of the work done against the solvent in order to form a solute cavity and an entropic penalty associated with the reorganisation of surrounding solvent molecules. Amongst the most popular class of solvation models are the polarisable continuum models (PCM) [157] in which the solvent cavity is represented by a number of overlapping spheres centred on the atoms. The ΔG_{cav} term is therefore very sensitive to the size of the spheres used to form the cavity. Evaluation of ΔG_{elec} is carried out using the SCRF methodology. In one implementation of this model (CPCM) [158] the apparent charges on the surface of the solute cavity interact with the solvent as if it is a conductor. The universal SMD model [159] was specifically developed for accurate predictions of ΔG_{hyd} for neutral and ionic species. It takes a more empirical approach, where it is assumed that the free energy associated with the non-electrostatic terms in Equation 5.2 is proportional to the solvent-exposed surface area. These non-electrostatic terms are parameterised using characteristic ‘surface tension’ terms associated with each atom. The electrostatic contribution is calculated using optimised intrinsic atomic radii for the atoms (called Coulomb radii) with the SCRF methodology. The SMD approach therefore employs a single set of parameters (Coulomb radii and atomic surface tension coefficients) to describe the contributions on the rhs of Equation 5.2.

Single-point energy calculations were performed at the optimised geometries in the gas phase using the CPCM and SMD solvation models. For each ion (TcO_4^- , SO_4^{2-} and Cl^-) ΔG_{hyd} was determined by subtracting the energy of the ion in gas phase from the energy in solution and compared to the experimental values reported in Table 5.2. The energies obtained using B3LYP and M06 functionals were compared. The effect of solute cavity size in the CPCM model was investigated by comparing ΔG_{hyd} for cavities generated from the atomic radii of either the universal force field (UFF) [160] or the united atom topological model for Kohn-Sham theory (UAKS) [161].

The results were largely independent of the DFT functional employed, with B3LYP (Table 5.3) yielding roughly comparable results to M06 (Table 5.4). These tables show ΔG_{hyd} obtained from each solvation model and the absolute error compared to

experiment ($\Delta\Delta G_{\text{hyd}}$). For small ions such as those investigated here, the favourable electrostatic interactions with the solvent model easily outweigh the unfavourable terms due to the formation of the solute cavity, leading to a favourable ΔG_{hyd} in each case. ΔG_{elec} is dependent on the strength of specific hydrogen bonding interactions between the ions and H_2O , which is stronger in ions with a higher charge, resulting in ΔG_{hyd} for SO_4^{2-} being approximately 3-4 times more favourable than for TcO_4^- . Despite the expectation that ions of the same valence will have roughly comparable values of ΔG_{elec} , ΔG_{hyd} for the monovalent anions shows that TcO_4^- releases less energy than Cl^- . This difference is a result of TcO_4^- having a more positive ΔG_{cav} due to it requiring a much larger cavity. This argument is supported by the trend of steadily decreasing experimental hydration free energies down Group 7 as the halide anions increase in size (eg. for I^- , $\Delta G_{\text{hyd}} = -280 \text{ kJ mol}^{-1}$ from experiment).

| Anion | CPCM (UFF) | | CPCM (UAKS) | | SMD | |
|--------------------|-------------------------|-------------------------------|-------------------------|-------------------------------|-------------------------|-------------------------------|
| | ΔG_{hyd} | $\Delta\Delta G_{\text{hyd}}$ | ΔG_{hyd} | $\Delta\Delta G_{\text{hyd}}$ | ΔG_{hyd} | $\Delta\Delta G_{\text{hyd}}$ |
| TcO_4^- | -228 | +23 | -281 | -30 | -273 | -22 |
| SO_4^{2-} | -929 | +135 | -1007 | +57 | -987 | +77 |
| Cl^- | -292 | +53 | -307 | +38 | -341 | +4 |

Table 5.3 Comparison of ΔG_{hyd} for anions using implicit solvation models and the B3LYP functional. Units: kJ mol^{-1} .

| Anion | CPCM (UFF) | | CPCM (UAKS) | | SMD | |
|--------------------|-------------------------|-------------------------------|-------------------------|-------------------------------|-------------------------|-------------------------------|
| | ΔG_{hyd} | $\Delta\Delta G_{\text{hyd}}$ | ΔG_{hyd} | $\Delta\Delta G_{\text{hyd}}$ | ΔG_{hyd} | $\Delta\Delta G_{\text{hyd}}$ |
| TcO_4^- | -228 | +23 | -280 | -29 | -274 | -23 |
| SO_4^{2-} | -938 | +126 | -1019 | +45 | -997 | +67 |
| Cl^- | -293 | +52 | -310 | +35 | -338 | +7 |

Table 5.4 Comparison of ΔG_{hyd} for anions using implicit solvation models and the M06 functional. Units: kJ mol^{-1} .

The CPCM solvation model is very sensitive to the atomic radii used to form the solute cavity. CPCM-UFF solvation models result in very poor agreement with experiment, especially for SO_4^{2-} ($\Delta\Delta G_{\text{hyd}} = +135$ (B3LYP) and $+126$ (M06) kJ mol^{-1}), but significant improvements can be found by employing UAKS radii instead ($\Delta\Delta G_{\text{hyd}} = +57$ (B3LYP) and $+47$ (M06) kJ mol^{-1}) suggesting that the error is at least in part due to an unrealistic cavity size. The SMD model makes reasonably accurate predictions of ΔG_{hyd} for monovalent anions, especially Cl^- ($\Delta\Delta G_{\text{hyd}} < 10$ kJ mol^{-1}), but performs poorly in comparison to the CPCM-UAKS model in the case of SO_4^{2-} . ΔG_{hyd} for TcO_4^- is underestimated using CPCM-UFF but overestimated by CPCM-UAKS suggesting that the correct ΔG_{hyd} could be obtained by tuning the cavity to some intermediate size.

Implicit solvation techniques can be used to compute ΔG_{hyd} for neutral molecules reasonably accurately. However, the results presented here indicate that implicit solvation models cannot be used to predict accurate values for ions. The assumptions that the electrostatic interactions between a solute and the solvent are independent of the solvent's explicit molecular structure and that the dielectric response of the medium is uniform are poor for ionic species. In addition, highly charged species such as SO_4^{2-} have much larger ΔG_{hyd} and require solvation models with a much smaller error to obtain the same degree of chemical accuracy. The CPCM model was benchmarked at the B3LYP/6-31+G* level by Takano and Houk [162]. They calculated mean unsigned errors (MUEs) for ΔG_{hyd} of monovalent anions using different cavity sizes. They found MUEs of 39 kJ mol^{-1} and 13 kJ mol^{-1} for UFF and UAKS, respectively. CPCM-UAKS compares well to the MUE obtained for anions using the SMD model at the B3LYP/6-31G* level, $\text{MUE} = 26$ kJ mol^{-1} [159], although it is possible that SMD would show improved results if benchmarked in an analogous manner to CPCM-UAKS (ie. with a set of diffuse functions on the ions).

Predictions of ΔG_{hyd} could be improved by capturing the specific solute-solvent interactions by also including a number of H_2O molecules in the explicit solute cavity. This approach would require sufficient statistical sampling to take into account all possible H_2O configurations around the ion. Although the SCRf method used in these implicit solvent models is normally efficient, a prohibitively large number of QM calculations would be needed, especially in the case of highly charged species such as SO_4^{2-} where the effects of the ion extend deep into the solvent.

5.3 Development of a Classical Force Field

Ion hydration can instead be modelled using a classical simulation approach. For MD simulations a force field for the oxyanions of the form in Equation 4.37 (minus the dihedral angle term) is required. Initially bonded and non-bonded parameters were either taken from the literature or determined using DFT calculations. Non-bonded parameters were then optimised to fit the DFT interaction between the oxyanions and H₂O. All of the DFT calculations discussed in this section use the M06 functional in conjunction with the 6-311+G* basis set for all atoms other than Tc (def2-TZVP).

5.3.1 Initial Parameter Set

For SO₄²⁻ equilibrium bond lengths and angles were set to the quantum mechanically optimised values and the force constants for S – O bond stretching and O – S – O angle bending were taken from the literature [163]. However, classical force field parameters for TcO₄⁻ have not previously been reported. In lieu of any literature values we have used the O – S – O bending force constant for the O – Tc – O angle. However, the Tc – O bond stretch force constant was obtained by fitting to a potential energy surface generated using DFT. In this approach the Tc – O bond is constrained to a distance either side of the equilibrium bond length and the corresponding potential energy obtained by a geometry optimisation calculation. The force constant was then determined by calculating the second derivative of the variation in $v_{\text{bond}}(r_{\text{TcO}})$ about the Tc – O bond (Figure 5.1).

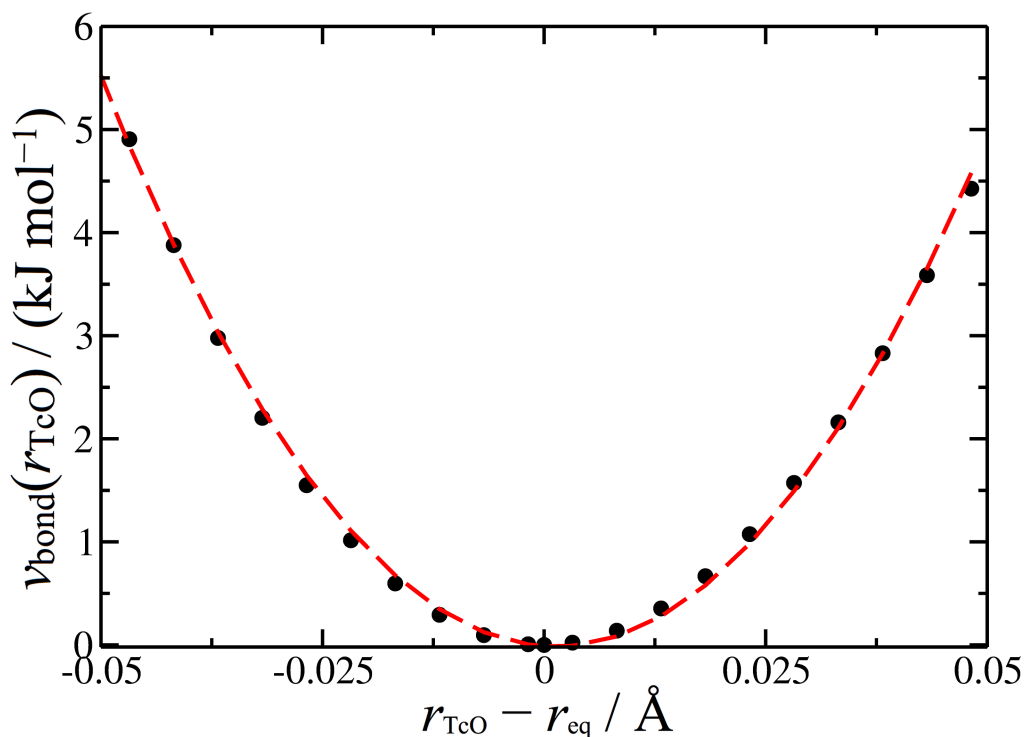


Figure 5.1 Potential energy surface for the Tc – O bond stretch generated at the M06 level of theory.

The initial partial charges of the atoms in the oxyanions were determined from the DFT optimised geometries according to the Merz-Singh-Kollmann scheme [164, 165]. In this approach the electrostatic potential is calculated at a number of grid points located on several spherical, concentric layers surrounding the oxyanion. Atomic charges are then adjusted to fit the electrostatic potential as closely as possible, under the condition that the overall charge of the ion is maintained. In this case the electrostatic potential was calculated at one point per \AA^2 over four different layers. Since the deprotonated oxyanions are perfectly tetrahedral the partial charges for each oxygen atom were identical: $-0.685 e$ ($X = \text{Tc}$) and $-0.920 e$ ($X = \text{S}$). Initially, OPLS [166] VDW parameters were used for the oxyanions, apart from σ_{Tc} and ϵ_{Tc} , which were taken from Cundari *et al.* [167].

5.3.2 Parameter Optimisation

The force field was optimised to fit the DFT calculations for the interaction between each oxyanion and a single H_2O molecule. The fitted quantities were the distance between the oxygen atom in water and the oxygen atom in the oxyanion, r_{eq} , which

was taken from the optimised geometry for the structure in Figure 5.2 and the energy of interaction, ΔE , calculated by

$$\Delta E = E_{\text{DFT}}(\text{XO}_4^{n-} - \text{H}_2\text{O}) - E_{\text{DFT}}(\text{XO}_4^{n-}) - E_{\text{DFT}}(\text{H}_2\text{O}) \quad (5.3)$$

where $E_{\text{DFT}}(\text{XO}_4^{n-} - \text{H}_2\text{O})$ is the ground state energy corresponding to the single optimised structure in Figure 5.2 and the second and third terms are the ground state energies of the isolated oxyanion and H_2O .

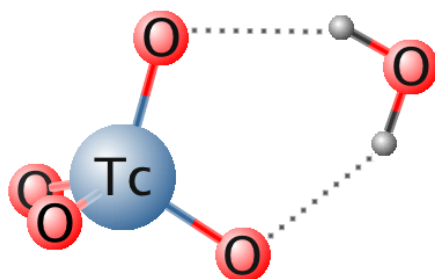


Figure 5.2 Model used to parameterise the TcO_4^- force field. The same procedure was used for SO_4^{2-} .

Although many classical models of H_2O are available, no single model is able to accurately reproduce all of the structural and dynamic properties of bulk water in a molecular simulation. In this thesis the popular extended simple point charge (SPC/E) model [168], which represents H_2O as a rigid body, was used. The non-bonded parameters of the SPC/E model (Table 5.5) consist of a single Lennard-Jones site centred on the oxygen and point charges on all three atoms. Despite it being relatively inexpensive and simple, the SPC/E model compares favourably to other models in reproducing many of the properties of bulk water [169]. It is therefore considered suitable for the simulations of hydrated anions in this thesis.

| Non-bonded | | | |
|------------------------------|-----------|-----------------------------------|-------------------------|
| <i>i</i> | $q_i (e)$ | $\epsilon_i (\text{kJ mol}^{-1})$ | $\sigma_i (\text{\AA})$ |
| O | -0.8476 | 0.650 | 3.166 |
| H | -0.4238 | - | - |
| Bonded | | | |
| O – H bond (\AA) | | | 1.000 |
| H – O – H angle ($^\circ$) | | | 109.47 |

Table 5.5 Force field parameters for the SPC/E model of water.

The conjugate gradient method, as implemented in DL_POLY Classic [141], was used to minimise the energy of the structure in Figure 5.2, modelled as two isolated molecules in a vacuum. By adjusting the non-bonded oxygen parameters in successive minimisation calculations agreement with DFT was improved. Any changes in q_O were accompanied with a modification in q_X so as to maintain the same overall ionic charge.

The values of r_{eq} and ΔE obtained using the optimised force field are compared to the equivalent quantities from the DFT calculations in Table 5.6. The final set of parameters used to obtain these values is given in Table 5.7. There is no literature data to compare with our TcO_4^- force field parameters but the optimised SO_4^{2-} parameters are very similar to other classical force fields [170], giving us confidence in our parameterisation approach. SO_4^{2-} has a much stronger interaction with H_2O ($\Delta E = -126.7 \text{ kJ mol}^{-1}$) compared to TcO_4^- ($\Delta E = -52.8 \text{ kJ mol}^{-1}$). This is largely due to the differences in oxygen partial charges; $q_O = -1.075 e$ (SO_4^{2-}) compared to $q_O = -0.930 e$ (TcO_4^-). In addition σ_O is much smaller for SO_4^{2-} (3.250 \AA) compared to TcO_4^- (3.860 \AA) resulting in much closer contacts with H_2O .

| Anion | ΔE (kJ mol ⁻¹) | | r_{eq} (Å) | |
|-------------------------------|------------------------------------|-------------|---------------------|-------------|
| | DFT | Force Field | DFT | Force Field |
| TcO ₄ ⁻ | -53.1 | -52.8 | 2.951 | 2.926 |
| SO ₄ ²⁻ | -127.0 | -126.7 | 2.764 | 2.710 |

Table 5.6 Comparison of ΔE and r_{eq} calculated using the optimised force field and DFT for the two oxyanions.

| Non-bonded | | | | |
|-------------------------------|----------|-----------------------------------|--|--------------------------|
| | <i>i</i> | <i>q_i</i> (<i>e</i>) | <i>ε_i</i> (kJ mol ⁻¹) | <i>σ_i</i> (Å) |
| TcO ₄ ⁻ | Tc | 2.720 | 1.0080 | 2.655 |
| | O | -0.930 | 0.2090 | 3.860 |
| SO ₄ ²⁻ | S | 2.300 | 0.8370 | 3.550 |
| | O | -1.075 | 0.6500 | 3.250 |

| Bond Stretch | | |
|---------------------|--|---------------------------|
| <i>i-j</i> | <i>k_r</i> (kJ mol ⁻¹ Å ⁻²) | <i>r_{eq}</i> (Å) |
| Tc-O | 2094.5 | 1.7045 |
| S-O | 2198.7 | 1.4870 |

| Angle Bend | | |
|-------------------|--|---------------------------|
| <i>i-j-k</i> | <i>k_θ</i> (kJ mol ⁻¹ rad ⁻²) | <i>θ_{eq}</i> (°) |
| O-X-O | 585.8 | 109.47 |

Table 5.7 Final optimised force field parameters used for TcO₄⁻ and SO₄²⁻.

In an analogous approach to the oxyanions, the Cl⁻ – H₂O interaction was investigated using DFT, from which *r_{eq}* and ΔE were 3.127 Å and -63.1 kJ mol⁻¹. Several common Cl⁻ force fields compatible with the SPC/E model were tested for agreement with the DFT results (Table 5.8). The parameters from Lamoureux and Roux [171] and Horinek *et al.* [172] accurately predict *r_{eq}* but overestimate ΔE . However, the parameters of Joung *et al.* [173] ($\sigma_{\text{Cl}} = 4.834$ Å, $\varepsilon_{\text{Cl}} = 0.0555$ kJ mol⁻¹ and $q_{\text{Cl}} = -1.000$ *e*), designed to accurately reproduce experimental ΔG_{hyd} , were in good agreement with ΔE from the DFT calculations so the optimisation step was deemed unnecessary for Cl⁻.

| Parameter Set | ΔE (kJ mol ⁻¹) | ΔE error (%) | r_{eq} (Å) | r_{eq} error (%) |
|-----------------------------|---------------------------------------|-------------------------|------------------------|------------------------------|
| Lamoureux and Roux [171] | -61.9 | 1.9 | 3.114 | 0.4 |
| Horinek <i>et al.</i> [172] | -60.1 | 4.8 | 3.162 | 1.1 |
| Joung <i>et al.</i> [173] | -62.7 | 0.6 | 3.074 | 1.7 |

Table 5.8 The performance of several Cl⁻ force fields and the percentage errors in ΔE and r_{eq} compared to the DFT calculations.

Once fitted the optimised force field for all the ions were within 0.5 kJ mol⁻¹ and 0.06 Å of ΔE and r_{eq} calculated using DFT. The parameters were therefore deemed sufficiently accurate for modelling the properties of the ions in solution and used in the classical simulations discussed in the remainder of this thesis.

5.4 Molecular Dynamics Simulations

Using the newly parameterised force field, MD simulations of the anions in water were performed. To account for the effects of bulk aqueous solution the ions were placed in a cubic box ($L = 32$ Å) containing 1093 SPC/E H₂O molecules. An equilibration run of 0.1 ns was performed before generating statistics from a 10 ns simulation, saving configurations for analysis every 200 fs.

5.4.1 Hydrated Structure

The structure of hydrated ions in the MD simulations can be investigated by generating radial distribution functions, $g_{\alpha-\beta}(r)$. $g_{\alpha-\beta}(r)$ is the probability of finding a pair of atom types, α and β , distance r apart, relative to a random distribution of those atoms at the same density,

$$g_{\alpha-\beta}(r) = \frac{V}{4\pi r^2 \delta r N_{\alpha} N_{\beta}} \left\langle \sum_{i=1}^{N_{\alpha}} \sum_{j=1}^{N_{\beta}} \delta(r - r_{\alpha_i \beta_j}) \right\rangle \quad (5.4)$$

where the double summation counts over the number of α and β pairs separated by distance r . The volume term, V , is included to ensure that $g_{\alpha-\beta}(r)$ is equal to unity at

large r (ie. α has no influence over the position of atom type β and vice versa) and the factor $4\pi r^2 \delta r$ is the volume of a spherical shell of width δr . Any values of r for which $g_{\alpha-\beta}(r)$ is not equal to one indicate some form of long-range order. When $g_{\alpha-\beta}(r) > 1$ the corresponding value of r is favourable and when $g_{\alpha-\beta}(r) < 1$ this value of r is unfavourable. In a solid, radial distribution functions have a number of intense peaks corresponding to the atoms in their equilibrium lattice positions but for a liquid the situation is more complicated. In practice the Dirac delta function is replaced by a procedure that involves separating r into discrete bins and compiling a histogram.

The radial distribution functions of the oxyanions in solution are compared in Figure 5.3 to show the differences in structure of the surrounding H₂O molecules. The peaks in $g_{X-OW}(r)$ and $g_{O-OW}(r)$ ($X = \text{Tc or S}$, $OW = \text{O in H}_2\text{O}$) correspond to the hydration shells. A shelf-like feature that appears in the second hydration shell of $g_{O-OW}(r)$ near 5.5 Å ($X = \text{Tc}$) and 5.0 Å ($X = \text{S}$) is due to the interaction of waters held in the first hydration shell with O atoms on the opposite side of the oxyanion. This was also observed in a previously obtained $g_{X-OW}(r)$ for SO_4^{2-} [170] and appears to be characteristic of oxyanions in aqueous solution. The ‘effective’ or hydrated radius of an ion, r_H , is typically defined as the position of maximum of the first peak in $g_{X-OW}(r)$. For SO_4^{2-} this is at 3.78 Å, which is in excellent agreement with the experimental hydrated radius of 3.79 Å [174]. The primary $g_{X-OW}(r)$ peak for TcO_4^- is at a much greater radial distance (4.40 Å) than the equivalent SO_4^{2-} peak, mainly due to the difference in $X - \text{O}$ bond length between the two oxyanions but also in part due to the larger σ_O in TcO_4^- . The hydrated radius of TcO_4^- has not previously been reported. For SO_4^{2-} there is significant peak in $g_{X-OW}(r)$ at 5.95 Å that corresponds to its second hydration shell. However, in $g_{X-OW}(r)$ for TcO_4^- no further peaks appear beyond the primary hydration shell and the H₂O structure is representative of bulk solution. This indicates that SO_4^{2-} induces order in the surrounding solvent to a greater degree and at larger distances than TcO_4^- .

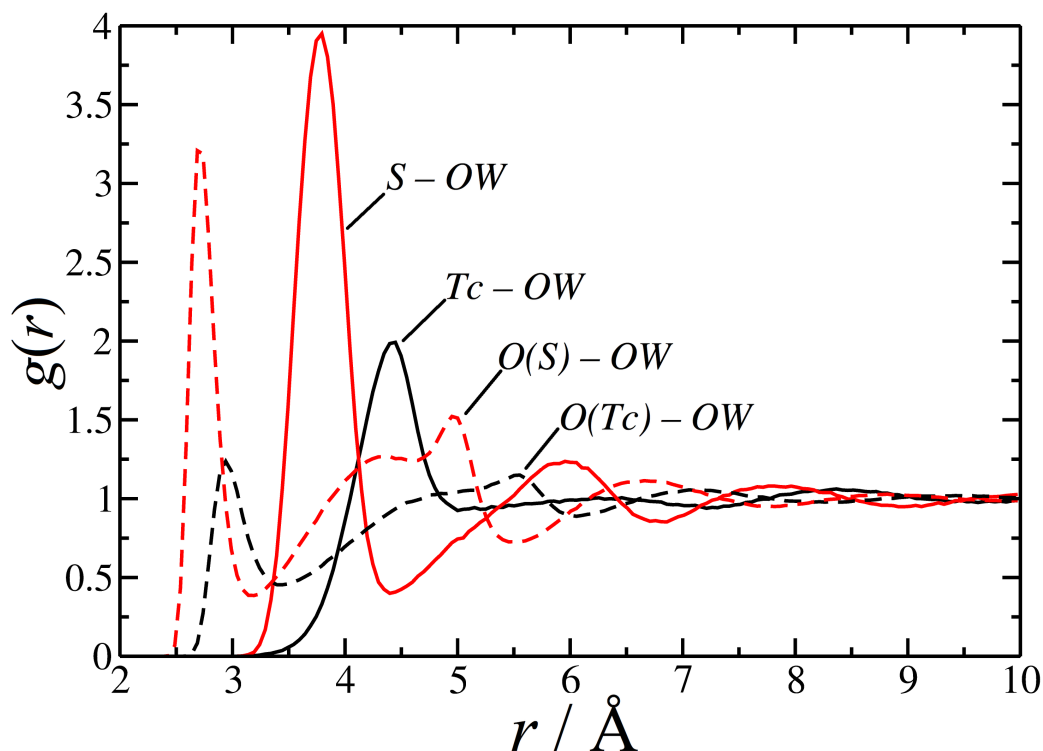


Figure 5.3 Radial distribution functions showing the structure of SPC/E water molecules around XO_4^{n-} ions. $g_{\text{X-OW}}(r)$ is represented by solid lines and $g_{\text{O-OW}}(r)$ by dashed lines. $\text{X} = \text{Tc}$ (black) and $\text{X} = \text{S}$ (red).

The intensities of the peaks in $g_{\text{X-OW}}(r)$ and $g_{\text{O-OW}}(r)$ are a measure of the strength of interaction between the oxyanions and their accompanying primary and secondary hydration shells. The intensity of the peak corresponding to the primary shell is related to the strength of hydrogen bonds between the oxygen in XO_4^{n-} and hydrogen in H_2O . Due to the higher charge of its oxygen, SO_4^{2-} forms much stronger hydrogen bonds with H_2O than TcO_4^- , as evidenced by the peaks in $g_{\text{O-HW}}(r)$ (Figure 5.4).

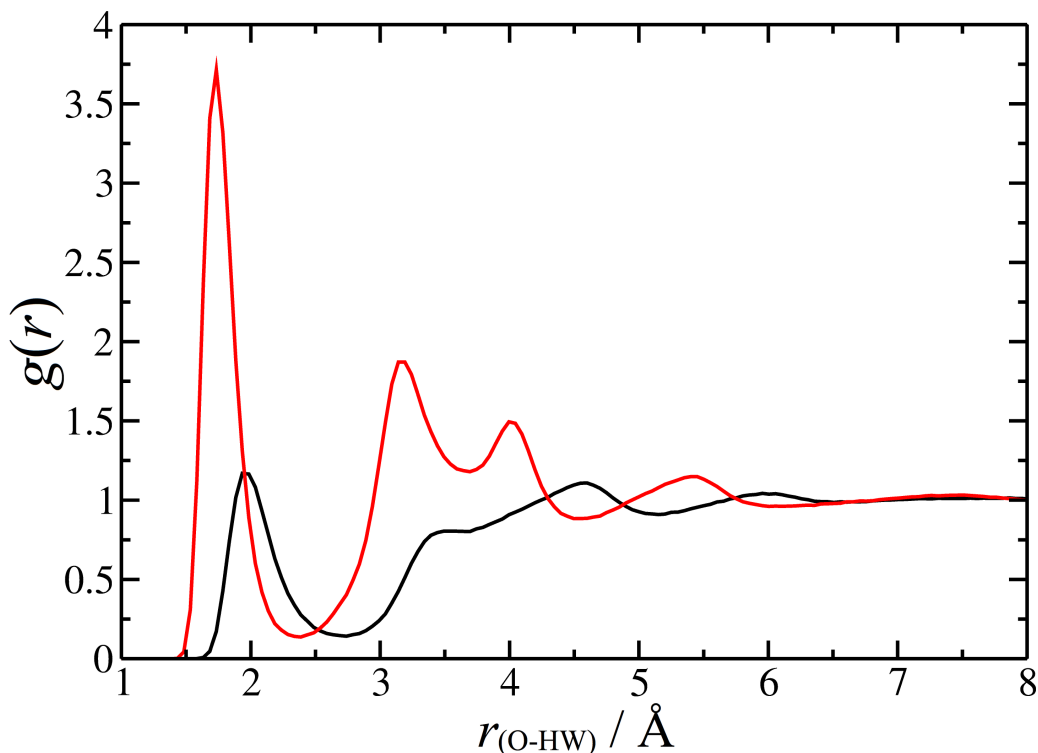


Figure 5.4 $g_{\text{O-HW}}(r)$ for XO_4^{n-} in SPC/E H_2O . $\text{X} = \text{Tc}$ (black) and $\text{X} = \text{S}$ (red).

The integral of $g_{\text{X-OW}}(r)$ (Figure 5.5) gives the average number of OW atoms within a given radius of atom X. Using this approach the number of H_2O molecules in the primary and secondary hydration shells can be determined by integrating up to the position of the minima after the peak for that shell. In the primary hydration shell of TcO_4^- (within 5.0 Å) there are 13.3 H_2O molecules. SO_4^{2-} has exactly the same number of H_2O s in its primary hydration shell (within 4.4 Å) and has another 31.5 in the second hydration shell (within 6.8 Å). The difference can be visualised in the simulation snapshots in Figure 5.6 where XO_4^{n-} and all of its surrounding H_2O s not in a bulk environment, defined using the peaks in $g_{\text{X-OW}}(r)$ (ie. those less than 5.0 and 6.8 Å from Tc and S, respectively), are shown.

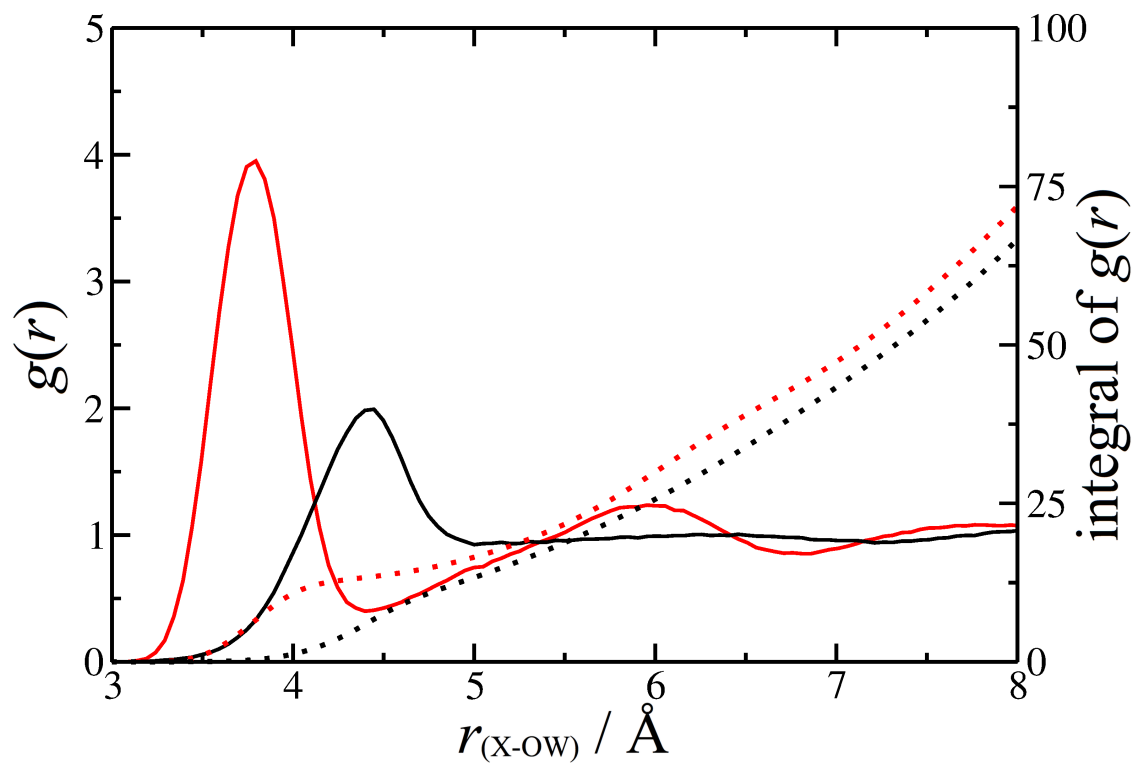


Figure 5.5 $g_{x-ow}(r)$ (solid line), and its integral (dotted line), for X = Tc (black) and X = S (red), in H₂O.

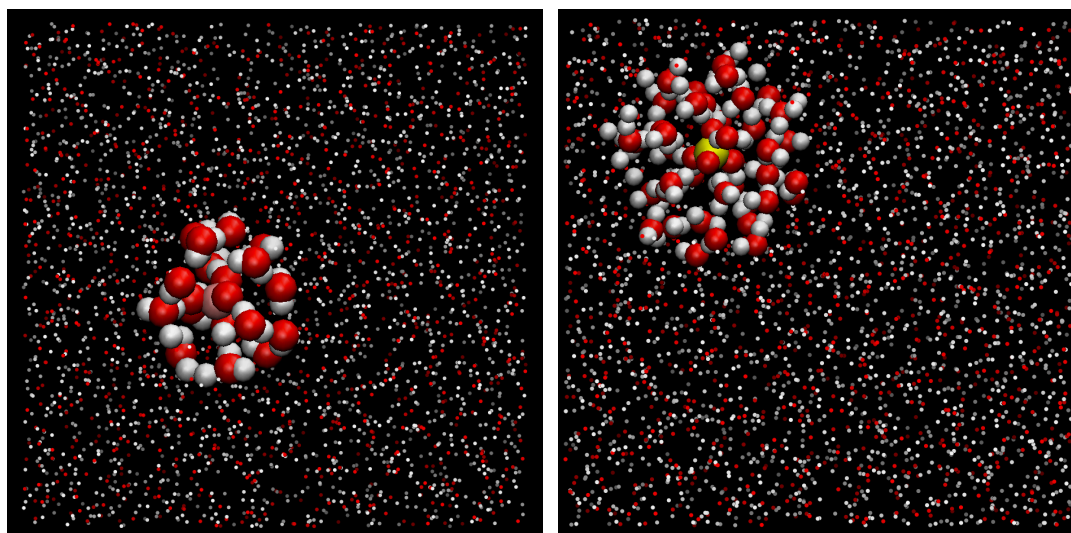


Figure 5.6 Snapshot from the MD simulations showing H₂O structure around TcO₄⁻ (left) and SO₄²⁻ (right). The colours correspond to element type; Tc (pink), S (yellow), O (red), H (white).

For Cl⁻, $g_{Cl-ow}(r)$ (Figure 5.7) shows that the primary hydration shell, containing 7.0 H₂O molecules, is at 3.15 Å. This is somewhat smaller than experiment (3.32 Å)

[174]. In comparison to the oxyanions it has a smaller hydrated radius and fewer H₂O in its primary hydration shell due to the smaller radius of the isolated Cl⁻ ion (1.8 Å [145] compared to 2.52 Å (TcO₄⁻ [108]) and 2.30 Å (SO₄²⁻ [145])). The shape of $g_{\text{Cl-OW}}(r)$ is an intermediate between SO₄²⁻ and TcO₄⁻ since its ionic charge lies between those of the two types of oxyanion oxygen atoms.

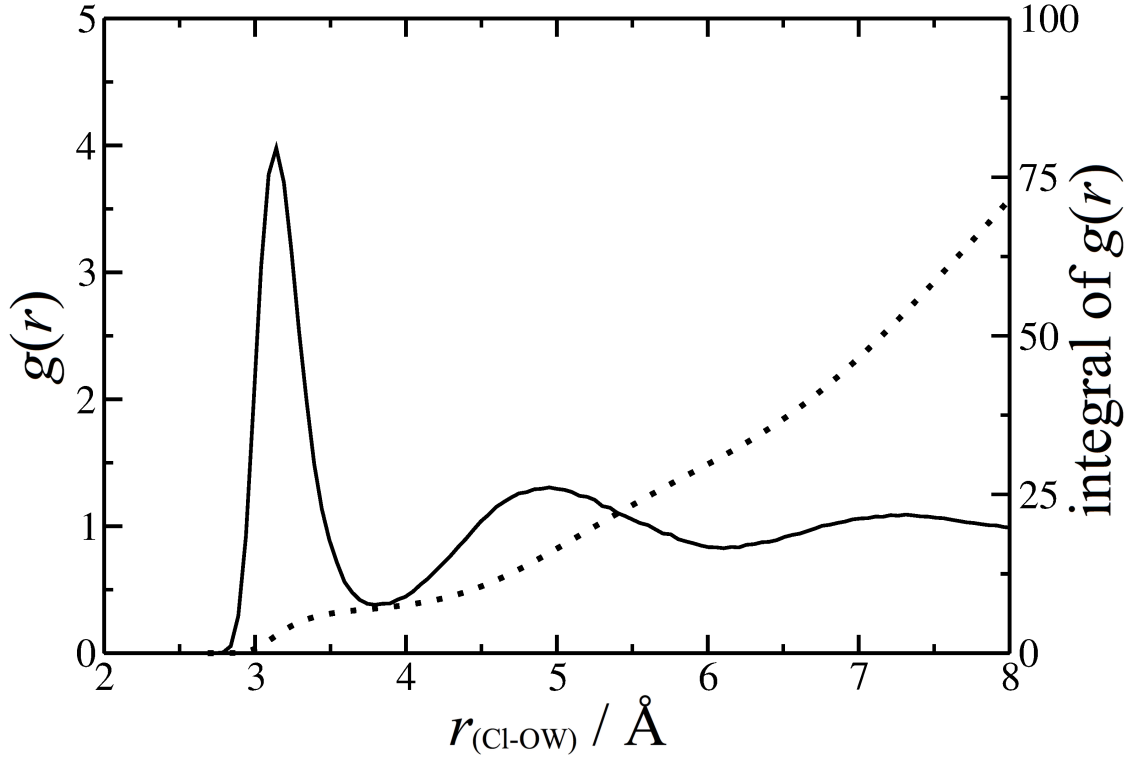


Figure 5.7 $g_{\text{Cl-OW}}(r)$ (solid) and its integral (dots) for Cl⁻ in SPC/E H₂O.

5.4.2 Transport Properties

Diffusion in a binary mixture of components i and j is defined by four different coefficients; two intradiffusion coefficients, D_{ii} and D_{jj} , describing the thermal motion of the individual components and two interdiffusion coefficient, D_{ij} and D_{ji} , that describes the motion of one component in the other. Since the fluxes, \mathbf{J} , and chemical potentials, μ , of the two components are intrinsically linked

$$\mathbf{J}_i = -D_{ii}\nabla\mu_i - D_{ij}\nabla\mu_j \quad (5.5)$$

$$\mathbf{J}_j = -D_{jj}\nabla\mu_j - D_{ji}\nabla\mu_i$$

a single diffusion coefficient for the mixture, D , can be defined. In the limit of infinite dilution of species i in j the interdiffusion coefficient approaches a characteristic tracer diffusion coefficient, D_T . In environmental waters ions are often present in very low concentrations and experimental studies of XO_4^{n-} in H_2O typically report tracer diffusion coefficients.

In a simulation the translational motion of an ion can be measured by calculating its mean-square displacement (MSD) as an ensemble average over all ions of type i and all time origins, t_0 . MSDs, shown in Figure 5.8, were obtained from the trajectories using the DL_POLY post-analysis utility over a 200 ps period. The diffusion coefficients for the anions in H_2O were calculated from their MSDs according to the Einstein relation [175],

$$D = \frac{1}{6} \lim_{t \rightarrow \infty} \frac{d\langle |\mathbf{r}_i(t_0 + t) - \mathbf{r}_i(t_0)|^2 \rangle}{dt} \quad (5.6)$$

where the slope of the MSD plot, obtained by linear regression, is divided by six. Firstly, this method was validated by calculating D for a simulation of pure H_2O (the self-diffusion coefficient). The value obtained ($2.6 \times 10^{-9} \text{ m}^2 \text{ s}^{-1}$) was greater than the experiment ($2.3 \times 10^{-9} \text{ m}^2 \text{ s}^{-1}$) [176] but in good agreement with the previously published value for the SPC/E model ($2.5 \times 10^{-9} \text{ m}^2 \text{ s}^{-1}$) [169]. The diffusion coefficients obtained from MSDs for the ions in Figure 5.8 ($L = 32 \text{ \AA}$) correspond to a XO_4^{n-} concentration of 0.05 mol dm^{-3} , due to finite size effects. Additional 10 ns simulations were conducted by the same methodology but with different box sizes ($L = 25, 39$ and 45 \AA). The diffusion coefficient at infinite dilution, D^∞ , was then estimated by obtaining diffusion coefficients from these simulations and extrapolating a plot of $1/L$ against D to $1/L = 0$ (Figure 5.9). After extrapolating to zero, D^∞ can be scaled to account for the known underprediction of the viscosity of bulk SPC/E water to obtain D_T ,

$$D_T = \frac{\eta_{\text{SPCE}}}{\eta_{\text{water}}} D^\infty \quad (5.7)$$

where η_{SPCE} is the viscosity of bulk SPC/E water ($0.729 \times 10^{-3} \text{ kg m}^{-1} \text{ s}^{-1}$ [177]) and η_{water} is the viscosity of bulk water ($0.896 \times 10^{-3} \text{ kg m}^{-1} \text{ s}^{-1}$ [177]). Calculated values of D_T for TcO_4^- and SO_4^{2-} were 1.13×10^{-9} and $0.91 \times 10^{-9} \text{ m}^2 \text{ s}^{-1}$, respectively. The

larger value for TcO_4^- reflects the fact that it is more weakly hydrated, leading to faster water exchange dynamics than occurs around SO_4^{2-} and indicates that it is much more mobile in solution. The value obtained for SO_4^{2-} is in good agreement with the published experimental value for this ion of $1.06 \times 10^{-9} \text{ m}^2 \text{ s}^{-1}$ [154].

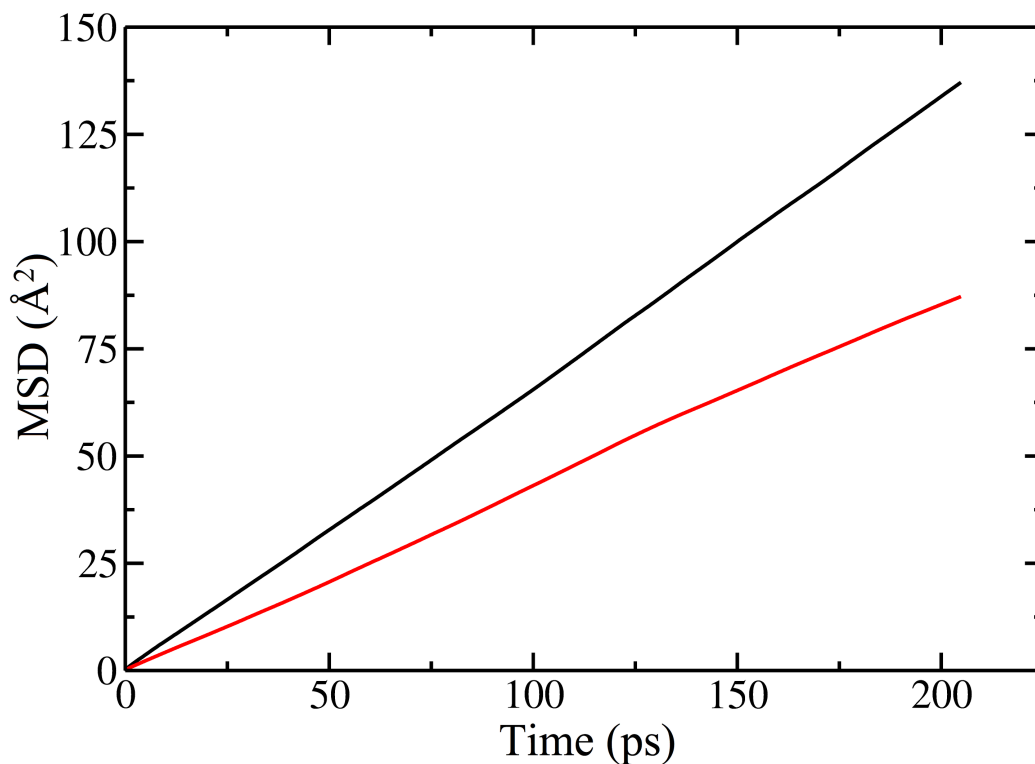


Figure 5.8 MSDs of XO_4^{n-} where $X = \text{Tc}$ (black) and S (red), obtained from the $L = 32 \text{ \AA}$ simulation cell.

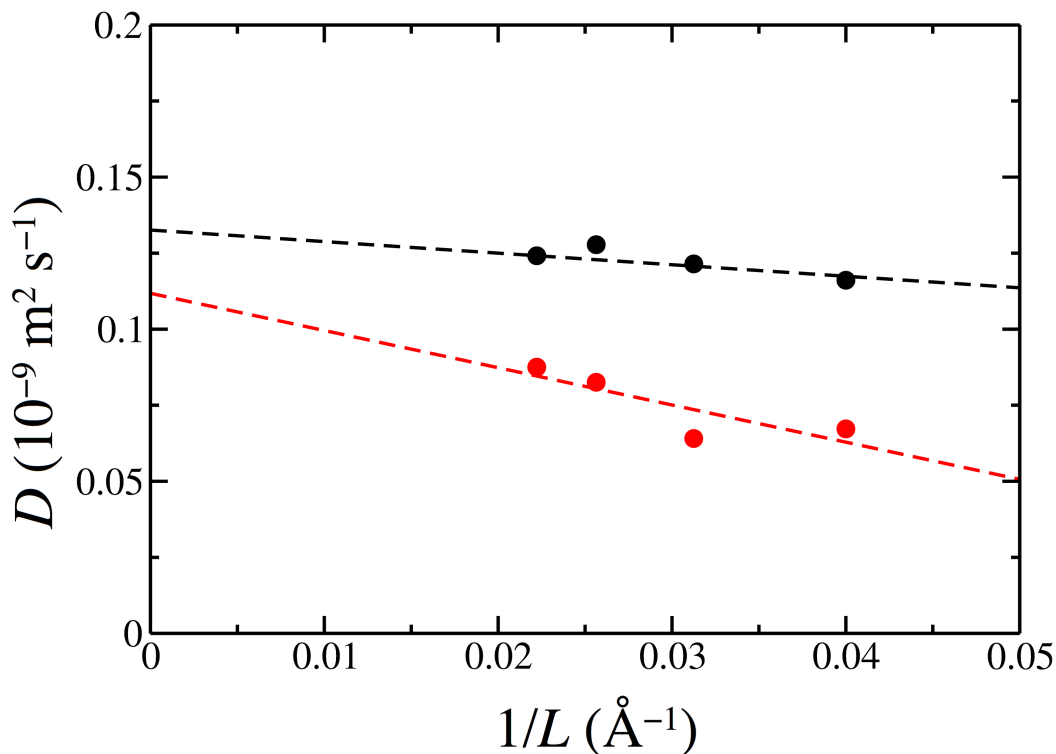


Figure 5.9 Diffusion coefficients for XO_4^{n-} in water, where $\text{X} = \text{Tc}$ (black) and S (red) obtained from simulations with various cell lengths.

5.4.3 Enthalpy of Hydration

The enthalpy of a given configuration can be obtained using the equation

$$H = U + PV \quad (5.8)$$

where U is the internal energy. A separate simulation of 1093 SPC/E H_2O molecules was performed to enable estimation of ΔH_{hyd} by taking the difference in mean ensemble enthalpy between this pure H_2O simulation and the simulation containing the hydrated anion. For each anion ΔH_{hyd} is given in Table 5.9. ΔH_{hyd} is always negative because of the favourable electrostatic interactions between the ion and surrounding H_2O molecules. The divalent SO_4^{2-} has the most negative ΔH_{hyd} because it forms stronger hydrogen bonds with H_2O than the monovalent anions. Despite the fact that Cl^- and TcO_4^- carry the same charge, Cl^- has a more favourable ΔH_{hyd} due to its higher charge density. For TcO_4^- the difference from experiment is quite small (error = 5.5%) but the estimate for SO_4^{2-} is poor (error = 12.6%). Corrections that account for the finite size of the simulation cell would lead to a more accurate

determination of ΔH_{hyd} . These include the interaction of the anion with itself (via the Ewald sum) in the periodic images of the simulation cell as well as the incorrect orientation of H₂O molecules caused by the periodic images of the anion. The importance of these correction terms increases with the magnitude of ΔH_{hyd} . Experimentally, determination of ΔH_{hyd} requires knowledge of the enthalpy of formation of the ion and H⁺, which is treated as a reference state. ΔH_{hyd} for H⁺ sets the scale for the calculation but a wide range of values for this have been reported ranging from $-1091 \text{ kJ mol}^{-1}$ to $-1150 \text{ kJ mol}^{-1}$ [178] so the experimental data also carries large uncertainties.

| Anion | ΔH_{hyd} | Error (%) |
|-------------------------------|-------------------------|-----------|
| TcO ₄ ⁻ | -256 | 5.5 |
| SO ₄ ²⁻ | -1282 | 12.6 |
| Cl ⁻ | -391 | 6.5 |

Table 5.9 Anion ΔH_{hyd} obtained from the MD simulations and the percentage error compared to experiment. Units: kJ mol^{-1} .

5.5 Conclusions

In order to solve this particular remediation problem, adsorbent materials must be designed to exploit differences in the hydrated properties between TcO₄⁻ and common competing anions present in the environment such as SO₄²⁻. Many of these properties have been investigated in this chapter and a comparison of some of the structural and dynamic properties obtained from the MD simulations is given in Table 5.10. TcO₄⁻ is a much more polarisable ion than SO₄²⁻ due a combination of its size and overall charge. As a result it does not form strong hydrogen bonds with H₂O or have a well-defined second hydration shell and has a much less favourable ΔH_{hyd} (and subsequently ΔG_{hyd}) contributing to its extremely high mobility in the environment compared to other ions. Although some of the calculated properties are only approximate (eg. ΔH_{hyd}) the differences between the two oxyanions are clear.

There are two competing effects that contribute to the entropy of hydration of small ions; the disruption of the normal hydrogen-bonding network of water (entropically

favourable) compared with the translational and orientational ordering it induces in the solvent structure on formation of the hydration shells (entropically unfavourable). The degree to which ions induce long-range order in the solvent can be visualised using the relative intensities of the peaks in $g_{X-Ow}(r)$. These kinds of effects are described by the Hofmeister series, which ranks ions based on the strength of their interaction with H₂O. SO₄²⁻ is at the far end of the strongly hydrated species (Kosmotropes) and species similar to TcO₄⁻ (such as ClO₄⁻) are at the other end (Chaotropes).

| Hydrated Ion Property | TcO ₄ ⁻ | SO ₄ ²⁻ |
|---|-------------------------------|-------------------------------|
| r_H (Å) | 4.40 | 3.79 |
| Primary $N(H_2O)$ | 13.3 | 13.3 |
| Secondary $N(H_2O)$ | - | 31.5 |
| D_T ($10^{-9} \text{ m}^2 \text{ s}^{-1}$) | 1.13 | 0.91 |
| ΔH_{hyd} (kJ mol ⁻¹) | -256 | -1282 |

Table 5.10 Summary of selected data obtained from the MD simulations of the two hydrated oxyanions.

The best way of validating the oxyanion models would be to calculate an accurate value for ΔG_{hyd} and compare to experiment. Unfortunately, a quantum mechanical approach that employs an implicit solvation model does not account for the specific interactions between ions and H₂O leading to significant errors. If the H₂O molecules in direct contact with the anion were explicitly considered in the quantum mechanical portion of the calculation this could lead to an improvement. However it can be seen from $g_{X-Ow}(r)$ that this would require a prohibitively large number of calculations to take into account all possible H₂O configurations around the anion. Hydration free energies could be more accurately calculated with a classical MD approach using Bennett's acceptance ratio method or thermodynamic integration but this is outside the scope of this thesis.

Chapter Six

Adsorption of Oxyanions to the Fe³⁺-EDA Complex

6.1 Introduction

The potential of SAMMS, functionalised with transition metal EDA complexes, as an effective oxyanion sorbent material was discussed in Section 3.3.2. Yoshitake *et al.* [106, 113] found that Fe³⁺-EDA complexes in the monolayer were able to bind several oxyanions each, leading to the conclusion that Fe³⁺ had the highest capacity of all the transition metals they investigated. The octahedral environment of Fe³⁺ is thought to consist of two bidentate EDA ligands (through which the complex is tethered to the amorphous silica surface) and two other ligands that are able to exchange with oxyanions in solution. However, there are uncertainties relating to the initial monolayer complex such as whether it exists as the *cis* or *trans* isomer or if Cl⁻ or H₂O occupy the final ligand sites. In addition, to properly understand the observed selectivity for monovalent (eg. TcO₄⁻) and divalent (SO₄²⁻) oxyanions, an explanation of the precise mechanism of adsorption to these functionalised materials is required. In an attempt to resolve some of these uncertainties, DFT and MD are used in this chapter to model the Fe³⁺-EDA complex and simulate its selective adsorption of TcO₄⁻ and SO₄²⁻ from aqueous solution via the ligand exchange reaction in Figure 6.1. In this chapter it is assumed that the observed selectivity is solely dependent on the chemistry of the Fe³⁺-EDA complex so neither the propyl tethers nor the inorganic support are considered.

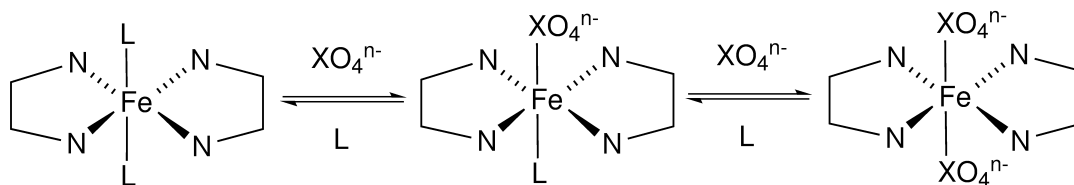


Figure 6.1 Exchange of ligands, L (L = Cl⁻/H₂O), with a general oxyanion, XO₄ⁿ⁻ (X = Tc/S), on the Fe³⁺-EDA complex. EDA hydrogen atoms are omitted for clarity and each species is in aqueous solution.

6.2 Quantum Mechanical Models

6.2.1 Structure of the Initial Fe³⁺-EDA Complex

The first step in this chapter is to determine the relative stabilities of the *cis* and *trans* isomers of the Cl⁻ (Figure 6.2) or H₂O coordinated Fe³⁺-EDA complex using DFT. The ground state energies were obtained from the geometries of the complexes optimised at the M06/6-311+G* level of theory. The low spin state was more stable than the corresponding high spin state by 12.3 kJ mol⁻¹ for [Fe(EDA)₂(H₂O)₂]³⁺ and 15.8 kJ mol⁻¹ for [Fe(EDA)₂(Cl)₂]⁺. DFT functionals commonly overestimate the preference of Fe³⁺ complexes to occupy the low-spin state [179], but the M06 functional is known to perform well in comparison to other functionals for transition metal chemistry applications [150, 180]. For L = Cl⁻ the *trans* complex was lower in energy than *cis* by 19.6 kJ mol⁻¹ but when L = H₂O the *cis* complex was 7.2 kJ mol⁻¹ more stable than *trans*. If, as reported experimentally, the complex is coordinated by Cl⁻ ligands rather than H₂O then the *trans*-[Fe(EDA)₂(Cl)₂]⁺ complex is most likely to be present. However, in SAMMS the complex is bound to the surface of MCM-41; steric effects caused by tethering in combination with the fact that the MCM-41 surface is amorphous and curved means the monolayer is unlikely to be well defined and may have some *cis* character.

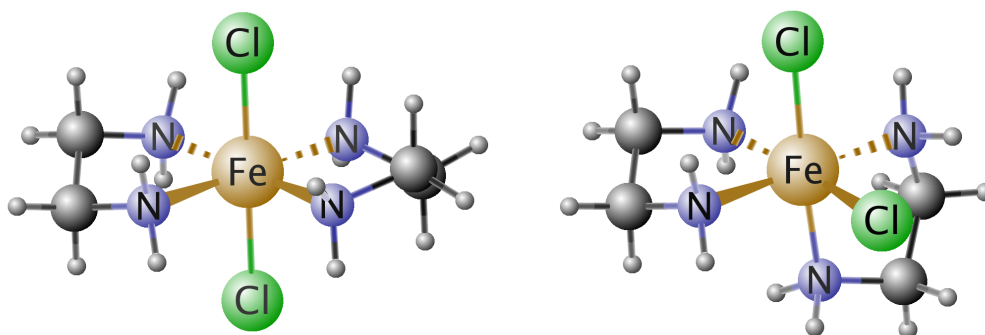


Figure 6.2 The geometry of the *trans* (left) and *cis* (right) isomers of the initial [Fe(EDA)₂(Cl)₂]⁺ complex.

6.2.2 Free Energy of Ligand Exchange

The ligand exchange reaction is considered within the context of the thermodynamic cycle in Figure 6.3, where the overall Gibbs free energy change, $\Delta G_{\text{ex, aq}}$, is defined as the change in free energy on transferring an oxyanion from bulk solution to being coordinated to the complex. $\Delta G_{\text{ex, aq}}$ can be expressed as

$$\Delta G_{\text{ex, aq}} = \Delta G_{\text{ex, g}} + \Delta G_{\text{hyd, P}} - \Delta G_{\text{hyd, R}} \quad (6.1)$$

where $\Delta G_{\text{ex, g}}$ is the free energy of exchange in the gas phase and $\Delta G_{\text{hyd, R}}$ and $\Delta G_{\text{hyd, P}}$ are the reactant and product hydration free energies. Therefore a ligand exchange reaction will only occur if there is a sufficient energetic driving force to overcome $\Delta G_{\text{hyd, R}}$. For each reaction $\Delta G_{\text{ex, aq}}$ was determined by performing DFT geometry optimisations of the gas-phase complexes to obtain $\Delta G_{\text{ex, g}}$ as well as separate single-point calculations at the optimised geometries with an implicit solvation model to obtain $\Delta G_{\text{hyd, R}}$ and $\Delta G_{\text{hyd, P}}$ at the B3LYP/6-311+G* level of theory. ΔG_{hyd} for each anion was taken from Table 5.3. Since in Section 5.1.2 the CPCM-UAKS and SMD solvation models were found to be roughly comparable both are investigated in this section. Only the *trans* isomers of the H₂O and Cl⁻ coordinated complexes were considered and $\Delta G_{\text{ex, aq}}$ was calculated for both the first and second ligand exchange reactions shown in Figure 6.1.

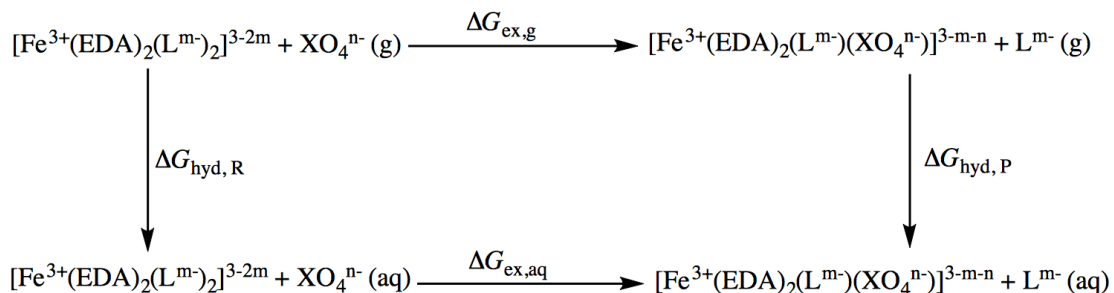


Figure 6.3 Contributions to the aqueous ligand exchange process. L = H₂O/Cl⁻, X = Tc/S.

The results are presented in Table 6.1 (CPCM-UAKS) and Table 6.2 (SMD). Overall the values of $\Delta G_{\text{ex, g}}$ are very large (up to $-2900 \text{ kJ mol}^{-1}$) but the mediating effect of the solvent reduces the magnitude of these free energy differences. Generally, ΔG_{hyd} is greater for complexes or ligands with higher charges due to stronger electrostatic interactions with the solvent. There is some consistency in $\Delta G_{\text{ex, aq}}$ between the two

solvation models for the $\text{TcO}_4^-/\text{Cl}^-$ exchange reactions; 21.5 kJ mol^{-1} (CPCM-UAKS) compared to 20.7 kJ mol^{-1} (SMD) for the first exchange with Cl^- and 18.6 kJ mol^{-1} and 23.6 kJ mol^{-1} for the second. Although these results suggest the exchange of TcO_4^- for Cl^- is unfavourable, corrections to $\Delta G_{\text{ex,aq}}$ can be applied to account for the difference between the anion's experimental (Table 5.2) and calculated (Table 5.3) ΔG_{hyd} . However, once these corrections are made the agreement between CPCM-UAKS (eg. $\Delta G_{\text{hyd}} = -46.8 \text{ kJ mol}^{-1}$ for the first exchange) and SMD ($\Delta G_{\text{hyd}} = -5.3 \text{ kJ mol}^{-1}$) is poor. Other inconsistencies between CPCM-UAKS and SMD are observed for the first SO_4^{2-} exchange with H_2O and both TcO_4^- exchanges with H_2O where CPCM-UAKS predicts a slightly unfavourable reaction and SMD predicts a favourable reaction. Both solvation models predict anomalously large and negative $\Delta G_{\text{ex,aq}}$ for the second SO_4^{2-} exchange with either H_2O or Cl^- ; the differences between these particular exchange reactions and the others are that they involve computation of ΔG_{hyd} for a negatively charged Fe^{3+} -EDA complex.

Errors in the calculation of $\Delta G_{\text{ex,aq}}$ arise for the same reasons as discussed in Section 5.1.2, ie. the inability of implicit solvation models to account for the specific interactions of charged species with H_2O . Determination of $\Delta G_{\text{ex,aq}}$ involves four separate ΔG_{hyd} calculations and the error in a single calculation for a monovalent anion is approximately 20 kJ mol^{-1} . This is the case even for complexes that are charge neutral overall, eg. $[\text{Fe}(\text{EDA})_2(\text{SO}_4)(\text{Cl})]^0$, as the specific interactions between the anionic ligands and H_2O are still unaccounted for. The reactions in which TcO_4^- exchange for Cl^- are expected to have the smallest errors since they involve only singly charged ions and complexes. Even for these processes, under the assumption that each ΔG_{hyd} calculation has an error of 20 kJ mol^{-1} , the total uncertainty in $\Delta G_{\text{ex,aq}}$ is 40 kJ mol^{-1} . The results are highly variable depending on the chosen solvation model and predictions of $\Delta G_{\text{ex,aq}}$ using this quantum mechanical approach were therefore deemed too inaccurate and unreliable.

| Initial Complex | Final Complex | $\Delta G_{\text{hyd,R}}$ | $\Delta G_{\text{hyd,P}}$ | $\Delta G_{\text{ex,g}}$ | $\Delta G_{\text{ex,aq}}$ |
|--|--|---------------------------|---------------------------|--------------------------|---------------------------|
| $[\text{Fe}(\text{EDA})_2(\text{Cl})_2]^+$ | $[\text{Fe}(\text{EDA})_2(\text{TcO}_4)(\text{Cl})]^+$ | -658.2 | -764.0 | 127.3 | 21.5 |
| $[\text{Fe}(\text{EDA})_2(\text{Cl})_2]^+$ | $[\text{Fe}(\text{EDA})_2(\text{SO}_4)(\text{Cl})]^0$ | -1384.6 | -564.2 | -797.4 | 23.0 |
| $[\text{Fe}(\text{EDA})_2(\text{TcO}_4)(\text{Cl})]^+$ | $[\text{Fe}(\text{EDA})_2(\text{TcO}_4)_2]^+$ | -737.3 | -845.3 | 131.7 | 23.6 |
| $[\text{Fe}(\text{EDA})_2(\text{SO}_4)(\text{Cl})]^0$ | $[\text{Fe}(\text{EDA})_2(\text{SO}_4)_2]^-$ | -1263.8 | -759.9 | -655.4 | -151.5 |
| $[\text{Fe}(\text{EDA})_2(\text{H}_2\text{O})_2]^{3+}$ | $[\text{Fe}(\text{EDA})_2(\text{TcO}_4)(\text{H}_2\text{O})]^{2+}$ | -2171.4 | -1089.0 | -1078.3 | 4.2 |
| $[\text{Fe}(\text{EDA})_2(\text{H}_2\text{O})_2]^{3+}$ | $[\text{Fe}(\text{EDA})_2(\text{SO}_4)(\text{H}_2\text{O})]^+$ | -2897.8 | -564.4 | -2328.5 | 4.9 |
| $[\text{Fe}(\text{EDA})_2(\text{TcO}_4)(\text{H}_2\text{O})]^{2+}$ | $[\text{Fe}(\text{EDA})_2(\text{TcO}_4)_2]^+$ | -1325.9 | -581.7 | -743.9 | 0.3 |
| $[\text{Fe}(\text{EDA})_2(\text{SO}_4)(\text{H}_2\text{O})]^+$ | $[\text{Fe}(\text{EDA})_2(\text{SO}_4)_2]^-$ | -1527.7 | -496.2 | -1205.5 | -174.1 |

Table 6.1 The free energy terms contributing to the thermochemical cycle for ligand exchange using the CPCM-UAKS solvation model. Units: kJ mol^{-1} .

| Initial Complex | Final Complex | $\Delta G_{\text{hyd,R}}$ | $\Delta G_{\text{hyd,P}}$ | $\Delta G_{\text{ex,g}}$ | $\Delta G_{\text{ex,aq}}$ |
|--|--|---------------------------|---------------------------|--------------------------|---------------------------|
| $[\text{Fe}(\text{EDA})_2(\text{Cl})_2]^+$ | $[\text{Fe}(\text{EDA})_2(\text{TcO}_4)(\text{Cl})]^+$ | -595.8 | -702.4 | 127.3 | 20.7 |
| $[\text{Fe}(\text{EDA})_2(\text{Cl})_2]^+$ | $[\text{Fe}(\text{EDA})_2(\text{SO}_4)(\text{Cl})]^0$ | -1241.9 | -432.5 | -797.4 | 12.0 |
| $[\text{Fe}(\text{EDA})_2(\text{TcO}_4)(\text{Cl})]^+$ | $[\text{Fe}(\text{EDA})_2(\text{TcO}_4)_2]^+$ | -770.5 | -883.5 | 131.7 | 18.6 |
| $[\text{Fe}(\text{EDA})_2(\text{SO}_4)(\text{Cl})]^0$ | $[\text{Fe}(\text{EDA})_2(\text{SO}_4)_2]^-$ | -1146.6 | -630.1 | -655.4 | -138.9 |
| $[\text{Fe}(\text{EDA})_2(\text{H}_2\text{O})_2]^{3+}$ | $[\text{Fe}(\text{EDA})_2(\text{TcO}_4)(\text{H}_2\text{O})]^{2+}$ | -2064.2 | -1033.7 | -1078.3 | -47.8 |
| $[\text{Fe}(\text{EDA})_2(\text{H}_2\text{O})_2]^{3+}$ | $[\text{Fe}(\text{EDA})_2(\text{SO}_4)(\text{H}_2\text{O})]^+$ | -2710.2 | -435.3 | -2328.5 | -53.5 |
| $[\text{Fe}(\text{EDA})_2(\text{TcO}_4)(\text{H}_2\text{O})]^{2+}$ | $[\text{Fe}(\text{EDA})_2(\text{TcO}_4)_2]^+$ | -1344.3 | -640.9 | -743.9 | -40.5 |
| $[\text{Fe}(\text{EDA})_2(\text{SO}_4)(\text{H}_2\text{O})]^+$ | $[\text{Fe}(\text{EDA})_2(\text{SO}_4)_2]^-$ | -1498.8 | -387.5 | -1205.5 | -94.2 |

Table 6.2 The free energy terms contributing to the thermochemical cycle for ligand exchange using the SMD solvation model. Units: kJ mol^{-1} .

6.3 Development of a Classical Force Field for Fe³⁺-EDA

One alternative to obtaining $\Delta G_{\text{ex, aq}}$ by the quantum mechanical approach is to use classical atomistic simulations. To simulate the ligand exchange reaction a force field must simultaneously be able to reproduce the behaviour of each anion in solution as well as in the coordination environment of the Fe³⁺ cation. For the Fe³⁺-EDA complexes all bonds were constrained to their OPLS distances [181] using the SHAKE algorithm [133]. Angle bend parameters were taken from the AMBER force field [182] and non-bonded and torsional parameters were from the OPLS force field [166, 181]. Additional N – Fe – N harmonic angle potentials were employed to maintain either the *cis* or *trans* geometry about the Fe³⁺ cation [183], necessary due to the inability of a classical force field of this type to maintain this feature of the geometry of the transition metal complex. The initial VDW parameters for Fe, σ_{Fe} and ϵ_{Fe} , were originally obtained by fitting to *ab initio* calculations of Fe³⁺ with H₂O by Curtiss *et al.* [184]. The full set of parameters used to model the Fe³⁺-EDA complexes are given in Table 6.3.

In a similar approach to that taken in Section 5.3.2, the non-bonded parameters of Fe were optimised to match the gas phase potential energy of the interactions between ligand with the Fe³⁺-EDA complex (optimised at the M06/6-311+G* level of theory), shown in Figure 6.4. However, standard transferable force fields cannot account fully for the electronic subtleties of the d-block coordination complexes or ligand polarisabilities, which are expected to be vastly different in the ligands under examination here. Using the oxyanion parameters initially optimised to fit the interaction with H₂O no single combination of σ_{Fe} and ϵ_{Fe} values correctly fitted the interaction between Fe³⁺ and each ligand. As a result ligand specific parameters were developed to address these limitations. For the atom directly bound to Fe³⁺ in each ligand (TcO₄⁻, SO₄²⁻, Cl⁻ and H₂O) σ_{Fe} was adjusted to take a different value, necessary to account for the large variations in polarisation of the ligands by Fe³⁺. Using this approach ΔE and r_{eq} were fitted to within 1 kJ mol⁻¹ and 0.05 Å, as shown in Table 6.4, apart from H₂O and SO₄²⁻. In these exceptions the ΔE term was still fitted correctly but r_{eq} was slightly too long. The conjugate gradient method, implemented using DL_POLY Classic [141], was used for this fitting procedure. The final set of σ_{Fe} parameters are given in Table 6.5.

Non-bonded

| <i>i</i> | $q_i (e)$ | $\epsilon_i (\text{kJ mol}^{-1})$ | $\sigma_i (\text{\AA})$ |
|----------|-----------|-----------------------------------|-------------------------|
| Fe | 3.0000 | 0.4435 | * |
| N | -0.8400 | 0.7113 | 3.300 |
| C | 0.1500 | 0.2761 | 3.500 |
| H-[N] | 0.3600 | - | - |
| H-[C] | -0.0150 | 0.0627 | 2.500 |

Equilibrium Bond Lengths

| <i>i-j</i> | $k_r (\text{kJ mol}^{-1} \text{\AA}^{-2})$ | $r_{\text{eq}} (\text{\AA})$ |
|------------|--|------------------------------|
| N-C | - | 1.448 |
| C-C | - | 1.529 |
| N-H | - | 1.010 |
| C-H | - | 1.090 |

Angle Bend

| <i>i-j-k</i> | $k_\theta (\text{kJ mol}^{-1} \text{rad}^{-2})$ | $\theta_{\text{eq}} (^\circ)$ |
|--------------|---|-------------------------------|
| N-C-C | 470.28 | 109.47 |
| N-C-H | 334.72 | 109.50 |
| C-N-H | 292.88 | 109.50 |
| C-C-H | 313.80 | 110.70 |
| H-N-H | 364.84 | 106.40 |
| H-C-H | 276.14 | 107.80 |

Torsion

| <i>i-j-k-l</i> | $v_1 (\text{kJ mol}^{-1})$ | $v_2 (\text{kJ mol}^{-1})$ | $v_3 (\text{kJ mol}^{-1})$ |
|----------------|----------------------------|----------------------------|----------------------------|
| N-C-C-H | -4.238 | -2.966 | 1.979 |
| H-N-C-C | -0.795 | -1.745 | 1.749 |
| H-N-C-H | - | - | 1.674 |
| H-C-C-H | - | - | 1.330 |

Table 6.3 Force field parameters for the Fe³⁺-EDA complex.

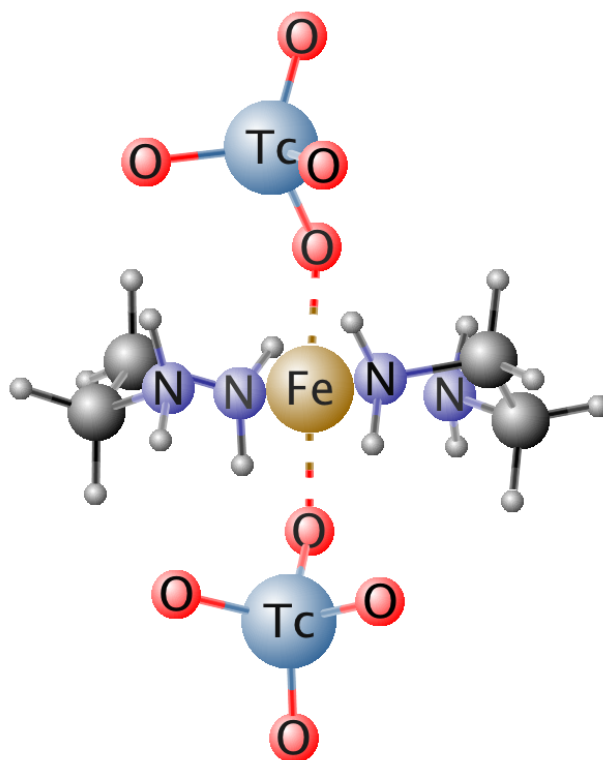


Figure 6.4 Model used to parameterise the force field by fitting ΔE and r_{eq} to the DFT interaction of two TcO_4^- ligands with *trans* Fe^{3+} -EDA from DFT. An analogous fitting procedure was used for the other ligands.

| Ligand | ΔE (kJ mol^{-1}) | | r_{eq} (\AA) | |
|----------------------|-------------------------------------|-------------|----------------------------------|-------------|
| | DFT | Force Field | DFT | Force Field |
| TcO_4^- | -2348.7 | -2348.4 | 1.893 | 1.850 |
| SO_4^{2-} | -3963.8 | -3963.8 | 1.896 | 2.148 |
| H_2O | -489.0 | -489.0 | 2.010 | 2.484 |
| Cl^- | -2615.2 | -2615.5 | 2.254 | 2.287 |

Table 6.4 Comparison of ΔE and r_{eq} for the interaction between Fe and each ligand calculated from the optimised force field and DFT.

| Ligand | $\sigma_{\text{Fe}} (\text{\AA})$ |
|-----------------------------------|-----------------------------------|
| H ₂ O (O) | 1.465 |
| TcO ₄ ⁻ (O) | 2.600 |
| SO ₄ ²⁻ (O) | 1.820 |
| Cl ⁻ | 3.095 |
| Other atom types | 1.700 |

Table 6.5 Final optimised values of σ_{Fe} for each ligand interaction.

6.4 PMF Simulations

MD simulations were performed in conjunction with the umbrella sampling technique to determine PMFs for the exchange of TcO₄⁻ and SO₄²⁻ with other ligands on the Fe³⁺-EDA complex. In each case the anions and Fe³⁺-EDA complexes were solvated by the random addition of approximately 1100 SPC/E H₂O molecules in a simulation cell of dimension 32 Å.

We require a PMF that describes the relative change in free energy between the situation where the anion is coordinated to Fe³⁺-EDA and where it is completely hydrated (at large separation from the Fe³⁺-EDA) and another ligand occupies this coordination site. The PMF for exchange of Cl⁻ with a H₂O on [Fe(EDA)₂(H₂O)₂]³⁺ was first calculated for comparison with the oxyanions and to elucidate the likely initial complex. PMFs were then obtained for each oxyanion ligand exchanging with a H₂O of [Fe(EDA)₂(H₂O)₂]³⁺ and with a Cl⁻ of [Fe(EDA)₂(Cl)₂]⁺ to study their relative $\Delta G_{\text{ex, aq}}$ for the possible initial complexes as well as a PMF for the direct exchange of TcO₄⁻ with a SO₄²⁻ of [Fe(EDA)₂(SO₄)₂]⁻, in the case where the complex has previously become saturated with an excess of SO₄²⁻. The umbrella biasing potential was applied using the PLUMED plugin [185] and the reaction coordinate for oxyanion exchange was defined as the distance between Fe³⁺ and the central atom of the oxyanion, X. We have used a biasing potential that takes the same form as Equation 4.86 where the target distance between Fe and X, r_{eq} , was gradually decreased in 0.25 Å intervals in adjacent simulation windows from 10 to 3 Å. The

force constant of the biasing potential, k_w , was typically set to $200 \text{ kJ mol}^{-1} \text{ \AA}^{-2}$. Each simulation ran for a total of 2 ns, the final 1 ns of which was used for the collection of statistics used to generate the PMFs. The overall potential energy function was then corrected for the bias and recombined using Equation 4.88 and WHAM [186]. During the equilibration period WHAM was used to check for sufficient statistical overlap between sampling in adjacent windows along the reaction coordinate. If there was insufficient overlap (ie. in the region where the PMF profile is steep) additional simulations with larger biasing force constants were conducted. $\Delta G_{\text{ex, aq}}$ is directly obtainable from the PMF by taking the difference in free energy at the minimum energy point, r_{min} , and at the maximum separation of 10 \AA . Since the simulations were conducted in the isothermal-isobaric ensemble the enthalpy associated with each exchange event, $\Delta H_{\text{ex, aq}}$, was computed over the same interval by taking the difference in mean ensemble enthalpy from extended simulations restrained at r_{min} and 10 \AA lasting 10 ns. $\Delta H_{\text{ex, aq}}$ was also calculated for each of the *cis* isomers of the complex. Finally the entropic contribution to exchange, $T\Delta S_{\text{ex, aq}}$, was computed by subtracting $\Delta H_{\text{ex, aq}}$ from $\Delta G_{\text{ex, aq}}$. For reactions in which ligand exchange is separated by a free energy barrier, $\Delta G_{\text{barrier}}$, the Eyring equation can be used to obtain an exchange rate, k_{ex} , defined by

$$k_{\text{ex}} = \frac{k_{\text{B}}T}{h} \exp\left(\frac{-\Delta G_{\text{barrier}}}{RT}\right) \quad (6.2)$$

Here, $\Delta G_{\text{barrier}}$ is the barrier in the forward direction (transferring an anion from aqueous solution to the complex). The PMFs allow for a direct comparison of the relative affinities of TcO_4^- and SO_4^{2-} for the Fe^{3+} -EDA complex and the computation of $\Delta H_{\text{ex, aq}}$ and $T\Delta S_{\text{ex, aq}}$ help explain the observed selectivity.

6.4.1 PMFs for Water Exchange on Fe^{3+} -EDA

The structure and coordination environment of the *trans*- $[\text{Fe}(\text{EDA})_2(\text{H}_2\text{O})_2]^{3+}$ complex was investigated using the radial distribution function for the Fe^{3+} and OW pair (Figure 6.5), $g_{\text{Fe-OW}}(r)$, obtained during a 10 ns simulation. There is an intense peak in $g_{\text{Fe-OW}}(r)$ at 2.4 \AA , associated with water molecules directly coordinated to the complex and the integral of $g_{\text{Fe-OW}}(r)$ clearly shows that this peak is associated with two H_2O ligands, which occupy the axial positions in this case.

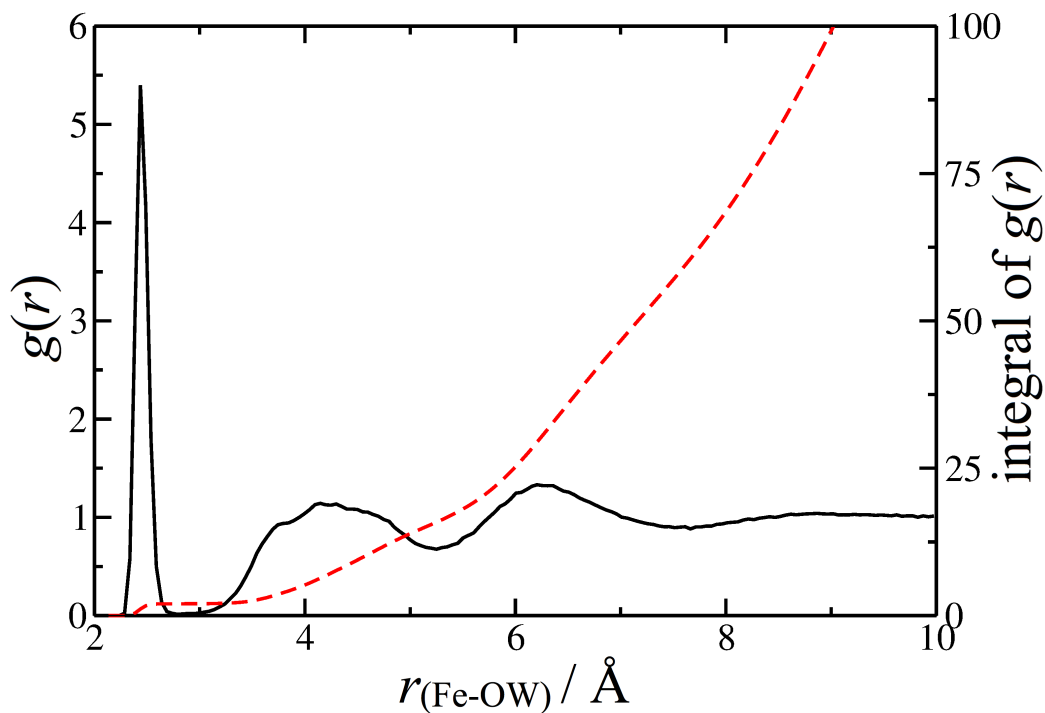


Figure 6.5 $g_{\text{Fe-OW}}(r)$ (black, solid line) and its integral (red, dashed line) obtained from a simulation of the Fe^{3+} -EDA complex in water.

Providing that a ligand exchange event has a small enough $\Delta G_{\text{barrier}}$ for it to occur several times during a typical MD simulation $g(r)$ can be used to estimate the PMF using the equation

$$W(r) = -RT \ln g(r) \quad (6.3)$$

During the simulation a number of H_2O exchange events take place enabling the PMF to be estimated either by using $g_{\text{Fe-OW}}(r)$ and Equation 6.3 or obtained using the umbrella sampling approach (Equation 4.83). The barriers to exchange in the reverse direction for these two approaches (Figure 6.6) are 15.1 and 14.9 kJ mol^{-1} , respectively, where the difference can be explained by the limited statistical sampling of the higher energy region in the former approach. Although the shapes of the two PMFs are similar, the one obtained from this first approach does not tend to zero, suggesting that one H_2O ligand is favoured over all others. This discrepancy can be rationalised by the fact the $g(r)$ method accounts for both possible axial ligand sites whereas the umbrella sampling method gives the free energy change associated with a single H_2O ligand exchange. The 14.9 kJ mol^{-1} barrier obtained by umbrella sampling, which corresponds to a H_2O exchange rate of 15.2 ns^{-1} , is much smaller

than the experimentally determined barrier for a fully solvated Fe^{3+} ion [187] (60.4 kJ mol^{-1}) and is evidence of the H_2O labilising effect of the chelating EDA ligands. The histogram generated from the WHAM (Figure 6.7) method shows that the entire reaction coordinate, $r_{\text{Fe-OW}}$, of the PMF profile was sufficiently sampled.

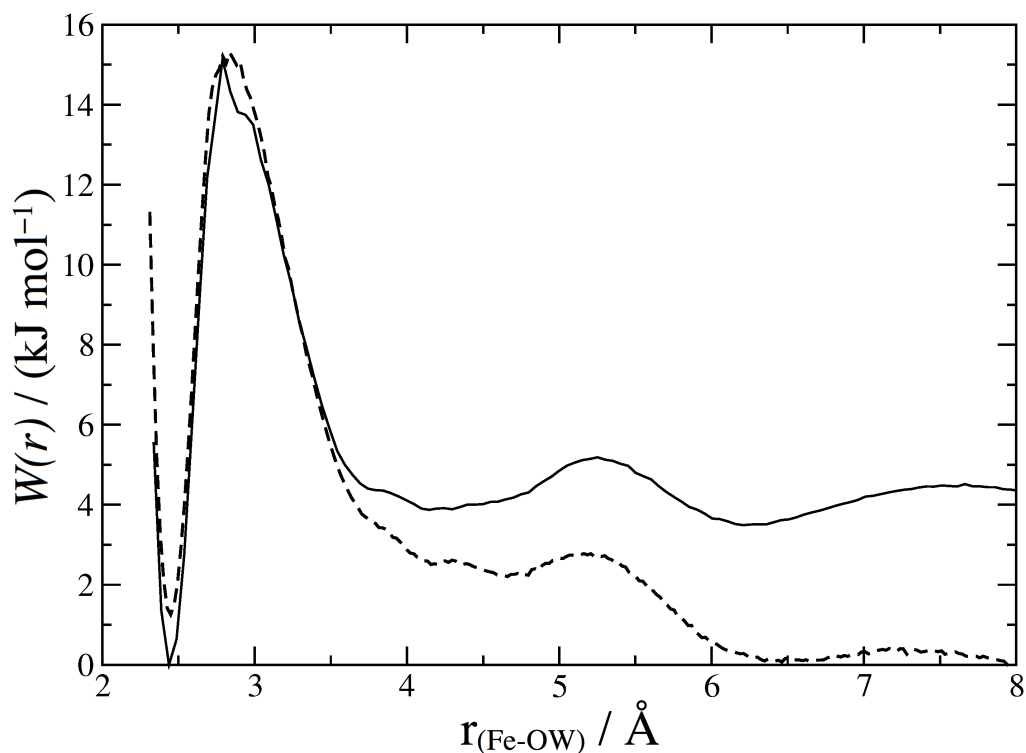


Figure 6.6 PMFs for H_2O exchange at the axial positions of the Fe^{3+} -EDA complex, estimated from $g_{\text{Fe-OW}}(r)$ (solid line), Equation 6.3, and obtained from umbrella sampling simulations and Equation 4.83 (dashed line). The PMF estimated from $g_{\text{Fe-OW}}(r)$ has been shifted to zero for the sake of comparison.

| Initial Complex | Final Complex | $\Delta G_{\text{ex, aq}}$ | $\Delta H_{\text{ex, aq}}$ | $T\Delta S_{\text{ex, aq}}$ | $\Delta G_{\text{barrier}}$ |
|--|--|----------------------------|----------------------------|-----------------------------|-----------------------------|
| $[\text{Fe}(\text{EDA})_2(\text{H}_2\text{O})_2]^{3+}$ | $[\text{Fe}(\text{EDA})_2(\text{H}_2\text{O})(\text{TcO}_4)]^{2+}$ | -165.4 | -190.2 | -24.8 | 12.6 |
| $[\text{Fe}(\text{EDA})_2(\text{H}_2\text{O})_2]^{3+}$ | $[\text{Fe}(\text{EDA})_2(\text{H}_2\text{O})(\text{SO}_4)]^+$ | -160.5 | -131.1 | 29.4 | 0.0 |
| $[\text{Fe}(\text{EDA})_2(\text{H}_2\text{O})_2]^{3+}$ | $[\text{Fe}(\text{EDA})_2(\text{H}_2\text{O})(\text{Cl})]^{2+}$ | -127.1 | -104.2 | 22.9 | 15.9 |
| $[\text{Fe}(\text{EDA})_2(\text{Cl})_2]^+$ | $[\text{Fe}(\text{EDA})_2(\text{Cl})(\text{TcO}_4)]^+$ | -26.4 | -74.5 | -48.1 | 66.7 |
| $[\text{Fe}(\text{EDA})_2(\text{Cl})_2]^+$ | $[\text{Fe}(\text{EDA})_2(\text{Cl})(\text{SO}_4)]^0$ | -60.0 | -54.6 | 5.4 | 30.3 |
| $[\text{Fe}(\text{EDA})_2(\text{SO}_4)_2]^-$ | $[\text{Fe}(\text{EDA})_2(\text{SO}_4)(\text{TcO}_4)]^0$ | -4.6 | -36.9 | -32.3 | 97.0 |

Table 6.6 Contributions to $\Delta G_{\text{ex, aq}}$ for each ligand exchange event on the *trans* Fe^{3+} -EDA complex at 298 K. Units: kJ mol^{-1} .

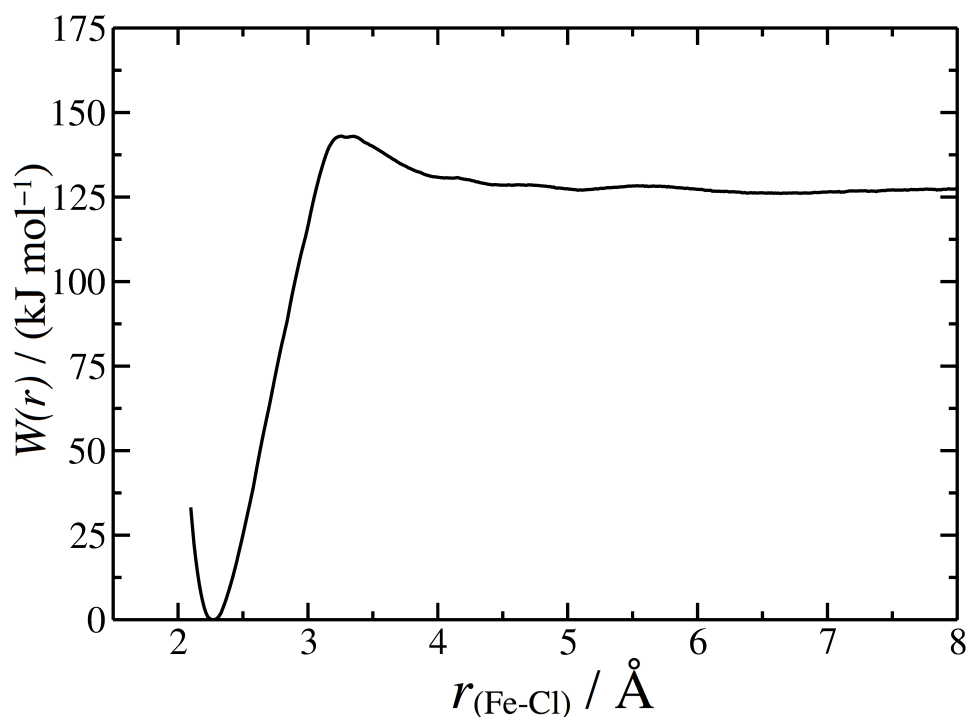


Figure 6.8 PMF for Cl^- exchange with H_2O .

Figure 6.9 shows that the exchange of either oxyanion for H_2O has a significant free energy driving force; $\Delta G_{\text{ex, aq}}$ is -165.4 and -160.5 kJ mol^{-1} for TcO_4^- and SO_4^{2-} , respectively, with the minimum energy at distances of 3.62 and 3.65 Å. For TcO_4^- exchange $\Delta H_{\text{ex, aq}}$ is favourable (-190.2 kJ mol^{-1}) but $T\Delta S_{\text{ex, aq}}$ is unfavourable

($-24.8 \text{ kJ mol}^{-1}$). $\Delta H_{\text{ex, aq}}$ for SO_4^{2-} exchange is less favourable ($-131.1 \text{ kJ mol}^{-1}$) but does have a favourable $T\Delta S_{\text{ex, aq}}$ term ($+29.4 \text{ kJ mol}^{-1}$). Both oxyanions were found to coordinate to the Fe^{3+} -EDA complex in a monodentate fashion, in agreement with the experimental observation [106]. The exchange of these ligands for H_2O is primarily driven by electrostatic attraction between the anion and Fe^{3+} . However, entropy also plays an important role in the selectivity of Fe^{3+} -EDA for oxyanions. The effect of SO_4^{2-} inducing greater long-range order in the surrounding H_2O molecules than TcO_4^- means that removing it from its fully hydrated environment and coordinating to the Fe^{3+} -EDA complex is more favourable entropically. Exchange of TcO_4^- is therefore greatly preferred to SO_4^{2-} in terms of enthalpy, but the overall calculated $\Delta G_{\text{ex, aq}}$ shows that SO_4^{2-} competes for Fe^{3+} -EDA suggesting the relative hydration entropies of the oxyanions, $T\Delta S_{\text{hyd}}$, are a critically important property for exchange reactions of this type. There is an apparent discrepancy in that this value might be expected to be similar to the equivalent TcO_4^- process ($-24.8 \text{ kJ mol}^{-1}$) as their $T\Delta S_{\text{hyd}}$ values are similar in Table 5.2. This can be resolved by considering that Cl^- is almost completely removed from its hydrated environment on coordination to the complex whereas TcO_4^- still has three oxygens that are partly hydrated. For TcO_4^- exchanging with H_2O , $\Delta H_{\text{ex, aq}}$ was the same for *cis* ($-190.1 \text{ kJ mol}^{-1}$) as the *trans* isomer. For SO_4^{2-} , exchange was less favourable ($-119.6 \text{ kJ mol}^{-1}$) by 11.5 kJ mol^{-1} compared to the equivalent process on the *trans* complex. If the oxyanion models are realistic then the difference in $T\Delta S_{\text{ex, aq}}$ between the two TcO_4^- and SO_4^{2-} exchange reactions should be equivalent to the difference in their hydration entropies, $T\Delta S_{\text{hyd}}$. It is encouraging that the $T\Delta S_{\text{ex, aq}}$ difference is $-54.2 \text{ kJ mol}^{-1}$ and the difference in $T\Delta S_{\text{hyd}}$ obtained experimentally (Table 5.2) is $-53.7 \text{ kJ mol}^{-1}$.

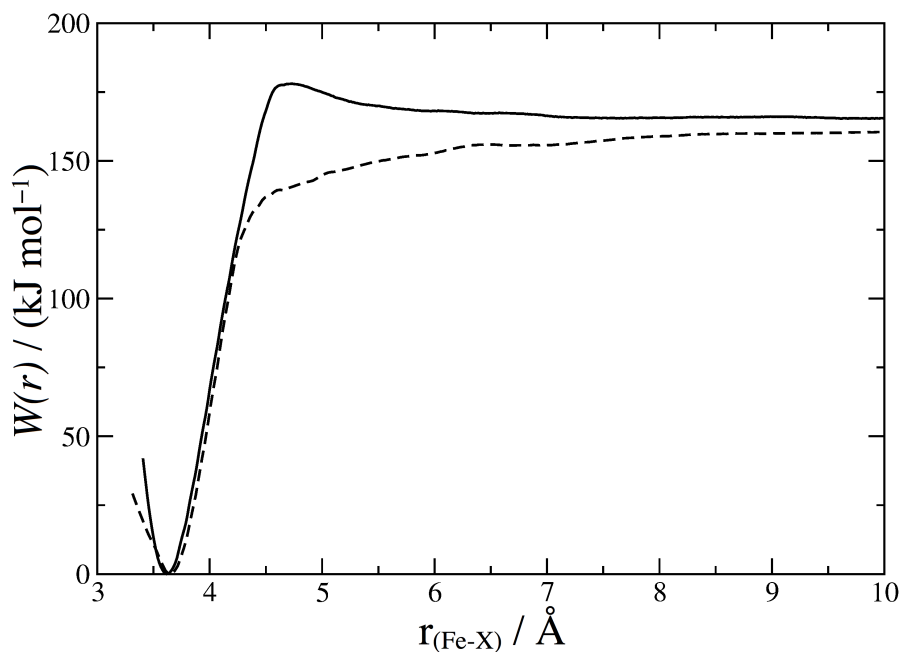


Figure 6.9 PMFs for XO_4^{n-} exchange with H_2O . $\text{X} = \text{Tc}$ (solid line) and $\text{X} = \text{S}$ (dashed line).

The difference in the shapes of the PMF profiles suggests that exchange with H_2O occurs by a slightly different mechanism for the two oxyanions; there is a small free energy barrier for TcO_4^- exchange but no barrier for SO_4^{2-} . The lack of any significant free energy barriers along this reaction coordinate suggests that the exchange of oxyanions with H_2O is not a kinetically limited process. Oxyanion exchange occurs at approximately 4.7 \AA for TcO_4^- and 4.5 \AA for SO_4^{2-} , respectively and typical atomic configurations from the simulation windows corresponding to these distances are compared in Figure 6.10. Despite the difference in the shape of the PMF profiles, the average $\text{Fe}^{3+} - \text{O}(\text{XO}_4^{n-})$ and $\text{Fe}^{3+} - \text{OW}$ distances at the point of exchange are similar. Analysis of the PMF profile shows that the coordination number of the complex is always six during the exchange of either oxyanion and no significant low energy intermediate complexes are observed, suggesting that oxyanion exchange occurs via an interchange mechanism in both cases.

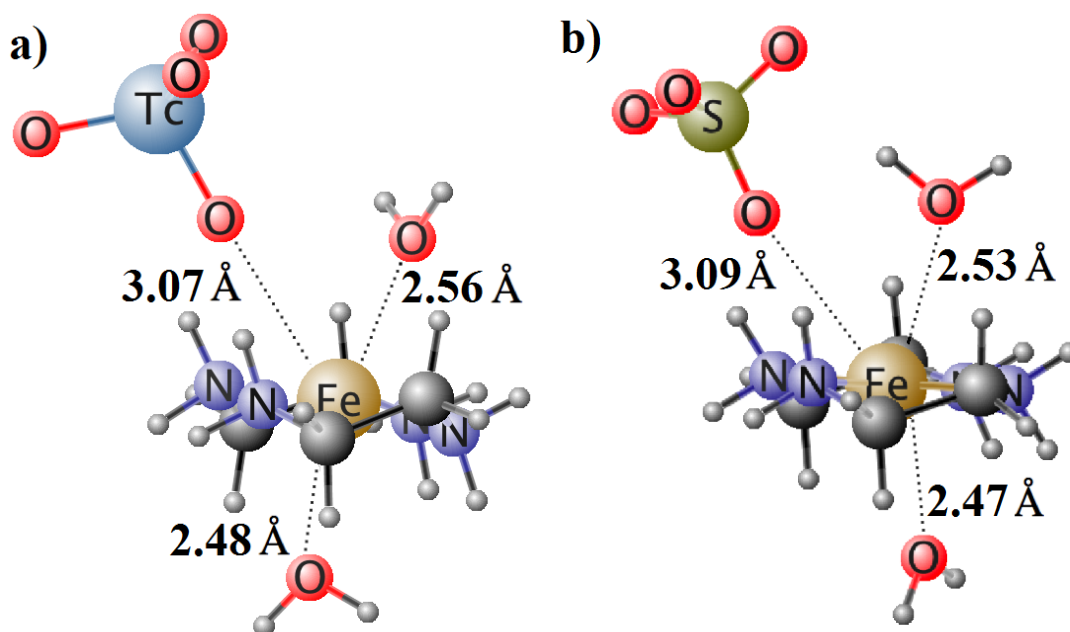


Figure 6.10 Snapshots of typical configurations at the point of XO_4^{n-} exchange with H_2O showing average Fe^{3+} - ligand distances; a) $\text{X} = \text{Tc}$, from the 4.75 Å window, b) $\text{X} = \text{S}$, from the 4.5 Å window.

6.4.3 PMFs for Oxyanion Exchange with Chloride on Fe^{3+} -EDA

$\Delta G_{\text{ex, aq}}$ for the exchange of oxyanions with Cl^- is obtained from the PMF profile in Figure 6.11 giving $-26.4 \text{ kJ mol}^{-1}$ for TcO_4^- and $-60.0 \text{ kJ mol}^{-1}$ for SO_4^{2-} , suggesting that this complex is selective for SO_4^{2-} by 33.6 kJ mol^{-1} . The reason for the selectivity difference is due to the more repulsive short-range interaction with Cl^- stemming from the larger σ_{O} parameter for TcO_4^- . These processes require free energy to overcome barriers of 66.7 and 30.3 kJ mol^{-1} , for TcO_4^- and SO_4^{2-} , respectively, corresponding to exchange rates of 12.6 s^{-1} and $3.0 \times 10^7 \text{ s}^{-1}$. No such energy input was required in the case of SO_4^{2-} exchanging with H_2O . The large barriers are due to the electrostatic repulsion between anionic ligands that are forced into close contact during exchange. Again, no energy minima were observed at the point of exchange suggesting that displacement of Cl^- with an oxyanion also proceeds via an interchange mechanism. TcO_4^- exchange is accompanied by a greater $\Delta H_{\text{ex, aq}}$ contribution ($-74.5 \text{ kJ mol}^{-1}$) than SO_4^{2-} exchange ($-54.6 \text{ kJ mol}^{-1}$) indicating that the difference between the $T\Delta S_{\text{ex, aq}}$ terms ($-48.4 \text{ kJ mol}^{-1}$ vs. 5.4 kJ mol^{-1} for TcO_4^- and SO_4^{2-} , respectively) is enough to overcome the difference in $\Delta H_{\text{ex, aq}}$ and is again an important factor in determining the selectivity for oxyanions. We find consistency in

the difference in $T\Delta S_{\text{ex, aq}}$ between the two oxyanions exchanging with H_2O ($-54.2 \text{ kJ mol}^{-1}$) and the corresponding Cl^- exchange events ($-53.5 \text{ kJ mol}^{-1}$). Shallow free energy minima, corresponding to hydrogen bonding between the oxyanion and the amine hydrogen atoms were observed during SO_4^{2-} exchange, most notably at 4.9 \AA . There is some evidence that similar energy minima are observed in the equivalent PMF profile exchange with H_2O . On the corresponding *cis* isomers $\Delta H_{\text{ex, aq}}$ was -86.0 and $-40.3 \text{ kJ mol}^{-1}$ for TcO_4^- and SO_4^{2-} exchange with Cl^- , respectively, increasing the complex's preference for TcO_4^- over SO_4^{2-} relative to the *trans* isomer, due to greater electrostatic repulsion from the adjacent Cl^- in the SO_4^{2-} case.

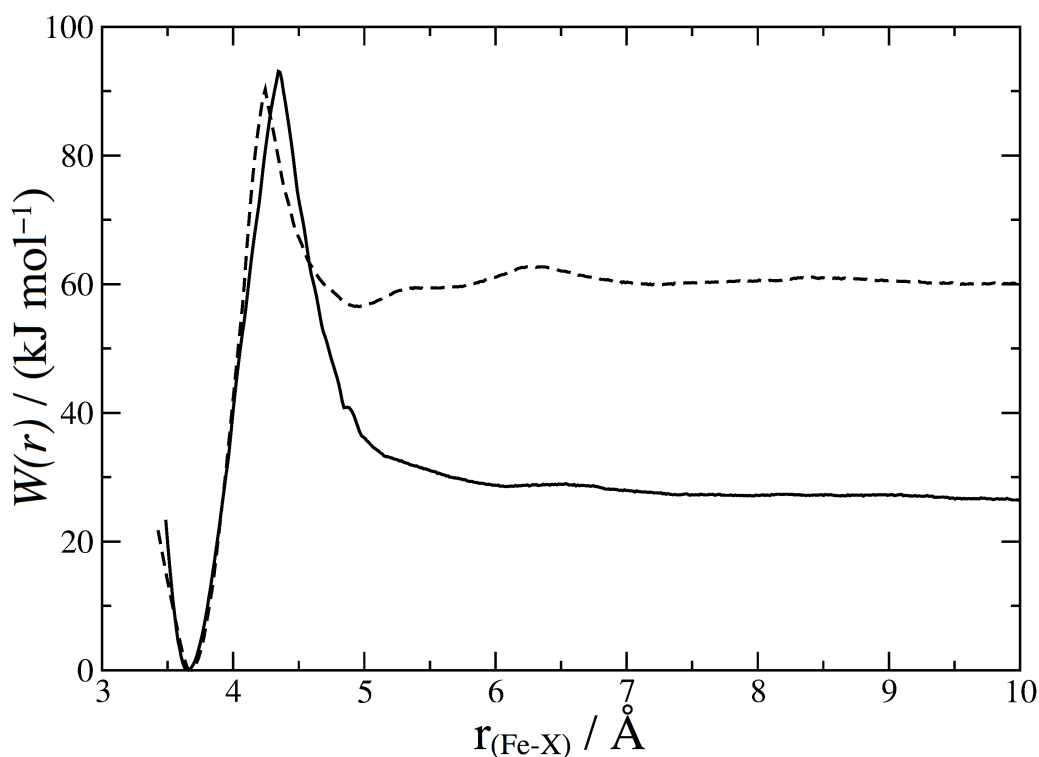


Figure 6.11 PMFs for XO_4^{n-} exchange with Cl^- . $\text{X} = \text{Tc}$ (solid line) and $\text{X} = \text{S}$ (dashed line).

6.4.4 PMF for Direct Exchange of TcO_4^- with SO_4^{2-} on Fe^{3+} -EDA

Following the evidence that oxyanion exchange for H_2O and Cl^- is favourable the Fe^{3+} -EDA complex is initially likely to become saturated with SO_4^{2-} due to its higher concentration in environmental waters. $\Delta G_{\text{ex, aq}}$ for direct TcO_4^- exchange with SO_4^{2-} is favoured by just -4.6 kJ mol^{-1} in excellent agreement with the difference in $\Delta G_{\text{ex, aq}}$

for the two H₂O exchange processes. The PMF profile in Figure 6.12 reveals that a 97.0 kJ mol⁻¹ barrier separates the two configurations. Such a barrier is not insurmountable and is equivalent to an oxyanion exchange rate of 0.22 hr⁻¹. The atomic coordinates shown in Figure 6.13 correspond to the positions labelled on the PMF profile in Figure 6.12. At a Fe³⁺ – Tc distance of 6.5 Å TcO₄⁻ approaches the complex in the equatorial plane, minimising electrostatic repulsion from the axial SO₄²⁻ ligands. At 4.3 Å the energy increases significantly as TcO₄⁻ is forced alongside SO₄²⁻. After exchange has taken place the TcO₄⁻ occupies the axial position and SO₄²⁻ is now forced in the equatorial plane, able to hydrogen bond with the EDA amines. Notably, the SO₄²⁻ ligand prefers to remain next to Fe³⁺-EDA complex after being displaced by TcO₄⁻ and does not return to solution. The fact that SO₄²⁻ does not fully re-solvate in these simulations accounts for an apparent discrepancy between the difference in $T\Delta S_{\text{hyd}}$ terms for the H₂O ligand exchanges (-54.2 kJ mol⁻¹) and $T\Delta S_{\text{hyd}}$ for direct exchange TcO₄⁻ with SO₄²⁻ (-32.3 kJ mol⁻¹). $\Delta H_{\text{ex,aq}}$ for exchange on the *trans* complex is -36.9 kJ mol⁻¹ whereas for *cis* exchange the increased electrostatic repulsion from two adjacent SO₄²⁻ destabilises the initial complex relative to the TcO₄⁻ coordinated complex and increases the magnitude of $\Delta H_{\text{ex,aq}}$ to -59.1 kJ mol⁻¹.

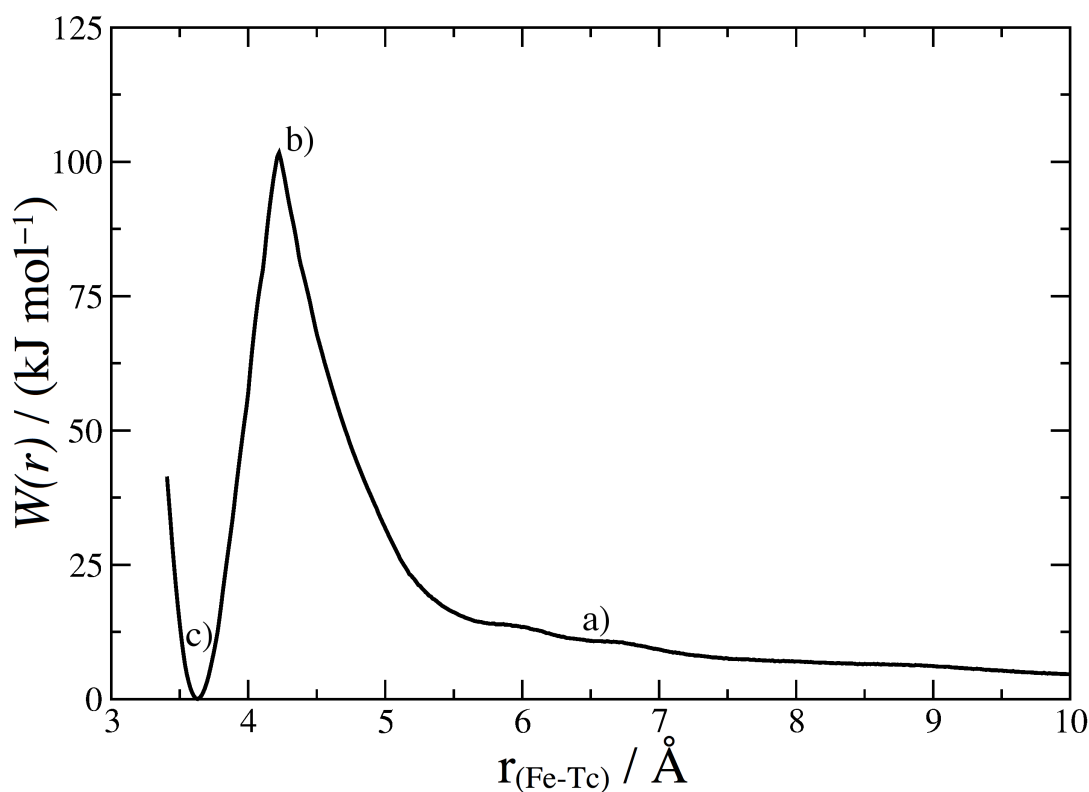


Figure 6.12 PMF for the exchange of TcO₄⁻ with SO₄²⁻ on Fe³⁺-EDA.

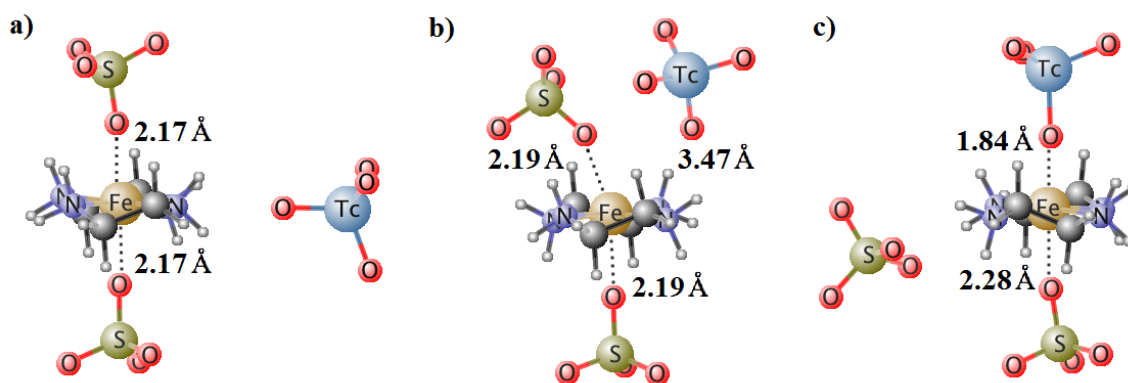


Figure 6.13 Snapshots obtained from the MD simulations for the exchange of TcO_4^- with SO_4^{2-} from the a) 6.5, b) 4.3 and c) 3.6 Å windows.

Assuming the overall entropy change is the same for ligand exchange on each isomer of the same complex, $\Delta G_{\text{ex,aq}}$ for *cis* can be estimated simply by adding the difference between $\Delta H_{\text{ex,aq}}$ for the two isomers to $\Delta G_{\text{ex,aq}}$ for the *trans* exchange. Overall, these geometric effects only have a minor effect on $\Delta G_{\text{ex,aq}}$ although the results suggest possible enhancement of the selectivity of the adsorbent material for TcO_4^- if the Fe^{3+} -EDA monolayer could be tailored so that oxyanion coordination sites were *cis* to each other.

6.5 Conclusions

From DFT, the *trans* isomer of the initial $[\text{Fe}(\text{EDA})_2(\text{Cl})_2]^+$ complex was found to be more stable than *cis* by 19.6 kJ mol^{-1} . MD simulations and the umbrella sampling technique were used to generate PMFs to investigate the selectivity of the complex for TcO_4^- and SO_4^{2-} . Any possible remediation material must be highly selective for TcO_4^- in order to clean up trace quantities. For an initial Fe^{3+} -EDA complex coordinated by two H_2O ligands, exchange of one H_2O with an oxyanion was found to proceed via an interchange mechanism and the complex preferred to bind TcO_4^- instead of SO_4^{2-} . This preference was replicated in the PMF profile for direct exchange of SO_4^{2-} with TcO_4^- . The free energies associated with these two exchange processes are consistent with each other but the preference for TcO_4^- is only marginal (approximately 5 kJ mol^{-1}). When Cl^- is coordinated to the initial complex instead, exchange by SO_4^{2-} was preferred. The various contributions to the free energies for aqueous ligand exchange were determined and the oxyanion hydration entropy was found to be critically important. If the performance of an oxyanion-SAMMS material

is determined solely by the chemistry of the Fe^{3+} -EDA monolayer complex it is difficult to see how the experimentally observed distribution coefficients are obtained. Other effects such as confining the solution to a pore or tethering the complex to the surface must be in part responsible for this selectivity. A better understanding of the use of oxyanion-SAMMS as a TcO_4^- remediation tool could be gained by instead using a full pore model which accounts for the effects of tethering the Fe^{3+} -EDA complex to the surface within a pore of MCM-41.

Chapter Seven

Models of the MCM-41 Mesoporous Support

7.1 Introduction

In this chapter a new approach to constructing MCM-41 models is presented. If a reliable model of MCM-41 is available molecular simulation can be used as an alternative to experiment for investigating of adsorption phenomena. In addition, models can help the designer to optimise the performance of the material for any one of its many applications, such as in SAMMS. Firstly, the models were validated by computing the CO₂ adsorption isotherm using grand canonical Monte Carlo (GCMC) simulations and compared to experiment. Then, a simple MC scheme involving a single adsorbate molecule was used to investigate the effect of pore diameter and wall thickness on the adsorption behaviour of several simple gases at very low pressure.

7.2 Previous Models of MCM-41

Although the structure of MCM-41 on the mesoscale is well known there has been much discussion over its structure on the nanoscale; namely the thickness of the pore walls, whether these walls are completely amorphous or partially crystalline and the presence of surface irregularities and micropores. This has led to a wealth of literature regarding MCM-41 models of varying complexities. The first attempt at building atomistic models of MCM-41 [188] consisted of randomly emplacing silica atoms around rings of frozen Lennard-Jones atoms that define the pores and employed periodic boundary conditions to model the bulk material. The initial structures were then relaxed using a three-body potential with the MD simulation technique but no adsorption studies were performed to validate the model. Maddox and Gubbins constructed a simplified model that consisted solely of oxygen atoms and simulated the adsorption of Ar and N₂ using a 1D potential dependent only on the distance of the adsorbate from the pore surface [189]. They improved the model by adding a variety of attractive surface sites better representative of the real material, improving agreement with the experimental adsorption isotherm at low pressure [190] and highlighting the importance of surface heterogeneity in MCM-41. This model is shown in Figure 7.1. Kleestorfer *et al.* carved pores from a lattice of α -quartz,

saturated the surface with hydroxyl groups and relaxed the structure in an MD simulation [191]. They then calculated stabilisation energies and found that the most stable MCM-41 structures had pore diameters ranging from 3.5 to 5 nm and wall thicknesses between 0.8 and 1.2 nm. Seaton *et al.* [192] studied three models of increasing complexity; one of the models accurately reproduced the experimental adsorption isotherm for CO₂. However the two simplified models, in which the surface was either homogeneous or completely crystalline underpredict adsorption, especially at low pressure. More recently various workers have built MCM-41 models by simulating the actual self-assembly process of micelles [193-195], with some even incorporating the silanol condensation process [196]. There have been numerous other attempts at building atomistic models of MCM-41 and these have previously been thoroughly reviewed and compared [197]. Many of the approaches are either too simplistic in their level of detail of the MCM-41 pore surface or require significant computational resource to construct just a single model.

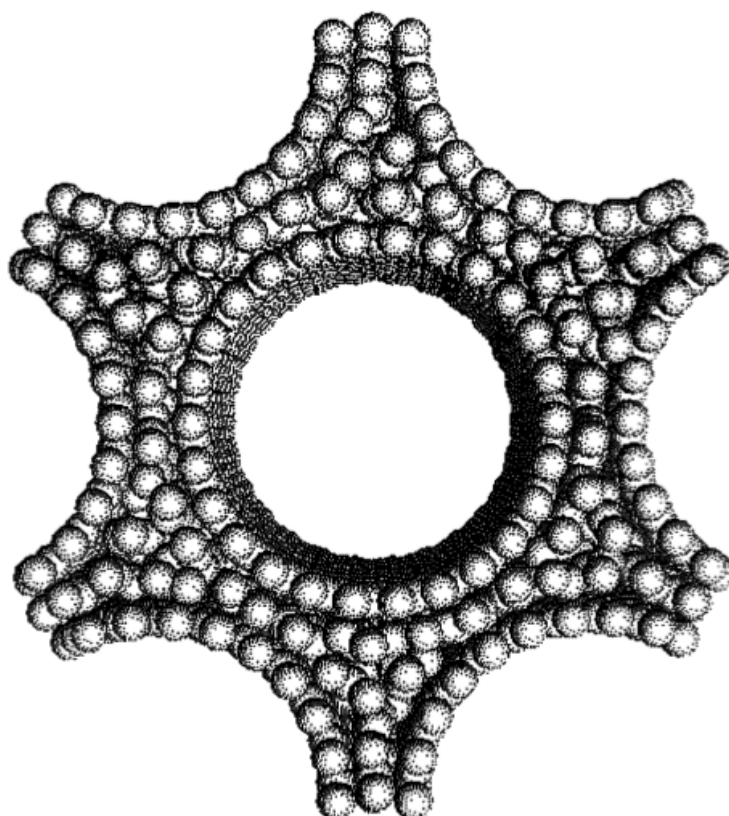


Figure 7.1 A view down the central pore of the Maddox *et al.* model of MCM-41 [190].

7.3 MCM-41 Model Construction and Validation

There is a need for a method of preparing simple yet realistic models of MCM-41 in such a way that easily allows for the structural parameters, such as pore diameters and wall thicknesses, to be optimised to enhance adsorption processes. In this section a new method for constructing realistic atomistic models of MCM-41 is presented. The new approach to building the models uses a modified BKS potential and a MD melt-quench routine, enabling the structural parameters of the material to be easily tuned.

7.3.1 Force Field Parameters

Forces between Si and O atoms were evaluated using the Buckingham type pair potential, v_{Buck} , which consists of a coulombic term and a short-range dispersion term,

$$v_{\text{Buck}}(r_{ij}) = \frac{z_i z_j}{r_{ij}} + A_{ij} \exp(-B_{ij} r_{ij}) - \frac{C_{ij}}{r_{ij}^6} + \frac{D_{ij}}{r_{ij}^{12}} - \frac{E_{ij}}{r_{ij}^8} \quad (7.1)$$

where A_{ij} , B_{ij} , C_{ij} are the BKS parameters for each interacting pair of atoms originally derived from *ab initio* calculations of silica clusters [198]. Two additional terms, D_{ij} and E_{ij} [199], were added to avoid the unphysical fusing of atoms at high temperatures caused by the attractive divergence of the BKS potential [200], by providing short-range repulsion. The VDW parameters for each interacting pair are given in Table 7.1 and the O and Si partial charges were -1.2 and $+2.4$, respectively.

| $i-j$ | O-O | Si-O |
|----------------------------------|-----------|------------|
| A_{ij} (eV) | 1388.7730 | 18003.7572 |
| B_{ij} (\AA^{-1}) | 2.7600 | 4.8732 |
| C_{ij} (eV \AA^6) | 175.0000 | 133.5381 |
| D_{ij} (eV \AA^{12}) | 180.0000 | 20.0000 |
| E_{ij} (eV \AA^8) | 24.0000 | 6.0000 |

Table 7.1 Parameters used in the preparation of MCM-41 models [198, 199].

7.3.2 Model Preparation

MCM-41 models were prepared using a MD melt-quench routine where the initial configuration was generated by cutting a cubic simulation cell from an α -quartz crystal. Care was taken to select stoichiometric quantities of Si and O atoms, with the total number of atoms ranging from 7290 to 27789, depending on the size of the model. Each initial configuration was melted using MD, in the isothermal-isobaric ensemble, by heating to 7300 K from room temperature at a rate of 100 K ps⁻¹ before quenching to 300 K at a controlled rate to obtain an amorphous silica configuration. The quench rates investigated ranged from 7000 to 1 K ps⁻¹. Radial distribution functions for pairs of O atoms, $g_{O-O}(r)$, were obtained from a 100 ps simulation to confirm that the silica had not recrystallized and analyse the effect of quench rate on the structure of the amorphous silica.

The mesoporous MCM-41 was generated by deleting all of the atoms within a chosen pore radius from the quenched silica configuration (Figure 7.2a); one pore was carved from the centre of the cell and a quarter of a pore from each of its corners, giving a total of two in each simulation cell (Figure 7.2b). Silicon atoms with incomplete valency (ie. those not in a tetrahedral oxygen environment) as well as any oxygens bonded only to these silicons were removed in the same procedure as Coasne *et al.* [201]. This was followed by a 2000 time step MD relaxation in the canonical ensemble at 1 K (Figure 7.2c), necessary to allow the initially high energy surface created by the artificial carving of the pores to relax and become representative of the real material. Finally, in order to attain a realistic concentration of surface silanol functionalities hydrogen atoms were added to all non-bridging oxygens (ie. all those with fewer than two silicons within 2.3 Å) on the surface (Figure 7.2d), pointing towards the centre of the pore. Figure 7.3 shows that the periodic image of this cell reproduces the hexagonal mesoporous network of MCM-41.

Two sets of models were constructed; one set of 12 models in which the wall thickness was kept constant and the pore diameter was varied (by carving different sized pores in each of the cells containing the quenched amorphous silica), and another set of 5 models in which the pore diameter was kept constant and the wall thickness varied (by carving the same sized pores from the 5 smallest cells).

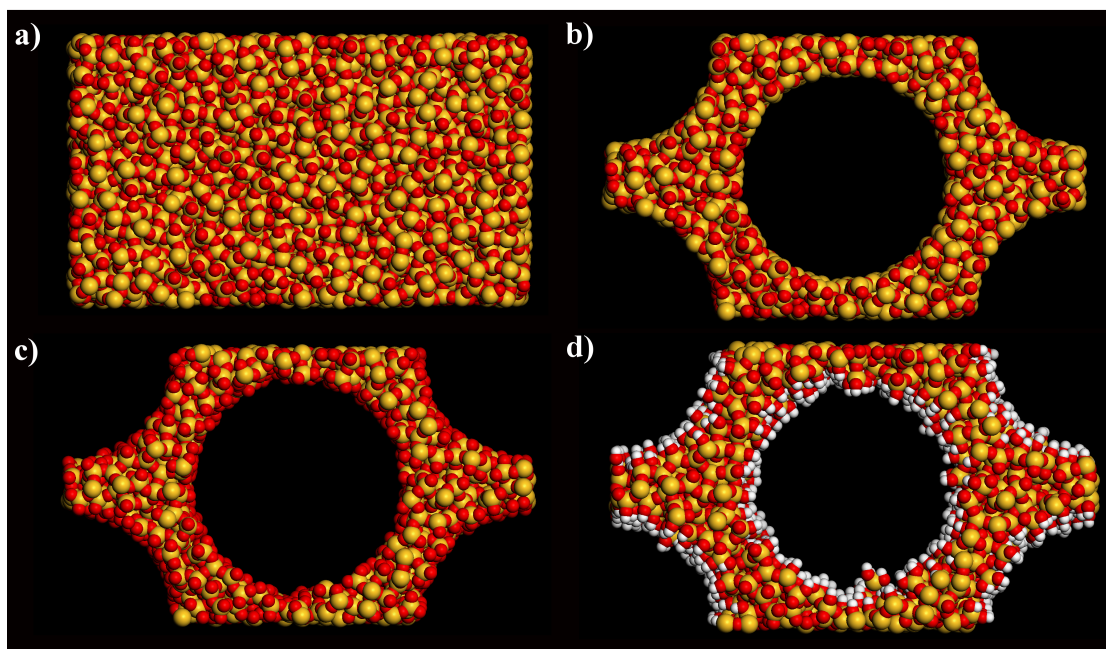


Figure 7.2 The sequence of steps in the preparation of the MCM-41 models; a) quenched amorphous silica, b) carving of cylindrical pores, c) relaxation after removal of silicon and oxygen atoms on the pore surface and d) addition of hydrogen atoms to non-bridging oxygen atoms. Yellow, red and white atoms are silicon, oxygen and hydrogen, respectively.

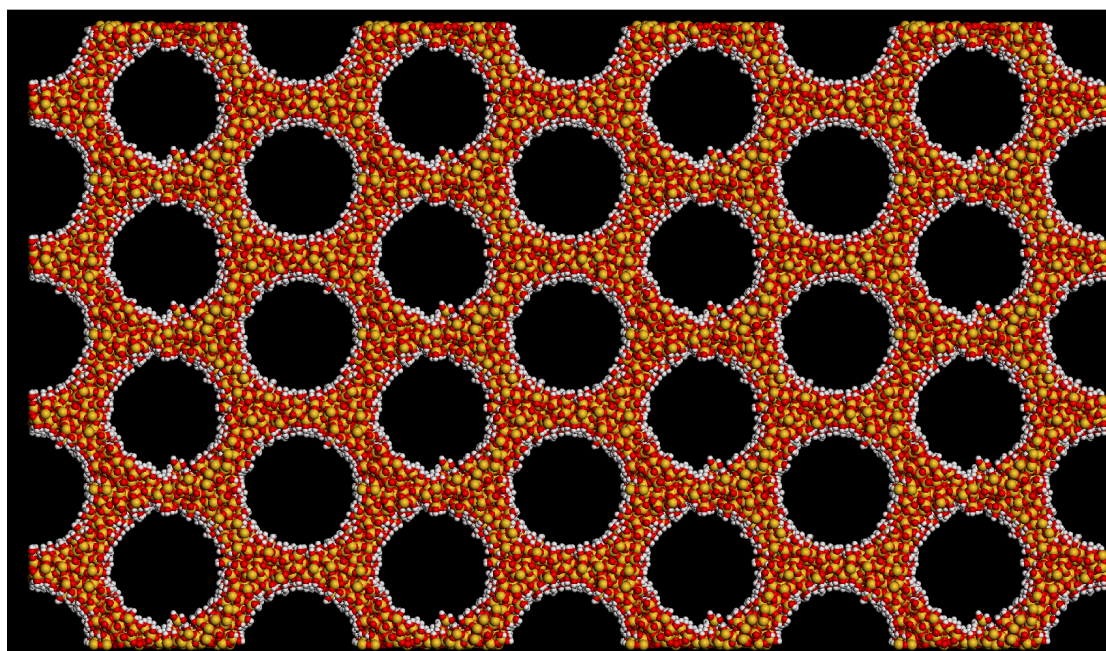


Figure 7.3 The periodic hexagonal mesoporous network of MCM-41, generated by replication of the central simulation cell four times in the x and y directions.

7.3.3 Validity of the Model Structure

The structural parameters of all the MCM-41 models, including pore diameter, wall thickness, surface area, pore volume and surface silanol density, are reported in the tables in Appendix Two. Many of these parameters are used to validate the models in the following sections.

Radial Distribution Functions

In Figure 7.4, the radial distribution functions for the oxygen atom pair, $g_{O-O}(r)$, in the silica melt at 7300 K are compared to those obtained after quenching the silica to 300 K at different rates. The silica melt has one broad peak centred on 2.6 Å and there is no long-range order beyond this peak. In contrast, the quenched silica has a more intense first peak as well as a second peak at 5 Å. As the quench rate is decreased these peaks converge, becoming more intense. The minimum at 3.0 Å present in the slower quenches is not present in the $g_{O-O}(r)$ for the 7000 K ps⁻¹ quench so models prepared using this quench rate still retain some characteristics of the melt structure. There is little difference in the shape of $g_{O-O}(r)$ between the 10 K ps⁻¹ quench rate model and the slowest quench (1 K ps⁻¹). Therefore, 10 K ps⁻¹ was found to be an acceptable compromise and the results reported herein are for models prepared using this quench rate.

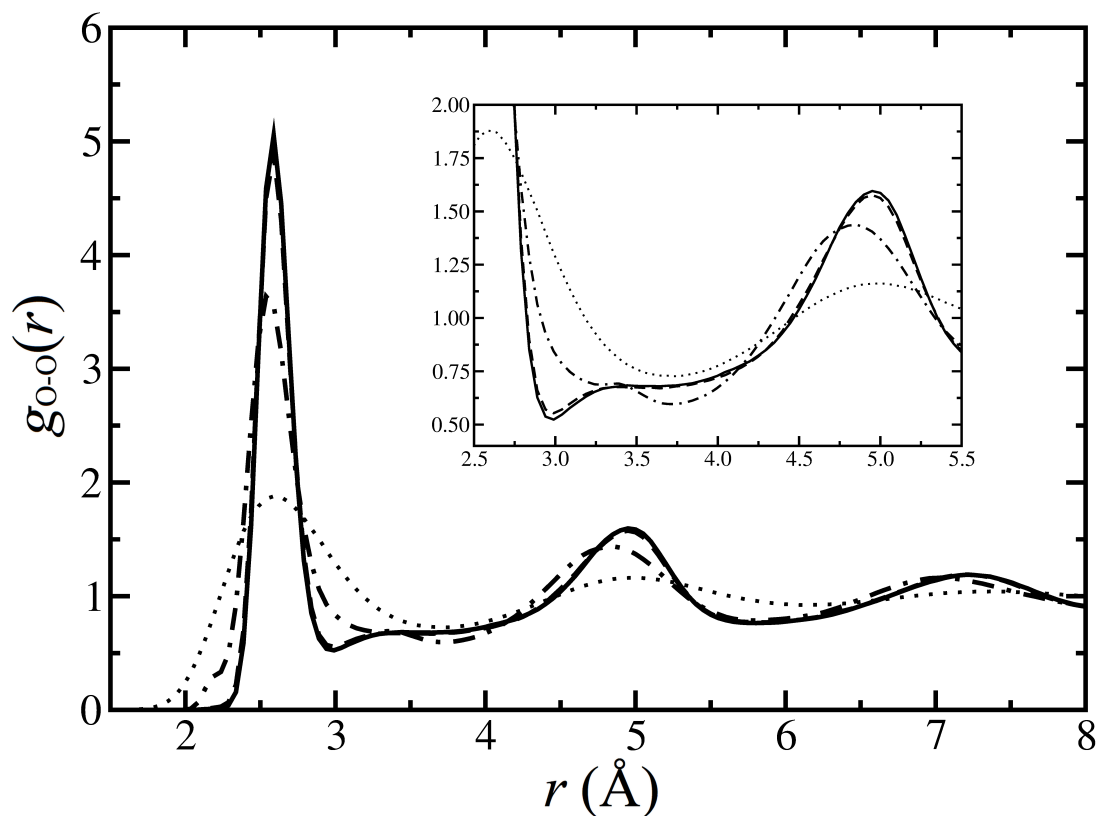


Figure 7.4 $g_{O-O}(r)$ in amorphous silica obtained after quenching from 7300 to 300 K at rates of 1 (solid line), 10 (dashes), and 7000 (dots/dashes) K ps⁻¹ and for the silica melt at 7300 K (dots). Inset: expanded $g_{O-O}(r)$ for the region between 2.5 and 5.5 Å.

Surface Area and Pore Volume

The internal surface area and free volume of each model were estimated using the Connolly method [202] as implemented in Materials Studio. The Connolly surface area is defined by the edge of a spherical probe rolling over the VDW surface of the material and is therefore dependent on the radius of the probe (Figure 7.5). This is different to the solvent accessible surface area approach in which the centre of the spherical probe is used to define the surface area instead [203]. A radius of 1.84 Å was chosen to match the experimental surface areas typically obtained by applying the Brunauer-Emmett-Teller (BET) analysis [204] to N₂ adsorption isotherms. Estimates of the pore diameter and wall thickness were then obtained from the calculated internal volume using simple geometric relations for a cylinder.

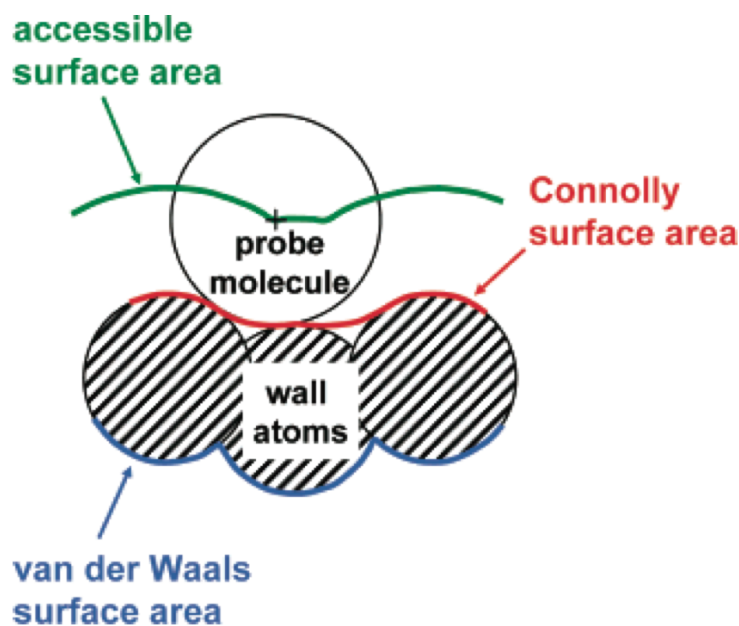


Figure 7.5 The difference between surface areas defined by the solvent accessible and Connolly approaches [203].

For the set of twelve models in which the wall thickness was kept constant (approx. 0.95 nm) the pore diameters ranged from 2.41 to 5.90 nm (Figure 7.6). In this series the calculated surface areas and pore volumes (per gram of MCM-41) were in the range of 979 to 1053 $\text{m}^2 \text{g}^{-1}$ and 0.43 to 0.98 $\text{cm}^3 \text{g}^{-1}$, respectively. The surface areas fall well within the wide range reported in the experimental literature (typically between 950 and 1250 $\text{m}^2 \text{g}^{-1}$). Although the surface area appears to be independent of pore diameter, the pore volume increases dramatically as the pore diameter increases. Experimentally, for an MCM-41 model with a pore diameter of 3.06 nm the pore volume is 1.01 $\text{cm}^3 \text{g}^{-1}$ [192]. Of our models, the one closest in size to this has a pore diameter of 3.16 nm and a pore volume of 0.56 $\text{cm}^3 \text{g}^{-1}$, which represents a significant underestimation of the experimental pore volume. Since this quantity is strongly dependent on the dimensions of the adsorbate molecule, the discrepancy may be due to the unrealistic spherical approximation of the Connolly probe used in these calculations. For the set of models with an approximately constant pore diameter (3.5 nm) the wall thicknesses vary from 0.45 to 1.76 nm. In these models both the surface area (1972 to 427 $\text{m}^2 \text{g}^{-1}$) and pore volume (1.13 to 0.27 $\text{cm}^3 \text{g}^{-1}$) dramatically decrease with wall thickness, although the wall thicknesses at the extreme ends of this range are perhaps unattainable in real MCM-41. For the model with a pore diameter and wall thickness of 3.5 and 0.95 nm, respectively, Figure 7.7 shows how reducing

the quench rate increases the surface area and pore volume. A quench rate slower than 1 K ps^{-1} may be desirable to obtain the most realistic surface, however, it was not computationally feasible to investigate slower quench rates than this.

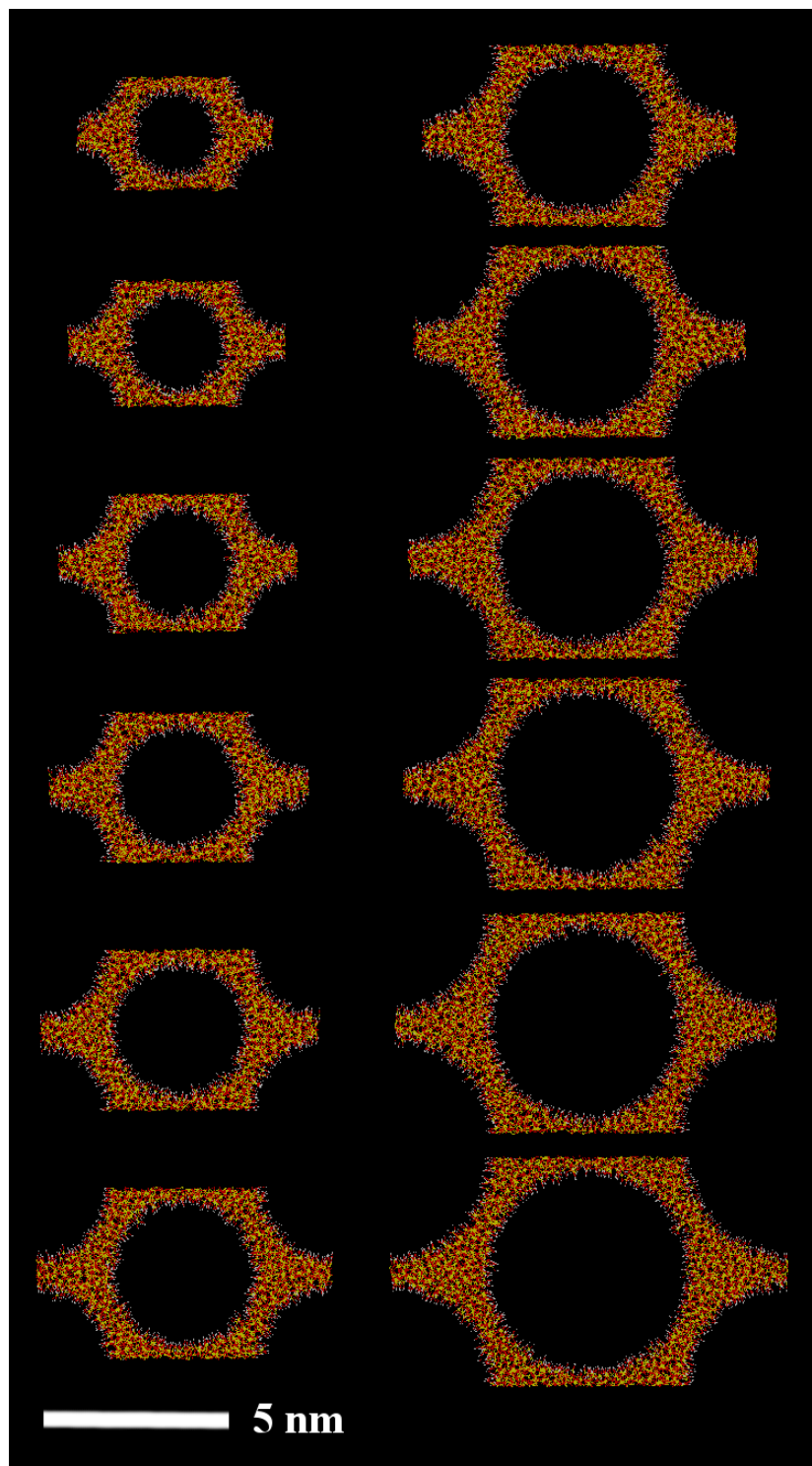


Figure 7.6 MCM-41 models with a wall thickness of 0.95 nm and pore diameters increasing from 2.41 nm (top left) to 5.90 nm (bottom right).

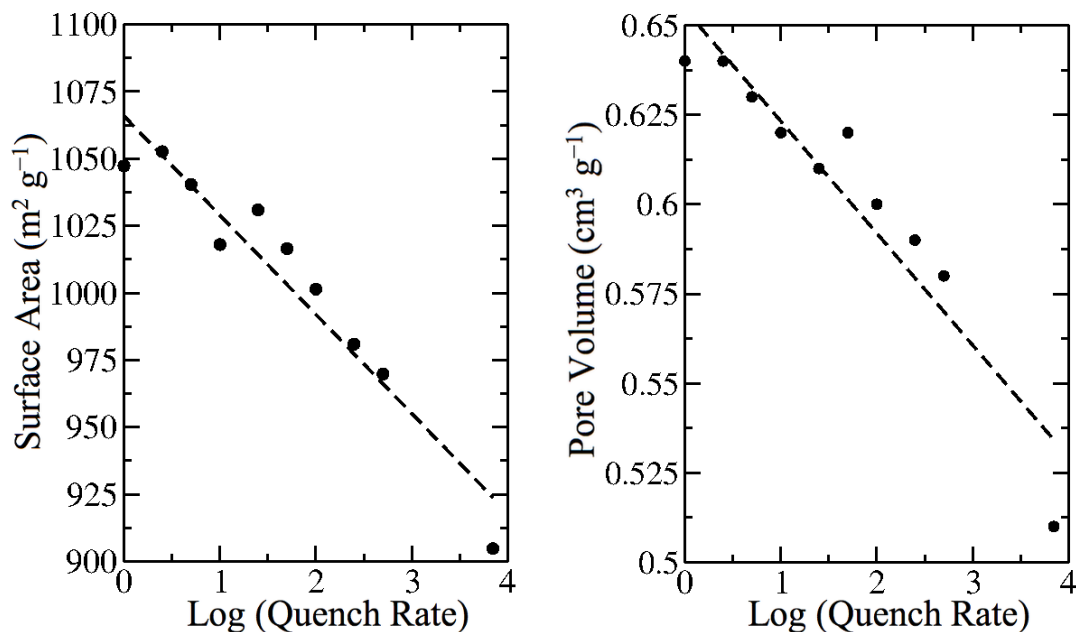


Figure 7.7 The dependence of surface area (left) and pore volume (right) on preparation quench rate for MCM-41 models with 3.5 nm pore diameter and 0.95 nm wall thickness.

Surface Silanols

By averaging over 100 different samples, Zhuravlev [85] concluded that amorphous silica surfaces have a silanol density of 4.9 OH nm^{-2} . This is significantly higher than the density calculated by some other workers (eg. Zhao *et al.*, 3.0 OH nm^{-2} [83]). The wide range reported for amorphous silicas in the experimental literature reflects the different morphologies of samples and experimental conditions of preparation. The surfaces of the amorphous silica models in this work were heterogeneous and consisted of a combination of Q^1 ($\text{SiO}(\text{OH})_3$), Q^2 ($\text{SiO}_2(\text{OH})_2$), Q^3 ($\text{SiO}_3(\text{OH})$) and Q^4 (siloxane) groups.

Our MCM-41 models have a silanol density of 6.17 OH nm^{-2} , averaged over both the varying pore diameter and wall thickness sets of models. The density increases with increased curvature of the pore surface, from 5.9 OH nm^{-2} for the largest pore (5.90 nm) to 7.0 OH nm^{-2} for the narrowest (2.41 nm) in the series of models in which pore diameter is varied. These densities are in good agreement with those reported experimentally for MCM-41 and the related MCM-48 [86]. There is no

evidence that preparing models with a slower quench rate leads to any significant change in silanol density.

7.4 Adsorption Isotherms

Not only is MCM-41 a useful and robust inorganic support in SAMMS, the potential of unfunctionalised MCM-41 as an effective material for gas separation problems has been recognized. This is especially the case for CO₂ removal from where the selectivity and adsorbent capacity of zeolites and activated carbons can be poor in the high temperature conditions encountered in flue gas mixtures [205]. The physical and chemical differences between two gas species may only be very small so changes in the size, shape, interconnectivity and chemical composition of the MCM-41 pores can be exploited to enhance selectivity. As a result there is a large quantity of available experimental adsorption data for CO₂ against which the MCM-41 models can be validated. In this section adsorption isotherms of CO₂ and N₂ are calculated using GCMC simulations and MCM-41 model parameters are optimised to improve agreement with the experimental adsorption isotherms.

7.4.1 Force Field Parameters

Initial parameters for amorphous silica were taken from Brodka *et al.* [206] where bridging, O^b, and non-bridging (ie. those on the surface), O^{nb}, oxygen atoms have different VDW diameters. The dispersion of Si and H can be considered negligible in these materials so they are only represented with partial charges. To obtain a neutral simulation cell q_{Si} was adjusted for each model; Si was chosen as our variable charge as it would be expected that adsorption is less sensitive to changes in the charge of Si than either of O or H. The surface of MCM-41 has an important charge distribution, due to its heterogeneous nature and a high concentration of surface silanol groups. It has been shown previously that an adsorbate model that accounts for this charge distribution is required for an accurate prediction of adsorption of N₂ in MCM-41, particularly at low pressure [207]. Here, the three-site transferrable potential for phase equilibria (TraPPE) models of N₂ and CO₂ (Table 7.2), which have rigid N-N and C-O bond distances of 1.10 and 1.16 Å, were used [208]. This force field is known to accurately predict the phase behaviour and quadrupole moments of these gas molecules. Starting with the Brodka and Zerda [206] value of 228.4 K, a single $\epsilon_{\text{O}}/k_{\text{B}}$

parameter for both types of oxygen was optimised to improve agreement with the experimental CO₂ adsorption isotherm.

| | N ₂ | | CO ₂ | |
|-------------------------|------------------|--------|-----------------|--------|
| | N _{COM} | N | C | O |
| σ_i (Å) | - | 3.310 | 2.800 | 3.050 |
| ε_i/k_B (K) | - | 36.0 | 27.0 | 79.0 |
| q_i (e) | +0.964 | -0.482 | +0.700 | -0.350 |

Table 7.2 TraPPE parameters for CO₂ and N₂ [208, 209].

7.4.2 Grand Canonical Monte Carlo Simulations

In the GCMC simulations, conducted using DL_MONTE [142], the adsorbent is considered frozen whereas the adsorbate molecules undergo random trial moves consisting of centre of mass translations, rotations, insertions and deletions. The internal geometry of the adsorbate was fixed during the simulations. The probabilities of attempting a particular MC move were 0.2 (translation), 0.2 (rotation) and 0.6 (insertion/deletion). Adjustable parameters were used to place a limit on the maximum permitted translation distance and rotation angle in order to maintain a constant ratio of accepting a move to attempting move of 0.37. These limits were recalculated after every 200 accepted moves. The acceptance rate of MC moves is calculated according to the Metropolis rules (Equation 4.59) in which the decision of whether to accept each move is based on the potential energies of the newly generated and previous configurations. Potential energies were evaluated as the sum of the LJ 12-6 potential (Equation 4.30), with cross terms obtained via the Lorentz-Berthelot combining rules, and the electrostatic potential energy (Equation 4.70) determined using the Ewald summation. VDW interactions were spherically truncated at 15 Å. In each simulation, the chemical potential of the adsorbate, μ_i , is imposed and the fluctuating number of molecules allowed to reach equilibrium by performing 10^7 MC moves. Subsequently, the ensemble average number of adsorbate molecules in the system, arising from the insertion and deletion of molecules, is calculated over 4×10^7 moves. A number of these simulations were conducted using closely spaced

values of μ_i in order to generate the adsorption isotherms showing the change in the ensemble average number of adsorbate molecules as a function of pressure, P .

The acceptance rules of the GCMC simulation are a function of μ_i , which can be written as

$$\mu_i = \mu_i^0 + k_B T \ln a_i \quad (7.2)$$

where μ_i^0 is the chemical potential of the standard state. The activity of the gas, a_i , is given by

$$a_i = \frac{f_i}{f_i^0} \quad (7.3)$$

where f_i is the fugacity (or ‘effective’ pressure) of component i , which is related to the true pressure, P_i , by

$$f_i = \gamma_i P_i \quad (7.4)$$

where γ_i is the dimensionless fugacity coefficient. At very low pressure gases become ideal so

$$\lim_{P_i \rightarrow 0} \frac{f_i}{P_i} = 1 \quad (7.5)$$

However, at higher pressure the system departs from ideal behaviour and the difference between f_i and P_i is significant. The value of f_i measured in the simulations was converted to P_i using Equation 7.4, where γ_i was calculated from the Peng-Robinson equation of state using the critical constants ($T_c = 304.1$ K (CO₂) and 126.2 K (N₂), $P_c = 7.38$ MPa (CO₂) and 3.39 MPa (N₂)) and acentric factors (0.239 (CO₂) and 0.039 (N₂)) of the gases [210]. For consistency with typical experimental conditions the CO₂ isotherm was calculated at 265 K and the N₂ isotherm at 77 K.

7.4.3 Carbon Dioxide

The initial parameter set for the amorphous silica results in an underestimation of the amount of CO₂ adsorbed at low pressure (Figure 7.8). The final set of parameters after optimization of ε_O is given in Table 7.3. A number of values for ε_O/k_B have been proposed in the literature ranging from 147 to 230 K [211], in part due to the large

variation in wall thicknesses and surface silanol densities of the real material against which parameters are fitted. It should be noted that the optimised value of ε_O/k_B in this work (300 K) is the largest reported. The overall shape of the simulated isotherm shown in Figure 7.9, calculated with the newly optimised parameters, was in good agreement with the experimental adsorption isotherm, indicating that this MCM-41 model may have both a similar pore diameter and wall thickness to the experimental sample. This corresponds to a model with a mean pore diameter and wall thickness of 3.16 and 0.95 nm. A material with these dimensions is predicted, from the high pressure region of the adsorption isotherm, to have a maximum CO₂ capacity of 13.9 mmol g⁻¹. The adsorption isotherm has a capillary condensation step at intermediate pressure, which is characteristic of mesoporous materials, and is classified as Type IV according to the IUPAC definitions [212]. Although the pressure at which capillary condensation occurs was slightly underestimated there was extremely good agreement between the simulated and experimental isotherms at low pressure (less than 1 atm) and this is the region most sensitive to the fluid-solid potential. The final configurations of the adsorbate molecules in the simulations corresponding to the pressures labelled in Figure 7.9a are shown in Figure 7.10.

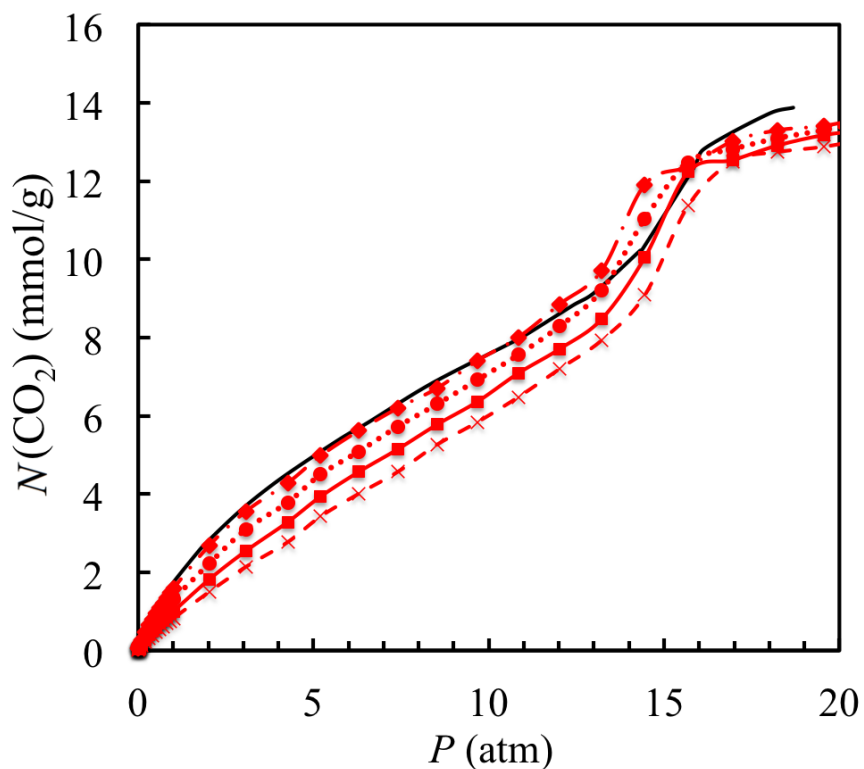


Figure 7.8 Optimisation of ε_0 to fit the simulated (red) CO₂ adsorption isotherm to experiment (black). $\varepsilon_0/k_B = 228.4$ K (dashes), 250 K (solid), 275 K (dots) and 300 K (dashes/dots).

| Parameters | O ^b | O ^{nb} | Si | H |
|-------------------------|----------------|-----------------|---------------|-------|
| σ_i (Å) | 2.70 | 3.00 | - | - |
| ε_i/k_B (K) | 300.0 | 300.0 | - | - |
| q_i (e) | -0.629 | -0.533 | 1.256 - 1.277 | 0.206 |

Table 7.3 Optimised parameters for MCM-41 used in the MC simulations [206].

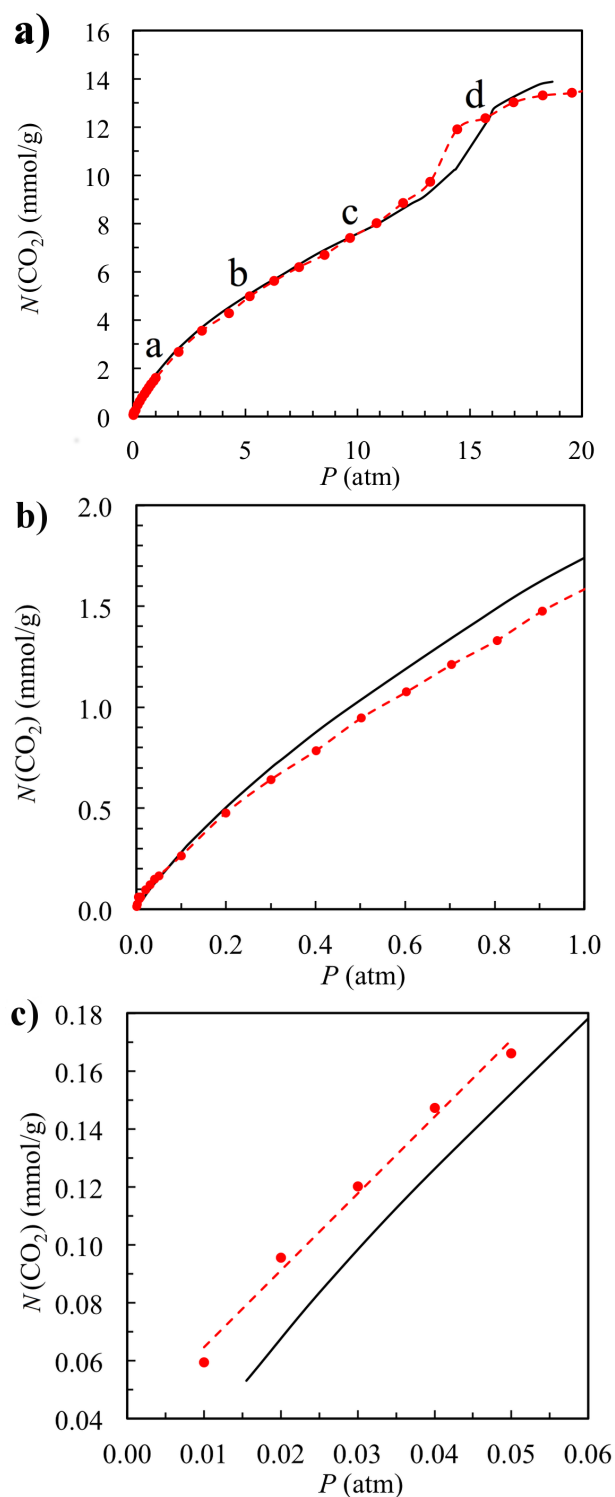


Figure 7.9 Isotherm for CO₂ adsorption to MCM-41 with a pore diameter of 3.16 nm at 265 K for the pressure regions: a) up to the pore filling, b) less than 1 atm and c) the linear region. The solid black line is the experimental data and the red circles indicate the simulated data. The red dashed line through the simulated data is a guide to the eye in a) and b) and a line of best fit in the linear region for c).

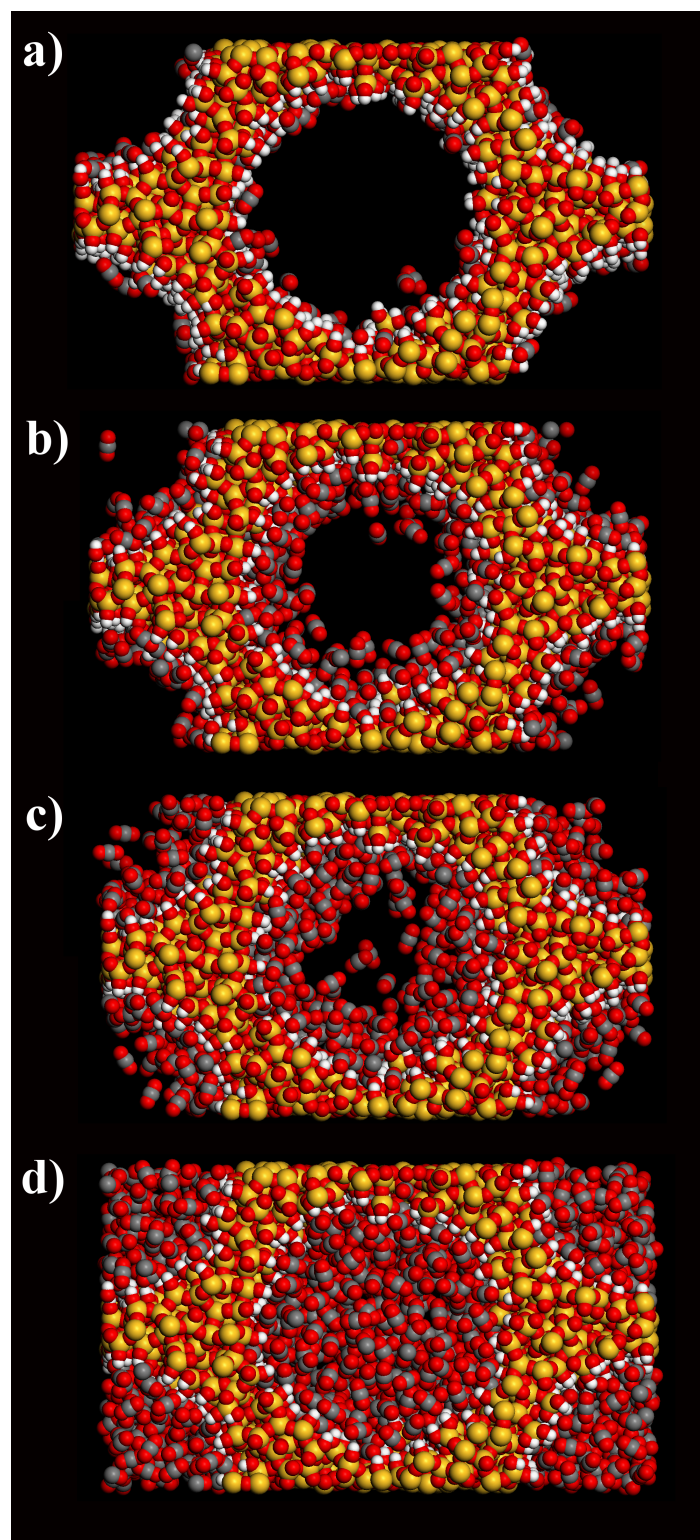


Figure 7.10 Final configurations of GCMC simulations for CO₂ adsorption in MCM-41 at pressures: a) prior to monolayer formation (1 atm), b) on formation of a monolayer (5 atm), c) multilayer formation prior to capillary condensation (10 atm) and d) for the pore approaching its maximum capacity (15 atm).

Figure 7.11 shows the simulated CO₂ adsorption isotherms for some of the narrower pore diameter MCM-41 materials, with pore diameters ranging from 2.41 to 3.85 nm and a constant wall thickness of 0.95 nm. The maximum CO₂ capacities of these models range from 11.1 to 16.7 mmol g⁻¹ and the capillary condensation step occurs at higher pressures and becomes more distinctive as the pore diameter increases. At low and intermediate pressures adsorption is greatest for the models with the smallest pore diameter and largest surface silanol density.

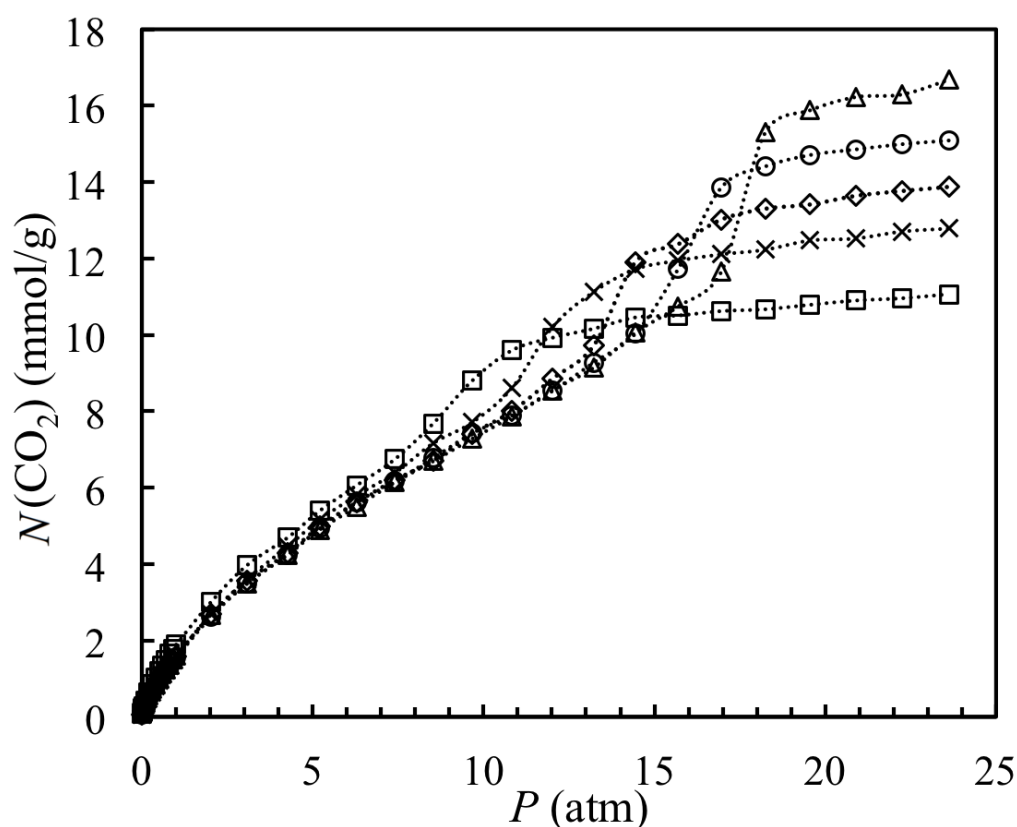


Figure 7.11 Simulated isotherms for adsorption of CO₂ in MCM-41 with pore diameters of 2.41 (squares), 2.81 (crosses), 3.16 (diamonds), 3.50 (circles) and 3.85 (triangles) nm.

7.4.4 Dinitrogen

The shape of the adsorption isotherm for N₂ (Figure 7.12) is in agreement with experiment [189]. The pore filling pressure of N₂ (0.3 atm) is much lower than CO₂ (12 atm) and adsorption at very low pressure is much greater for N₂, which is a result of the N₂ isotherm being obtained at a much lower temperature. At these pressures the

adsorbate molecules lack the sufficient kinetic energy required to escape the potential energy well due to the surface.

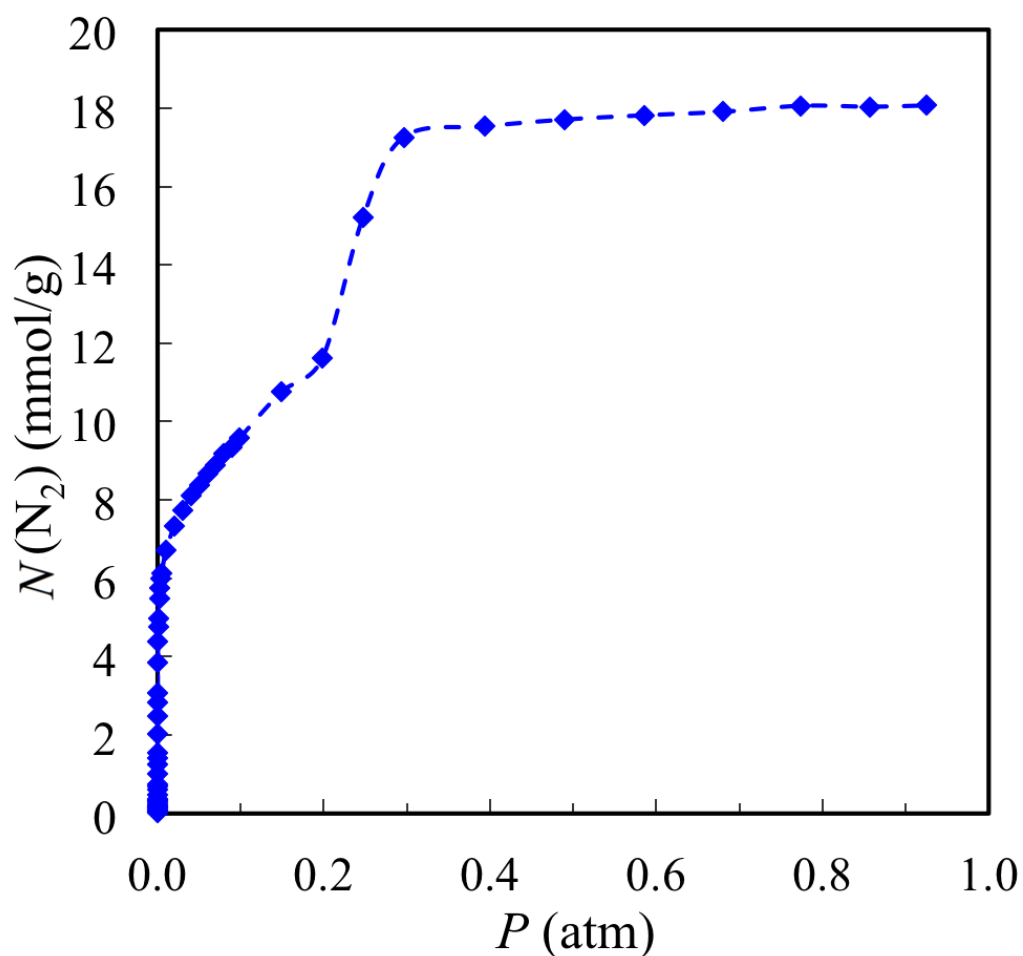


Figure 7.12 Simulated isotherm for adsorption of N_2 in MCM-41 with a pore diameter of 3.16 nm at 77 K.

It should be noted that in the approach taken here the adsorption isotherms yield the absolute number of adsorbate molecules and not the excess number, as is reported in experimental adsorption isotherms [213]. However, the difference between these two definitions is considered negligible in the pressure regions studied.

7.5 Isosteric Heats of Adsorption

The MCM-41 models can be further validated by limiting the study of gas adsorption to the very low pressure region of the isotherm. This region is of particular interest because the adsorption process is largely independent of interactions between adsorbate molecules and therefore extremely sensitive to minor changes in the structure and energetics of the adsorbent. In the absence of interactions with other adsorbate species a single molecule is able to make a completely unhindered exploration of the entire surface of the adsorbent.

The differential enthalpy of adsorption of a fluid is defined as the heat released upon transferring a mole of that fluid from its ideal state to the adsorbed state on a solid surface [214]

$$\Delta H = H_{\text{ads}} - H_{\text{g}} \quad (7.6)$$

where the H_{ads} and H_{g} are the enthalpies of the adsorbed and ideal states. The enthalpies of the two states can be defined in terms of their internal energies, U_{ads} and U_{g} , by the equations

$$H_{\text{g}} = U_{\text{g}} + RT \quad H_{\text{ads}} \approx U_{\text{ads}} \quad (7.7)$$

since the volume of the adsorbed phase is negligible compared to the volume of the ideal gas. The isosteric heat of adsorption, q_{st} , is defined as the negative of the difference in enthalpy

$$q_{\text{st}} = -\Delta H \quad (7.8)$$

and can therefore be obtained in terms of the internal energies of the two states by substitution of Equation 7.7 into Equation 7.8, yielding

$$q_{\text{st}} = U_{\text{g}} - U_{\text{ads}} + RT \quad (7.9)$$

The isosteric heat of adsorption can simply be written as

$$q_{\text{st}} = RT - \Delta U \quad (7.10)$$

where ΔU is change in internal energy.

7.5.1 Adsorption at Zero Coverage

For materials with a heterogeneous surface such as MCM-41 the isosteric heat would be expected to rapidly decrease as a function of adsorbate loading from its initially large value at very low pressure (or ‘zero coverage’) as the most attractive surface sites become occupied with adsorbate atoms or molecules. The isosteric heat of adsorption at zero coverage, q_{st}^0 , is given by

$$q_{st}^0 = \lim_{P \rightarrow 0} q_{st} \quad (7.11)$$

and the Henry law constant is defined by the slope of the adsorption isotherm in this pressure region

$$K_H = \lim_{P \rightarrow 0} \frac{N}{P} \quad (7.12)$$

where N is the amount adsorbed. Equations 7.11 and 7.12 can be used to characterise adsorption in the very low pressure region of the isotherm for a given adsorbate and adsorbent. Neither can be obtained easily from experiment because of the practical difficulties associated with studying adsorption in porous materials at such low pressures.

7.5.2 Development of a Monte Carlo Algorithm

A MC algorithm was used to investigate the adsorption of simple gases to MCM-41 at zero coverage. In this algorithm a single adsorbate molecule was randomly translated and rotated within the simulation cell to compute Z_{NVT} and the ensemble average of U using Equations 4.56 and 4.57. Since there is only one adsorbate molecule in the simulation U is purely dependent on the interaction potential between the adsorbate and the MCM-41 atoms, which was evaluated with the same parameters and potential energy function as those used in the GCMC simulations in Section 7.4.1. The isosteric heat at zero coverage for the adsorbate was then obtained from the simulation using

$$q_{st}^0 = k_B T - \langle U \rangle \quad (7.13)$$

and K_H determined using the relation [215]

$$K_H = \frac{1}{A} \left(\frac{Z_{NVT}}{k_B T} \right) \quad (7.14)$$

where A is the surface area of the MCM-41 surface. In order to make the calculated values of K_H directly comparable with those typically reported in experiments it was multiplied by the volume of the simulation cell. The simulation continued until q_{st}^0 converged to within 1.0 J mol^{-1} over 10^7 MC moves. Due to the amorphous nature of the material it is possible for the adsorbate to be randomly inserted into energetically favourable yet physically inaccessible positions. To avoid these configurations being incorporated into the Boltzmann weighted average any inserted particle that has a local density of MCM-41 atoms representative of the bulk solid (Figure 7.13) is immediately rejected. The maximum permitted number of oxygen atoms, N_O , within a 5.0 \AA radius of the inserted adsorbate molecule was set to 30.

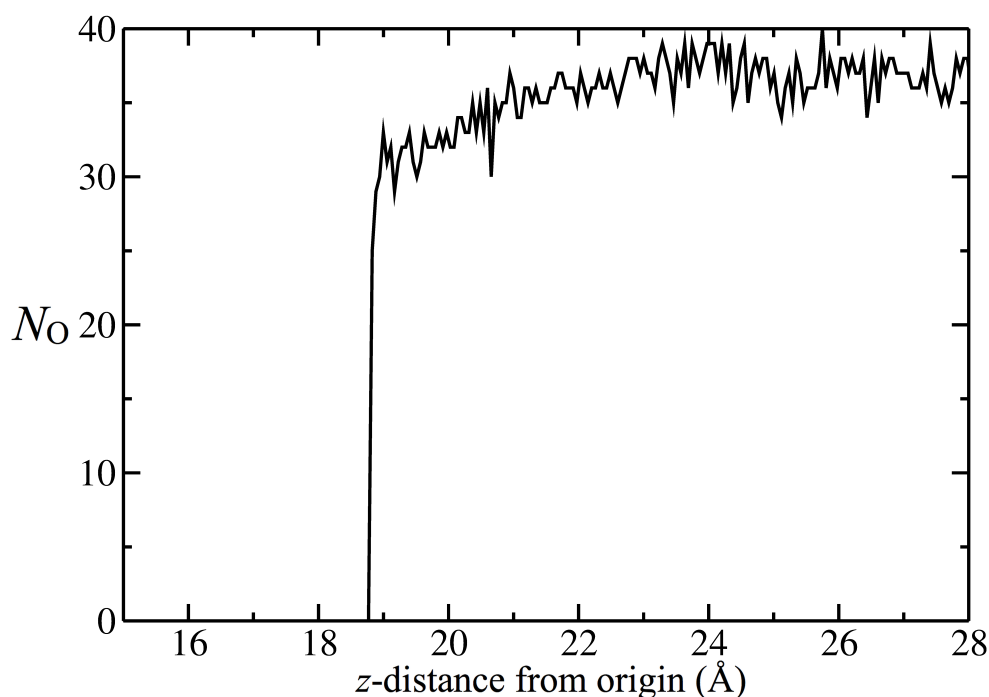


Figure 7.13 Density profile for oxygen atoms, N_O , within a 5.0 \AA radius of atom i in an MCM-41 model.

Validation of the Ewald Sum

In the MC algorithm, the electrostatic component of the interaction potential between the adsorbate and MCM-41 was calculated using the Ewald sum. In order to validate

the implementation of the Ewald sum the electrostatic potential energy of the 3.16 nm pore diameter MCM-41 model was calculated and Table 7.4 compares this with energies obtained from DL_POLY Classic [141]. The initial calculation was performed using the DL_POLY Classic optimised Ewald parameters; $\alpha = 0.3208 \text{ \AA}^{-1}$, $k_{\max} = 23, 13$ and 15 in the x, y and z dimensions and a real space cut off of 15 \AA . α was then varied either side of the optimised value to check agreement with DL_POLY Classic. Using these parameters the relative errors between the zero coverage program and DL_POLY Classic were no greater than 0.03% . Table 7.4 shows how the relative real (V_N^{real}) and reciprocal space ($V_N^{\text{recip}} + V_N^{\text{self}}$) contributions to the overall electrostatic energy change with α . When α is small V_N^{elec} is dominated by the real space sum and when α is large the energy is dominated by the reciprocal space sum. Since the choice of α in the Ewald sum must be arbitrary, if both the real and reciprocal space contributions are correctly converging, a plot of V_N^{elec} against α (Figure 7.14) should show a plateau around the optimised value of α . Divergence of V_N^{elec} either side of the stable region of α is due to poor convergence of the Ewald sum. If α is too large the Ewald sum will slowly converge, requiring a prohibitive number of reciprocal lattice vectors; if it is too small, the Ewald sum has no contribution from reciprocal space and effectively reduces to a Coulomb sum, which is conditionally convergent. Due to the scaling of q_{Si} to neutralize the MCM-41 models the Fuchs correction was equal to zero in this example. A second plot of V_N^{elec} of MCM-41 against α (Figure 7.15) corresponds to the case where the material is fully deprotonated. In this calculation the simulation cell has an overall negative charge and the plot shows the importance of using the Fuchs correction, V_N^{neut} , in avoiding the spurious build up of background charge, particularly when a small α parameter is used.

The final step taken to validate the Ewald sum was to compute the Madelung constant for sodium chloride using the equation

$$\frac{V_N^{\text{elec}}}{N} = -\frac{M|z_i z_j|}{L/2} \quad (7.15)$$

where M is the Madelung constant, N is the number of ion pairs and $L/2$ is the lattice parameter. The program correctly computed M (1.748) for a 2.184 nm^3 sodium chloride crystal with $\alpha = 0.4119 \text{ \AA}^{-1}$ and $k_{\max} = 7$, in each direction.

| α (\AA^{-1}) | V_N^{real} (10^6 kJ mol^{-1}) | $V_N^{\text{recip}} + V_N^{\text{self}}$ (10^6 kJ mol^{-1}) | V_N^{elec} (10^6 kJ mol^{-1}) | V_N^{elec} (DL_POLY) (10^6 kJ mol^{-1}) | Error (%) |
|-----------------------------------|---|--|---|--|--------------|
| 0.050 | -1.7689 | -0.1169 | -1.8858 | -1.8862 | 0.02 |
| 0.100 | -1.6607 | -0.2336 | -1.8943 | -1.8947 | 0.02 |
| 0.200 | -1.4286 | -0.4669 | -1.8955 | -1.8960 | 0.03 |
| 0.300 | -1.1957 | -0.6998 | -1.8955 | -1.8960 | 0.03 |
| 0.321 | -1.1475 | -0.7481 | -1.8955 | -1.8960 | 0.03 |
| 0.350 | -1.0800 | -0.8155 | -1.8955 | -1.8960 | 0.03 |
| 0.500 | -0.7434 | -1.1551 | -1.8984 | -1.8989 | 0.03 |
| 1.000 | -0.0907 | -2.2396 | -2.3303 | -2.3308 | 0.02 |
| 2.000 | -0.0006 | -4.5008 | -4.5014 | -4.5024 | 0.02 |

Table 7.4 The relative contributions to the Ewald sum and a comparison of the total sum with DL_POLY Classic using the 3.16 nm pore diameter MCM-41 model.

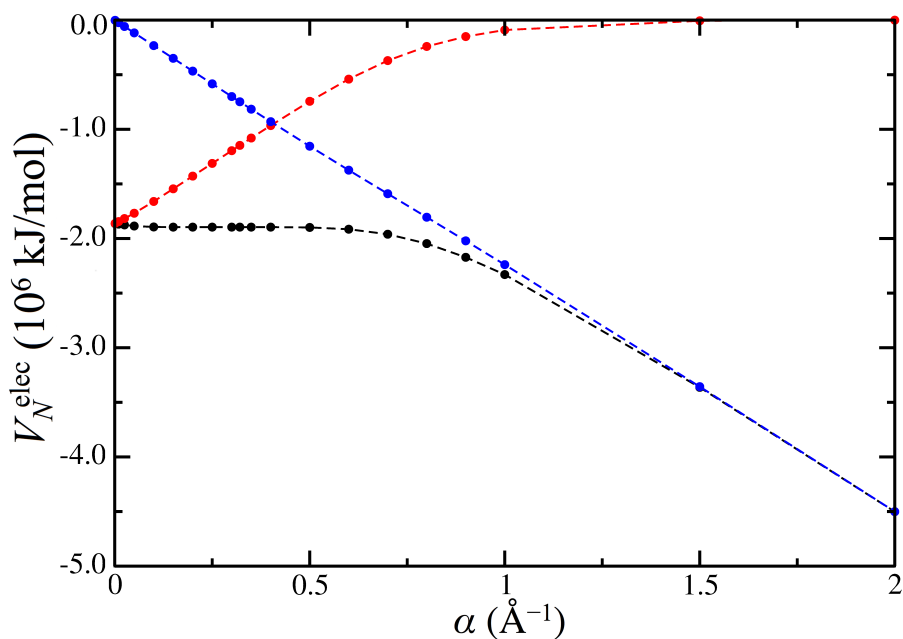


Figure 7.14 V_N^{real} (red) and $V_N^{\text{recip}} + V_N^{\text{self}}$ (blue) contributions to the overall energy V_N^{elec} (black) as a function of α in the Ewald summation for the electrostatic energy of the neutral 3.16 nm pore diameter and 0.95 nm wall thickness MCM-41 model.

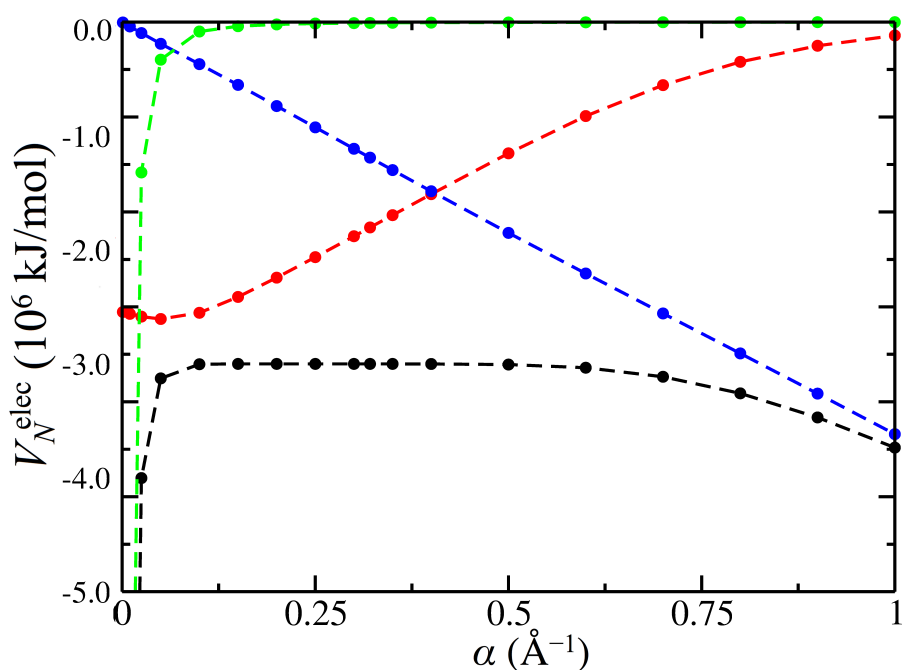


Figure 7.15 V_N^{real} (red), $V_N^{\text{recip}} + V_N^{\text{self}}$ (blue) and V_N^{neut} (green) contributions to the overall energy V_N^{elec} (black) as a function of α in the Ewald summation for the electrostatic energy of the deprotonated 3.16 nm pore diameter MCM-41 model.

Tabulation of the Ewald Sum

Since the MC algorithm involved random sampling rather than Metropolis sampling somewhere in the region of 10^8 to 10^{10} MC moves were required for convergence of a single calculation. Evaluation of the Ewald summation was only made feasible by pre-tabulating the electrostatic potential due to the adsorbent, $\phi_{\text{elec}}(\mathbf{r})$, on a grid; from which the electrostatic potential energy could be determined by 3D linear interpolation.

$$V_N^{\text{elec}}(\mathbf{r}) = z_i \phi_{\text{elec}}(\mathbf{r}) \quad (7.16)$$

The values of q_{st}^0 obtained from simulations in which the potential was tabulated at different resolutions were compared to a simulation where the Ewald sum is calculated at every new configuration (Figure 7.16). A grid spacing smaller than 0.2 \AA was found to give errors in q_{st}^0 of less than 0.2 kJ mol^{-1} but there appeared to be little further improvement for finer grids than this. As a result, the maximum spacing of the tabulated electrostatic potential in the simulations was set to 0.2 \AA .

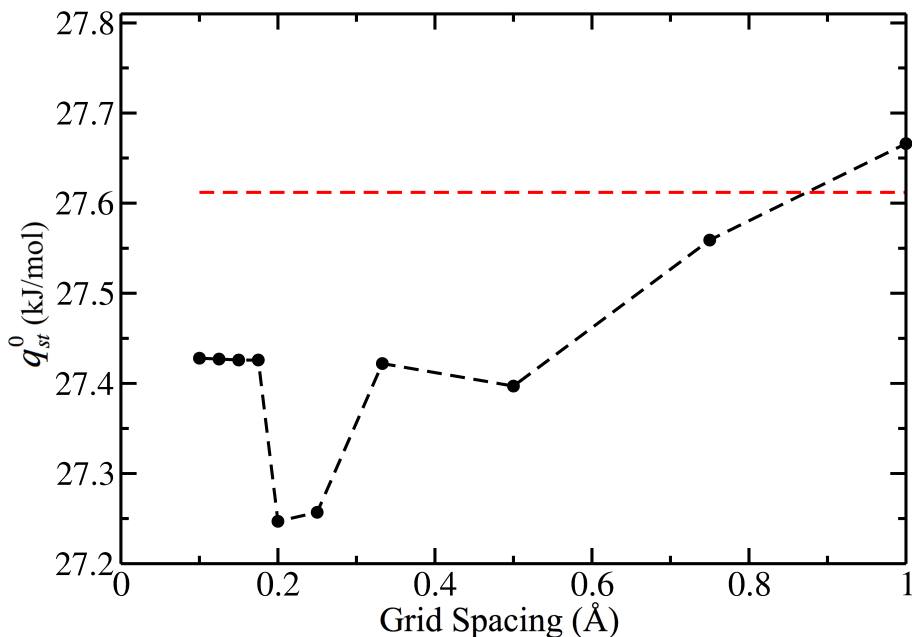


Figure 7.16 q_{st}^0 obtained from a calculation of CO_2 in MCM-41 (pore diameter = 3.5 nm) using the Ewald potential tabulated at different grid resolutions (black) compared to the value obtained for the computation of the Ewald sum at every new configuration (red).

7.5.3 Isothermic Heats of Adsorption in Amorphous Silica

Using the newly optimised MCM-41 parameters the effect of preparation quench rate, pore diameter and wall thickness on q_{st}^0 and K_H for each of four gases (CO_2 , N_2 , Kr and Ar) was investigated. Two of these have a quadrupole moment (CO_2 and N_2) and are modelled using the TraPPE parameters in Table 7.3 because they are likely to be sensitive to the charge distribution of the surface. The other two (Kr and Ar) are modelled using a single LJ site. The importance of using CO_2 and N_2 models with a charge distribution was investigated by also performing calculations using single-site CO_2 and N_2 models. The parameters for single site adsorbate models are given in Table 7.5.

| Parameters | N_2 | CO_2 | Ar | Kr |
|-------------------------|--------------|---------------|-------|-------|
| σ_i (Å) | 3.798 | 3.941 | 3.405 | 3.636 |
| ε_i/k_B (K) | 71.4 | 195.2 | 119.8 | 166.4 |

Table 7.5 Parameters for single-site models of the gas adsorbate species [209, 216].

MCM-41

It was first necessary to investigate the variation of q_{st}^0 for the models prepared at different quench rates (all of which have approximately the same pore diameter (3.5 nm) and wall thickness (0.95 nm)). Figure 7.17 shows that for very fast quench rates q_{st}^0 fluctuates and this is more pronounced for gases with a larger q_{st}^0 such as CO_2 . The fluctuations are a result of a quench rate that is too fast generating an unrealistic configuration of atoms on the surface of MCM-41. As the quench rate is decreased q_{st}^0 starts to converge, however, a compromise must be reached between obtaining a realistic structure and the speed at which the MCM-41 models can be prepared.

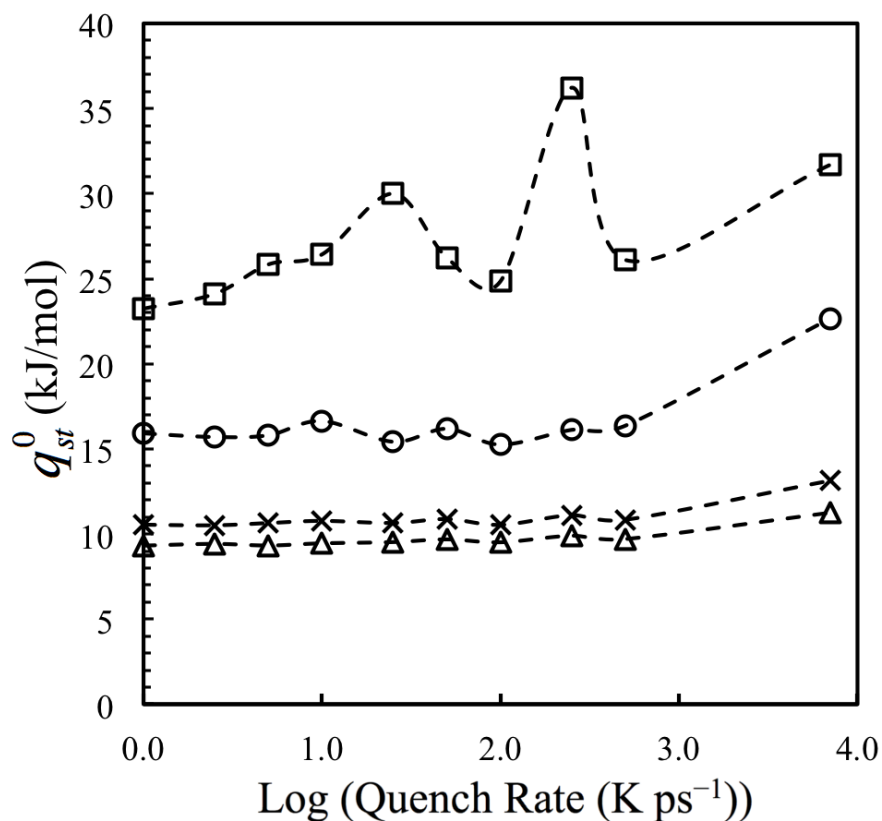


Figure 7.17 The convergence of q_{st}^0 with decreasing quench rate for CO₂ (squares), Kr (circles), Ar (crosses) and N₂ (triangles) in MCM-41. The dashed lines are added as a guide to the eye.

The values q_{st}^0 and K_H for each adsorbate, averaged over all pore diameters at a constant wall thickness, are given in Table 7.6. The average q_{st}^0 for CO₂ was found to be 26.5 kJ mol⁻¹, in approximate agreement with experimental value (32 kJ mol⁻¹) [104]. We believe the slight under prediction is due to the fact that the real material may have a small number of surface irregularities and exposed Si atoms that would result in an increase in q_{st}^0 . Irregularities are thought to be uncommon in MCM-41 so much larger models would be required to incorporate a realistic concentration of them. The average for CO₂ is much larger than for N₂, Ar and Kr and demonstrates that at very low pressures CO₂ preferentially adsorbs to MCM-41 over these other gases.

| Adsorbate | q_{st}^0 kJ mol ⁻¹ | K_H (mmol g ⁻¹ atm ⁻¹) |
|-----------------|------------------------------------|--|
| CO ₂ | 26.5 | 0.93 |
| N ₂ | 9.1 | 0.10 |
| Ar | 10.5 | 0.12 |
| Kr | 16.4 | 0.31 |

Table 7.6 q_{st}^0 and K_H in MCM-41, averaged over 12 models with pore diameters ranging from 2.41 to 5.90 nm and a pore wall thickness of 0.95 nm.

The variation in q_{st}^0 and K_H with pore diameter was investigated at 298 K (Figure 7.18). For adsorbates with a small q_{st}^0 there is a trend of increasing q_{st}^0 as the pore diameter decreases, which has been observed previously during experimental studies of N₂ and Ar adsorption [80]. This geometrical effect is due to the increased curvature (and therefore higher density of silanols on the surface) in narrower pore models and is most pronounced in the case of N₂, where q_{st}^0 increases from 8.4 kJ mol⁻¹ for a material with a pore diameter of 5.90 nm to 10.6 kJ mol⁻¹ for 2.41 nm pore diameter. For adsorbates with a larger q_{st}^0 (Kr and CO₂), the trend of increasing q_{st}^0 due to narrower pores and increased silanol density is not seen. The isosteric heat for these adsorbates is much more sensitive to the extent of surface heterogeneity and the specific configuration of atoms at the surface. No trend was observed for K_H in models with different pore diameters for any of the adsorbates studied.

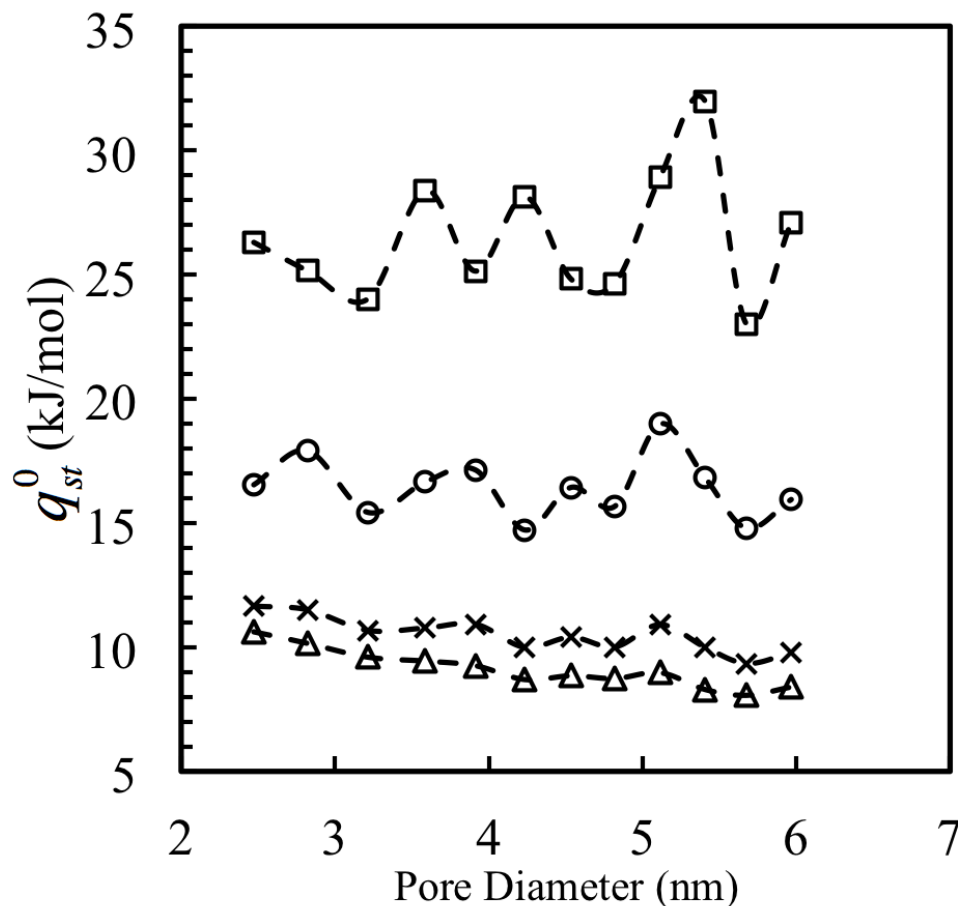


Figure 7.18 The relationship between q_{st}^0 and pore diameter for the four adsorbates studied; CO₂ (squares), Kr (circles), Ar (crosses) and N₂ (triangles), at 298 K in a MCM-41 model with pore walls of 0.95 nm thickness.

MCM-41 materials with thick pore walls are known to have greater thermal and hydrothermal stability than those with thin walls [82]. For the five models with different pore wall thicknesses (ranging from 0.45 to 1.76 nm) no trend in q_{st}^0 was observed. In contrast to the pore diameter independence of K_H this quantity decreases rapidly from a model with 0.45 nm walls ($1.532 \text{ mmol g}^{-1} \text{ atm}^{-1}$) to one with 1.76 nm walls ($0.480 \text{ mmol g}^{-1} \text{ atm}^{-1}$) for CO₂. Although the total internal surface area of these models are roughly similar the difference is a result of the decreasing surface area per mass unit of the material, decreasing from $1018 \text{ m}^2 \text{ g}^{-1}$ for 0.95 nm walls to $428 \text{ m}^2 \text{ g}^{-1}$ for 1.76 nm walls.

As well as using Equation 7.14, K_H can be estimated from the linear, vanishing pressure part of the adsorption isotherms (less than 0.05 atm in the case of Figure

7.9c, for CO₂). In order to facilitate comparison between the two approaches, separate MC calculations were performed using the same MCM-41 model as was used to generate the isotherms in Section 7.4, at 265 K (CO₂) and 77 K (N₂). There was approximate agreement between these two approaches. For CO₂, K_H was 2.81 mmol g⁻¹ atm⁻¹ (from Equation 7.14) compared to 2.65 mmol g⁻¹ atm⁻¹ (from the isotherm). For N₂, K_H was 1.0×10^8 mmol g⁻¹ atm⁻¹ (from Equation 7.14), compared to 5.7×10^7 mmol g⁻¹ atm⁻¹ (from the isotherm). The differences are due to a poor prediction from the isotherms due to large fluctuations in the number of particles resulting in significant uncertainties in the amount of gas adsorbed in the very low pressure region. This also highlights the problem encountered in estimating K_H experimentally by extrapolation from adsorption isotherms. In general, CO₂ prefers to adsorb perpendicular to the surface, where the most favourable adsorption sites (Figure 7.20) correspond to end-on adsorption in small pockets that are a result of the heterogeneous and rough nature of the surface.

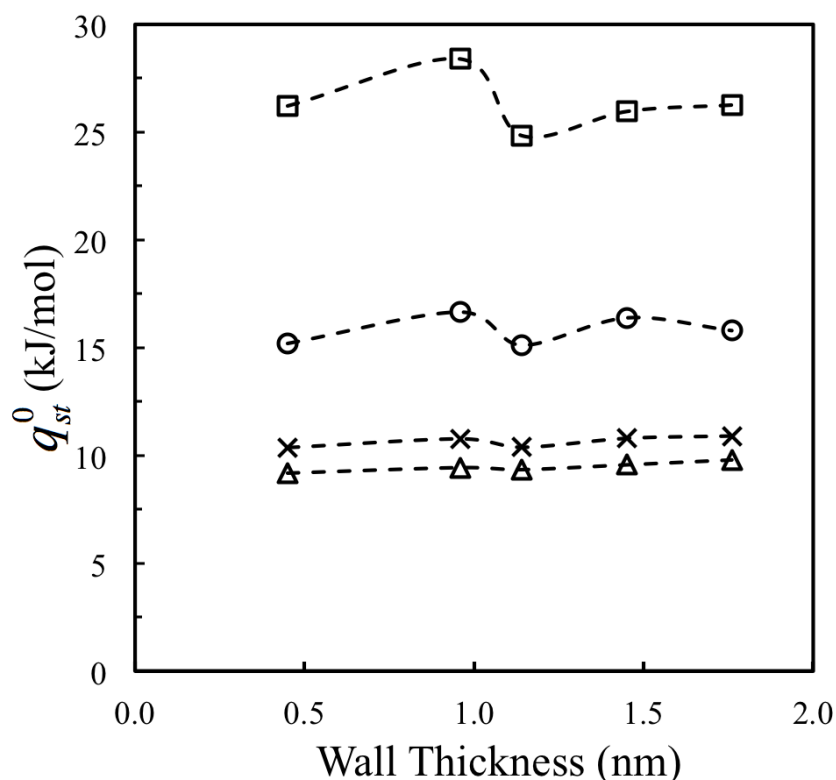


Figure 7.19 The effect of MCM-41 model wall thickness on q_{st}^0 for the four adsorbates studied; CO₂ (squares), Kr (circles), Ar (crosses) and N₂ (triangles), at 298 K for models with a constant pore diameter of 3.5 nm.

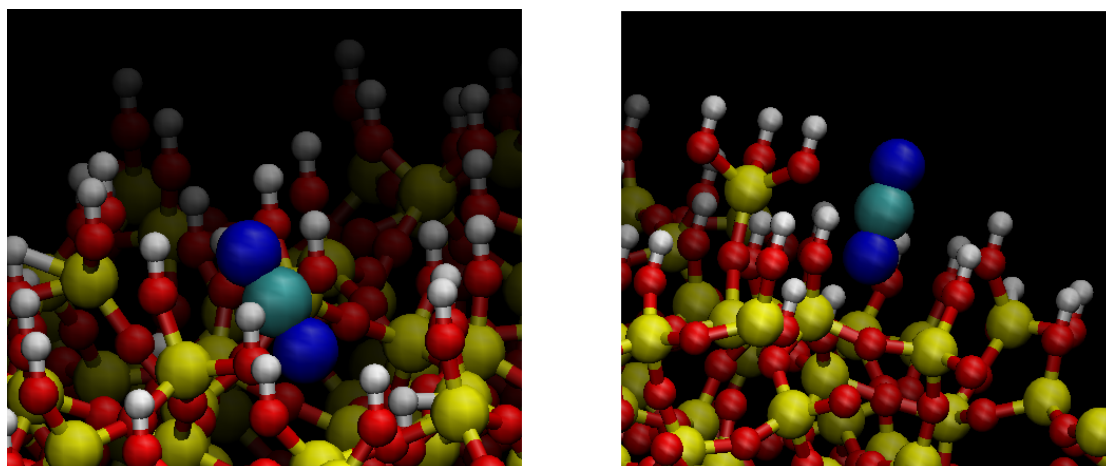


Figure 7.20 Favourable end-on adsorption of CO₂ on the amorphous silica surface.

The results for adsorption of CO₂ and N₂, modelled using the single-site model parameters in Table 7.5, are shown in Table 7.7. For these models q_{st}^0 was calculated to be 28.0 and 9.2 kJ mol⁻¹ for CO₂ and N₂. For the three-site TraPPE models these values were larger (28.4 and 9.4 kJ mol⁻¹). Although adsorption is slightly under predicted using the simplified single-site CO₂ and N₂ models the difference from the models with a charge distribution is not significant, indicating that the costly Ewald summation can be avoided if only an approximate calculation of q_{st}^0 is required.

| Adsorbate | q_{st}^0 (kJ mol ⁻¹) | K_H (mmol g ⁻¹ atm ⁻¹) |
|-----------------|---------------------------------------|--|
| CO ₂ | 28.0 | 1.421 |
| N ₂ | 9.2 | 0.067 |

Table 7.7 Adsorption data for CO₂ and N₂ in MCM-41 with a pore diameter of 3.5 nm and wall thickness of 0.95 nm at 298 K.

Adsorption in a Slit-Pore

To enable comparison of the curved pore surface in MCM-41 with a flat surface (in order to mimic MCM-41 in the large pore limit, which would otherwise require a very large simulation cell) a slit-pore model was constructed. This was prepared according to exactly the same procedure as the MCM-41 models but by carving out a

rectangular slit instead of a cylindrical one (as shown in Figure 7.2b) with an approximate pore diameter of 3.5 nm. The slit-pore model is shown in Figure 7.21. The density of silanols on the slit pore surface is 5.0 OH nm^{-2} , in excellent agreement with Zhuravlev's observations [85]. This is much lower than the density in MCM-41 models, which ranges from 7.0 to 5.9 OH nm^{-2} in our models. q_{st}^0 and K_{H} were also calculated for each of the adsorbate molecules in the slit-pore model to establish the effects of surface curvature (Table 7.8). The isosteric heats calculated for CO_2 and N_2 in the slit pore were 23.7 and 6.8 kJ mol^{-1} , respectively, which are much lower than in MCM-41, and adsorption of these species therefore appears to be sensitive to the surface silanol density. For the spherical adsorbates q_{st}^0 did not decrease in the slit pore ($q_{\text{st}}^0(\text{Ar}) = 11.5 \text{ kJ mol}^{-1}$ and $q_{\text{st}}^0(\text{Kr}) = 18.4 \text{ kJ mol}^{-1}$ compared to MCM-41 and are therefore insensitive to changes in surface silanol density.

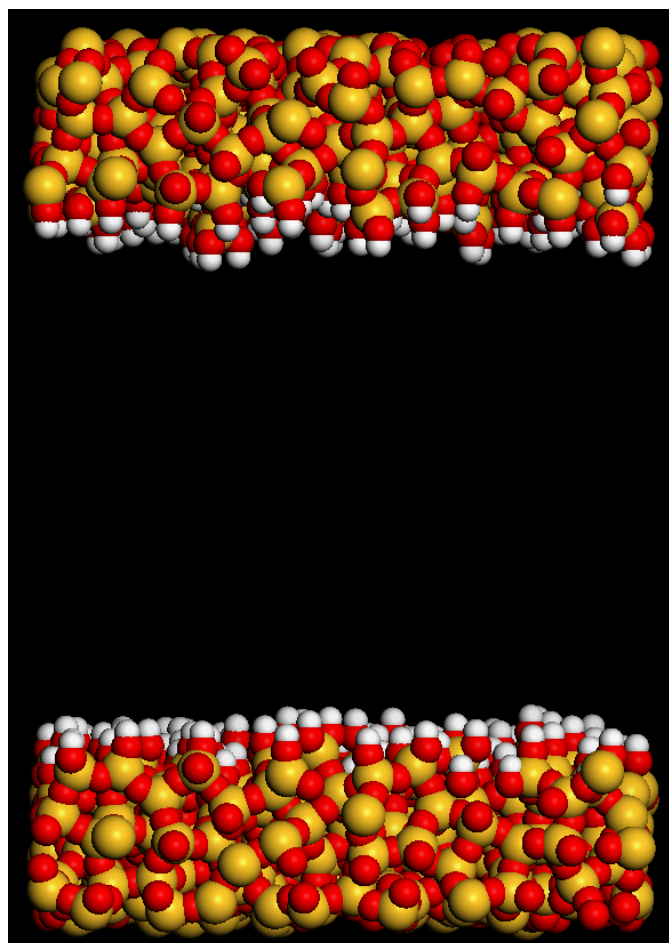


Figure 7.21 The slit-pore model with a diameter of 3.5 nm.

| Adsorbate | q_{st}^0 (kJ mol ⁻¹) | K_H (mmol g ⁻¹ atm ⁻¹) |
|-----------------|---------------------------------------|--|
| CO ₂ | 23.7 | 0.332 |
| N ₂ | 6.8 | 0.057 |
| Ar | 11.5 | 0.106 |
| Kr | 18.4 | 0.297 |

Table 7.8 q_{st}^0 and K_H for each adsorbate in the amorphous silica slit-pore at 298 K.

7.6 Conclusions

In general, it was predicted that optimum adsorption of simple gas species to MCM-41 materials (large q_{st}^0 and K_H) at low pressure can be achieved with narrow pore diameters in agreement with experiment [80], although this trend is not obvious in the case of CO₂ and Kr. Henry law constants were predicted using two approaches; firstly by determining the gradient of the adsorption isotherm in the linear regions, and secondly using Equation 7.14, involving a simulation in which a single adsorbate molecule that was allowed to make a free and unhindered exploration of the adsorbent model surface. The two methods were in good agreement for CO₂ resulting in Henry law constants of 2.65 and 2.81 mmol g⁻¹ atm⁻¹, respectively.

Models could be built with a slower and more realistic quench rate, but this would require a simulation timescale inaccessible to conventional molecular simulation. Another improvement could be made to our model by accounting more accurately for adsorbate-adsorbent interactions by abandoning the simple Lennard-Jones 12-6 potential and instead adopting a more complex form that includes induction effects such as the PN-TrAZ potential [217]. However, using the approach in this chapter, quench rates of less than 10 K ps⁻¹ result in models that predict the CO₂ adsorption isotherm and isosteric heat (26.5 kJ mol⁻¹) at zero coverage to a reasonable degree of accuracy.

Although adsorption of TcO_4^- to SAMMS is a chemical adsorption process, the MCM-41 model parameters were validated against experimental data for CO_2 physical adsorption to the bare material. The approach in which the MCM-41 model was constructed enables easy alteration of the pore diameter and wall thickness for a variety of applications such as the inorganic support in SAMMS. Validation of the model structure at very low pressure is advantageous because this is the region most sensitive to the adsorbent potential. The MCM-41 force field parameters optimised in this chapter can be used in the simulations of the final SAMMS model.

Chapter Eight

Functionalised MCM-41

8.1 Introduction

The relative affinities of TcO_4^- and SO_4^{2-} for the Fe^{3+} -EDA complexes in aqueous solution were established in Chapter Six. The results showed that the divalent SO_4^{2-} has the potential to inhibit adsorption of TcO_4^- . However, experiments have shown that oxyanion-SAMMS are selective for various monovalent oxyanions over SO_4^{2-} . Chapter Six does not attempt to account for the effects of porous confinement or the presence of the amorphous silica surface and this may be the cause of the discrepancy between the results reported in that chapter and the experiments of Yoshitake *et al.* [106]. In this chapter, models of functionalised amorphous silica, similar to the materials used in those experiments, are prepared. The monolayer structures are investigated using MD simulations and PMFs are generated to establish the preference of the two competing oxyanions for the pore. Finally, we attempt to rationalise the selectivity shown in the PMFs; firstly by calculating the electrostatic potential in the pore, and secondly by investigating oxyanion dehydration on entering the pore.

8.2 Previous Models of Functionalised MCM-41

No models of functionalised porous amorphous silica materials for use in an aqueous environment have previously been reported. One challenge of modelling materials of this type is the poor availability of general transferable force fields that can simultaneously describe both the inorganic and organic components of the material. In addition the nature of the monolayer is not well understood due to the difficulties of probing porous materials using conventional experimental techniques. A limited number of models have been prepared for gas adsorption applications, in particular, CO_2 separation. It has been shown experimentally that the capacity and selectivity of amino-functionalised MCM-41 is greatly enhanced compared to the bare material, due to the affinity between the mildly acidic CO_2 and the basic NH_2 .

Chaffee [218] constructed the first atomistic model of functionalised MCM-41 by swapping tri-methoxyaminopropyl groups for the surface silanols that resulted in the greatest energy relief, until a density of 1.5 tethers nm^{-2} was achieved [106]. He noted that obtaining a very high monolayer density was not possible, due to the fact that once an organic chain had been added, the chain lies flat, due to the formation of hydrogen bonds between the organic amines and surface silanols, therefore blocking the access of subsequent chains. This observation helps to explain why these materials have monolayer densities much lower than the theoretical maximum (ie. the density of silanols) and consequently much lower CO_2 adsorption capacities than expected. Schumacher *et al.* [219] constructed a model of MCM-41 functionalised with phenyl and amino groups. The functionalities were added to the surface by randomly exchanging the surface silanols for organic chains disregarding steric hindrance. They then used a MC scheme to swap the chains to more energetically favourable sites, until a local minimum was found, attaining a more realistic distribution for the monolayer. The adsorption isotherm for CO_2 in phenyl-functionalised MCM-41 was accurately reproduced using GCMC simulations. However, agreement with the experimental data for the amine monolayers was poor. The same methodology was later used to investigate adsorption of CO_2 to a wider range of monolayers, including halide functionalities [220]. Finally, Builes and Vega [221] constructed a model of MCM-41 functionalised with aminopropyl chains. Their approach involved swapping the first two atoms in each chain with all possible surface silanols until a local energy minimum was found. Using the resulting structure, each monolayer chain was grown sequentially using a coupled-decoupled configurational bias algorithm. In their algorithm, if growth of the chain was blocked it was randomly translated to a new grafting site. Since they accounted for the chemically specific nature of interactions between CO_2 and NH_2 , their adsorption isotherms were in very good agreement with experiment, especially in the low pressure region. Previous simulations only allowed for a physisorption mechanism.

8.3 A New Model for Functionalised MCM-41

In the experiments of Yoshitake *et al.* [106] the monolayer was first prepared by grafting the $(\text{H}_2\text{NCH}_2\text{CH}_2\text{NHCH}_2\text{CH}_2\text{CH}_2\text{Si}(\text{OCH}_3)_3)$ organosilane precursor to MCM-41 via a condensation reaction between a methoxy- group of the silane and a silanol on the surface [106]. The possibility of further condensation reactions between

the unreacted methoxy- groups and other silanols means that the monolayer is likely to consist of functionalities grafted onto a mix Q^1 , Q^2 and Q^3 Si atoms, as shown in Figure 8.1. In the experiments the propyl-EDA monolayer was simply used as a precursor for the generation of transition metal EDA complex monolayers, such as $[\text{Fe}(\text{EDA})_2(\text{Cl})_2]^+$ by addition of FeCl_3 (Figure 8.2). Here, we attempt to build functionalised MCM-41 models of both the monolayer types pictured in Figure 8.1 and 8.2.

Since the oxyanion contaminants of interest only exist in aqueous conditions the chemistry of the amorphous silica surface when in contact with solution must be considered. The point of zero charge (pH_{PZC}) of a surface is defined as the pH at which it has no overall charge. In amorphous silica the pH_{PZC} is a balance between the two equilibria controlling protonation and deprotonation of its surface silanols. Since the pH_{PZC} of amorphous silica (2 – 3.5) [222] is at least several units below the pH of typical solutions in the environment (6.5 – 8.5) [32], only the equilibrium for surface deprotonation needs to be considered in our models

$$K_a = \frac{[\text{SiO}^-][\text{H}^+]}{[\text{SiOH}]} \quad (8.1)$$

where K_a is the acid dissociation constant. For silanols on the surface of amorphous silica $\text{p}K_a = 6$ [223]. In this chapter the pH of the pore solution is assumed to be several units greater than the $\text{p}K_a$ of the surface so that the surface is dominated by deprotonated silanols.

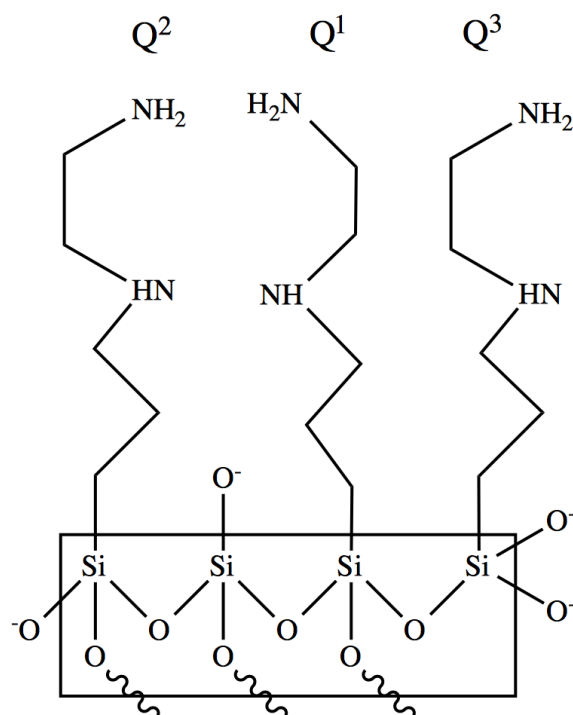


Figure 8.1 Q¹, Q² and Q³ chains comprising the propyl-EDA functionalised amorphous silica surface.

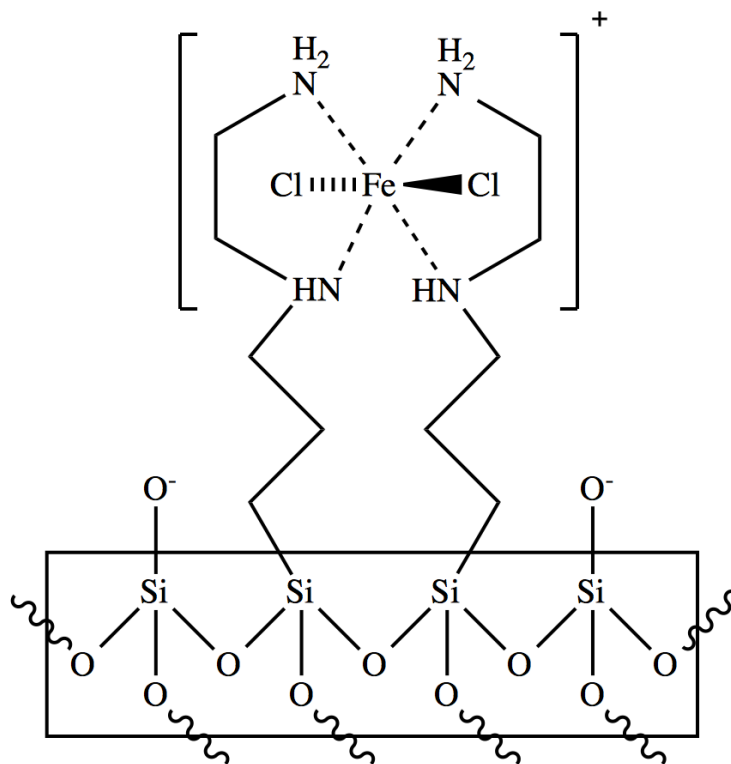


Figure 8.2 The $[\text{Fe}(\text{EDA})_2(\text{Cl})_2]^+$ complex, formed by addition of FeCl_3 to a propyl-EDA functionalised amorphous silica surface.

8.3.1 Model Preparation

Using the amorphous silica models prepared in Chapter Seven, the functionalised materials shown in Figures 8.1 and 8.2 were generated by randomly selecting and replacing OH groups on the surface with propyl-EDA chains. In this approach the first CH₂ group in the propyl-EDA chain was added 1.91 Å away from the Si atom, mimicking the grafting approach to functionalisation. This completely random approach to functionalisation is justified since an amorphous silica surface would not be expected to have a well-defined monolayer due to the irregular distribution of silanols. The coordinates of the atoms in the chain were modified to be completely planar to minimise overlap with adjacent functionalities in the initial configuration. For surfaces functionalised with the [Fe(EDA)₂(Cl)₂]⁺ complex the approach to adding organic chains was not completely random. In this case the first grafting site for the complex was chosen at random, but the second site was chosen by selecting the silanol closest to 5.0 Å from the first site, creating a pair of adjacent EDA ligands. Fe³⁺ was placed in the centre of the four N atoms in the pair of EDAs, before the Cl⁻ ligands were positioned normal to the EDA – Fe – EDA plane at a Fe – Cl distance (2.25 Å) taken from optimised DFT geometry in Table 6.4.

Firstly, in order to study the behaviour of a single monolayer group on a flat surface, two separate functionalised models of the slit pore were prepared; one with the propyl-EDA chain and the other with the [Fe(EDA)₂(Cl)₂]⁺ complex, where the organic chains were initially added pointing directly into the centre of the slit-pore ($z = 0$). Secondly, models of MCM-41 with a full monolayer of each type of functionality were generated. The MCM-41 model used (pore diameter = 2.81 nm) was chosen to best match the material synthesised by Yoshitake *et al.* (pore diameter = 2.63 nm) [106]. The monolayers were prepared by successively swapping propyl-EDA groups for surface silanols, again pointing directly into the centre of the pore. The only restriction was that once a Si atom had been functionalised it was prevented from being functionalised a second time (in the case of Q² or Q³ silanols). Such a restriction is justified, as the approach of a second organosilane precursor molecule would be sterically hindered by existing functionalities on that Si atom. The functionalisation process was continued until the experimentally reported monolayer density was attained (1.40 propyl-EDA nm⁻²).

8.3.2 Force Field Parameters

Since the classical force field parameters for the transition metal complex and the amorphous silica surface have been addressed in the previous chapters the only remaining parameters required to model the fully functionalised MCM-41 material are those of the alkyl chains linking the surface to the EDA ligands. The chains were considered to be covalently bound to a Si atom on the surface. A united atom model was used, in which each neutral CH₂ group is modelled as a single bead. Equations 4.35 and 4.36 were used to account angle bending and torsional motions, respectively, and bond distances were constrained using the SHAKE algorithm. The Si – C – C – C torsion was taken from Stimson and Wilson [224] and the angle bending and torsional terms overlapping the coarse grained regime of the propyl tether and the all atom regime of the EDA ligand (CH₂ – N – C, CH₂ – CH₂ – CH₂ – N and CH₂ – CH₂ – N – C) were taken from the OPLS force field [181]. The Si – CH₂ bond length, Si – CH₂ – CH₂ angle and CH₂ – CH₂ – CH₂ angle were all taken from a model of a self-assembled alkyl monolayer on a Si(111) surface [225].

All non-bonded interactions were calculated as the sum of the Lennard-Jones 12-6 potential (Equation 4.30) and electrostatic contributions (Equation 4.70). Cross parameters were determined according to the Lorentz-Berthelot combining rules (Equation 4.31) where σ_i and ϵ_i for the ions, transition metal complex and MCM-41 surface were taken from Chapter Five, Six and Seven, respectively. VDW parameters for the only new particle type in this chapter, the CH₂ in the propyl chain, were taken from Zhang and Jiang [225]. The charge on the first N atom in the propyl-EDA chain was adjusted from its value in the isolated complex in Chapter Six to account for it now being a secondary amine, which have different charges to primary amines in the OPLS force field. The charge on the Si atom (to which the propyl-EDA chain was covalently bound) was modified slightly to ensure overall neutrality of the propyl-EDA chain. The full set of parameters from the Si grafting site up to the secondary N atom are given in Table 8.1.

| Non-bonded | | | |
|--|---|-----------------------------------|------------------------------|
| <i>i</i> | $q_i (e)$ | $\epsilon_i (\text{kJ mol}^{-1})$ | $\sigma_i (\text{\AA})$ |
| Si | 1.2447 | - | - |
| CH ₂ | 0.0000 | 0.3820 | 3.950 |
| N | -0.7800 | 0.7113 | 3.300 |
| Equilibrium Bond Length | | | |
| <i>i-j</i> | $k_r (\text{kJ mol}^{-1} \text{\AA}^{-2})$ | $r_{\text{eq}} (\text{\AA})$ | |
| Si – CH ₂ | - | 1.910 | |
| CH ₂ – CH ₂ | - | 1.529 | |
| Angle Bend | | | |
| <i>i-j-k</i> | $k_\theta (\text{kJ mol}^{-1} \text{rad}^{-2})$ | $\theta_{\text{eq}} (^\circ)$ | |
| Si – CH ₂ – CH ₂ | 800.00 | 110.00 | |
| CH ₂ – CH ₂ – CH ₂ | 520.00 | 114.60 | |
| CH ₂ – CH ₂ – N | 470.28 | 109.47 | |
| CH ₂ – N – C | 433.46 | 107.20 | |
| Torsion | | | |
| <i>i-j-k-l</i> | $\nu_1 (\text{kJ mol}^{-1})$ | $\nu_2 (\text{kJ mol}^{-1})$ | $\nu_3 (\text{kJ mol}^{-1})$ |
| Si – CH ₂ – CH ₂ – CH ₂ | 5.903 | -1.134 | 13.158 |
| CH ₂ – CH ₂ – CH ₂ – N | 10.008 | -2.820 | 2.301 |
| CH ₂ – CH ₂ – N – C | 1.741 | -0.536 | 2.908 |

Table 8.1 Parameters for the organic chain linking the amorphous silica to the first N atom in the propyl-EDA chain.

8.3.3 Simulation Protocol

MD simulations were performed to analyse the structures of the functionalised amorphous silica models. In these simulations the amorphous silica, including the first atom (Si) in each the monolayer group, was considered to be frozen whereas the

monolayer is completely flexible. For these simulations the canonical ensemble was used instead of isothermal-isobaric ensemble because the atomic coordinates of frozen atoms cannot be scaled appropriately in the event of a volume change. The initial models were equilibrated for 100 ps in the absence of H₂O. During the initial stages of this equilibration period the time step was gradually increased from 10⁻⁷ fs to 2 fs and harmonic bond potentials were used to tether the two Cl⁻ ligands to the Fe³⁺; both these steps were necessary to slowly relax the system away from the highly unfavourable initial geometry without losing the structural integrity of the monolayer complex. After equilibration, the bond potential between Fe³⁺ and Cl⁻ was removed and only non-bonded interactions between this pair were calculated.

Once the model had been equilibrated with an empty pore, the pore space was filled with SPC/E H₂O and all of the hydrogens atoms were removed from the silica surface to account for silanol deprotonation. In the case of the slit pore functionalised with a single monolayer group a further 100 ps was sufficient to equilibrate the system. For [Fe(EDA)₂(Cl)₂]⁺ functionalised MCM-41, one Cl⁻ ion per complex was added at a random position in the pore space at the same time as the water. A longer equilibration run of 2 ns was required for this model. After equilibration, a 10 ns simulation of [Fe(EDA)₂(Cl)₂]⁺ functionalised MCM-41 was performed to generate radial distribution functions and density profiles in order to study the configuration of Cl⁻ ions in the pore.

8.3.4 Monolayer Structure

Slit Pore

During the first equilibration simulation (in the absence of H₂O) of the slit pore functionalised with a single propyl-EDA chain, the chain lay flat on the surface, maximising interactions between the amines in EDA and the amorphous silica silanols. This process was also observed in the previous simulations of related materials for CO₂ capture [218]. However, once water had been added to the pore the propyl-EDA chain stands up into the pore due to the favourable interactions between the amines in EDA and H₂O. A snapshot from the final configuration of each of these equilibration runs is shown in Figure 8.3. The fact that the organic chains point towards the centre of the pore once water has been added explains why much higher densities of monolayers are reported in SAMMS (where one or two interfacial water

layers are present during functionalisation) than materials prepared in the complete absence of water, where the access of organosilane molecules is blocked by previously grafted groups lying flat on the surface. In that sense, the models reported here are more representative of the material prepared by Yoshitake *et al.* [106] than SAMMS [105]. A single $[\text{Fe}(\text{EDA})_2(\text{Cl})_2]^+$ complex on the slit pore surface stands up, with the complex orienting the Cl – Fe – Cl plane parallel to the surface, rather than perpendicular to it (Figure 8.4). Such a configuration is both more favourable geometrically but also minimises electrostatic repulsion between the Cl^- ions in the complex and the negatively charge surface.

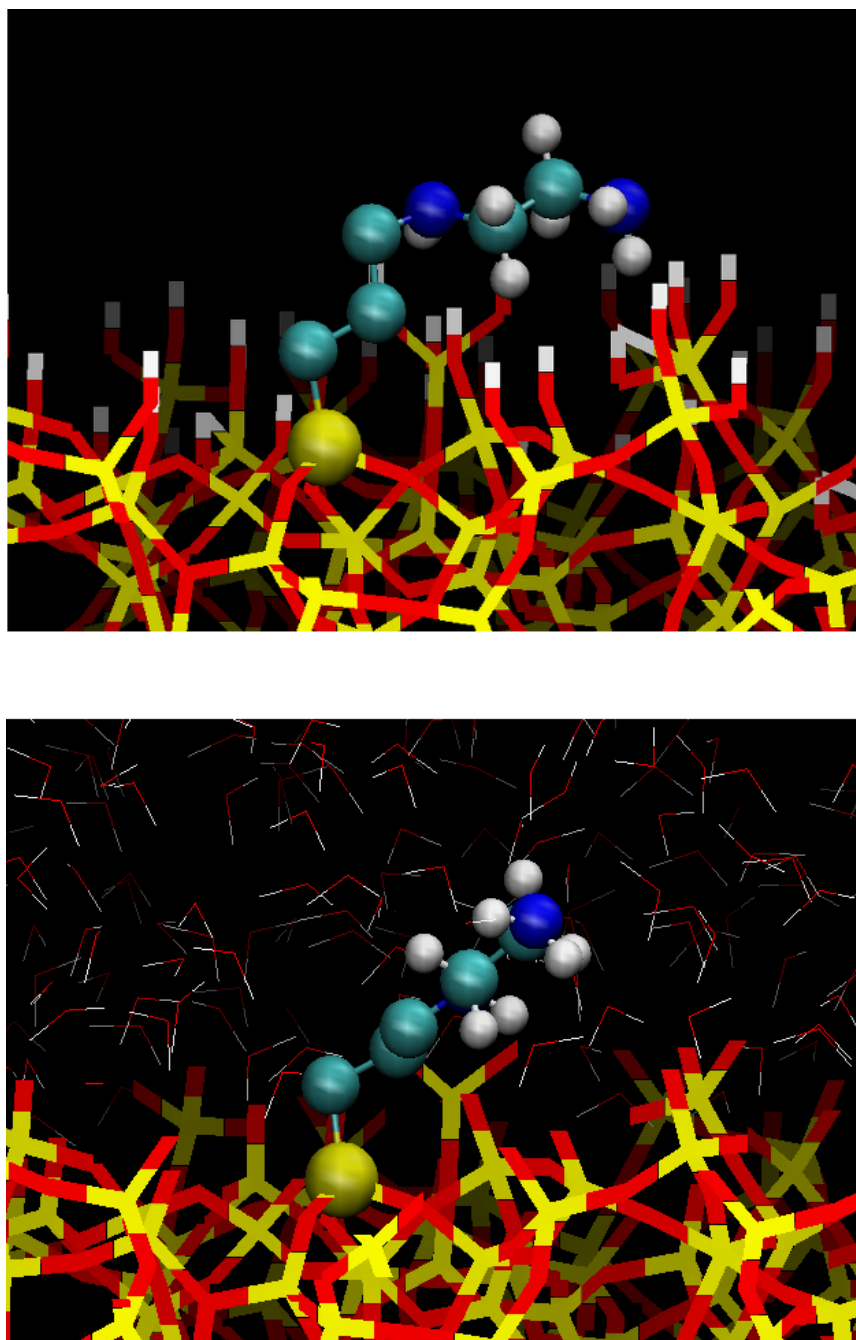


Figure 8.3 A single propyl-EDA chain on the slit pore surface at the end of equilibration in the gas phase (top) and in aqueous solution (bottom).

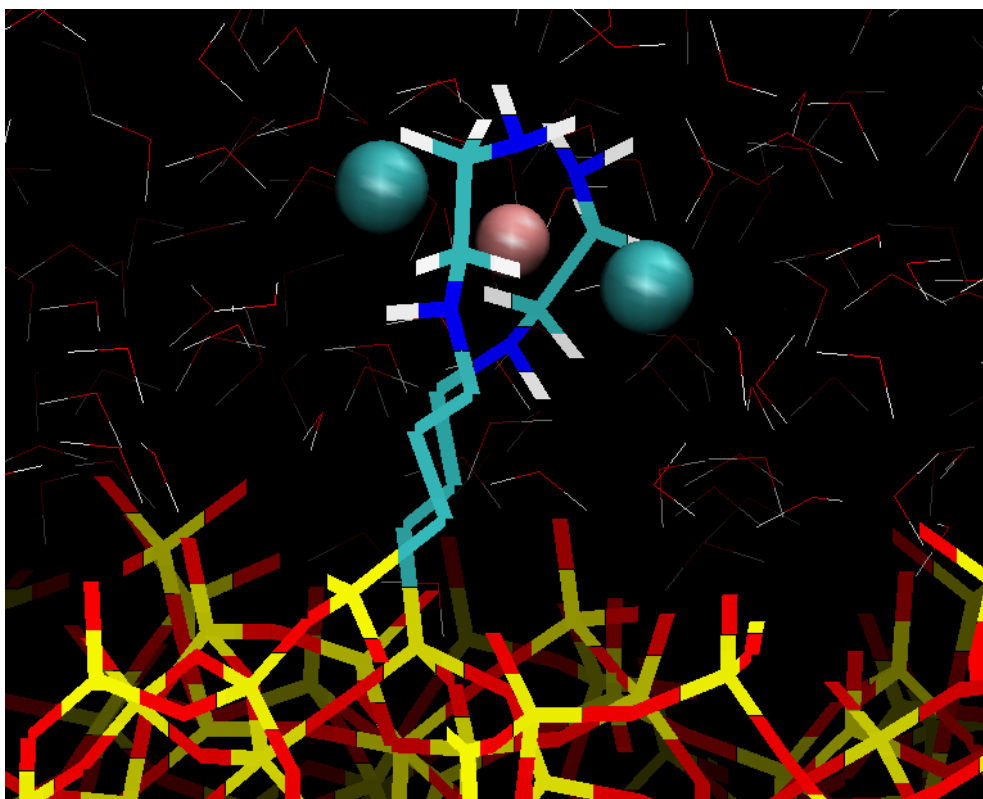


Figure 8.4 A single $[\text{Fe}(\text{EDA})_2(\text{Cl})_2]^+$ complex on the slit pore surface at the end of 100 ps of equilibration in solution. The pink and turquoise spheres are the Fe^{3+} and Cl^- ions, respectively.

MCM-41

The target monolayer density of 1.40 propyl-EDA nm^{-2} corresponds to 164 functional groups on the surface of this MCM-41 model, determined using the surface area calculated in Chapter Seven ($1023.5 \text{ m}^2 \text{ g}^{-1}$). The silanol density of the bare MCM-41 surface was 6.41 OH nm^{-2} so this monolayer density corresponds to 22% of the silanols being replaced by a propyl-EDA chain. Since each Fe^{3+} ion was coordinated by two EDA ligands the number of complexes in the $[\text{Fe}(\text{EDA})_2(\text{Cl})_2]^+$ functionalised model was 82 . In general, the complexes orient themselves in the same way as on the slit pore surface. However, the curvature of the surface and interactions between complexes in the monolayer means that this is not always the case.

Yoshitake *et al.* [106] proposed that up to three oxyanions could be removed from solution, by exchanging with the Cl^- ions bound to each complex. The radial distribution function for the Fe – Cl pair, $g_{\text{Fe-Cl}}(r)$, in the $[\text{Fe}(\text{EDA})_2(\text{Cl})_2]^+$ monolayer is shown in Figure 8.5. From the integral of $g_{\text{Fe-Cl}}(r)$, it is clear that the intense peak at

2.3 Å corresponds to the first two Cl⁻ ions, ie. those directly coordinated to the complex. A much weaker second peak at approximately 4.6 Å is associated with the third Cl⁻ ion per Fe³⁺, those added to the pore space prior to equilibration in solution, and is a result of hydrogen bonds between the Cl⁻ ions and amine hydrogens in EDA. The fact that this peak is so weak indicates that the Cl⁻ ions are only loosely bound to the monolayer and are in equilibrium with fully hydrated Cl⁻ ions in the pore solution.

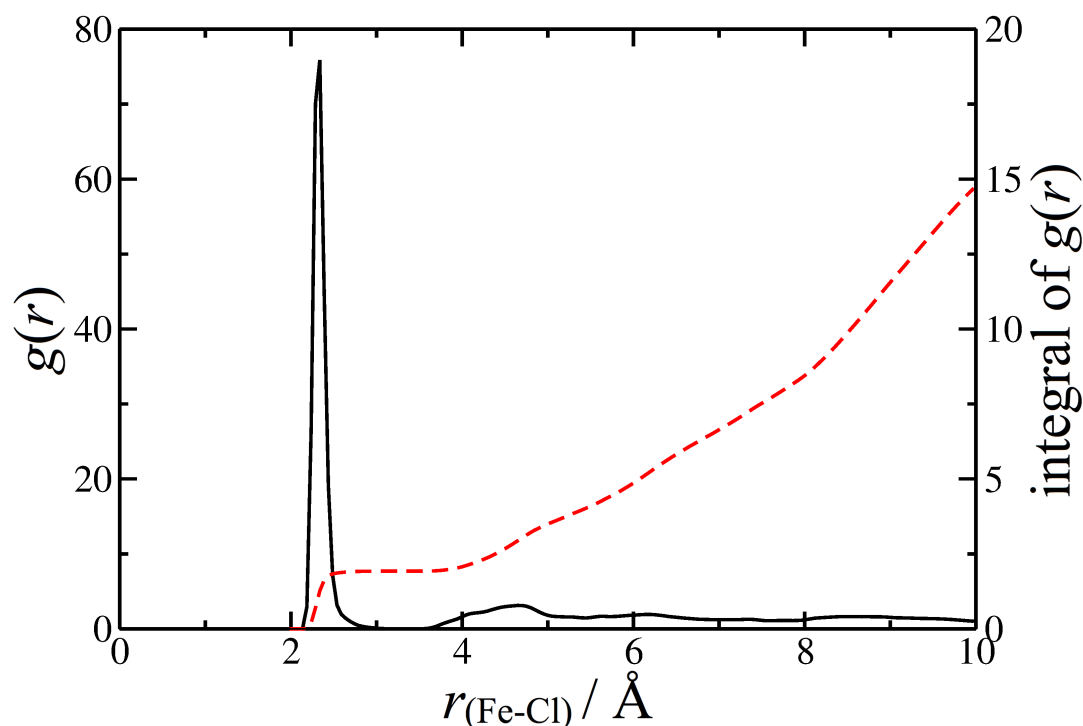


Figure 8.5 The radial distribution function (black, solid line) and its integral (red, dashed) for the Fe – Cl pair.

Figure 8.6 shows the radial density profile of Fe³⁺ and Cl⁻ ions in the central pore of the model. For Fe³⁺, there is an intense peak at 10.6 Å, corresponding to the position of these ions in the monolayer complex. This implies an effective pore diameter of 21.2 Å, which is 6.9 Å narrower than the bare MCM-41 pore. The Fe³⁺ peak is flanked on either side by those corresponding to the Cl⁻ ions directly bound to the Fe³⁺ at 10.2 Å and 11.0 Å. These Cl⁻ ions are just 0.4 Å from the Fe³⁺ (in the *x-y* plane) supporting the previous observation that the Cl – Fe – Cl plane is parallel to the surface (ie. in the *z*-direction). Closer to the centre of the pore there are two peaks in the Cl⁻ density profile, at 6.2 and 7.4 Å, and these correspond to the weakly bound ion on the outside of the [Fe(EDA)₂(Cl)₂]⁺ complex. The density of Cl⁻ ions close to the

centre of the pore (less than 5 Å) is very low. Despite the bare MCM-41 surface being negatively charged, once it has been functionalised with $[\text{Fe}(\text{EDA})_2(\text{Cl})_2]^+$ complexes the internal surface of the pore is positive. An electrical double layer, consisting of Cl^- ions that are weakly bound to the outside of the complex, acts to neutralise the surface. This interpretation can be visualised in the snapshot of the pore configuration taken from the end of the 10 ns simulation in Figure 8.7, which clearly shows a depletion in the Cl^- ion concentration in the centre of the pore, relative to the edge.

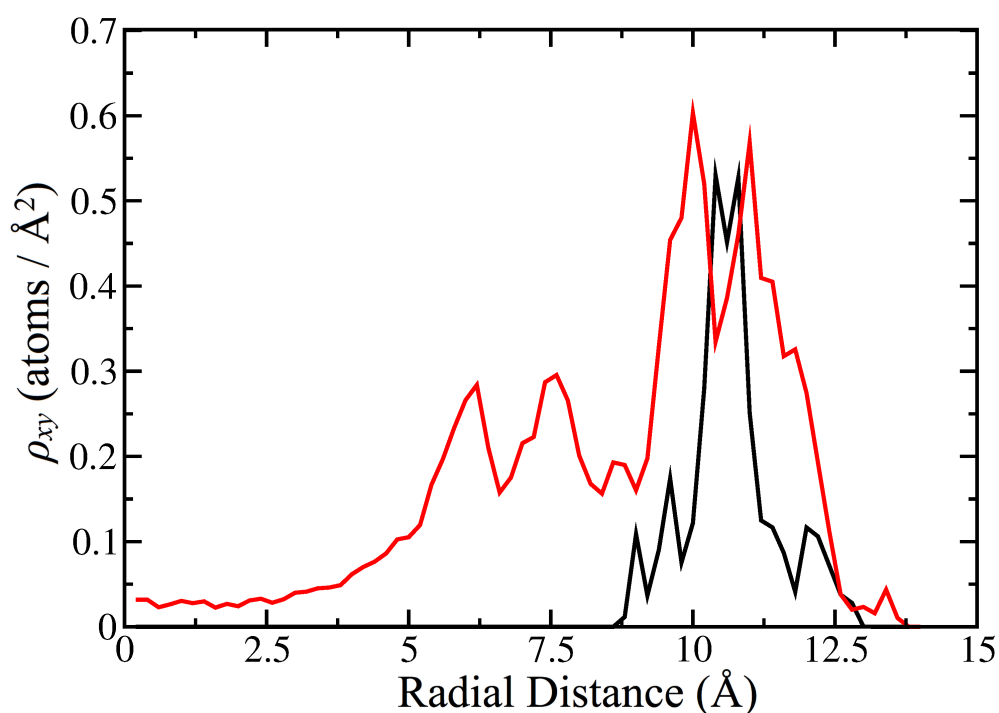


Figure 8.6 Radial density profiles, ρ_{xy} , of Fe^{3+} (black) and Cl^- (red) in the $[\text{Fe}(\text{EDA})_2(\text{Cl})_2]^+$ functionalised MCM-41 pore.

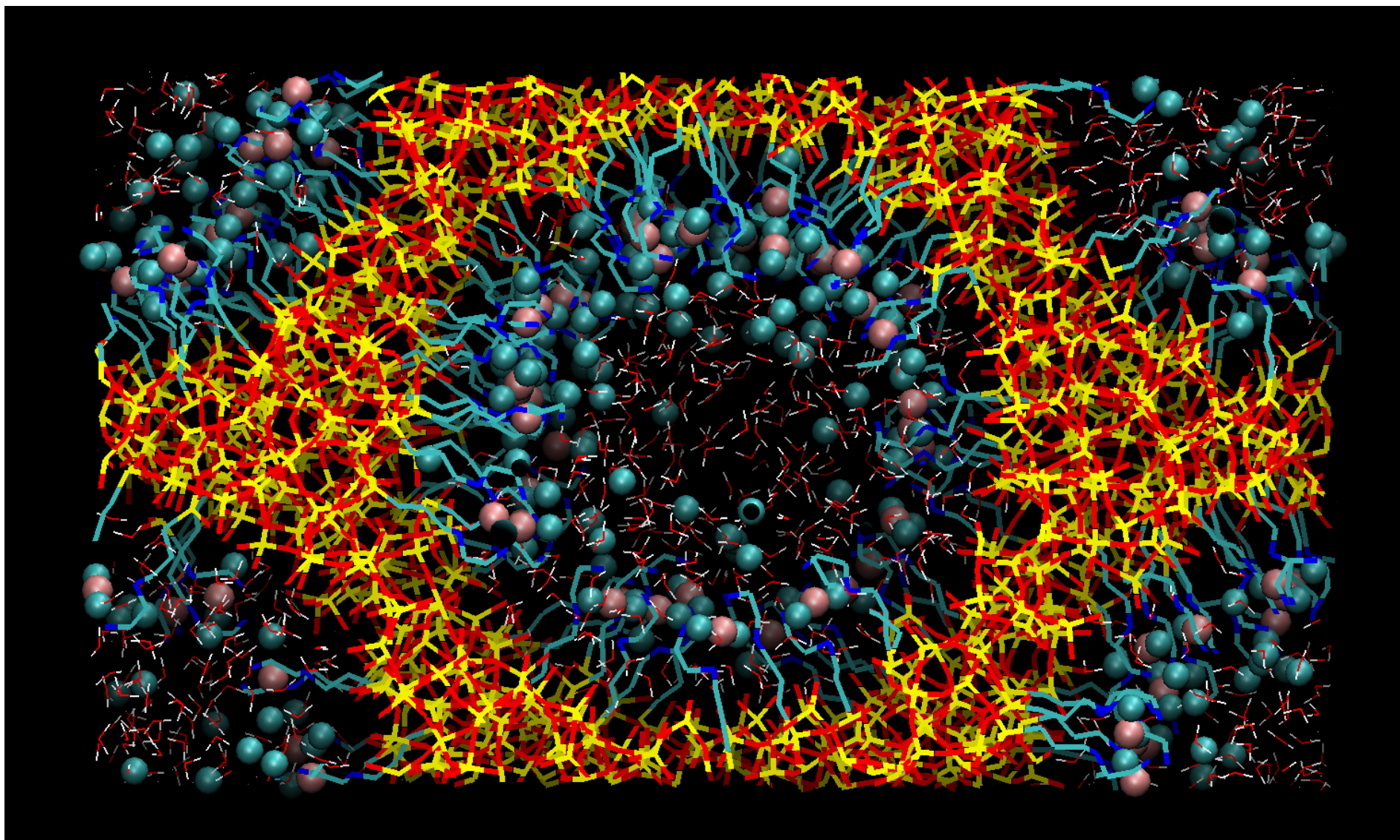


Figure 8.7 The model of MCM-41 (bare pore diameter = 2.81 nm) functionalised with a monolayer of $[\text{Fe}(\text{EDA})_2(\text{Cl})_2]^+$ complexes where the pores have been filled with one Cl^- ion per complex and SPC/E water.

8.4 Determining the Affinity of Oxyanions for Functionalised MCM-41 Pores

In order to establish the affinity of each oxyanion for the functionalised MCM-41 pore it is necessary consider their transfer into the pore from bulk solution. The aim of this section is to generate models that are suitable for simulating this process, obtain PMFs that describe the free energy change as the oxyanions enter the pore and propose an explanation for the pore's selectivity.

8.4.1 Model Preparation

Three of the MCM-41 models (with wall thicknesses of 0.95 nm) prepared in Chapter Seven were investigated; those with pore diameters of 2.41, 2.81 and 3.16 nm. The central part of the simulation cell for these models in the z -direction was retained but atoms greater than 1.25 nm from the centre ($z = 0$) were deleted, resulting in an 'open' pore that was 2.5 nm long. The surfaces of the cleaved faces were prepared according to the same procedure as the internal pore surfaces in Chapter Seven (ie. removal of all Si and O atoms with incomplete valency followed by minimisation). The pore models were functionalised with propyl-EDA chains using the same approach and target density as Section 8.3.1, with the added restriction that only silanols on the internal surface of the pore could be functionalised by propyl-EDA, and not those on the newly cleaved face of the material. SPC/E water molecules were added to fill both the pore space and the reservoir either side of the MCM-41 pore. A 2 ns equilibration simulation was performed using the same parameters and methodology described in Section 8.3.2 and the equilibrated configuration of each of these pore models can be visualised in Figure 8.8.

8.4.2 Simulation Protocol

A suitable reaction coordinate for the PMF describing the process of TcO_4^- and SO_4^{2-} entering the MCM-41 pores is the z -coordinate of the oxyanion. In each simulation window the oxyanion was first placed in the water reservoir of the equilibrated 'open' pore. Then, the PLUMED plugin [185] was used to bias the position of the centre of the oxyanion, using a harmonic potential of the form of Equation 4.86, along the z -coordinate of the simulation cell. The PMF was obtained from $z = -20$ to 20 \AA using a total of 21 simulation windows at 2 \AA intervals, each of which had a biasing force constant, k_w , of $10 \text{ kJ mol}^{-1} \text{ \AA}^{-2}$. Once the biasing potential had been applied a 3 ns

simulation was performed. Statistics from the final 2 ns were used to generate the PMFs. WHAM was used to recombine the simulation windows, correct for the potential bias and to check that there was sufficient overlap in sampling between adjacent windows. The configuration of the $z = 20 \text{ \AA}$ window for TcO_4^- in one of the models after equilibration is shown in Figure 8.9. The relevant free energy barriers could be obtained from a PMF spanning only half of the reaction coordinate sampled here ($z = 0$ to 20 \AA). However, plotting the PMF from one side of the pore to the other ($z = -20$ to 20 \AA) confirms whether all values of the reaction coordinate have been sampled sufficiently, since the free energies in the water reservoir on either side of the pore should be identical.

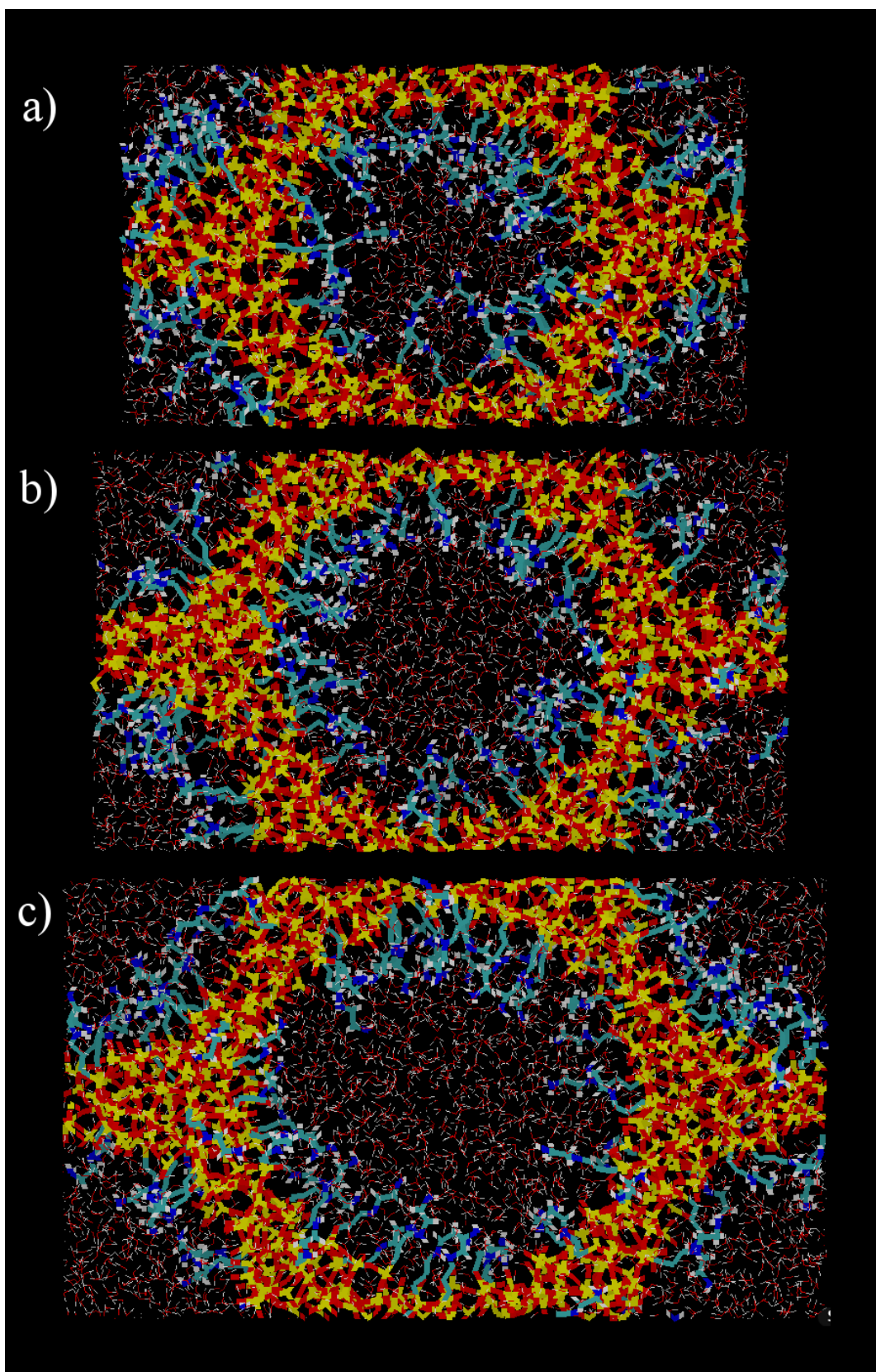


Figure 8.8 A snapshot of the external face (x - y plane) of the ‘open’ propyl-EDA functionalised MCM-41 models (pore diameters of a) 2.41 nm, b) 2.81 nm and c) 3.16 nm) used in the PMF simulations.

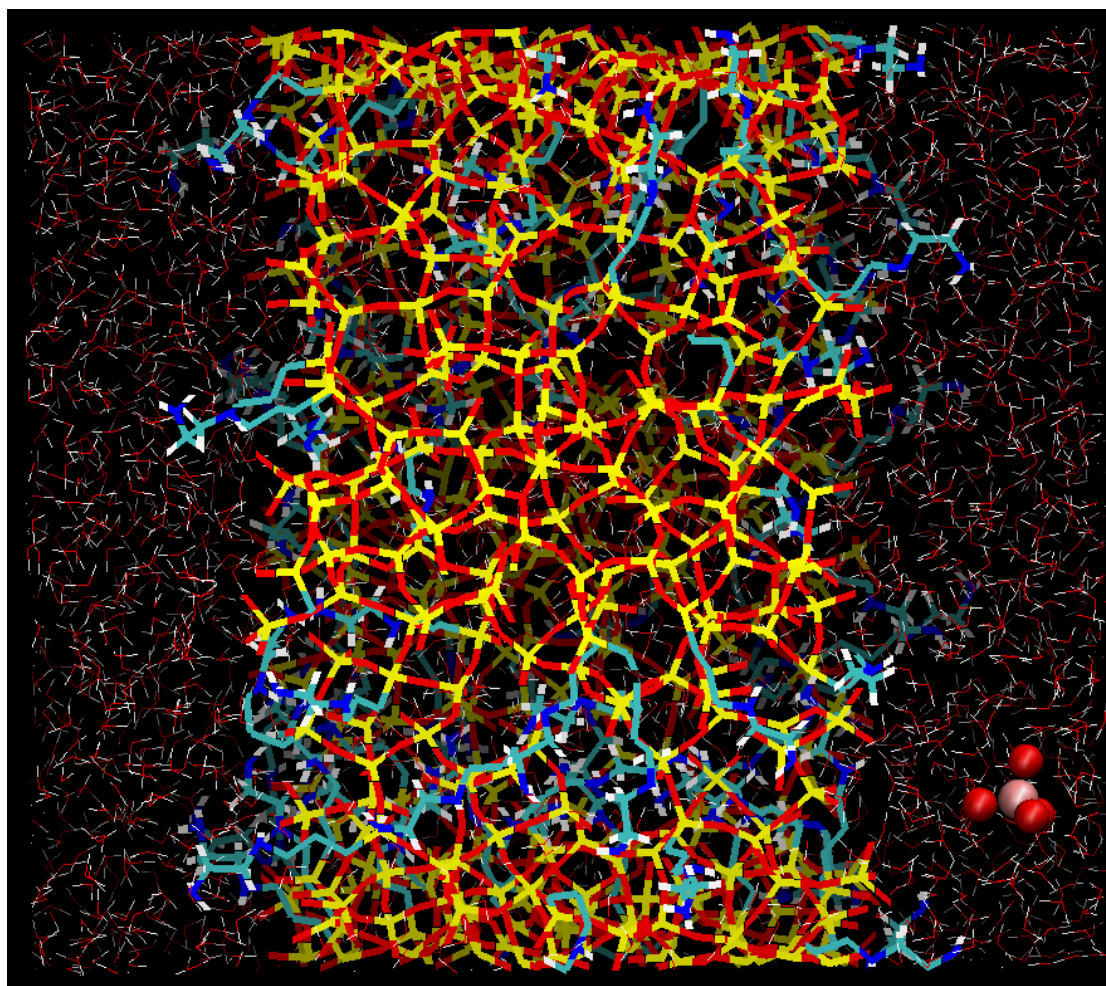


Figure 8.9 A snapshot of the side (x - z plane) of the propyl-EDA functionalised MCM-41 model, taken from the $z = 20$ Å window of the PMF for TcO_4^- entering the 2.81 nm pore diameter model.

8.4.3 PMFs for Oxyanions Entering the Functionalised Pore

Since these simulations were performed in the canonical ensemble the energies obtained from the PMFs are Helmholtz free energies. The barrier for entry into the pore, $\Delta F_{\text{barrier}}$, is defined as the difference between the free energy when the oxyanion is outside the pore in the water reservoir ($z = -20$ or 20 Å) and the free energy when the oxyanion is in the middle of the pore ($z = 0$ Å). The PMFs for TcO_4^- and SO_4^{2-} pore entry are shown in Figure 8.10 and $\Delta F_{\text{barrier}}$ associated with each process is given in Table 8.2. The size of the barrier to oxyanion pore entry increases as the pore diameters narrow. For TcO_4^- , $\Delta F_{\text{barrier}} = 36.7$ kJ mol $^{-1}$ in the 2.41 nm pore, 23.7 kJ mol $^{-1}$ in the 2.81 nm pore and 22.5 kJ mol $^{-1}$ in the 3.16 nm pore. The corresponding values for SO_4^{2-} were 61.1, 37.4 and 34.4 kJ mol $^{-1}$. The barriers for the

monovalent TcO_4^- were 60 – 65% of the size of those for the divalent SO_4^{2-} suggesting that the propyl-EDA functionalised pores are selective for TcO_4^- .

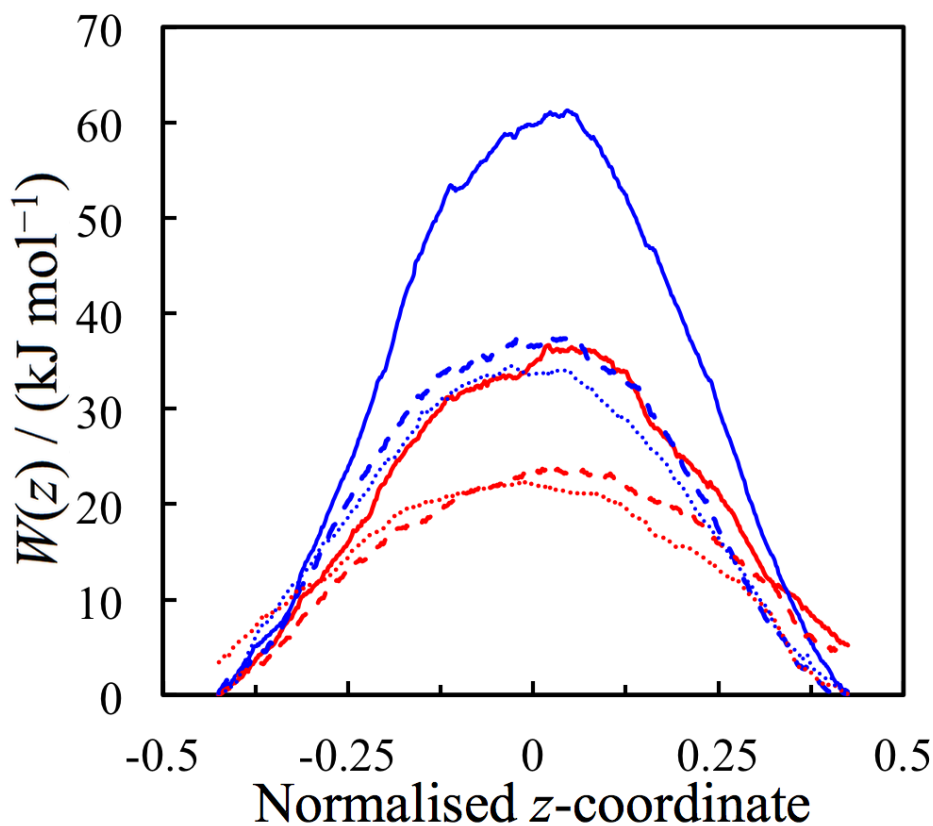


Figure 8.10 PMFs for TcO_4^- (red) and SO_4^{2-} (blue) entering propyl-EDA functionalised MCM-41 models, with pore diameters of 2.41 (solid), 2.81 (dashes) and 3.16 (dots) nm.

| Pore Diameter (nm) | $\Delta F_{\text{barrier}}$ (kJ mol^{-1}) | |
|-----------------------|--|--------------------|
| | TcO_4^- | SO_4^{2-} |
| 2.41 | 36.7 | 61.1 |
| 2.81 | 23.7 | 37.4 |
| 3.16 | 22.5 | 34.4 |

Table 8.2 $\Delta F_{\text{barrier}}$ associated with each oxyanion entering the propyl-EDA functionalised MCM-41 pores.

An attempt was made to generate PMFs for oxyanions entering an ‘open’ $[\text{Fe}(\text{EDA})_2(\text{Cl})_2]^+$ functionalised pore in the same manner as for the propyl-EDA pore. However, during equilibration many of the Cl^- counterions are forced from the pore and enter the water reservoir. When this occurs the pore models are not representative of the real material so reliable PMFs could not be generated using this approach.

8.4.4 Electrostatic Potential in Functionalised Pores

Two possibilities for the cause of the pore selectivity for ions were investigated. The first is based on the charge of the oxyanions and the surface of the pore [226]. The second is the possibility of size exclusion caused by confinement [227].

Electrostatic Potential Profiles in Propyl-EDA Functionalised Pores

The deprotonation of unfunctionalised silanols on the surface of MCM-41 results in a negatively charged surface and the possible repulsion of anions. To investigate the possibility of pore valence selectivity for the oxyanions, profiles of the electrostatic potential through the middle ($x = 0, y = 0$) of the central pore were calculated for each functionalised model. We are interested in the relative change in electrostatic potential on entering the pore so calculations were performed at 1 Å intervals to generate a profile from one end of the simulation cell ($z = -L_z/2$) to the other ($z = L_z/2$). An additional 5 ns MD simulation of the open pore models was performed so that the potential at each point could be averaged over 1250 configurations, obtained every 4 ps. At each point the electrostatic potential was calculated using the tabulated Ewald sum (Section 7.5.2) using $\alpha = 0.3208 \text{ \AA}^{-1}$, $k_{\text{max}} = 23, 13$ and 15 in the x, y and z -dimensions and a real space cut off of 15 Å. In the calculation, the potential due to all of the adsorbent atoms (MCM-41 and propyl-EDA tethers) was calculated but the potential due to H_2O molecules was ignored. However, the charge-screening effect of water was accounted for afterwards in an average way by dividing the electrostatic potential by the relative permittivity of water (78.0) at each point. The Fuchs correction (Equation 4.80) is particularly important in these calculations in order to correct for the non-zero overall charge of the simulation cell due to silanol deprotonation.

The electrostatic potential profiles in each of the three pore models are shown in Figure 8.11. Since the length of the simulation cells were not the same in each model

(due to them being prepared by quenching in the isothermal-isobaric ensemble) the z -coordinate was normalised. The narrowest pore (2.41 nm prior to functionalisation with propyl-EDA) has the most negative potential in the centre of the pore (6.17 V), reducing to 4.62 V for the 2.81 nm pore and 4.00 V for the widest pore (3.16 nm). This is due to the closer proximity of the negatively charged walls of the MCM-41 surface in narrower pores. However, these values must be treated with caution since the potential should plateau in the centre of the pore. The fact that they do not suggests that longer pore models are required to account fully for the long-range effects of the coulombic interaction.

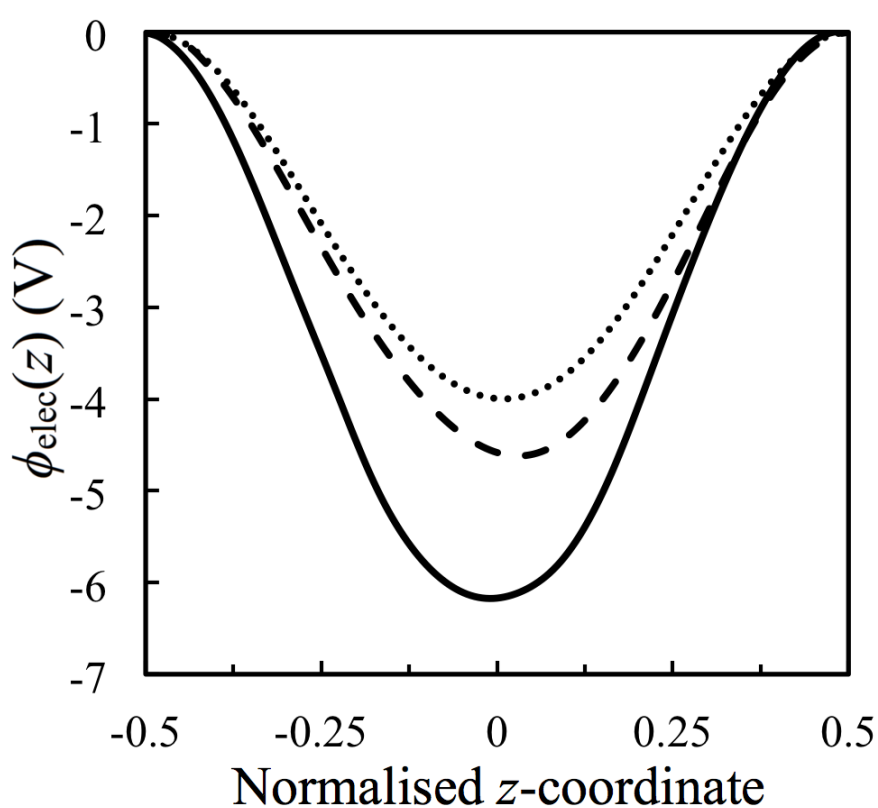


Figure 8.11 Profiles of the mean electrostatic potential through the open propyl-EDA functionalised MCM-41 with pore diameters of 2.41 (solid), 2.81 (dashed) and 3.16 (dots) nm.

Estimation of PMFs using the Electrostatic Potential Profiles

Estimations of the free energy barriers, ΔF_{elec} , can be made using the electrostatic potential profiles and Equation 7.16. The estimates can then be compared to those obtained using atomistic simulations and the umbrella sampling approach (Figure

8.10) to establish whether the pore's selectivity is due to the electrostatic potential. The estimate assumes that there are no entropic contributions and that electrostatics effects dominate over VDWs interactions. This assumption is reasonable since the profiles are obtained at a position ($x = 0, y = 0$) where the Lennard-Jones 12-6 potential due to the surface has effectively decayed to zero.

The estimated PMFs for the oxyanions in each pore are shown in Figure 8.12 and the barriers to pore entry are given alongside the magnitude of the electrostatic potential in the pore in Table 8.3. The shapes of the profiles are very similar to the PMFs obtained from the umbrella sampling simulations (Figure 8.10). In this calculation, ΔF_{elec} for TcO_4^- entry into the pore is exactly 50% of that for SO_4^{2-} , compared to 60 – 65% in the umbrella sampling approach. The difference is due to the fact that the electrostatic potential profile was obtained exactly in the centre of the pore, whereas the oxyanions do not stay in the centre of the pore ($x = 0$ and $y = 0$) during the umbrella sampling simulations. The monolayer extends closer to the centre of the pore resulting in interactions between the oxyanions and the propyl-EDA monolayer during the simulations. In the electrostatic potential approach the estimated barriers for the widest pore studied is exactly 65% (TcO_4^- and SO_4^{2-}) of ΔF_{elec} for the narrowest pore. However, the corresponding difference in the umbrella sampling approach are 62% (TcO_4^-) and 56% (SO_4^{2-}). Again the difference is expected to be due to deviations of the oxyanions from the centre of the pore in the umbrella sampling simulations, which have a disproportionate effect of increasing $\Delta F_{\text{barrier}}$ for the narrowest pore. This argument also explains why ΔF_{elec} for TcO_4^- in the narrowest (2.41 nm) pores is similar to ΔF_{elec} for SO_4^{2-} in the two wider pores (2.81 and 3.16 nm) but in the umbrella sampling approach it is much smaller.

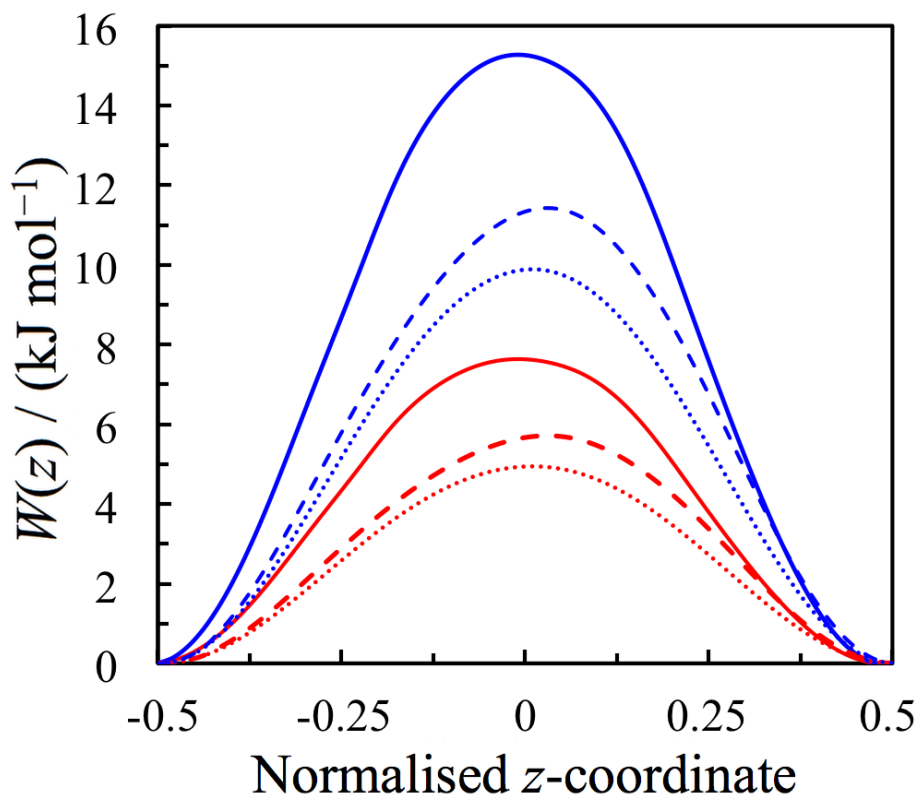


Figure 8.12 PMFs estimated from the electrostatic potential profiles for XO_4^{n-} , ($\text{X} = \text{Tc}$ (red) and $\text{X} = \text{S}$ (blue)) entering open propyl-EDA functionalised MCM-41 models with pore diameters of 2.41 (solid), 2.81 (dashed) and 3.16 (dots) nm.

| Pore Diameter (nm) | $ \phi_{\text{elec}} $ (V) | ΔF_{elec} (kJ mol ⁻¹) | |
|-----------------------|----------------------------|--|--------------------|
| | | TcO_4^- | SO_4^{2-} |
| 2.41 | 6.2 | 7.6 | 15.3 |
| 2.81 | 4.6 | 5.7 | 11.4 |
| 3.16 | 4.0 | 4.9 | 9.9 |

Table 8.3 The magnitude of the electrostatic potential in the centre of the pore and the estimated Helmholtz free energy barriers for oxyanion pore entry.

The absolute values of $\Delta F_{\text{barrier}}$ and ΔF_{elec} are not in agreement. For example, $\Delta F_{\text{barrier}}$ for SO_4^{2-} entering the narrowest pore is 61.1 kJ mol⁻¹ using the umbrella sampling

approach but ΔF_{elec} is 15.3 kJ mol^{-1} from the estimation based on the electrostatic potential. This is due to the false assumption that the relative permittivity of bulk water is the correct value for water in the functionalised MCM-41 pores. In these pores significant ordering of water is likely at the interface with the silica and the propyl-EDA chains, resulting in poor screening of charge. This argument is supported by the fact that the difference is most significant for the narrowest pores (eg. $\Delta F_{\text{barrier}}$ is a factor of 4.0 greater than ΔF_{elec} for entry of SO_4^{2-} into the 2.41 nm pore but only 3.5 times greater for entry into the 3.16 nm pore) where the relative permittivity of water has the greatest deviation from its bulk value.

Electrostatic Potential Profiles in $[\text{Fe}(\text{EDA})_2(\text{Cl})_2]^+$ Functionalised Pores

The electrostatic potential in the periodic $[\text{Fe}(\text{EDA})_2(\text{Cl})_2]^+$ functionalised MCM-41 model was calculated from the 10 ns simulation at 1 \AA intervals from $z = -L_z/2$ to $z = L_z/2$ (Figure 8.13). Due to the uneven monolayer distribution there are large fluctuations in the potential along the length of the pore. Since there are no water reservoirs in this model the pore is periodic in the z direction so there should be no systematic variation in the electrostatic potential along the length of the pore. The potential, averaged over the whole profile, was -0.92 V . This negative potential helps to explain the preference of Cl^- ions to reside at the edge of the pore rather than the centre (shown the radial density profile in Figure 8.6) and also explains why many of the ions are forced out of the pore when the ‘open’ model of the $[\text{Fe}(\text{EDA})_2(\text{Cl})_2]^+$ functionalised surface is simulated. Equation 7.16 can again be used to estimate the free energy barrier from the potential for each oxyanion entering the pore. The barriers to entry were 89 kJ mol^{-1} for TcO_4^- and 178 kJ mol^{-1} for SO_4^{2-} . Equation 6.2 can be used to calculate the corresponding permeation rates of the two oxyanions; $1.65 \times 10^{-3} \text{ s}^{-1}$ for TcO_4^- and $4.40 \times 10^{-19} \text{ s}^{-1}$ for SO_4^{2-} . At this rate TcO_4^- permeation into the pore would occur during the typical timescale of an experiment whereas SO_4^{2-} entry would not be observed.

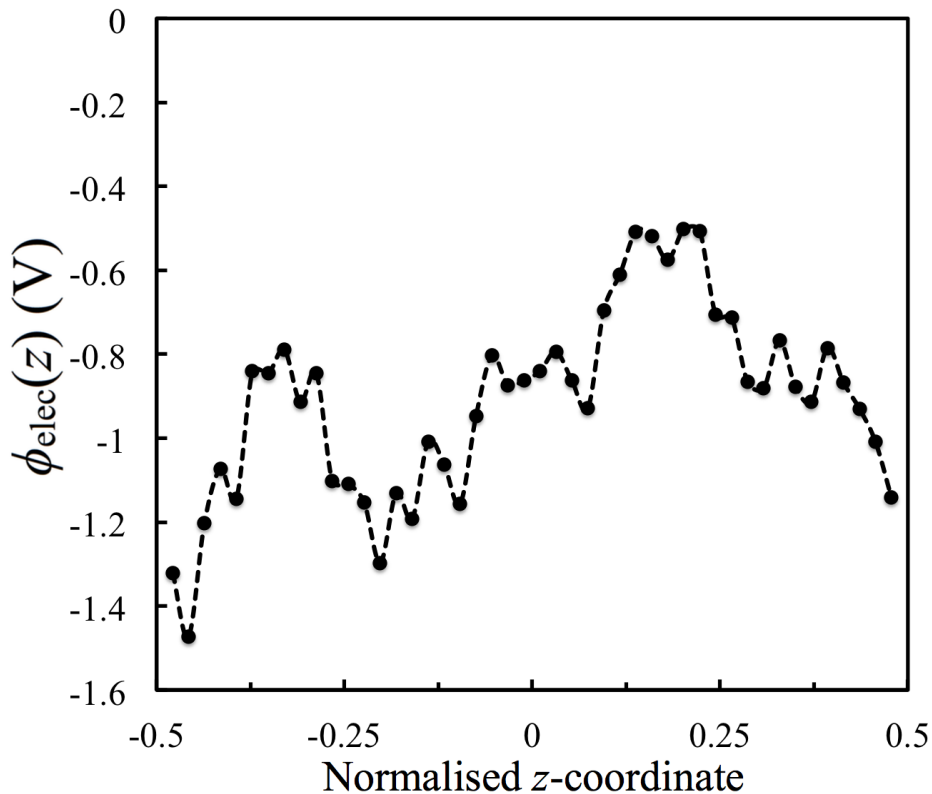


Figure 8.13 Electrostatic potential profile in the periodic $[\text{Fe}(\text{EDA})_2(\text{Cl})_2]^+$ functionalised pore.

The ability of nanoporous materials to allow some ions to permeate but not others by a valence selectivity mechanism has been observed in biological ion channels [226]. This case is particularly interesting since the pore sizes are large and it is the layer of Cl^- that generates a negative electrostatic potential in the pore, despite having a positively charged $[\text{Fe}(\text{EDA})_2(\text{Cl})_2]^+$ monolayer surface. The concept of ‘charge inversion’ due to electrical double layer formation has previously been reported in simulations of electrolytes flowing through bare silica pores [228].

8.4.5 Oxyanion Dehydration in Functionalised Pores

The second possible cause of the observed selectivity of porous materials for ions is size exclusion. Here, the size of an ion is defined by its hydrated radius rather than its bare ionic radius. Even if a bare ion is small enough to fit into a narrow pore, it may not be wide enough for the ion’s accompanying hydration shell. If this is the case, the ion may have to partially dehydrate to enter the pore. Even though the entropy of dehydration is expected to be favourable because H_2O molecules are returned to bulk

solution from their ordered environment around an ion, this will be far outweighed by the enthalpic penalty, leading to the possibility of significant free energy barriers to pore entry. It is possible to envisage a situation in which species with large ionic radii and poorly defined hydration shells (eg. TcO_4^-) are able enter a pore, but species with smaller radii inducing a higher degree of order in the surrounding solvent (eg. SO_4^{2-}) are prevented from entering that same pore.

Typically, the hydrated radius of an ion, r_H , is defined as the position of the first maximum in $g_{\text{X-Ow}}(r)$. Using Figure 5.5 and this definition of r_H , TcO_4^- is much larger ($r_H = 4.40 \text{ \AA}$) than SO_4^{2-} ($r_H = 3.78 \text{ \AA}$). However, $g_{\text{S-Ow}}(r)$ also has another intense peak, at 5.95 \AA , corresponding to the secondary hydration shell, whereas $g_{\text{Tc-Ow}}(r)$ does not, leading to the possibility of SO_4^{2-} ion exclusion based on the strength of the secondary hydration shell. The possibility of this ion exclusion mechanism was investigated by plotting the number of H_2O molecules in the primary and secondary hydration shells of SO_4^{2-} as it passes through the narrowest (pore diameter = 2.41 nm) open propyl-EDA functionalised MCM-41 material. The number of H_2O molecules, $n(\text{H}_2\text{O})$, in the SO_4^{2-} hydration shell was obtained in each of the simulation windows used to generate the PMFs. $n(\text{H}_2\text{O})$ was defined as the integral at the position of the first minimum after the relevant peak in $g_{\text{S-Ow}}(r)$ (Figure 5.5).

The change in $n(\text{H}_2\text{O})$ in each hydration shell as SO_4^{2-} passes through the pore is shown in Figure 8.14. The primary hydration shell of SO_4^{2-} is unaffected by porous confinement. However its secondary hydration shell is disrupted to some extent in the pore. Since the pore diameter is not constant due to the random distribution of functional groups in the monolayer the effect is not uniform throughout the pore. If oxyanion dehydration by confinement were the cause of the differences in selectivity for TcO_4^- over SO_4^{2-} seen in the PMFs then $n(\text{H}_2\text{O})$ for SO_4^{2-} would be expected to reduce dramatically when the oxyanion enters the pore. This effect is not observed. It was determined in Section 8.3.4 that the monolayer narrows the pore by 6.9 \AA compared to the bare MCM-41, resulting in a pore radius of 8.6 \AA in this case. Ion selectivity by confinement is not seen in these pores because this radius of the pore is wider than that of the secondary hydration shell of SO_4^{2-} (6.8 \AA). The fact that the PMFs do not plateau in the centre of the pore suggests that the selectivity mechanism is due to a long-range effect, also supporting the electrostatic potential argument. If

oxyanion dehydration were the cause of selectivity seen in the PMFs, they would be expected to plateau as soon as the oxyanion enters the pore.

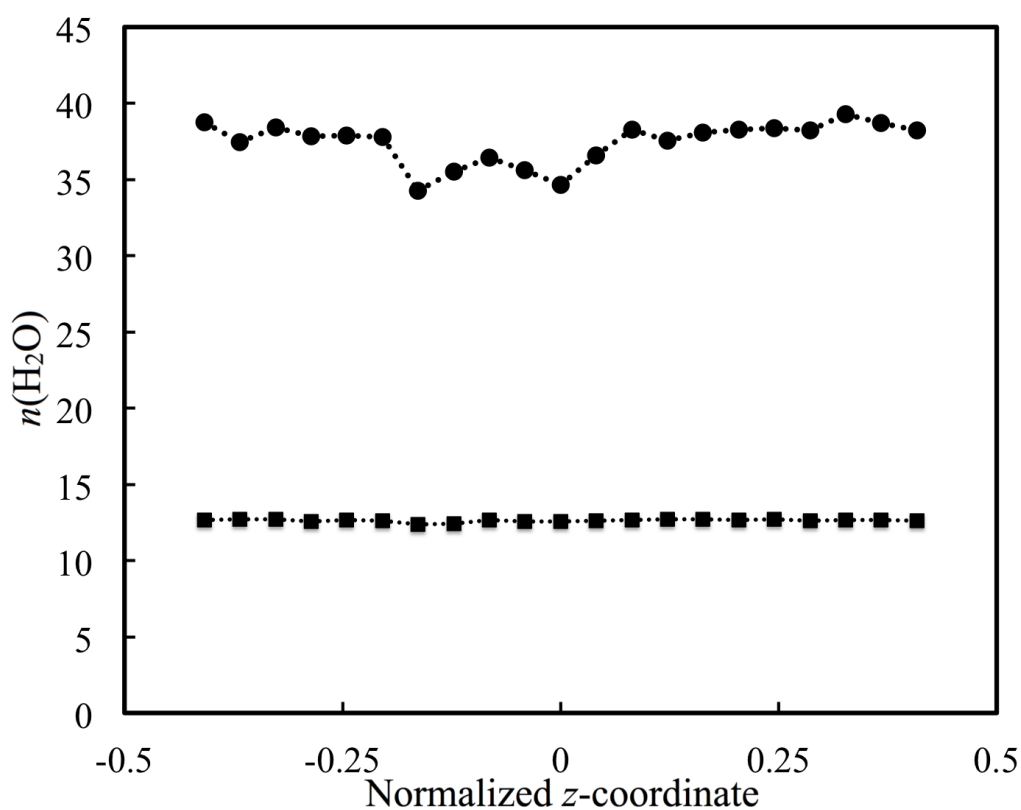


Figure 8.14 Number of H₂O molecules in the primary (squares) and secondary (circles) hydration shells of SO₄²⁻ (ie. those less than 4.4 Å and 6.8 Å from S, respectively) in each window for the 2.41 nm pore diameter model.

8.5 Conclusions

This chapter is believed to be the first reported simulation of ionic solutions in the pores of functionalised MCM-41 materials. The models were prepared simply by exchanging silanols on the surface of the amorphous silica with propyl-EDA chains and are an accurate representation of the material synthesised by Yoshitake *et al.* [106]. PMFs that describe the free energy change as the radioactive TcO₄⁻ and the competing SO₄²⁻ enter the pore from aqueous solution were calculated using umbrella sampling. The resulting Helmholtz free energy barriers showed that the entry of oxyanions into the pores is unfavourable, particularly in the case of SO₄²⁻. The PMFs were rationalised by plotting the electrostatic potential profiles through the middle of the central pore in the model and the observed selectivity is a result of the repulsive

potential due to the charged pore walls of MCM-41. However, in a real ionic solution cationic counterions would act to neutralise the surface to some extent by binding to deprotonated surface silanols. Equilibrating a concentrated solution of counterions at the charged amorphous silica interface is not possible using atomistic simulations and equilibrium models are instead required to describe such a system.

The propyl-EDA monolayer was used as a precursor for the construction of a model of the $[\text{Fe}(\text{EDA})_2(\text{Cl})_2]^+$ monolayer. The structure of the monolayer in the $[\text{Fe}(\text{EDA})_2(\text{Cl})_2]^+$ functionalised pore was studied by plotting the radial distribution function for the Fe – Cl pair and density profiles of Fe^{3+} and Cl^- ions, showing that Cl^- ions weakly interact with the outer sphere of the complex on the surface of the pore. Reliable PMFs for oxyanions entering into the pores of this material could not be obtained using umbrella sampling because of the expulsion of Cl^- counterions into the water reservoir due to its negative electrostatic potential in the pore (-0.92 V). It is believed that this negative potential may be the cause of the experimentally observed selectivity for monovalent ions over the divalent SO_4^{2-} in oxyanion-SAMMS. Methods that are suitable for calculating $\Delta F_{\text{barrier}}$ in a periodic pore model are required, such as the thermodynamic integration technique. However, such calculations are outside the scope of this thesis.

Chapter Nine

Speciation of Oxyanions at the Silica – Water Interface

9.1 Introduction

The surface of amorphous silica will have a net negative charge if its pH_{pzc} is exceeded by the pH of the solution it contacts. Helmholtz proposed that if a charged surface is placed in contact with an ionic solution then an electrical double layer [145] of counterions will form at the interface. Atomistic simulations are not well suited for studying this phenomenon since a very large simulation would be required to include a statistically relevant number of ions in a dilute ionic solution and equilibration times for a concentrated solution would be prohibitively long. Instead, Poisson-Boltzmann (PB) theory can be used to investigate the equilibrium properties of such a system. In this chapter, a solution containing the oxyanions (TcO_4^- and SO_4^{2-}) is considered to be in contact with an amorphous silica surface and PB theory is used to obtain the electrostatic potential and oxyanion concentration profiles in this ionic solution. The effect of bulk solution pH on these profiles is investigated and the relevance of the calculations for the selectivity of oxyanion-SAMMS for TcO_4^- and SO_4^{2-} is discussed.

The equilibrium properties of a system of interacting ions near a charged surface can be treated using the one-dimensional PB equation

$$\frac{d^2 \phi_{\text{elec}}}{dz^2} = \frac{e}{\varepsilon_r \varepsilon_0} \sum_i^N q_i [X_i] \exp \left[\frac{q_i e \phi_{\text{elec}}(z)}{k_B T} \right] \quad (9.1)$$

where N is the number of ionic species, $\phi_{\text{elec}}(z)$ is the mean electrostatic potential at a distance z normal to the surface, $[X_i]$ is the bulk concentration of ion X_i in solution and ε_r is the relative permittivity of the solvent. In this form the problem is reduced to one dimension where the planar charged surface (at $z = 0$) extends infinitely in x and y and the concentration profiles of ions are obtained in the z direction. The central tenet of PB theory is the mean-field approximation, which means that the correlated positions of individual ions in the system are neglected and only their mean

equilibrium distributions are considered. In addition to this approximation PB theory relies on several other key assumptions:

1. Only coulombic interactions between charged species are accounted for; dipole-dipole and dipole-induced dipole interactions are neglected.
2. Finite-size effects are ignored; charges are modelled as point-like objects.
3. Ions are mobile within a solvent that is considered a continuous medium with a fixed dielectric constant.

Analytical solutions to the PB equation, such as the Gouy-Chapman-Stern model [145], are only possible for very simple electrolytes. The PB equation must be solved numerically for more complex mixtures of ions, such as those encountered in the aqueous environment.

9.2 Calculation Setup

The calculation follows the methodology of Lochhead *et al.* [229] and was implemented by adapting a program originally developed to investigate the electrostatic properties of a buffer solution at the surface of cantilever arrays used as sensors [230].

9.2.1 Modelling the Solution

The model ionic solution was a mix of the potassium salts of the two oxyanions (KTcO_4 and K_2SO_4) in their fully dissociated form in water ($\epsilon_r = 78.0$). Chemical equilibria for water dissociation and subsequent protonation of the oxyanions must be considered to obtain estimates of the bulk concentrations of ions. The acid dissociation constants of water and the oxyanions are given in Table 9.1. Accounting for the possibility of oxyanion protonation, the species in solution include H^+ , OH^- , K^+ , TcO_4^- , HTcO_4 , SO_4^{2-} , HSO_4^- and H_2SO_4 . Since all the equilibria in Table 9.1 involve $[\text{H}^+]$ they are not independent of each other and must be solved self-consistently, under the conditions of fixed ionic strength

$$I = \frac{1}{2} \sum_i^N [X_i] q_i^2 \quad (9.2)$$

and pH. Initially, two different bulk solution compositions were considered at pH 7. The first calculation was performed with equal concentrations of TcO_4^- and SO_4^{2-} ($10^{-3} \text{ mol dm}^{-3}$) and the second, which contains trace concentrations of TcO_4^- ($10^{-10} \text{ mol dm}^{-3}$) compared to SO_4^{2-} ($10^{-3} \text{ mol dm}^{-3}$), is more representative of a contaminated groundwater scenario. Finally, the effect of pH on the concentration and potential profiles for the second solution composition was investigated.

| Equilibrium Reaction | $\text{p}K_a$ |
|---|---------------|
| $\text{H}_2\text{O} \leftrightarrow \text{H}^+ + \text{OH}^-$ | 14 |
| $\text{HTcO}_4 \leftrightarrow \text{H}^+ + \text{TcO}_4^-$ | 0.033 |
| $\text{H}_2\text{SO}_4 \leftrightarrow \text{H}^+ + \text{HSO}_4^-$ | -2 |
| $\text{HSO}_4^- \leftrightarrow \text{H}^+ + \text{SO}_4^{2-}$ | 1.99 |

Table 9.1 Acid dissociation constants for species in solution [108, 145].

9.2.2 Modelling the Surface

The extent to which the silanol groups on the surface of amorphous silica are ionised will determine the electrostatic potential at the surface. As discussed in Chapter Eight, since the pH_{pzc} for amorphous silica is low (2 – 3.5 [222]) the surface will be negatively charged in the range of pH (6.5 – 8.5 [32]) encountered in environmental groundwater. The calculations performed in this chapter are restricted to a planar surface, with a uniformly smeared charged density, proportional to the concentration of fully dissociated silanol groups for the amorphous silica slit pore ($[\text{SiO}^-] = 5.0 \text{ nm}^{-2}$), determined in Section 7.3.2. Cations in the electrical double layer are in equilibrium with those chemically bound to the surface, where the extent of binding is governed by the formation constant

$$K_M = \frac{[\text{SiOM}]}{[\text{SiO}^-][\text{M}^+]_0} \quad (9.3)$$

where $[M^+]_0$ is the concentration of cations at the surface. The equilibrium constants introduce chemical specificity into the ionic interactions with the surface, which are otherwise indistinguishable in PB theory. Cation binding has the effect of reducing the overall charge density of the surface.

The surface charge density after ion binding was obtained from the equation [229]

$$\sigma = \frac{-e[\text{SiO}^-]}{(1 + K_H[\text{H}^+]_0 + K_K[\text{K}^+]_0)} \quad (9.4)$$

where the local concentration of ions at the surface (or any distance from the surface) can be obtained from the Boltzmann distribution

$$[X_i]_z = [X_i] \exp \left[\frac{-q_i e \phi_{\text{elec}}(z)}{k_B T} \right] \quad (9.5)$$

Values for K_H and K_K of 10^6 [223] and 0.3162 [231] $\text{dm}^3 \text{mol}^{-1}$ were used. Here, K_H is taken from the reciprocal of K_a for amorphous silica silanols. The electrostatic potential at the surface was then calculated from the surface charge density using the Grahame equation [232]

$$\frac{\sigma}{\epsilon_r \epsilon_0} = - \sqrt{\frac{2k_B T}{\epsilon_r \epsilon_0} \sum_i^N [X_i] \left[\exp \left[\frac{-q_i e \phi_{\text{elec}}(z)}{k_B T} \right] - 1 \right]} \quad (9.6)$$

$\phi_{\text{elec}}(0)$, σ and $[X_i]_0$ were determined by solving Equations 9.3, 9.4 and 9.6 simultaneously, under the condition that the total charge of ions in solution must be equal and opposite to the charge on the surface. Once the electrostatic potential at the surface is known the full potential profile can be obtained by numerical integration of Equation 9.1. The mean concentration profiles for the ions, which are assumed to be in thermodynamic equilibrium having adjusted to the electrostatic potential profile, were then obtained using Equation 9.5.

9.2.3 Determination of Activity Coefficients

In ionic solutions interactions between individual species lead to deviations from ideal behaviour. The thermodynamic activity of a species, a_i , accounts for deviations from ideality and is related to the concentration of i by

$$a_i = \gamma_i [X_i] \quad (9.7)$$

where γ_i is the single ion activity coefficient. In solutions of almost pure water, ions only come into close contact with solvent molecules, γ_i tends to unity and a_i is equal to $[X_i]$. Ion activity coefficients in low and intermediate ionic strength solutions can be computed accurately using the Debye-Huckel and Truesdell-Jones models [32], respectively. Neither of these approaches account for effects seen at high concentrations (above 1 mol dm^{-3}), such as short-range interactions between ions of the same charge or ternary interactions, so they cannot be used for calculating activity coefficients in solutions with high ionic strengths. In the models considered here the ionic strength of bulk solutions are no greater than $4.0 \times 10^{-3} \text{ mol dm}^{-3}$. However, electrical double layer formation leads to much higher concentrations at the surface so the Pitzer model [233] is used to calculate single ion activity coefficients. The Pitzer model is a virial coefficient approach that consists of linear combinations of empirical parameters that can be used to describe the interactions between ions in the presence of a solvent. For example the activity coefficient for cation M , γ_M , is determined from the concentrations of the other cations, c and c' , and anions, a and a' , in the solution using the equation

$$\begin{aligned} \ln \gamma_M = & q_M^2 f + \sum_a [X_a] (2B_{Ma} + ZC_{Ma}) + |q_M| \sum_c \sum_a [X_c] [X_a] C_{ca} \\ & + \sum_c [X_c] \left(2\Phi_{Mc} + \sum_a [X_a] \psi_{Mca} \right) \\ & + \sum_a \sum_{a'} [X_a] [X_{a'}] \psi_{Maa'} \end{aligned} \quad (9.8)$$

where f is a function dependent on the ionic strength, B , C and Φ are the binary interaction parameters and ψ is a ternary interaction parameter. The Pitzer interaction parameters used in this work are given in Tables 9.2 and 9.3, where β^0 and β^1 are used to determine B . These parameters are consistent with the notation used in the

PHRQPITZ program [234], developed for modelling geochemical reactions in brines. Since the activity coefficient of one ion is dependent on the concentrations of all the others, which are unknown prior to the start of the calculation, they must be determined using an iterative scheme, whereby they are set to unity the first time the Grahame equation is solved. Figure 9.1 summarises the main features of the PB calculation, including the activity coefficient loop, in a flow chart.

| <i>i</i> | <i>j</i> | β^0 | β^1 | <i>C</i> | Φ |
|-----------------|-------------------------------|-----------|-----------|----------|---------|
| H ⁺ | K ⁺ | - | - | - | 0.0050 |
| H ⁺ | TcO ₄ ⁻ | 0.2162 | - | - | - |
| H ⁺ | SO ₄ ²⁻ | 0.0298 | - | 0.0438 | - |
| H ⁺ | HSO ₄ ⁻ | 0.2065 | 0.5560 | - | - |
| K ⁺ | OH ⁻ | 0.1298 | 0.3200 | 0.0041 | - |
| K ⁺ | TcO ₄ ⁻ | -0.0578 | 0.0060 | - | - |
| K ⁺ | SO ₄ ²⁻ | 0.0500 | 0.7793 | - | - |
| K ⁺ | HSO ₄ ⁻ | -0.0003 | 0.1735 | - | - |
| OH ⁻ | SO ₄ ²⁻ | - | - | - | -0.0013 |

Table 9.2 Pitzer parameters for the binary interaction between atoms *i* and *j* [235].

| <i>i</i> | <i>j</i> | <i>k</i> | Ψ |
|----------------|-------------------------------|-------------------------------|---------|
| H ⁺ | K ⁺ | SO ₄ ²⁻ | 0.1970 |
| H ⁺ | K ⁺ | HSO ₄ ⁻ | -0.0265 |
| K ⁺ | OH ⁻ | SO ₄ ²⁻ | -0.0500 |
| K ⁺ | SO ₄ ²⁻ | HSO ₄ ⁻ | -0.0677 |
| K ⁺ | SO ₄ ²⁻ | TcO ₄ ⁻ | -0.0020 |

Table 9.3 Pitzer parameters for the ternary interaction between atoms *i*, *j* and *k* [235].

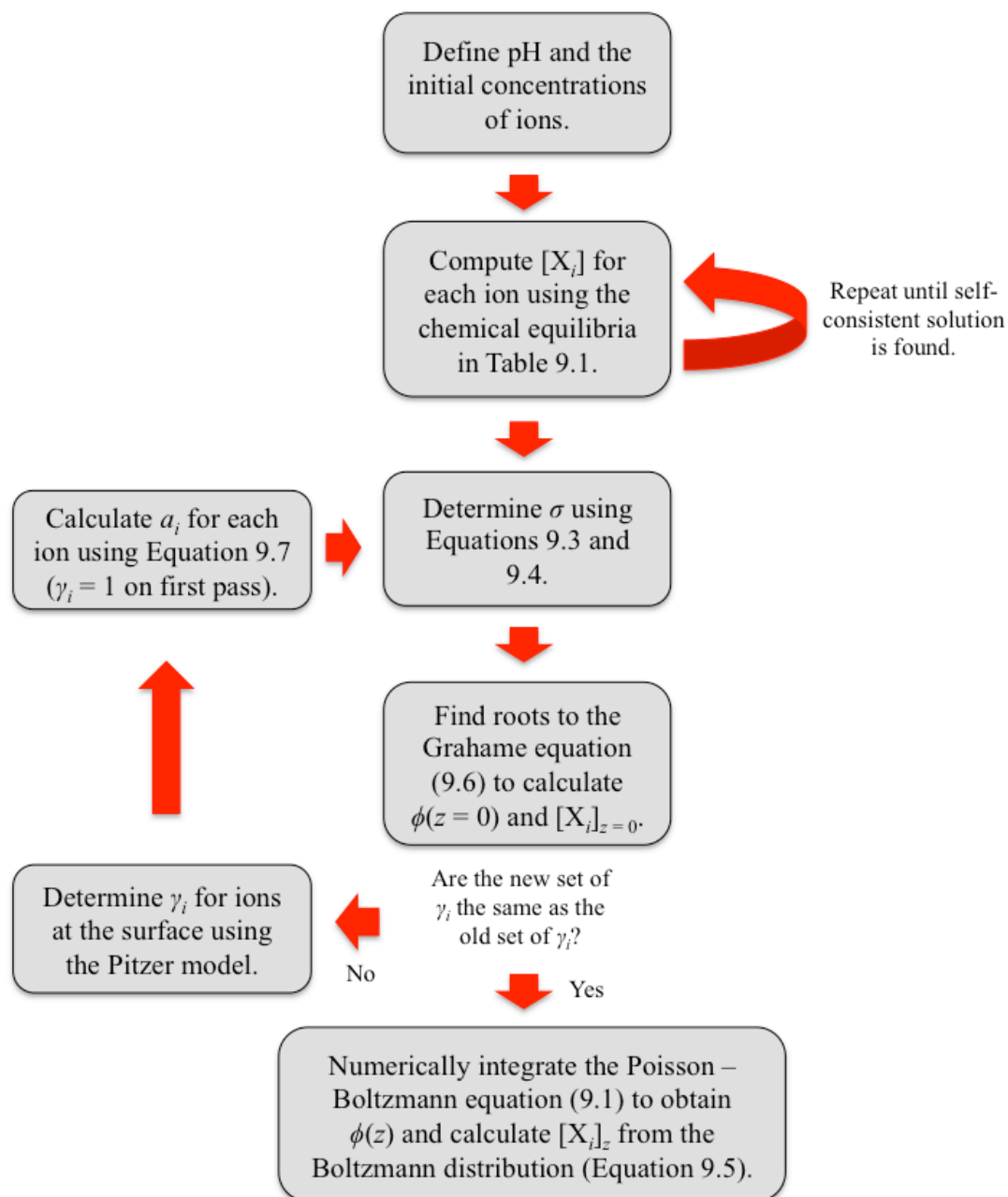


Figure 9.1 A flow chart summarising the procedure for determining the electrostatic potential profile and ion concentration profiles using Poisson-Boltzmann theory.

9.3 Results and Discussion

9.3.1 Concentration Effects

The electrostatic potential profile for the solution containing equal concentrations of SO_4^{2-} and TcO_4^- ($I = 4.0 \times 10^{-3} \text{ mol dm}^{-3}$) is given in Figure 9.2. ϕ_{elec} is most negative at the surface (-267 mV) but it increases to -108 mV at 4.0 nm . In this case the electrostatic potential decays very slowly to zero due to the combined high surface charge density and low ionic strength.

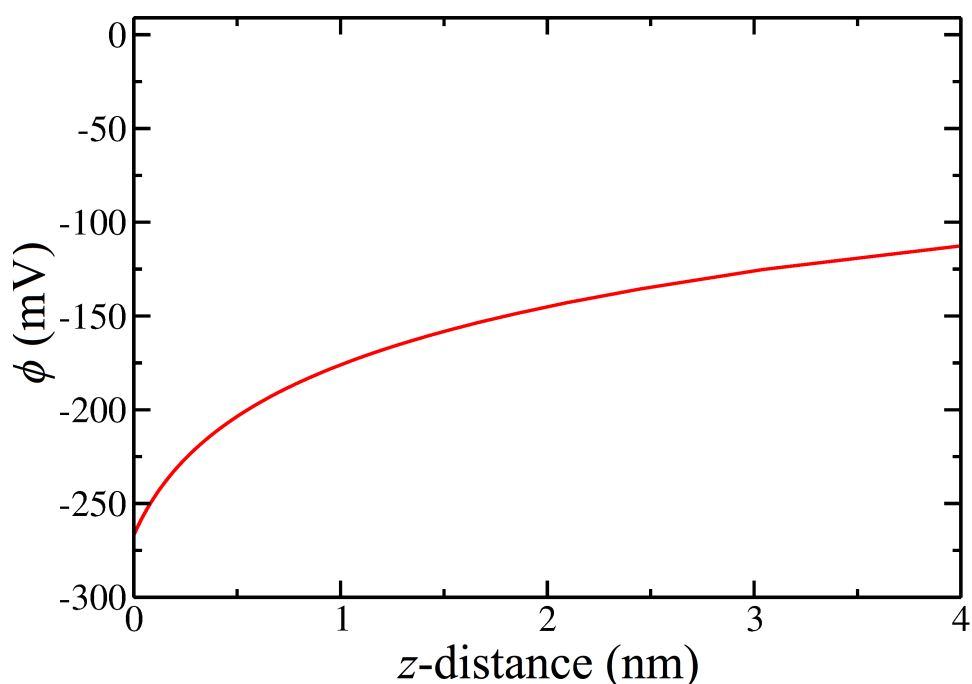


Figure 9.2 Profile of the electrostatic potential in solution near an amorphous silica surface at bulk solution pH 7.

Figure 9.3 shows the concentration profiles of the ionic species in solution near the amorphous silica surface. The fully protonated oxyanions (HTcO_4 and H_2SO_4) are omitted from the figure since they are neutral and therefore not considered in the PB theory. HSO_4^- is also omitted as it is present only in very minor concentrations compared to the fully deprotonated ion at this pH. The increase in H^+ and K^+ concentrations near the surface relative to the bulk indicate the formation of an electrical double layer. The concentrations of cations at the surface were $[\text{H}^+] = 2.89 \times 10^{-4} \text{ mol dm}^{-3}$ (pH 3.54) and $[\text{K}^+] = 8.66 \text{ mol dm}^{-3}$. Adsorption of cations to the surface acts to neutralize the surface charge; the percentages of sites

neutralized by H^+ and K^+ were 20% and 59% respectively, leaving 21% ionized sites. Conversely, the concentration of anions is depleted near the surface, due to electrostatic repulsion. This effect is far more significant for dianions than monoanions ($[\text{SO}_4^{2-}] = 5.89 \times 10^{-17} \text{ mol dm}^{-3}$ vs. $[\text{TcO}_4^-] = 2.73 \times 10^{-9} \text{ mol dm}^{-3}$), due to greater electrostatic repulsion and the exponential dependence on charge in Equation 9.1.

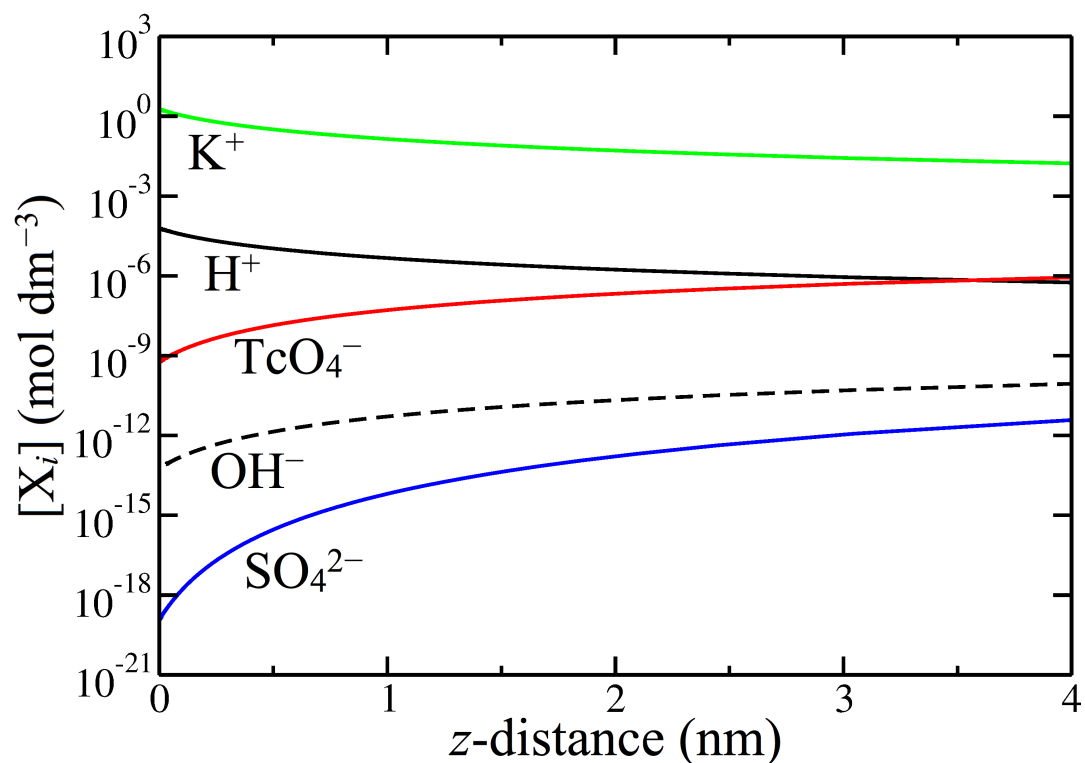


Figure 9.3 Ion concentration profiles for a solution containing $10^{-3} \text{ mol dm}^{-3}$ concentrations of KTcO_4 and K_2SO_4 at pH 7 in contact with an amorphous silica surface. Concentrations of H^+ (solid) and OH^- (dashed) ions are shown with a black line and K^+ , TcO_4^- and SO_4^{2-} are shown with green, red and blue lines, respectively.

The solution composition used to generate the concentration profiles in Figure 9.3 is unrealistic in a contaminated groundwater situation where SO_4^{2-} would be present in vast excess compared to TcO_4^- . The second calculation, in which the initial concentration of SO_4^{2-} ($[\text{K}_2\text{SO}_4] = 10^{-3} \text{ mol dm}^{-3}$) is seven orders of magnitude greater than TcO_4^- ($[\text{KTcO}_4] = 10^{-10} \text{ mol dm}^{-3}$), addresses such a situation. In this case the solution ionic strength ($I = 3.0 \times 10^{-3} \text{ mol dm}^{-3}$) is dominated by K_2SO_4 . When in contact with this solution the surface has a smaller percentage of sites bound by cations, due to the decrease in concentration of K^+ . The percentage of charged

surface sites bound by H^+ and K^+ are 26% and 53%, leaving 21% of sites ionized. The electrostatic potential at the surface is more negative than in the previous case (-274 mV), decreasing to -114 mV at 4.0 nm. The concentration profiles for this solution are shown in Figure 9.4. At large distances from the surface the concentrations of the two oxyanions tend toward their bulk concentration ($[\text{SO}_4^{2-}] > [\text{TcO}_4^-]$). At distances of less than 1.0 nm from the surface this trend is reversed ($[\text{TcO}_4^-] > [\text{SO}_4^{2-}]$) due to the increased electrostatic repulsion felt by the dianionic SO_4^{2-} compared to the monoanionic TcO_4^- . At the surface the concentration of TcO_4^- is 531 times greater despite the concentration of SO_4^{2-} being seven orders of magnitude higher in bulk solution.

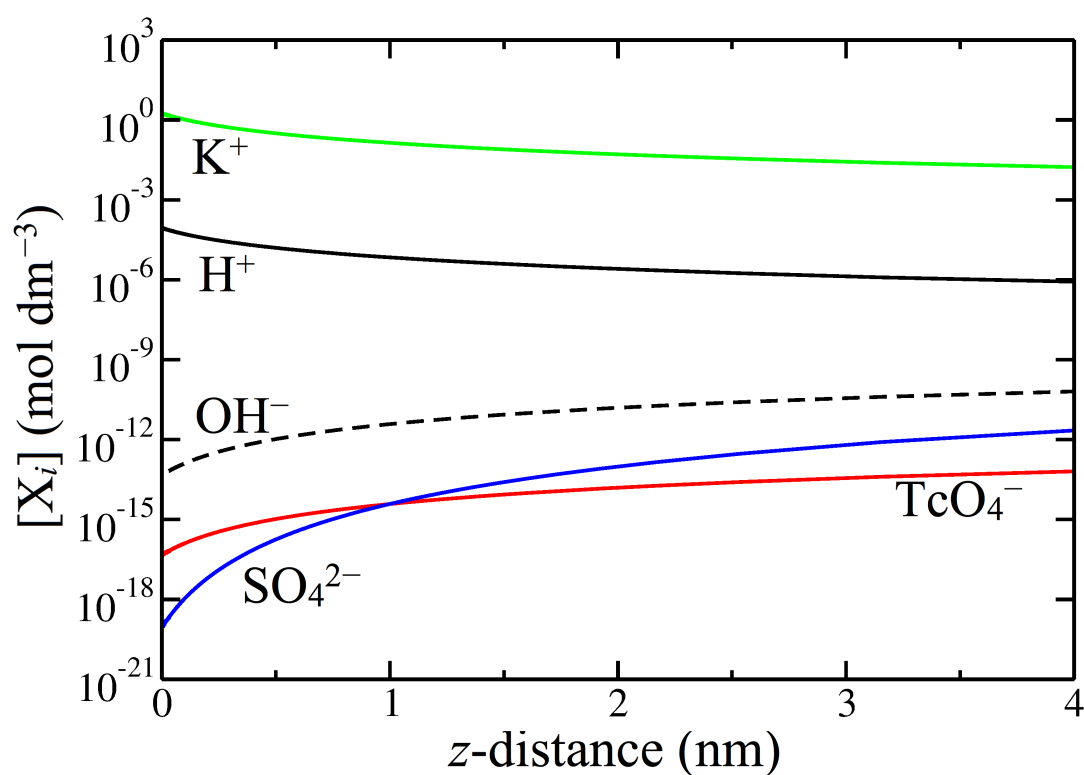


Figure 9.4 Ion concentration profiles for a solution containing 10^{-3} mol dm^{-3} of K_2SO_4 and 10^{-10} mol dm^{-3} of KTcO_4 at bulk pH 7 in contact with an amorphous silica surface. Concentrations of H^+ (solid) and OH^- (dashed) ions are shown with a black line and K^+ , TcO_4^- and SO_4^{2-} are shown with green, red and blue lines, respectively.

9.3.2 pH Effects

In an experiment it may be possible to vary the pH of a sample of contaminated water in order to affect the relative concentrations of ions near the surface of an adsorbent

material. The effect of changing the pH on the electrostatic potential profile using a solution with the same bulk oxyanion concentrations ($1.0 \times 10^{-10} \text{ mol dm}^{-3}$ (KTcO₄) and $1.0 \times 10^{-3} \text{ mol dm}^{-3}$ (K₂SO₄)) is shown in Figure 9.5. As the bulk solution pH increases, the H⁺ ion concentration at the surface decreases, resulting in a greater percentage of ionized surface sites. This makes the electrostatic potential near the surface more negative. At bulk pH 1 only 0.2% of surface silanols are ionized and the electrostatic potential at the surface is consequently much lower (−15.2 mV) compared to the surface in contact with a solution with bulk pH 7 (−274 mV). However, calculations performed at a bulk pH below that the pH_{pzc} of the surface (2 – 3.5) are unrealistic since the model does not account for the possibility of the surface becoming fully protonated. At this point SiOH₂⁺ groups are thought to dominate the amorphous silica surface, resulting in a net positive charge. The model can therefore only be deemed useful for solutions that have a pH several units greater than the pH_{pzc} of the surface.

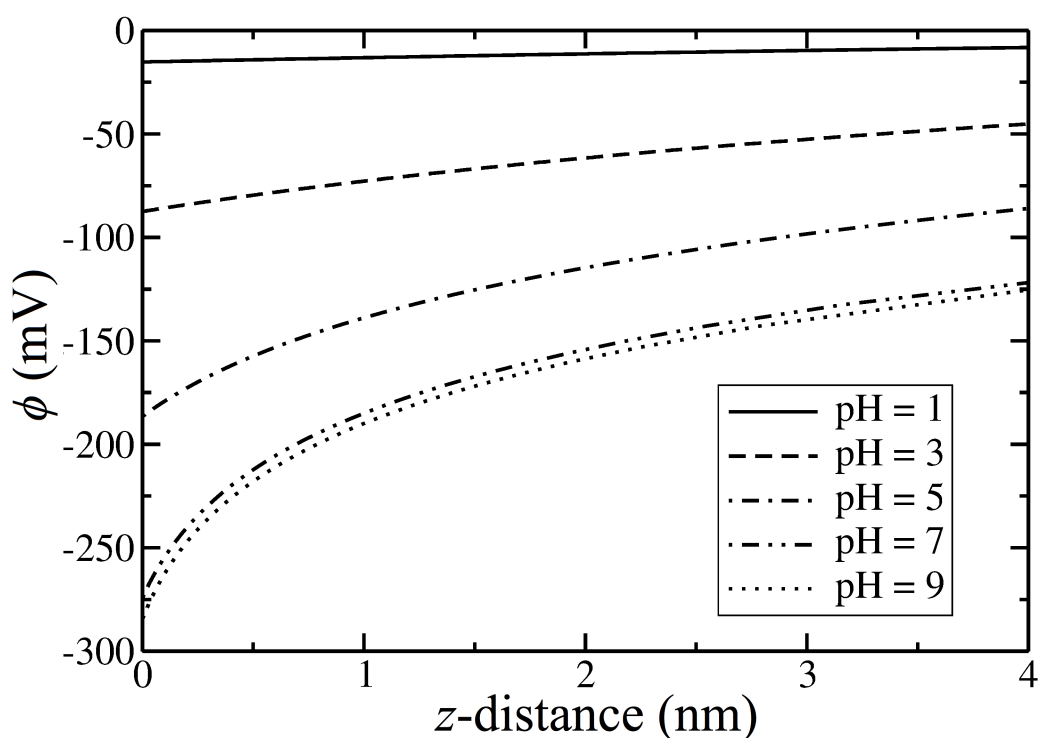


Figure 9.5 Effect of bulk pH on electrostatic potential near the charged amorphous silica surface.

The effect of bulk pH on the concentrations of oxyanions 1.0 nm from the surface is shown in Figure 9.6. The values obtained at pH 7 correspond to the crossover in the

TcO_4^- and SO_4^{2-} concentrations shown previously in Figure 9.4. Table 9.4 shows the surface potential and the resulting concentrations of oxyanions at 1.0 nm for solutions with pH 4 – 9. At low pH the concentration of SO_4^{2-} was found to be several orders of magnitude greater than TcO_4^- . As the magnitude of the surface charge was increased (increasing bulk pH) electrostatic repulsion from the surface increased. This effect has a more significant impact on the SO_4^{2-} concentration profile. At pH 7 the concentrations of the two oxyanions are very similar and as the bulk pH is increased further TcO_4^- becomes the dominant species in this region. Above pH 9 there is little change in the relative concentrations as further decreases in $[\text{H}^+]$ do not affect the percentage of ionized surface sites as K^+ is the dominant bound cation. If the model could account for a fully protonated surface it would become positively charged at low pH and the concentration of oxyanions near the surface would actually be greater than in bulk solution. The electrical double layer would then be dominated by SO_4^{2-} due to its higher charge than the other anions in this system (OH^- and TcO_4^-).

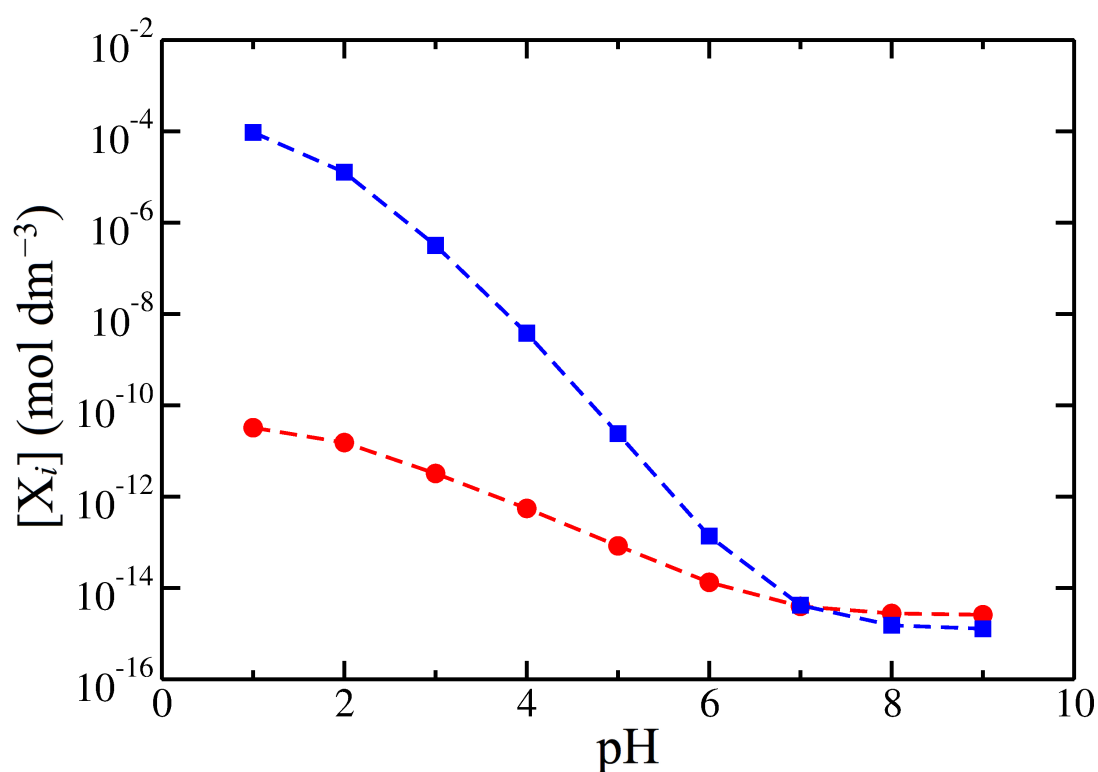


Figure 9.6 Dependence of $[\text{TcO}_4^-]$ (red, circles) and $[\text{SO}_4^{2-}]$ (blue, squares) on bulk solution pH, 1.0 nm from the surface.

| pH | Ionised Surface Sites (%) | ϕ_{elec} (mV) | $[TcO_4^-]$ (mol dm ⁻³) | $[SO_4^{2-}]$ (mol dm ⁻³) |
|----|---------------------------|--------------------|-------------------------------------|---------------------------------------|
| 4 | 3.2 | -106.7 | 5.52×10^{-13} | 3.81×10^{-9} |
| 5 | 6.8 | -138.9 | 8.34×10^{-14} | 2.41×10^{-11} |
| 6 | 13.5 | -166.9 | 1.33×10^{-14} | 1.37×10^{-13} |
| 7 | 20.7 | -184.2 | 3.96×10^{-15} | 4.19×10^{-15} |
| 8 | 23.1 | -187.5 | 2.77×10^{-15} | 1.52×10^{-15} |
| 9 | 23.4 | -188.6 | 2.60×10^{-15} | 1.28×10^{-15} |

Table 9.4 The effect of bulk pH on the extent of surface ionisation, electrostatic potential and oxyanion concentration, 1.0 nm from the surface.

9.4 Conclusions

Oxyanions are repelled from amorphous silica due to its high surface charge density when it is in contact with a solution that has a pH greater than its pH_{pzc} . Repulsion of the divalent SO_4^{2-} anion is greater than for the monovalent TcO_4^- . As a result, at pH 7, the concentration of TcO_4^- is much larger than SO_4^{2-} at distances less than 1 nm from the surface, even when its bulk concentration is seven orders of magnitude smaller. This effect is likely to be enhanced in MCM-41 where ionic solutions are confined in a cylindrical pore, leading to the possibility of ions being prevented from entering the pore. However, in SAMMS this effect will only be important for a low density monolayer of propyl-EDA, where many silanols remain unfunctionalised. The results also suggest that this effect is strongly dependent on the bulk pH of the solution.

The PB calculations, which allow equilibrium ion concentrations to be determined, are only made possible because of a number of fundamental assumptions. Despite the introduction of chemical specificity using the equilibrium constants and Pitzer model there is an inherent loss of detail compared to atomistic simulations. The mean-field approximation may not be valid for the case of divalent ions near a surface and entropic effects (which are significantly different for solvated mono- and divalent

ions) are ignored completely. In addition, the assumption that the solvent can be treated as a dielectric continuum is hard to justify near to the interface of a highly charged surface, such as for amorphous silica, where significant water ordering is likely.

Chapter Ten

Conclusions

Highly selective materials are required both for the remediation of land already contaminated with radioactive ions and for potential deployment in the near-field region of proposed nuclear waste repositories. Radioactive ions can prove difficult to clean up due to the variable pH/ E_h conditions and relatively high concentrations of competing species found in groundwater. SAMMS is a material that has previously been shown to be an effective adsorbent for the remediation of trace levels of environmental contaminants due to a combination of its highly selective chemical interface and the stability provided by the amorphous silica MCM-41 support. In the case of oxyanions, experiments have shown monolayers of transition metal EDA complexes to be selective for monovalent ions over divalent ions. As a result this material offers considerable promise for the removal of the problematic ^{99}Tc , present as TcO_4^- , which is often inhibited by the presence of competing ions. Only once the reasons for the selectivity of SAMMS have been properly understood can the materials designer optimise its structure and chemistry to maximise selectivity for the TcO_4^- ion.

The first aim of this work was to construct a realistic atomistic model of the SAMMS material. Although some models of functionalised MCM-41 have previously been reported (for simulating the adsorption of CO_2 , with relevance for carbon capture and storage technology) we believe the model reported here is the first of functionalised MCM-41 for use as an adsorbent in aqueous solution. The second aim of this study was to use the model to gain further insight into the cause of the material's selectivity for TcO_4^- (and therefore other monovalent oxyanions) over common competing anions, such as SO_4^{2-} . At the start of this thesis it was hypothesised that the selectivity for monovalent oxyanions was partly due to the mesoscopic structure of the material and not solely dependent on the chemistry at the monolayer complex.

This chapter summarises the main conclusions from the work, with particular emphasis on suggestions for how the designer of SAMMS could optimize its structure in order to enhance its selectivity, followed by some general remarks about TcO_4^-

remediation. In addition, the suitability of modelling methods applied in this work is assessed. Finally, the scope for future improvements to the models and proposals for additional simulations are discussed.

10.1 Summary of Key Findings

Based purely on an electrostatic argument the Fe^{3+} -EDA complex in SAMMS would be expected to have a much greater affinity for SO_4^{2-} than TcO_4^- . The PMFs obtained for oxyanion adsorption to the *trans*- $[\text{Fe}(\text{EDA})_2(\text{Cl})_2]^+$ complex support this prediction. The free energy of ligand exchange of SO_4^{2-} for Cl^- ($\Delta G_{\text{ex,aq}} = -60.0 \text{ kJ mol}^{-1}$) was more favourable than the equivalent TcO_4^- exchange ($\Delta G_{\text{ex,aq}} = -26.4 \text{ kJ mol}^{-1}$), indicating that the presence of SO_4^{2-} may inhibit TcO_4^- adsorption in aqueous solution. This is contrary to the experimental observations so the validity of the assumption that only the chemistry of the Fe^{3+} -EDA complex in the monolayer need be considered should be questioned. It was also observed that in the *cis* isomer of the complex adjacent Cl^- ligands repel SO_4^{2-} more than TcO_4^- , indicating that improvements to the selectivity could be achieved by engineering the monolayer to have *cis* complexes.

In Chapter Seven models of the mesoporous inorganic support in SAMMS, MCM-41, were constructed using an MD melt-quench scheme. The simple models of MCM-41 were sufficiently accurate to predict the adsorption isotherm and the isosteric heat of adsorption for CO_2 . The approach taken lends itself to easily varying the structural parameters of the material such as its pore diameter and wall thickness. Then, in the following chapter, one of the MCM-41 models (chosen to match the pore diameter of the material used in oxyanion adsorption experiments of Yoshitake *et al.* [106]) was functionalised with propyl-EDA chains. During a gas phase MD simulation of the functionalised surface the monolayer groups lie flat on the amorphous silica surface. However, after the pore had been filled with H_2O and simulated for a further 100 ps the propyl chains stand up into solution. This observation helps to explain the difference in the low monolayer densities reported by Yoshitake *et al.* [106] (prepared in the complete absence of H_2O) and the much higher densities obtained by Fryxell *et al.* [105] (prepared with one or two monolayers of water). It was proposed that in dry conditions the propyl-EDA chains lie flat on the surface and act to inhibit the grafting of additional chains. The model of $[\text{Fe}(\text{EDA})_2(\text{Cl})_2]^+$ functionalised MCM-41 (which

can be visualised in Figure 8.7) is thought to be an accurate representation of the real oxyanion adsorbent material synthesised by Yoshitake *et al.* [106]. After addition of the third charge-balancing Cl^- to the pore, an MD simulation showed that these ions interact weakly with the EDA ligands in the positively charged monolayer.

In Chapter Eight the transfer of oxyanions from bulk solution to the propyl-EDA functionalised pore was simulated. Entry of SO_4^{2-} into the pore was accompanied by a more significant free energy barrier ($\Delta F_{\text{barrier}} = 37.4 \text{ kJ mol}^{-1}$) than TcO_4^- entry ($\Delta F_{\text{barrier}} = 23.7 \text{ kJ mol}^{-1}$). The difference was a result of deprotonation of silanols (due to their low $\text{p}K_a$) on the amorphous silica surface that create a negative electrostatic potential in the pore, repelling divalent anions to a greater extent than monovalent ones. In reality, cations in solution would form an electrical double layer, reducing the charge density of the surface. Atomistic simulations are not well suited to studying the electrical double layer due to the long equilibration times required for systems involving strong electrostatic interactions in solution. Instead, the equilibrium properties of such a system were investigated using PB theory. The results of these calculations showed that SO_4^{2-} is repelled from the amorphous silica surface to a greater extent than TcO_4^- . The effect is dependent on the pH of the contacting ionic solution; at low bulk pH more of the silanols are protonated, reducing the charge density of the surface. Such an effect would only become significant in SAMMS if it had a low monolayer density, as there would still be a high percentage of unmodified silanols on the surface. However, a low monolayer density would reduce the overall oxyanion capacity of SAMMS, as there would be fewer Fe^{3+} adsorption sites.

When $[\text{Fe}(\text{EDA})_2(\text{Cl})_2]^+$ complexes in the monolayer are formed by the addition of FeCl_3 , the pore surface is no longer defined by the amorphous silica. Instead, the positively charged monolayer should be considered as the surface. It is charge-balanced by an electrical double layer consisting of Cl^- ions, which generates a negative potential in the pore solution. At the centre of the pore the mean electrostatic potential in our model was found to be -0.92 V , calculated using the Ewald sum. Reliable free energy barriers associated with oxyanion entry into the $[\text{Fe}(\text{EDA})_2(\text{Cl})_2]^+$ functionalised pores could not be obtained from umbrella sampling due to the repulsion of Cl^- ions from the pore into bulk solution, reducing the pore's electrostatic potential. However, using the calculated electrostatic potential in the centre of the pore the barriers were estimated for each oxyanion ($\Delta F_{\text{barrier}} =$

89 kJ mol⁻¹ for TcO₄⁻ and $\Delta F_{\text{barrier}} = 178$ kJ mol⁻¹ for SO₄²⁻). Therefore, SO₄²⁻ is likely to be prevented from entering the negatively charged pore in the first place, despite the preference of SO₄²⁻ to bind to an isolated Fe³⁺-EDA complex. It is important to note that these results not only have implications for TcO₄⁻ remediation with SAMMS but also for the removal of many other problematic oxyanion contaminants, such as H₂AsO₄⁻.

10.2 General Remarks for TcO₄⁻ Remediation

Since ion adsorption processes involve the transfer of an ion from its hydrated phase to the adsorbed phase on the surface of a material it is crucial to understand the properties of an ion in aqueous solution in addition to the chemistry of the adsorbent. TcO₄⁻ and SO₄²⁻ display extremely contrasting properties in aqueous solution. In Chapter Five some of these were investigated using MD simulations and summarised in Table 5.10. The differences are generally due to the much lower charge density of TcO₄⁻ than SO₄²⁻. The small and highly charged SO₄²⁻ forms stronger hydrogen bonds with H₂O (Figure 5.4), resulting in well-defined hydration shells (Figure 5.3) compared to TcO₄⁻, which only weakly interacts with H₂O. The relative strength of ionic interactions with H₂O are commonly described by the Hofmeister series [154]. The differences between the interactions of each oxyanion with water result in the experimental ΔG_{hyd} for SO₄²⁻ (-1064 kJ mol⁻¹ [154]) being approximately four times larger than ΔG_{hyd} for TcO₄⁻ (-251 kJ mol⁻¹ [108]). It is no coincidence that two of the anions that pose the most significant remediation challenges to the nuclear industry (TcO₄⁻ and I⁻) both have very low ΔG_{hyd} (-280 kJ mol⁻¹ [154]) compared to other competing species. Ions at the weakly hydrating end of the Hofmeister series are extremely mobile in the environment (the tracer diffusion coefficient of TcO₄⁻ in H₂O was calculated in Section 5.4.2) and adsorbent materials could be designed to exploit this. For instance, since TcO₄⁻ has such a low ΔG_{hyd} and does not induce any long-range order in H₂O beyond its primary hydration shell, the effects of porous confinement, which serves to partially dehydrate the anion, should be small. However, partial dehydration of the strongly hydrating SO₄²⁻ anion, which has a well-defined secondary hydration shell, must come at a significant free energy cost. This effect was observed to some extent in Section 8.4.5 where the number of H₂O molecules in the secondary hydration shell of SO₄²⁻ was reduced in the pore compared to the number in bulk solution. The pore diameters of SAMMS are too

large to properly investigate this effect. However, there is considerable potential for the use of well defined nanoporous materials (eg. graphene oxide membranes [227]) to exploit Hofmeister effects and filter highly mobile and low charge density ions such as TcO_4^- .

10.3 Suitability of Computational Modelling Techniques

The novel multiscale approach to building models of SAMMS presented here captures both the chemical specificity of the monolayer complex and the overall mesoscopic structure of the material. In order to make the construction of such a model feasible a pragmatic approach to constructing the models was sometimes adopted. For instance, it cannot be argued that the MCM-41 model includes the same level of detail as some others proposed in the literature [195]. Despite this, the simulated adsorption isotherm for CO_2 in MCM-41 was in excellent agreement with experiment. In addition, the relative simplicity of the model means that its structural parameters can easily be modified to optimise its performance as an adsorbent. A pragmatic approach was also taken to functionalising the MCM-41 surface with the monolayer, which involved swapping silanol groups for the propyl-EDA chain. Chaffee's method [218], in which the chains were swapped to new grafting sites until an energy minimum was found, would result in a more realistic monolayer structure.

The use of DFT calculations in conjunction with an implicit solvation model resulted in errors of approximately 10% in anion ΔG_{hyd} . No experimental ΔG_{hyd} data was available for the Fe^{3+} -EDA complexes, but the size of the errors are likely to be similar. An approach to determining $\Delta G_{\text{ex,aq}}$ for ligands on the complex purely based on DFT calculations was therefore deemed unsuitable in this work. Conversely, modelling this process using standard transferable force fields fails to capture the chemical specificity of the interaction between the transition metal complex and the two oxyanions, which have very different polarisabilities. The development of ligand specific Fe^{3+} VDW parameters is therefore justified, and was achieved in this work by fitting classical force field parameters to DFT calculations. By incorporating the specificity for ligands into the Fe^{3+} parameters rather than the oxyanions, the oxyanion force fields remain transferable. If a polarisable model of the oxyanions existed this would eliminate the need for ligand specific parameters altogether.

Umbrella sampling was both useful for studying the adsorption of oxyanions to the Fe^{3+} -EDA complex and for simulating their entry into the pore. However, the method has some serious limitations. For instance, in order to simulate the process of oxyanions entering the pore using umbrella sampling a simulation cell that contains both the pore and a water reservoir was required. Unfortunately, this allows the Cl^- counterions to diffuse out of the pore and into the bulk solution. In addition, for the umbrella sampling technique to work well there is a need for good overlap in sampling over the entire reaction coordinate studied. Large force constants are required to sample regions of the reaction coordinate where the PMF profile is steep (eg. at ligand exchange in Figure 6.12) so many simulation windows are needed in these situations.

10.4 Scope for Further Work

10.4.1 Model Development

Polarisable oxyanion force fields could be implemented using the Drude particle method [236], where a charged particle is connected to an atom by a harmonic spring, and polarisation is represented by displacement of this particle under the influence of a local electric potential. The polarisability of ions can be tuned by adjusting the strength of the spring and the magnitude of the charge on the Drude particle. Oxyanion force fields could be further validated by accurate determination of ΔG_{hyd} . The thermodynamic integration technique, which can be used to measure the free energy change between two states by slowly varying control parameters, is well suited to the problem of determining ionic hydration free energies [237].

GCMC simulations could be used to obtain the adsorption isotherm CO_2 in the propyl-EDA functionalised MCM-41 in order to validate it against available experimental data [219]. The low pressure region of this isotherm could be used to optimize the force field parameters for the propyl-EDA chains, using a similar approach to the fitting of bare MCM-41 parameters in Chapter Seven.

The overall strategy of fitting a classical force field to the QM potential energy surface to capture the monolayer specificity, combined with the generation of simple atomistic MCM-41 models, followed by swapping the functional groups for surface silanols, could be repeated to build a model of any SAMMS material. Using many of

the same force field parameters as in this work, the functionalised model could easily be adapted to conduct simulations relevant to other challenging remediation problems, eg. for the removal of Hg^{2+} using thiol-SAMMS [95]. Once force field parameters that capture the specific nature of the Hg^{2+} – thiol interaction are obtained (by fitting to QM calculations), this would simply involve swapping the propyl-EDA groups in the monolayer for thiol functionalities.

10.4.2 Additional Simulations

Since umbrella sampling was deemed unsuitable for obtaining the free energy change of an oxyanion entering the $[\text{Fe}(\text{EDA})_2(\text{Cl})_2]^+$ functionalised pore, alternative techniques are required. The simplest way of finding the relative free energy difference between the two oxyanions entering the pore would be to simulate TcO_4^- in the periodic ‘closed’ pore model and gradually transform it into SO_4^{2-} using thermodynamic integration. The difference in free energy obtained from this calculation could then be compared to the estimate based on the mean electrostatic potential in the pore, calculated in Section 8.4.4.

The reaction ensemble Monte Carlo (RxMC) method [238] combines normal MC sampling with trial moves that account for chemical reactions by the formation and destruction of chemical bonds. This technique has previously been used to simulate chemical adsorption processes with large free energy barriers in porous materials [239] and is therefore ideally suited to address the problem described in this thesis. It could also be used to obtain distribution coefficients that are directly comparable to experiment.

The continuum model described in Chapter Nine, based on PB theory, addresses the problem of oxyanions in a solution in contact with a charged amorphous silica surface. Such a situation is only relevant in SAMMS when the monolayer density is very low. An extension of this work would involve defining the pore surface as the position of the positively charged monolayer rather than the deprotonated amorphous silica. Intrinsic ion binding constants, required for the weakly interacting Cl^- binding to the complex could be obtained from atomistic simulations. If the model was further adapted to deal with a cylindrical geometry rather than a planar one, calculated equilibrium electrostatic potential profiles similar to Figure 9.1, could be directly

compared with those calculated using the Ewald summation in the atomistic simulations.

Prior to using oxyanion-SAMMS in a real remediation scenario, process models could be used to assess their practicality and cost-effectiveness on an industrial scale. Commercial software, previously developed for process modelling of ion-exchange zeolites, could be used for this purpose. In addition, before deployment the resistance of the organic monolayer to radiation damage would have to be investigated to establish whether release of radioisotopes from the monolayer could occur. This issue would be much more significant for the clean up of higher activity radioisotopes such as ^{137}Cs or ^{90}Sr , rather than ^{99}Tc , which is a relatively low activity β -emitter.

References

1. *Climate Change Synthesis Report*, Intergovernmental Panel on Climate Change (IPCC), **2014**.
2. *Managing Radioactive Waste Safely: A Framework for Implementing Geological Disposal*, UK Government White Paper number Cm7386, **2008**.
3. *Spent nuclear fuel for disposal in the KBS-3 repository*, Technical Report TR-10-13, SKB, **2010**.
4. Beswick A. J., Gibb F. G. F., Travis K. P., *Proceedings of the ICE - Energy*, **2014**, 167, 47-66.
5. *Generic Repository Studies: Generic post-closure Performance Assessment Report number N/080*, UK Nirex Limited, **2003**.
6. *Monitoring our Environment: Discharges and Monitoring in the United Kingdom, Annual Report*, Sellafield Ltd, **2013**.
7. Serne R. J., Rapko B. M., *Technetium Inventory, Distribution and Speciation in Hanford Tanks*, Pacific Northwest National Laboratory, **2014**.
8. Feng X., Fryxell G. E., Wang L. Q., Kim A. Y., Liu J., Kemner K. M., *Science*, **1997**, 276, 923-926.
9. Frenkel D., Smit B., *Understanding Molecular Simulation, From Algorithms to Applications*, 2nd Ed., Academic Press, **2002**.
10. Perrier C., Segre E., *Journal of Chemical Physics*, **1937**, 5, 712-716.
11. Perrier C., Segre E., *Nature*, **1937**, 140, 193-194.
12. Boyd G. E., Sites J. R., Larson Q. V., Baldock C. R., *Physical Review*, **1955**, 99, 1030-1031.
13. Curtis D. B., Benjamin T. M., Gancarz A. J., *Oklo reactors: natural analogs to nuclear waste repositories*, US DOE, **1981**.

14. Kenna B. T., Kuroda P. K., *Journal of Inorganic & Nuclear Chemistry*, **1961**, 23, 142-144.
15. Icenhower J. P., Qafoku N. P., Martin W. J., Zachara J. M., *The Geochemistry of Technetium: A Summary of the Behaviour of an Artificial Element in the Natural Environment*, Pacific Northwest National Laboratory, **2008**.
16. Garten C. T., *Environment International*, **1987**, 13, 311-321.
17. Garcia-Leon M., *The Japan Society of Nuclear and Radiochemical Sciences*, **2005**, 6, 253-259.
18. Smith V., Fegan M., Pollard D., Long S., Hayden E., Ryan T. P., *Journal of Environmental Radioactivity*, **2001**, 56, 269-284.
19. *Annual Reports on Discharges and Monitoring of the Environment in the United Kingdom*, British Nuclear Fuels Ltd, **2002**.
20. Aarkrog A., Dahlgaard H., Hallstadius L., Holm E., Mattson S., Rioseco J., *Technetium in the Environment*, Elsevier Appl. Sci. Pub., **1986**.
21. Aarkrog A., Carlsson L., Chen Q. J., Dahlgaard H., Holm E., Huynhngoc L., Jensen L. H., Nielsen S. P., Nies H., *Nature*, **1988**, 335, 338-340.
22. Seaborg G. T., Segre E., *Physical Review*, **1939**, 55, 0808-0814.
23. McAfee J. G., Thakur M. L., *Journal of Nuclear Medicine*, **1976**, 17, 480-487.
24. Jurisson S. S., Lydon J. D., *Chemical Reviews*, **1999**, 99, 2205-2218.
25. Schwochau K., *Technetium. Chemistry and Radiopharmaceutical Applications* Wiley-VCH, **2000**.
26. Kuhl D. E., Edwards R. Q., *Radiology*, **1963**, 80, 653-662.
27. Lieser K. H., Bauscher C., *Radiochimica Acta*, **1987**, 42, 205-213.
28. Hidaka H., Shinotsuka K., Holliger P., *Radiochimica Acta*, **1993**, 63, 19-22.
29. Parnell J., *Mineralogical Magazine*, **1996**, 60, 581-593.

30. Schulte E. H., Scoppa P., *Science of the Total Environment*, **1987**, 64, 163-179.
31. Aarkrog A., Boelskifte S., Dahlgaard H., Duniec S., Hallstadius L., Holm E., Smith J. N., *Estuarine Coastal and Shelf Science*, **1987**, 24, 637-647.
32. Langmuir D., *Aqueous Environmental Geochemistry*, Prentice-Hall, **1997**.
33. Newcomer D. R., Thornton E. C., Liikala T. L., *Groundwater Chemistry and Hydrogeology of the Upper Saddle Mountains Basalt-Confined Aquifer South and Southeast of the Hanford Site*, US DOE, **2002**.
34. Schulthess C. P., Wijnja H., Yang W., *Sorption: Oxyanions in Encyclopedia of Soils in the Environment*, Elsevier, **2005**, 548-555.
35. Routson R. C., Jansen G., Robinson A. V., *Health Physics*, **1977**, 33, 311-317.
36. Wolfrum C., Bunzl K., *Journal of Radioanalytical and Nuclear Chemistry-Articles*, **1986**, 99, 315-323.
37. Wildung R. E., McFadden K. M., Garland T. R., *Journal of Environmental Quality*, **1979**, 8, 156-161.
38. van Loon L. R., Desmet G. M., Cremers A., *The Influence of the chemical form of technetium on its uptake by plants in Speciation of Fission and Activation Products in the Environment*, Oxford, **1985**.
39. The Ionising Radiations Regulations 1999 (IRR99), Government Statute, 3232, United Kingdom.
40. Cataldo D. A., Wildung R. E., Garland T. R., *Plant Physiology*, **1983**, 73, 849-852.
41. Khalil F. Y., Aksnes G., *Acta Chemica Scandinavica*, **1973**, 27, 3832-3838.
42. Aldridge S., Warwick P., Evans N., Vines S., *Chemosphere*, **2007**, 66, 672-676.

43. Palmer D. A., Meyer R. E., *Journal of Inorganic & Nuclear Chemistry*, **1981**, 43, 2979-2984.
44. Vandergraaf T. T., Ticknor K. V., George I. M., *Reactions Between Technetium in Solution and Iron-Containing Minerals Under Oxidic and Anoxic Conditions in Geochemical Behavior of Disposed Radioactive Waste*, 246, American Chemical Society, **1984**.
45. Wildung R. E., Li S. W., Murray C. J., Krupka K. M., Xie Y., Hess N. J., Roden E. E., *Fems Microbiology Ecology*, **2004**, 49, 151-162.
46. Cui D. Q., Eriksen T. E., *Environmental Science & Technology*, **1996**, 30, 2259-2262.
47. Cui D. Q., Eriksen T. E., *Environmental Science & Technology*, **1996**, 30, 2263-2269.
48. Byegard J., Albinsson Y., Skarnemark G., Skälberg M., *Radiochimica Acta*, **1992**, 58-9, 239-244.
49. Lieser K. H., Bauscher C., *Radiochimica Acta*, **1988**, 44-5, 125-128.
50. Zhang P. C., Krumhansl J. L., Brady P. V., *Radiochimica Acta*, **2000**, 88, 369-373.
51. Winkler A., Bruhl H., Trapp C., Bock W. D., *Radiochimica Acta*, **1988**, 44-5, 183-186.
52. Anderson B. E., Becker U., Helean K. B., Ewing R. C., *Perrhenate and pertechnetate Behavior on iron and sulfur-bearing compounds in 30th Symposium on Scientific Basis for Nuclear Waste Management*, Materials Research Society, Boston, MA, **2006**.
53. Watson J. H. P., Ellwood D. C., *Nuclear Engineering and Design*, **2003**, 226, 375-385.
54. Elwear S., German K. E., Peretrukhin V. F., *Journal of Radioanalytical and Nuclear Chemistry-Articles*, **1992**, 157, 3-14.

55. Bird G. W., Lopata V. J., *Solution Interaction of Nuclear Waste Anions with Selected Geological Materials in Scientific Basis for Nuclear Waste Management, International Symposium on the Scientific Basis for Nuclear Waste Management*, 2, Plenum Press, New York, **1980**.
56. Lloyd J. R., Macaskie L. E., *Applied and Environmental Microbiology*, **1996**, 62, 578-582.
57. Henrot J., *Health Physics*, **1989**, 57, 239-245.
58. Hess N. J., Xia Y. X., Rai D., Conradson S. D., *Journal of Solution Chemistry*, **2004**, 33, 199-226.
59. Ashley K. R., Whitener G. D., Schroeder N. C., Ball J. R., Radzinski S. D., *Solvent Extraction and Ion Exchange*, **1998**, 16, 843-859.
60. Delcul G. D., Bostick W. D., Trotter D. R., Osborne P. E., *Separation Science and Technology*, **1993**, 28, 551-564.
61. Gu B. H., Brown G. M., Bonnesen P. V., Liang L. Y., Moyer B. A., Ober R., Alexandratos S. D., *Environmental Science & Technology*, **2000**, 34, 1075-1080.
62. Goh K.-H., Lim T.-T., Dong Z., *Water Research*, **2008**, 42, 1343-1368.
63. Kang M. J., Rhee S. W., Moon H., Neck V., Fanghanel T., *Radiochimica Acta*, **1996**, 75, 169-173.
64. Wang S., Alekseev E. V., Juan D., Casey W. H., Phillips B. L., Depmeier W., Albrecht-Schmitt T. E., *Angewandte Chemie-International Edition*, **2010**, 49, 1057-1060.
65. Fei H., Bresler M. R., Oliver S. R. J., *Journal of the American Chemical Society*, **2011**, 133, 11110-11113.
66. Gu B. H., Dowlen K. E., Liang L. Y., Clausen J. L., *Separations Technology*, **1996**, 6, 123-132.

67. Li D., Kaplan D. I., Knox A. S., Crapse K. P., Diprete D. P., *Journal of Environmental Radioactivity*, **2014**, *136*, 56-63.
68. Wang Y. F., Gao H. Z., Yeredla R., Xu H. F., Abrecht M., *Journal of Colloid and Interface Science*, **2007**, *305*, 209-217.
69. Vinsova H., Vecernik P., Jedinakova-Krizova V., *Radiochimica Acta*, **2006**, *94*, 435-440.
70. Fryxell G. E., *Synthesis of Nanostructure Hybrid Sorbent Materials in Environmental Applications of Nanomaterials: Synthesis, Sorbents and Sensors*, Imperial College Press, **2007**.
71. Ponder S. M., Darab J. G., Mallouk T. E., *Environmental Science & Technology*, **2000**, *34*, 2564-2569.
72. Darab J. G. *et al.*, *Chemistry of Materials*, **2007**, *19*, 5703-5713.
73. Mattigod S. V., Fryxell G. E., Alford K., Gilmore T., Parker K., Serne J., Engelhard M., *Environmental Science & Technology*, **2005**, *39*, 7306-7310.
74. Liu J., Feng X. D., Fryxell G. E., Wang L. Q., Kim A. Y., Gong M. L., *Advanced Materials*, **1998**, *10*, 161-166.
75. Kresge C. T., Leonowicz M. E., Roth W. J., Vartuli J. C., Beck J. S., *Nature*, **1992**, *359*, 710-712.
76. Beck J. S. *et al.*, *Journal of the American Chemical Society*, **1992**, *114*, 10834-10843.
77. Kruk M., Jaroniec M., Kim J. H., Ryoo R., *Langmuir*, **1999**, *15*, 5279-5284.
78. Ravikovitch P. I., Vishnyakov A., Neimark A. V., Carrott M., Russo P. A., Carrott P. J., *Langmuir*, **2006**, *22*, 513-516.
79. Sonwane C. G., Bhatia S. K., *Journal of Physical Chemistry B*, **2000**, *104*, 9099-9110.

80. Neimark A. V., Ravikovitch P. I., Grun M., Schuth F., Unger K. K., *Journal of Colloid and Interface Science*, **1998**, *207*, 159-169.
81. Carrott M., Candeias A. J. E., Carrott P. J. M., Ravikovitch P. I., Neimark A. V., Sequeira A. D., *Microporous and Mesoporous Materials*, **2001**, *47*, 323-337.
82. Mokaya R., *Journal of Physical Chemistry B*, **1999**, *103*, 10204-10208.
83. Zhao X. S., Lu G. Q., Whittaker A. K., Millar G. J., Zhu H. Y., *Journal of Physical Chemistry B*, **1997**, *101*, 6525-6531.
84. Jentys A., Kleestorfer K., Vinek H., *Microporous and Mesoporous Materials*, **1999**, *27*, 321-328.
85. Zhuravlev L. T., *Langmuir*, **1987**, *3*, 316-318.
86. Landmesser H., Kosslick H., Storek W., Fricke R., *Solid State Ionics*, **1997**, *101*, 271-277.
87. Cassiers K., Linssen T., Mathieu M., Benjelloun M., Schrijnemakers K., Van Der Voort P., Cool P., Vansant E. F., *Chemistry of Materials*, **2002**, *14*, 2317-2324.
88. Xu X. C., Song C. S., Andresen J. M., Miller B. G., Scaroni A. W., *Microporous and Mesoporous Materials*, **2003**, *62*, 29-45.
89. Corma A., *Chemical Reviews*, **1997**, *97*, 2373-2419.
90. Walcarius A., Collinson M. M., *Annual Review of Analytical Chemistry*, **2009**, *2*, 121-143.
91. Slowing, II, Trewyn B. G., Giri S., Lin V. S. Y., *Advanced Functional Materials*, **2007**, *17*, 1225-1236.
92. Fryxell G. E., Lin Y. H., Wu H., Kemner K. M., *Nanoporous Materials III*, **2002**, *141*, 583-590.
93. Fryxell G. E., Liu J., Mattigod S., *Materials Technology*, **1999**, *14*, 188-191.

94. Olkhovyk O., Jaroniec M., *Chemically-Modified Mesoporous Silicas and Organosilicas for Adsorption and Detection of Heavy Metal Ions in Environmental Applications of Nanomaterials. Synthesis, Sorbents and Sensors*, Imperial College Press, **2007**.
95. Chen X. B., Feng X. D., Liu J., Fryxell G. E., Gong M. L., *Separation Science and Technology*, **1999**, *34*, 1121-1132.
96. Fryxell G. E., Lin Y. H., Fiskum S., Birnbaum J. C., Wu H., Kemner K., Kelly S., *Environmental Science & Technology*, **2005**, *39*, 1324-1331.
97. Lin Y. H., Fryxell G. E., Wu H., Engelhard M., *Abstracts of Papers of the American Chemical Society*, **2001**, *222*, 3962-3966.
98. Mattigod S. V., Fryxell G. E., Serne R. J., Parker K. E., *Radiochimica Acta*, **2003**, *91*, 539-545.
99. Tanev P. T., Chibwe M., Pinnavaia T. J., *Nature*, **1994**, *368*, 321-323.
100. Chen Y. C., Huang X. C., Luo Y. L., Chang Y. C., Hsieh Y. Z., Hsu H. Y., *Science and Technology of Advanced Materials*, **2013**, *14*, 044407.
101. Walcarius A., Mercier L., *Journal of Materials Chemistry*, **2010**, *20*, 4478-4511.
102. Burkett S. L., Sims S. D., Mann S., *Chemical Communications*, **1996**, 1367-1368.
103. Caravajal G. S., Leyden D. E., Quinting G. R., Maciel G. E., *Analytical Chemistry*, **1988**, *60*, 1776-1786.
104. Mello M. R., Phanon D., Silveira G. Q., Llewellyn P. L., Ronconi C. M., *Microporous and Mesoporous Materials*, **2011**, *143*, 174-179.
105. Fryxell G. E., Liu J., Hauser T. A., Nie Z. M., Ferris K. F., Mattigod S., Gong M. L., Hallen R. T., *Chemistry of Materials*, **1999**, *11*, 2148-2154.
106. Yoshitake H., Yokoi T., Tatsumi T., *Chemistry of Materials*, **2003**, *15*, 1713-1721.

107. Yoshitake H., Yokoi T., Tatsumi T., *Chemistry of Materials*, **2002**, *14*, 4603-4610.
108. Stephan H. *et al.*, *Anion Separations: Fundamentals and Applications*, Kluwer, New York, **2003**.
109. Alberti G., Amendola V., Bergamaschi G., Colleoni R., Milanese C., Biesuz R., *Dalton Transactions*, **2013**, *42*, 6227-6234.
110. Kelly S. D., Kemmer K. M., Fryxell G. E., Liu J., Mattigod S. V., Ferris K. F., *Journal of Physical Chemistry B*, **2001**, *105*, 6337-6346.
111. Mattigod S. V., Fryxell G. E., Parker K. E., *Inorganic Chemistry Communications*, **2007**, *10*, 646-648.
112. Chouyyok W., Wiacek R. J., Pattamakomsan K., Sangvanich T., Grudzien R. M., Fryxell G. E., Yantasee W., *Environmental Science and Technology*, **2010**, *44*, 3073-3078.
113. Yokoi T., Tatsumi T., Yoshitake H., *Journal of Colloid and Interface Science*, **2004**, *274*, 451-457.
114. Yoshitake H., *New Journal of Chemistry*, **2005**, *29*, 1107-1117.
115. Born M., Oppenheimer R., *Annalen der Physik*, **1927**, *84*, 0457-0484.
116. Cramer C. J., *Essentials of Computational Chemistry: Theories and Models* John Wiley & Sons, **2002**.
117. Hohenberg P., Kohn W., *Physical Review B*, **1964**, *136*, B864-B871.
118. Kohn W., Sham L. J., *Physical Review*, **1965**, *140*, 1133-1138.
119. Becke A. D., *Physical Review A*, **1988**, *38*, 3098-3100.
120. Lee C. T., Yang W. T., Parr R. G., *Physical Review B*, **1988**, *37*, 785-789.
121. Becke A. D., *Journal of Chemical Physics*, **1993**, *98*, 5648-5652.

122. Boys S. F., *Proceedings of the Royal Society of London Series A*, **1950**, *200*, 542-544.
123. Hehre W. J., Stewart R. F., Pople J. A., *Journal of Chemical Physics*, **1969**, *51*, 2657-2664.
124. Krishnan R., Binkley J. S., Seeger R., Pople J. A., *Journal of Chemical Physics*, **1980**, *72*, 650-654.
125. Francl M. M., Pietro W. J., Hehre W. J., Binkley J. S., Gordon M. S., Defrees D. J., Pople J. A., *Journal of Chemical Physics*, **1982**, *77*, 3654-3665.
126. Schlegel H. B., *Journal of Computational Chemistry*, **1982**, *3*, 214-218.
127. Allen M. P., Tildesley D. J., *Computer Simulation of Liquids*, Oxford: Clarendon Press, **1989**.
128. Frenkel D., Smit B., *Understand Molecular Simulation: From Algorithms to Applications*, 2nd Ed., Academic Press, **2001**.
129. Metropolis N., Rosenbluth A. W., Rosenbluth M. N., Teller A. H., Teller E., *Journal of Chemical Physics*, **1953**, *21*, 1087-1092.
130. Verlet L., *Physical Review*, **1967**, *159*, 98-103.
131. Hockney R., *The potential calculation and some applications in Methods in Computational Physics*, *9*, Academic Press, **1970**.
132. Evans D. J., Morriss G., *Statistical Mechanics of Nonequilibrium Liquids*, 2nd Ed., Cambridge University Press, **2008**.
133. Ryckaert J. P., Ciccotti G., Berendsen H. J. C., *Journal of Computational Physics*, **1977**, *23*, 327-341.
134. Steinbach P. J., Brooks B. R., *Journal of Computational Chemistry*, **1994**, *15*, 667-683.
135. Abramowitz M., Stegun I. A., *Handbook of Mathematical Functions*, Dover, **1970**.

136. Smith W., *CCP5 Information Quarterly for Computer Simulation of Condensed Phases*, **1986**, 21, 37-45.
137. Fuchs K., Wills H. H., *Proceedings of the Royal Society of London Series A*, **1935**, 151, 0585-0602.
138. Torrie G. M., Valleau J. P., *Chemical Physics Letters*, **1974**, 28, 578-581.
139. Torrie G. M., Valleau J. P., *Journal of Computational Physics*, **1977**, 23, 187-199.
140. Frisch M. J. *et al.*, *Gaussian 09, Revision D.02*, Gaussian Inc., **2009** Wallingford, CT.
141. Smith W., Forester T. R., *Journal of Molecular Graphics*, **1996**, 14, 136-141.
142. Purton J. A., Crabtree J. C., Parker S. C., *Molecular Simulation*, **2013**, 39, 1240-1252.
143. Hoover W. G., *Physical Review A*, **1985**, 31, 1695-1697.
144. Melchionna S., Ciccotti G., Holian B. L., *Molecular Physics*, **1993**, 78, 533-544.
145. Atkins P., De Paula J., *Physical Chemistry*, 8th Ed., University Press, **2006**.
146. Krebs B., Hasse K. D., *Acta Crystallographica Section B-Structural Science*, **1976**, 32, 1334-1337.
147. Weigend F., Ahlrichs R., *Physical Chemistry Chemical Physics*, **2005**, 7, 3297-3305.
148. Andrae D., Haussermann U., Dolg M., Stoll H., Preuss H., *Theoretica Chimica Acta*, **1990**, 77, 123-141.
149. Ujaque G., Maseras F., Lledos A., *International Journal of Quantum Chemistry*, **2000**, 77, 544-551.
150. Zhao Y., Truhlar D. G., *Theoretical Chemistry Accounts*, **2008**, 120, 215-241.

151. Gancheff J., Kremer C., Kremer E., Ventura O. N., *Journal of Molecular Structure-Theochem*, **2002**, 580, 107-116.
152. Housecroft C., Sharpe A. G., *Inorganic Chemistry*, 3rd Ed., Prentice Hall, **2007**.
153. Guggenheim E. A., *Journal of Physical Chemistry*, **1929**, 33, 842-849.
154. Marcus Y., *Ions in Water and Biophysical Implications: From Chaos to Cosmos*, Springer, **2012**.
155. Marcus Y., *Ion Properties*, Dekker, **1997**.
156. Cramer C. J., Truhlar D. G., *Continuum Solvation Models: Classical and Quantum Mechanical Implementations*, in *Reviews in Computational Chemistry*, John Wiley & Sons, **2007**.
157. Miertus S., Scrocco E., Tomasi J., *Chemical Physics*, **1981**, 55, 117-129.
158. Barone V., Cossi M., *Journal of Physical Chemistry A*, **1998**, 102, 1995-2001.
159. Marenich A. V., Cramer C. J., Truhlar D. G., *Journal of Physical Chemistry B*, **2009**, 113.
160. Rappe A. K., Casewit C. J., Colwell K. S., Goddard W. A., Skiff W. M., *Journal of the American Chemical Society*, **1992**, 114, 10024-10035.
161. Barone V., Cossi M., Tomasi J., *Journal of Chemical Physics*, **1997**, 107, 3210-3221.
162. Takano Y., Houk K. N., *Journal of Chemical Theory and Computation*, **2005**, 1, 70-77.
163. Huige C. J. M., Altona C., *Journal of Computational Chemistry*, **1995**, 16, 56-79.
164. Singh U. C., Kollman P. A., *Journal of Computational Chemistry*, **1984**, 5, 129-145.

165. Besler B. H., Merz K. M., Kollman P. A., *Journal of Computational Chemistry*, **1990**, *11*, 431-439.
166. Jorgensen W. L., Tiradorives J., *Journal of the American Chemical Society*, **1988**, *110*, 1657-1666.
167. Cundari T. R., Fu W. T., *Inorganica Chimica Acta*, **2000**, *300*, 113-124.
168. Jorgensen W. L., Chandrasekhar J., Madura J. D., Impey R. W., Klein M. L., *Journal of Chemical Physics*, **1983**, *79*, 926-935.
169. Berendsen H. J. C., Grigera J. R., Straatsma T. P., *Journal of Physical Chemistry*, **1987**, *91*, 6269-6271.
170. Cannon W. R., Pettitt B. M., McCammon J. A., *Journal of Physical Chemistry*, **1994**, *98*, 6225-6230.
171. Lamoureux G., Roux B., *Journal of Physical Chemistry B*, **2006**, *110*, 3308-3322.
172. Horinek D., Mamatkulov S. I., Netz R. R., *Journal of Chemical Physics*, **2009**, *130*, 21.
173. Joung I. S., Cheatham T. E., III, *Journal of Physical Chemistry B*, **2008**, *112*, 9020-9041.
174. Nightingale E. R., *Journal of Physical Chemistry*, **1959**, *63*, 1381-1387.
175. Einstein A., *Annalen der Physik*, **1905**, *17*, 549-560.
176. Harris K. R., Woolf L. A., *Journal of the Chemical Society-Faraday Transactions I*, **1980**, *76*, 377-385.
177. Angel Gonzalez M., Abascal J. L. F., *Journal of Chemical Physics*, **2010**, *132*, 0961011-0961012
178. Rai N., Tiwari S. P., Maginn E. J., *Journal of Physical Chemistry B*, **2012**, *116*, 10885-10897.

179. Deeth R. J., Fey N., *Journal of Computational Chemistry*, **2004**, *25*, 1840-1848.
180. Cramer C. J., Truhlar D. G., *Physical Chemistry Chemical Physics*, **2009**, *11*, 10757-10816.
181. Rizzo R. C., Jorgensen W. L., *Journal of the American Chemical Society*, **1999**, *121*, 4827-4836.
182. Cornell W. D. *et al.*, *Journal of the American Chemical Society*, **1996**, *118*, 2309-2309.
183. Wiesemann F., Teipel S., Krebs B., Howeler U., *Inorganic Chemistry*, **1994**, *33*, 1891-1898.
184. Curtiss L. A., Halley J. W., Hautman J., Rahman A., *Journal of Chemical Physics*, **1987**, *86*, 2319-2327.
185. Bonomi M. *et al.*, *Computer Physics Communications*, **2009**, *180*, 1961-1972.
186. Kumar S., Bouzida D., Swendsen R. H., Kollman P. A., Rosenberg J. M., *Journal of Computational Chemistry*, **1992**, *13*, 1011-1021.
187. Helm L., Merbach A. E., *Chemical Reviews*, **2005**, *105*, 1923-1959.
188. Feuston B. P., Higgins J. B., *Journal of Physical Chemistry*, **1994**, *98*, 4459-4462.
189. Maddox M. W., Gubbins K. E., *International Journal of Thermophysics*, **1994**, *15*, 1115-1123.
190. Maddox M. W., Olivier J. P., Gubbins K. E., *Langmuir*, **1997**, *13*, 1737-1745.
191. Kleestorfer K., Vinek H., Jentys A., *Journal of Molecular Catalysis a-Chemical*, **2001**, *166*, 53-57.
192. He Y. F., Seaton N. A., *Langmuir*, **2003**, *19*, 10132-10138.
193. Siperstein F. R., Gubbins K. E., *Langmuir*, **2003**, *19*, 2049-2057.

194. Jorge M., Gomes J. R. B., Natalia M., Cordeiro D. S., Seaton N. A., *Journal of the American Chemical Society*, **2007**, *129*, 15414-15415.
195. Jorge M., Gomes J. R. B., Cordeiro M., Seaton N. A., *Journal of Physical Chemistry B*, **2009**, *113*, 708-718.
196. Jin L., Auerbach S. M., Monson P. A., *Langmuir*, **2013**, *29*, 766-780.
197. Sonwane C. G., Jones C. W., Ludovice P. J., *Journal of Physical Chemistry B*, **2005**, *109*, 23395-23404.
198. Vanbeest B. W. H., Kramer G. J., Vansanten R. A., *Physical Review Letters*, **1990**, *64*, 1955-1958.
199. Camellone M. F., Reiner J., Sennhauser U., Schlapbach L., *Efficient Generation of Realistic Model Systems of Amorphous Silica*, **2011**, arXiv:1109.2852.
200. Guissani Y., Guillot B., *Journal of Chemical Physics*, **1996**, *104*, 7633-7644.
201. Coasne B., Hung F. R., Pellenq R. J. M., Siperstein F. R., Gubbins K. E., *Langmuir*, **2006**, *22*, 194-202.
202. Connolly M. L., *Journal of Applied Crystallography*, **1983**, *16*, 548-558.
203. Dueren T., Millange F., Ferey G., Walton K. S., Snurr R. Q., *Journal of Physical Chemistry C*, **2007**, *111*, 15350-15356.
204. Brunauer S., Emmett P. H., Teller E., *Journal of the American Chemical Society*, **1938**, *60*, 309-319.
205. Van der Vaart R., Huiskes C., Bosch H., Reith T., *Adsorption-Journal of the International Adsorption Society*, **2000**, *6*, 311-323.
206. Brodka A., Zerda T. W., *Journal of Chemical Physics*, **1996**, *104*, 6319-6326.
207. Coasne B., Galarneau A., Di Renzo F., Pellenq R. J. M., *Langmuir*, **2010**, *26*, 10872-10881.

208. Potoff J. J., Siepmann J. I., *Aiche Journal*, **2001**, 47, 1676-1682.
209. Hirschfelder J. O., Curtiss C. F., Bird R. B., *Molecular Theory of Gases and Liquids in Structure of Matter Series*, Wiley, **1964**.
210. Prausnitz J. M., Lichtenthaler R. N., de Azevedo E. G., *Molecular Thermodynamics of Fluid-Phase Equilibria*, Prentice Hall, **1998**.
211. Herdes C., Ferreiro-Rangel C. A., Duren T., *Langmuir*, **2011**, 27, 6738-6743.
212. Sing K. S. W., Everett D. H., Haul R. A. W., Moscou L., Pierotti R. A., Rouquerol J., Siemieniewska T., *Pure and Applied Chemistry*, **1985**, 57, 603-619.
213. Nicholson D., Parsonage N. G., *Computer Simulation and the Statistical Mechanics of Adsorption*, Academic Press, **1982**.
214. Ruthven D. M., *Principles of Adsorption and Adsorption Processes*, John Wiley & Sons, **1984**.
215. Steele W. A., *The Interactions of Gases with Solid Surfaces in The International Encyclopedia of Physical Chemistry and Chemical Physics*, Pergamon Press, **1974**.
216. Poling B. E., Prausnitz J. M., O'Connell J. P., *The properties of gases and liquids*, 5th Ed., McGraw-Hill Professional, **2000**.
217. Pellenq R. J. M., Nicholson D., *Journal of Physical Chemistry*, **1994**, 98, 13339-13349.
218. Chaffee A. L., *Fuel Processing Technology*, **2005**, 86, 1473-1486.
219. Schumacher C., Gonzalez J., Perez-Mendoza M., Wright P. A., Seaton N. A., *Industrial & Engineering Chemistry Research*, **2006**, 45, 5586-5597.
220. Williams J. J., Wiersum A. D., Seaton N. A., Duren T., *Journal of Physical Chemistry C*, **2010**, 114, 18538-18547.
221. Builes S., Vega L. F., *Journal of Physical Chemistry C*, **2012**, 116, 3017-3024.

222. Kosmulski M., *Journal of Colloid and Interface Science*, **2002**, 253, 77-87.
223. Carre A., Lacarriere V., *Contact Angle, Wettability and Adhesion*, **2006**, 4, 267-280.
224. Stimson L. M., Wilson M. R., *Journal of Chemical Physics*, **2005**, 123, 0349081-03490810.
225. Zhang L. Z., Jiang S. Y., *Journal of Chemical Physics*, **2002**, 117, 1804-1811.
226. Corry B., Chung S. H., *Cellular and Molecular Life Sciences*, **2006**, 63, 301-315.
227. Joshi R. K., Carbone P., Wang F. C., Kravets V. G., Su Y., Grigorieva I. V., Wu H. A., Geim A. K., Nair R. R., *Science*, **2014**, 343, 752-754.
228. Lorenz C. D., Travesset A., *Physical Review E*, **2007**, 75, 0612021-0612025
229. Lochhead M. J., Letellier S. R., Vogel V., *Journal of Physical Chemistry B*, **1997**, 101, 10821-10827.
230. Sushko M. L., Harding J. H., Shluger A. L., McKendry R. A., Watari M., *Advanced Materials*, **2008**, 20, 3848-3853.
231. Berka M., Banyai I., *Journal of Colloid and Interface Science*, **2001**, 233, 131-135.
232. Grahame D. C., *Journal of Chemical Physics*, **1953**, 21, 1054-1060.
233. Pitzer K. S., *Activity Coefficients in Electrolyte Solutions*, in *Ion interaction approach: theory and data correlation*, CRC Press, **1991**.
234. Plummer L. N., Parkhurst D. L., Fleming G. W., Dunkle S. A., *A Computer Program Incorporating Pitzer's Equations for Calculations of Geological Reactions in Brines*, US Geological Survey, **1988**.
235. Neck V., Konnecke T., Fanghanel T., Kim J. I., *Journal of Solution Chemistry*, **1998**, 27, 107-120.

236. Lamoureux G., Roux B., *Journal of Chemical Physics*, **2003**, *119*, 3025-3039.
237. Straatsma T. P., Berendsen H. J. C., *Journal of Chemical Physics*, **1988**, *89*, 5876-5886.
238. Johnson J. K., Panagiotopoulos A. Z., Gubbins K. E., *Molecular Physics*, **1994**, *81*, 717-733.
239. Turner C. H., Brennan J. K., Johnson J. K., Gubbins K. E., *Journal of Chemical Physics*, **2002**, *116*, 2138-2148.

Appendix One

Classical Force Field Parameters

The full set of classical force field parameters used in this work is provided in this appendix. References are given in the main text.

| Non-bonded | | | |
|------------------------------|-----------|-----------------------------------|-------------------------|
| <i>i</i> | $q_i (e)$ | $\epsilon_i (\text{kJ mol}^{-1})$ | $\sigma_i (\text{\AA})$ |
| O | -0.8476 | 0.650 | 3.166 |
| H | -0.4238 | - | - |
| Bonded | | | |
| O – H bond (\AA) | | 1.000 | |
| H – O – H angle ($^\circ$) | | 109.47 | |

Table A1.1 SPC/E water.

| Non-bonded | | | | |
|-------------------------------|-----------|--------------------------------------|-------------------------|-------|
| <i>i</i> | $q_i (e)$ | $\varepsilon_i (\text{kJ mol}^{-1})$ | $\sigma_i (\text{\AA})$ | |
| TcO ₄ ⁻ | Tc | 2.720 | 1.0080 | 2.655 |
| | O | -0.930 | 0.2090 | 3.860 |
| SO ₄ ²⁻ | S | 2.300 | 0.8370 | 3.550 |
| | O | -1.075 | 0.6500 | 3.250 |
| Cl ⁻ | | -1.000 | 0.0555 | 4.834 |

| Bond Stretch | | |
|---------------------|--|------------------------------|
| <i>i-j</i> | $k_r (\text{kJ mol}^{-1} \text{\AA}^{-2})$ | $r_{\text{eq}} (\text{\AA})$ |
| Tc-O | 2094.5 | 1.7045 |
| S-O | 2198.7 | 1.4870 |

| Angle Bend | | |
|-------------------|---|-------------------------------|
| <i>i-j-k</i> | $k_\theta (\text{kJ mol}^{-1} \text{rad}^{-2})$ | $\theta_{\text{eq}} (^\circ)$ |
| O-X-O | 585.8 | 109.47 |

Table A1.2 Hydrated ions.

| Non-bonded | | | |
|---------------------------------|--|--|--|
| <i>i</i> | <i>q_i</i> (<i>e</i>) | <i>ε_i</i> (kJ mol ⁻¹) | <i>σ_i</i> (Å) |
| Fe | 3.0000 | 0.4435 | * |
| N | -0.8400 | 0.7113 | 3.300 |
| C | 0.1500 | 0.2761 | 3.500 |
| H-[N] | 0.3600 | - | - |
| H-[C] | -0.0150 | 0.0627 | 2.500 |
| Equilibrium Bond Lengths | | | |
| <i>i-j</i> | <i>k_r</i> (kJ mol ⁻¹ Å ⁻²) | <i>r_{eq}</i> (Å) | |
| N-C | - | 1.448 | |
| C-C | - | 1.529 | |
| N-H | - | 1.010 | |
| C-H | - | 1.090 | |
| Angle Bend | | | |
| <i>i-j-k</i> | <i>k_θ</i> (kJ mol ⁻¹ rad ⁻²) | <i>θ_{eq}</i> (°) | |
| N-C-C | 470.28 | 109.47 | |
| N-C-H | 334.72 | 109.50 | |
| C-N-H | 292.88 | 109.50 | |
| C-C-H | 313.80 | 110.70 | |
| H-N-H | 364.84 | 106.40 | |
| H-C-H | 276.14 | 107.80 | |
| Torsion | | | |
| <i>i-j-k-l</i> | <i>v₁</i> (kJ mol ⁻¹) | <i>v₂</i> (kJ mol ⁻¹) | <i>v₃</i> (kJ mol ⁻¹) |
| N-C-C-H | -4.238 | -2.966 | 1.979 |
| H-N-C-C | -0.795 | -1.745 | 1.749 |
| H-N-C-H | - | - | 1.674 |
| H-C-C-H | - | - | 1.330 |

Table A1.3 Fe³⁺-EDA complexes. Ligand specific parameters for Fe³⁺ are given in Table A1.4.

| Ligand | σ_{Fe} (Å) |
|-----------------------------------|--|
| H ₂ O (O) | 1.465 |
| TcO ₄ ⁻ (O) | 2.600 |
| SO ₄ ²⁻ (O) | 1.820 |
| Cl ⁻ | 3.095 |
| Other atom types | 1.700 |

Table A1.4 Ligand specific σ parameters for Fe³⁺.

| $i-j$ | O-O | Si-O |
|----------------------------------|-----------|------------|
| A_{ij} (eV) | 1388.7730 | 18003.7572 |
| B_{ij} (\AA^{-1}) | 2.7600 | 4.8732 |
| C_{ij} (eV \AA^6) | 175.0000 | 133.5381 |
| D_{ij} (eV \AA^{12}) | 180.0000 | 20.0000 |
| E_{ij} (eV \AA^8) | 24.0000 | 6.0000 |

Table A1.5 MCM-41 model preparation.

| Parameters | O ^b | O ^{nb} | Si | H |
|-------------------------|----------------|-----------------|---------------|-------|
| σ_i (Å) | 2.70 | 3.00 | - | - |
| ε_i/k_B (K) | 300.0 | 300.0 | - | - |
| q_i (e) | -0.629 | -0.533 | 1.256 - 1.277 | 0.206 |

Table A1.6 MCM-41 adsorption simulations.

| | N ₂ | | CO ₂ | |
|-------------------------|------------------|--------|-----------------|--------|
| | N _{COM} | N | C | O |
| σ_i (Å) | - | 3.310 | 2.800 | 3.050 |
| ε_i/k_B (K) | - | 36.0 | 27.0 | 79.0 |
| q_i (e) | +0.964 | -0.482 | +0.700 | -0.350 |

Table A1.7 Three-site TraPPE models of the gas adsorbates.

| Parameters | N ₂ | CO ₂ | Ar | Kr |
|-------------------------|----------------|-----------------|-------|-------|
| σ_i (Å) | 3.798 | 3.941 | 3.405 | 3.636 |
| ε_i/k_B (K) | 71.4 | 195.2 | 119.8 | 166.4 |

Table A1.8 Single-site models of the gas adsorbates.

| Non-bonded | | | |
|--|---|-----------------------------------|------------------------------|
| <i>i</i> | $q_i (e)$ | $\epsilon_i (\text{kJ mol}^{-1})$ | $\sigma_i (\text{\AA})$ |
| Si | 1.2447 | - | - |
| CH ₂ | 0.0000 | 0.3820 | 3.950 |
| N | -0.7800 | 0.7113 | 3.300 |
| Equilibrium Bond Length | | | |
| <i>i-j</i> | $k_r (\text{kJ mol}^{-1} \text{\AA}^{-2})$ | $r_{\text{eq}} (\text{\AA})$ | |
| Si – CH ₂ | - | 1.910 | |
| CH ₂ – CH ₂ | - | 1.529 | |
| Angle Bend | | | |
| <i>i-j-k</i> | $k_\theta (\text{kJ mol}^{-1} \text{rad}^{-2})$ | $\theta_{\text{eq}} (^\circ)$ | |
| Si – CH ₂ – CH ₂ | 800.00 | 110.00 | |
| CH ₂ – CH ₂ – CH ₂ | 520.00 | 114.60 | |
| CH ₂ – CH ₂ – N | 470.28 | 109.47 | |
| CH ₂ – N – C | 433.46 | 107.20 | |
| Torsion | | | |
| <i>i-j-k-l</i> | $\nu_1 (\text{kJ mol}^{-1})$ | $\nu_2 (\text{kJ mol}^{-1})$ | $\nu_3 (\text{kJ mol}^{-1})$ |
| Si – CH ₂ – CH ₂ – CH ₂ | 5.903 | -1.134 | 13.158 |
| CH ₂ – CH ₂ – CH ₂ – N | 10.008 | -2.820 | 2.301 |
| CH ₂ – CH ₂ – N – C | 1.741 | -0.536 | 2.908 |

Table A1.9 Propyl chains linking MCM-41 to the Fe³⁺-EDA complex.

Appendix Two

MCM-41 Model Structural Data

| Pore Diameter (nm) | Wall Thickness (nm) | Lattice Parameter (nm) | Pore Length (nm) | Number of Atoms | Surface Silanol Density (OH nm ⁻²) | Surface Area (m ² g ⁻¹) | Pore Volume (cm ³ g ⁻¹) |
|--------------------|---------------------|------------------------|------------------|-----------------|--|--|--|
| 2.41 | 0.95 | 3.36 | 4.70 | 3770 | 6.97 | 994.3 | 0.43 |
| 2.81 | 0.93 | 3.74 | 4.70 | 4270 | 6.41 | 1023.5 | 0.51 |
| 3.16 | 0.95 | 4.11 | 4.70 | 4864 | 6.44 | 1010.0 | 0.56 |
| 3.50 | 0.96 | 4.46 | 4.68 | 5398 | 6.47 | 1018.0 | 0.62 |
| 3.85 | 0.95 | 4.80 | 4.64 | 5822 | 6.24 | 1028.0 | 0.68 |
| 4.17 | 0.94 | 5.11 | 4.60 | 6225 | 6.00 | 1053.3 | 0.74 |
| 4.46 | 0.96 | 5.43 | 4.55 | 6743 | 6.13 | 1026.7 | 0.78 |
| 4.76 | 0.96 | 5.72 | 4.50 | 7230 | 6.35 | 979.8 | 0.81 |
| 5.04 | 0.97 | 6.01 | 4.45 | 7559 | 5.86 | 1017.2 | 0.85 |
| 5.35 | 0.95 | 6.30 | 4.41 | 7935 | 5.89 | 1000.5 | 0.91 |
| 5.60 | 0.96 | 6.57 | 4.35 | 8360 | 6.07 | 979.7 | 0.93 |
| 5.90 | 0.95 | 6.86 | 4.32 | 8684 | 5.86 | 986.2 | 0.98 |

Table A2.1 Set of 12 MCM-41 models with varying pore diameters.

| Pore Diameter (nm) | Wall Thickness (nm) | Lattice Parameter (nm) | Pore Length (nm) | Number of Atoms | Surface Silanol Density (OH nm⁻²) | Surface Area (m² g⁻¹) | Pore Volume (cm³ g⁻¹) |
|---------------------------|----------------------------|-------------------------------|-------------------------|------------------------|---|--|--|
| 3.53 | 0.45 | 4.11 | 4.70 | 3444 | 5.87 | 1972.1 | 1.13 |
| 3.50 | 0.96 | 4.46 | 4.68 | 5398 | 6.47 | 1018.0 | 0.62 |
| 3.53 | 1.14 | 4.80 | 4.64 | 7246 | 6.11 | 704.2 | 0.43 |
| 3.56 | 1.45 | 5.11 | 4.60 | 9135 | 6.00 | 544.3 | 0.34 |
| 3.56 | 1.76 | 5.43 | 4.55 | 11121 | 5.78 | 427.0 | 0.27 |

Table A2.2 Set of 5 MCM-41 models with varying wall thicknesses.

| Quench Rate (K ps ⁻¹) | Pore Diameter (nm) | Wall Thickness (nm) | Lattice Parameter (nm) | Pore Length (nm) | Number of Atoms | Surface Silanol Density (OH nm ⁻²) | Surface Area (m ² g ⁻¹) | Pore Volume (cm ³ g ⁻¹) |
|--------------------------------------|-----------------------|------------------------|---------------------------|---------------------|-----------------|---|---|---|
| 1 | 3.53 | 0.93 | 4.46 | 4.68 | 5280 | 6.21 | 1047.3 | 0.64 |
| 2.5 | 3.52 | 0.94 | 4.46 | 4.68 | 5276 | 6.14 | 1052.6 | 0.64 |
| 5 | 3.53 | 0.94 | 4.47 | 4.68 | 5320 | 6.13 | 1040.4 | 0.63 |
| 10 | 3.50 | 0.96 | 4.46 | 4.68 | 5398 | 6.47 | 1018.0 | 0.62 |
| 25 | 3.49 | 0.95 | 4.44 | 4.67 | 5372 | 6.23 | 1030.9 | 0.61 |
| 50 | 3.50 | 0.94 | 4.44 | 4.65 | 5341 | 6.27 | 1016.5 | 0.62 |
| 100 | 3.47 | 0.95 | 4.42 | 4.64 | 5360 | 6.36 | 1001.4 | 0.60 |
| 250 | 3.46 | 0.95 | 4.41 | 4.62 | 5373 | 6.22 | 980.9 | 0.59 |
| 500 | 3.43 | 0.97 | 4.40 | 4.62 | 5420 | 6.52 | 969.8 | 0.58 |
| 7000 | 3.32 | 0.98 | 4.30 | 4.51 | 5465 | 6.01 | 904.8 | 0.51 |

Table A2.3 MCM-41 models with approximately the same pore diameter and wall thickness prepared at different quench rates.